

University of Windsor

## Scholarship at UWindor

---

Electronic Theses and Dissertations

Theses, Dissertations, and Major Papers

---

2005

### Quality control and improvement of the aluminum alloy castings for the next generation of engine block cast components.

Robin Francis  
*University of Windsor*

Follow this and additional works at: <https://scholar.uwindsor.ca/etd>

---

#### Recommended Citation

Francis, Robin, "Quality control and improvement of the aluminum alloy castings for the next generation of engine block cast components." (2005). *Electronic Theses and Dissertations*. 3250.  
<https://scholar.uwindsor.ca/etd/3250>

This online database contains the full-text of PhD dissertations and Masters' theses of University of Windsor students from 1954 forward. These documents are made available for personal study and research purposes only, in accordance with the Canadian Copyright Act and the Creative Commons license—CC BY-NC-ND (Attribution, Non-Commercial, No Derivative Works). Under this license, works must always be attributed to the copyright holder (original author), cannot be used for any commercial purposes, and may not be altered. Any other use would require the permission of the copyright holder. Students may inquire about withdrawing their dissertation and/or thesis from this database. For additional inquiries, please contact the repository administrator via email ([scholarship@uwindsor.ca](mailto:scholarship@uwindsor.ca)) or by telephone at 519-253-3000ext. 3208.

# **Quality Control and Improvement of the Aluminum Alloy Castings for the Next Generation of Engine Block Cast Components**

by

Robin Francis

A Dissertation

Submitted to the Faculty of Graduate Studies and Research through  
Industrial and Manufacturing Systems Engineering in Partial Fulfillment of  
the Requirements for the Degree of Doctor of Philosophy at the University  
of Windsor

Windsor, Ontario, Canada

2005

© 2005 Robin Francis



Library and  
Archives Canada

Bibliothèque et  
Archives Canada

Published Heritage  
Branch

Direction du  
Patrimoine de l'édition

395 Wellington Street  
Ottawa ON K1A 0N4  
Canada

395, rue Wellington  
Ottawa ON K1A 0N4  
Canada

*Your file* *Votre référence*

*ISBN: 0-494-09697-7*

*Our file* *Notre référence*

*ISBN: 0-494-09697-7*

#### NOTICE:

The author has granted a non-exclusive license allowing Library and Archives Canada to reproduce, publish, archive, preserve, conserve, communicate to the public by telecommunication or on the Internet, loan, distribute and sell theses worldwide, for commercial or non-commercial purposes, in microform, paper, electronic and/or any other formats.

The author retains copyright ownership and moral rights in this thesis. Neither the thesis nor substantial extracts from it may be printed or otherwise reproduced without the author's permission.

#### AVIS:

L'auteur a accordé une licence non exclusive permettant à la Bibliothèque et Archives Canada de reproduire, publier, archiver, sauvegarder, conserver, transmettre au public par télécommunication ou par l'Internet, prêter, distribuer et vendre des thèses partout dans le monde, à des fins commerciales ou autres, sur support microforme, papier, électronique et/ou autres formats.

L'auteur conserve la propriété du droit d'auteur et des droits moraux qui protègent cette thèse. Ni la thèse ni des extraits substantiels de celle-ci ne doivent être imprimés ou autrement reproduits sans son autorisation.

---

In compliance with the Canadian Privacy Act some supporting forms may have been removed from this thesis.

Conformément à la loi canadienne sur la protection de la vie privée, quelques formulaires secondaires ont été enlevés de cette thèse.

While these forms may be included in the document page count, their removal does not represent any loss of content from the thesis.

Bien que ces formulaires aient inclus dans la pagination, il n'y aura aucun contenu manquant.

  
**Canada**

## Abstract

This research focuses on the quality control and improvement of the W319 aluminum alloy engine blocks produced at the NEMAK Windsor Aluminum Plant (WAP). The present WAP Quality Control (QC) system was critically evaluated using the cause and effect diagram and therefore, a novel Plant Wide Quality Control (PWQC) system is proposed. This new QC system presents novel tools for off line as well as on line quality control. The off line tool uses heating curve analysis for the grading of the ingot suppliers. The on line tool utilizes Tukey control charts of the Thermal Analysis (TA) parameters for statistical process control. An Artificial Neural Network (ANN) model has also been developed for the on-line prediction and control of the Silicon Modification Level (SiML).

The student t-statistical analysis has shown that even small scale variations in the Fe and Mn levels significantly affect the shrink porosity level of the 3.0L V6 engine block bulkhead. When the Fe and Mn levels are closer to their upper specification limits (0.4 wt.% and 0.3wt.%, respectively), the probability of low bulkhead shrink porosity is as high as 0.73. Elevated levels of Sn (~0.04 wt.%) and Pb (~0.03 wt.%) were found to lower the Brinell Hardness (HB) of the V6 bulkhead after the Thermal Sand Removal (TSR) and Artificial Aging (AA) processes. Therefore, Sn and Pb levels must be kept below 0.0050 wt.% and 0.02 wt.%, respectively, to satisfy the bulkhead HB requirements.

The Cosworth electromagnetic pump reliability studies have indicated that the life of the pump has increased from 19,505 castings to 43,904 castings (225% increase) after the implementation of preventive maintenance. The optimum preventive maintenance period of the pump was calculated to be 43,000 castings.

The solution treatment parameters (temperature and time) of the Novel Solution Treatment during the Solidification (NSTS) Process were optimized using ANN and the Simulated Annealing (SA) algorithm. The optimal NSTS process (516<sup>0</sup>C and 66 minutes) would significantly reduce the present Thermal Sand Removal (TSR) time (4 hours) and would avoid the problem of incipient melting without sacrificing the mechanical properties.

In order to improve the cast component characteristics and to lower the alloy price, a new alloy, Al 332, (Si=10.5 wt.% & Cu=2 wt.%) was developed by optimizing

the Si and Cu levels of 3XX Al alloys as a replacement for the W319 alloy. The predicted as cast characteristics of the new alloy were found to satisfy the requirements of Ford engineering specification WSE-M2A-151-A2/A4.

## List of Intellectual Property (IP) Claims

The author claims that the following original ideas are his Intellectual Property (IP) that were developed within the scope of this dissertation.

- The gage R&R Studies for ALTAP and Alu-Delta.
- The development of Tukey control limits for the melt solidification parameters for on-line process control at WAP.
- Development of a novel method using the Artificial Neural Network (ANN) for the on-line prediction of the Silicon Modification Level (SiML) of the W319 alloy without using the information from the unmodified alloy.
- The statistical analysis of the WAP chemistry and identification of the effect of very small scale changes in Fe and Mn levels on the bulkhead porosity of the WAP 3.0L V6 engine blocks.
- Statistical analysis of the effect of the changes in Sn and Pb on the bulkhead hardness and the revision of the control limits of the impurity elements of the W319 alloy.
- Reliability studies on the electromagnetic pump that established pump life distribution and optimum preventive maintenance period for the pump.
- Optimization of the Solution Treatment time and temperature of the Novel Solution Treatment during Solidification (NSTS) process using Artificial Neural Network and the Simulated Annealing algorithm.
- Contribution to the idea of how to predict the Growth Restriction Factor (GRF) and hence the Grain Size of the 3XX series of Al-Si alloys using the Silicon Equivalency ( $Si_{EQ}$ ) methodology.
- Development of a statistical model to predict the latent heat of solidification of the 3XX Al alloys using the TA parameter(s).
- An idea to predict the Thermal Characteristics of the 3XX Alloys using the Artificial Neural Network (ANN).
- An idea to use the Thermal Analysis data and desirability function approach to optimize the levels of Si and Cu of the 3XX series of Al alloys and hence to develop a new alloy (Al 332) as a possible replacement for the W319 alloy presently used at

WAP. The predicted as-cast casting characteristics of the new alloy was found to satisfy the requirements of the Ford engineering specification while lowering the alloy price.

## **Dedication**

I dedicate this dissertation to the memory of Dr. Sourindra P. Dutta, who departed this world on a snowy, windy morning in January 2002, and whose intellect, thirst for knowledge and humour filled heart was always a great source of inspiration.....



## **Acknowledgements**

I would like to take this opportunity to express my sincere thanks to Dr. J. H. Sokolowski, for his guidance and for the financial support during my Ph.D. studies. I also would like to thank Dr. R.S. Lashkari, for accepting me as his Ph.D student and for his guidance. I also thank the members of my Ph.D. committee: Dr. M. Ahmadi, Dr. A. Alpas, Dr. M. Wang and Dr. G. Zhang for their advice.

Special thanks to Dr. M.B. Djurdjevic for his valuable contributions, advice and friendship during this work. Also, I am very grateful to Dr. W.T. Kierkus, Dr. M. Kasprzak, and Dr. W. Kasprzak for their contributions, support and help.

I very much appreciate the assistance of R. Smillie, J. Burford, D. Cusinato, G. Byczynski, B. Henderson and the Staff at the WAP Spec lab and at the NEMAK Engineering Centre (NEC) for their support and collaboration.

Thanks to J. Robinson, S. Budinsky and the Staff, Technical Support Centre, University of Windsor for their assistance during this project. I also want to thank Mrs. M. Aniolek for her assistance with test sample polishing and the Image Analysis.

I am very thankful to Dr. D. Emadi, CANMET, for his assistance with the microstructure analysis and the hardness testing of the 3XX test samples and to Dr. F. Major of Alcan International for the pricing of the 3XX Alloys.

Thanks to Ms. E. Moosberger for her help with the editing of this dissertation and to Ms. J. Mummery for all the administrative help.

I express my gratitude to the American Foundry Society (AFS), ASM International, and McGraw-Hill Inc. for allowing me to use figures from some of their publications in my dissertation.

Thanks to Mr. D. Yousif, Dr. F. Hernandez and other IRC colleagues for their help and for the nice time we had. I am also thankful to former IRC graduates: Graciela Pelayo Chagoya, Emma Mares de la O, and Xin Chen for their contributions.

Thanks to Dr. T. Bolisetti and K. Das for their friendship and help.

I am very indebted to my family: my parents Francis and Aleykkutty, my sister Rajy and her family, my brother Justin and my uncles and aunts for their prayers and continued moral support. Finally, I bow before the Almighty for giving me the strength to follow the wisdom, rather than my feelings.

# Table of Contents

<b>Abstract</b> .....	<b>iii</b>
<b>List of Intellectual Property (IP) Claims</b> .....	<b>v</b>
<b>Dedication</b> .....	<b>vii</b>
<b>Acknowledgements</b> .....	<b>viii</b>
<b>List of Figures</b> .....	<b>xiii</b>
<b>List of Tables</b> .....	<b>xvii</b>
<b>List of Acronyms</b> .....	<b>xix</b>
<b>1. Introduction</b> .....	<b>1</b>
<b>2. Literature Review</b> .....	<b>4</b>
2.1 Metallurgy of Hypoeutectic Aluminum Silicon Alloys .....	4
2.1.1 Key Alloying and Impurity Elements .....	4
2.1.1.1 Silicon .....	4
2.1.1.2 Copper .....	4
2.1.1.3 Magnesium.....	5
2.1.1.4 Iron .....	5
2.1.1.5 Tin and Lead .....	6
2.1.2 Melt Treatment and Processing.....	6
2.1.2.1 Grain Refinement.....	7
2.1.2.2 Eutectic Silicon Modification .....	7
2.1.2.3 Degassing .....	9
2.1.3 Porosity in Castings .....	9
2.2 Thermal Analysis (TA) .....	11
2.2.1 Aluminum Thermal Analysis Platform (AITAP).....	13
2.2.2 Universal Metallurgical Simulator and Analyzer (UMSA).....	14
2.3 Silicon Equivalency ( $Si_{EQ}$ ) Algorithm and its Applications .....	14
2.3.1 Calculation of the Thermal Characteristics of the 3XX Series of Al Alloys....	15
2.3.2 Calculation of the Latent Heat of Solidification .....	17
2.4 Introduction to Heat Treatment.....	17
2.4.1 Solution Treatment.....	18
2.4.2. Quenching .....	19
2.4.3 Aging.....	20
2.4.4 Literature Review on the Heat Treatment of the Al 319 alloy.....	22
2.4.5 Heat Treatment of the W319 Alloy at the Windsor Aluminum Plant (WAP)..	24
2.4.6. Introduction to the Novel Solution Treatment during Solidification Process(NSTS).....	25
2.5 Artificial Intelligence Applications in the Metal Casting Industry.....	30
2.5.1 Artificial Neural Network (ANN).....	31
2.6. Literature Review on the Application of Optimization Methods in Materials Science .....	33

<b>3. Introduction to the Cosworth Casting Process and the Quality Control System at Windsor Aluminum Plant (WAP).....</b>	<b>37</b>
3.1 Quiescent Mold Filling Techniques for Aluminum Cast Components.....	37
3.2 Description of the Cosworth Precision Sand Process .....	37
3.2.1 Mold and Core Making .....	38
3.2.2 Melting of Ingots, Scrap Blocks and Cut off Risers .....	40
3.2.3 Liquid Melt Processing .....	40
3.2.4 Casting/Pouring.....	41
3.2.5 Thermal Sand Removal (TSR) and Air Quenching .....	43
3.3 Analysis of the Present Quality Control System at WAP .....	47
3.3.1 Fishbone Diagram of the Present Quality Control (QC) System at WAP .....	47
3.3.2 Quality Control of the W319 Ingots .....	47
3.3.3 Quality Control of the W319 Melt.....	49
3.3.4 Quality Control of the Engine Blocks.....	49
3.3.5 Quality Control of the Cosworth Pump .....	51
3.4 Assessment and Critique of the Present QC System at WAP.....	53
3.5 Proposed Novel Plant Wide Quality Control (PWQC) System for WAP .....	55
3.6 Project Objectives .....	57
<b>4. Experiments and Measurements Involving the W319 Alloy used at the Windsor Aluminum Plant (WAP).....</b>	<b>59</b>
4.1 Introduction .....	59
4.2 Chemical Composition and Specifications of the W319 Alloy .....	61
4.3 Windsor Aluminum Plant Data.....	61
4.3.1 Chemical Composition of the W319 Alloy.....	61
4.3.2 Hydrogen Measurements of the Melt.....	61
4.3.3 Brinell Hardness of the Cast Component.....	63
4.3.4 Casting Porosity by X-Ray Radiographic Analysis .....	63
4.3.5 Cosworth Pump Profile and Pump Maintenance Records .....	65
4.4 Experiments at the Windsor Aluminum Plant .....	65
4.4.1 Thermal Analysis Using the Unbiased Melt Sampling Device (UMSD) and the Aluminum Thermal Analysis Platform (AITAP).....	65
4.5 Experiments and Measurements Performed at the University of Windsor Casting Laboratory (UWCL) .....	67
4.5.1 Thermal Analysis Using the Universal Metallurgical Simulator and Analyzer (UMSA) .....	67
4.5.2 Metallographic Analysis of the Test Samples.....	68
4. 6 Previous IRC Experiments.....	70
4. 6.1 Thermal Analysis Experiments for the On-line Prediction of the Silicon Modification Level (SiML) of the W319 alloy.....	72
4.6.2 Novel Solution Treatment during Solidification (NSTS) Experiments of the W319 Alloy.....	72
<b>5. Experiments And Measurements Involving The 3xx Series of Al Alloys.....</b>	<b>75</b>
5.1 Introduction .....	75
5.2 Preparation of the 3XX Series of Al Alloys and their Chemical Compositions.....	75

5.3. Thermal Analysis (TA) of the 3XX Series of Al Alloys Using AITAP .....	76
5.4 Measurements and Metallurgical Characterization of the 3XX Series of Alloys...	76
5.4.1 Secondary Dendrite Arm Spacing (SDAS).....	76
5.4.2 Grain Size.....	78
5.4.3 Brinell Hardness.....	78
5.4.4 Latent Heat of Solidification.....	78
<b>6. Results And Discussions of the Experiments And Measurements Involving The W319 Al Alloy Used At WAP.....</b>	<b>80</b>
6.1 Introduction.....	80
6.2 Thermal Characterization of the Ingot, Melt and Engine Block Bulkhead Samples using the UMSA.....	80
6.2.1 Grading of the Ingot Suppliers for Consistent Casting Properties.....	84
6.3 Thermal Analysis of the WAP Melt .....	87
6.3.1 Repeatability and Reproducibility (R&R) Studies of AITAP and Alu-Delta...	87
6.3.2 Thermal Analysis of the WAP Melt Using AITAP .....	93
6.3.2.1 Process Capability Analysis of the WAP process.....	93
6.3.2.2 Development of the Tukey Control limits of the TA Parameters for the Statistical Process Control at WAP.....	98
6.4 Development of a Novel Methodology for the On-line Prediction of the Melt Silicon Modification Level (SiML) Using Artificial Neural Networks and Thermal Analysis.....	99
6.4.1 Introduction.....	99
6.4.2 Selection of the Input Parameters of the ANN .....	104
6.4.2.1 Analysis and Pre-processing of the Data .....	106
6.4.3 Neural Network Training .....	106
6.4.3.1 Multilayer Perceptron Neural Network (MLP).....	106
6.4.3.2 Radial Basis Function Networks (RBF).....	107
6.4.4. Testing of the Trained Neural Network .....	109
6.5 Analysis of the WAP Melt Chemistry .....	113
6.5.1 The Effect of Melt Chemistry on Casting Porosity.....	113
6.5.1.1 Image Analysis of the TA Samples with High and Low Levels of Fe and Mn .....	120
6.5.2 Effect of Melt Chemistry on the Hardness and Heat Treatability of the Engine Block .....	124
6.5.2.1 Statistical Analysis of the Relationship between Engine Block Bulkhead Hardness and the Chemical Composition .....	124
6.5.2.2 Thermal Characterization of the Soft Engine Block Samples .....	128
6.5.2.3 Image Analysis of the WAP Soft Engine Block Bulkhead Samples. ....	128
6.5.2.4 Matrix Microhardness Measurements of the Engine Block Samples with Elevated Levels of Sn and Pb .....	131
6.6 Analysis of the Electromagnetic Pump Performance and Reliability.....	139
6.6.1 Reliability Studies of the Pump .....	139
6.6.1.1 Calculation of the cost savings from Preventive Maintenance .....	144
6.6.1.2 Optimization of the Preventive Maintenance Time of the Pump.....	144
6.6.2 Analysis of the Voltage and Fill Profiles of the Pump .....	147

6.7 Optimization of the Solution Treatment Parameters of the Novel Solution Treatment During Solidification Process Using Artificial Neural Networks and Simulated Annealing Algorithm .....	147
6.7.1 Introduction.....	147
6.7.2. Steps for the Optimization of the NSTS Process .....	150
6.7.2.1 Experiments for the Database Collection.....	150
6.7.2.2 Modeling of the NSTS Process Using the Artificial Neural Networks (ANN) .....	150
6.7.2.3 Searching for an Optimal Solution Using Simulated Annealing (SA) Algorithm .....	151
6.7.2.4 Verification of the Optimal Solution Treatment Parameters by Experimentation .....	159
<b>7. Optimization of the Si and Cu levels of the 3XX Al Alloys for the Future Generation of Engine Blocks.....</b>	<b>161</b>
7.1 Introduction.....	161
7.2 Novel Algorithm for the Prediction of the Grain Growth Restriction Factor (GRF) and the Grain Size (GS) of Multicomponent Al-Si Alloys Using the Silicon Equivalency ( $Si_{EQ}$ ) Algorithm. ....	161
7.3 Thermal Analysis (TA) of the 3XX Al Alloys .....	165
7.3.1 Prediction of the TA Parameters Using Artificial Neural Networks (ANN)..	170
7.4 Optimization of the Si and Cu levels of the 3XX Aluminum Alloys .....	174
7.4.1 Secondary Dendrite Arm Spacing (SDAS) and Grain Size.....	174
7.4.2 Solidification Range.....	177
7.4.3. Latent Heat of Solidification.....	177
7.4.4 Brinell Hardness.....	178
7.4.5 Price of the Alloy .....	178
7.4.6 Optimization of the Si and Cu Contents of the 3XX Aluminum Alloys Using the Desirability Function Approach.....	178
<b>8. Conclusions And Recommendations.....</b>	<b>183</b>
8.1 Introduction.....	183
8.2 Scope for Future Work.....	187
<b>Appendix1: Calibration of The Thermal Analysis Platform.....</b>	<b>189</b>
<b>Appendix 2: Determination of Characteristic Thermal Analysis Parameters.....</b>	<b>208</b>
<b>References.....</b>	<b>214</b>
<b>VITA AUCTORIS.....</b>	<b>228</b>

## List of Figures

<b>Figure 2. 1:</b> SEM micrographs of the silicon crystals in an unmodified sample of the Al 356 alloy following deep etching (Bäckerud et al., 1990).....	8
<b>Figure 2.2:</b> SEM micrographs of the silicon crystals in a modified sample of the Al 356 alloy following deep etching (Bäckerud et al., 1990).....	8
<b>Figure 2.3:</b> Hardness as a function of aging time and temperature for the Al-4Cu Alloy. This alloy was solution treated for 48 hours at 520 <sup>0</sup> C, then water quenched to 25 <sup>0</sup> C (ASM International, 1992).....	21
<b>Figure 2.4:</b> Variation of the yield stress, and formation of precipitates with aging time (schematic drawing) (Dieter,1976).....	21
<b>Figure 2.5:</b> (a) Heating and cooling curves of the W319 alloy; (b) First Derivative versus Temperature curve.....	26
<b>Figure 2.6:</b> Comparison of the tensile properties of the heat treated WAP V6 3.0L engine blocks and test samples after the NSTS process at 510 <sup>0</sup> C for 30 minutes followed by Artificial Aging (AA) at 200 <sup>0</sup> C for 2 hours (Chen, 2003).....	29
<b>Figure 2.7:</b> Comparison between the solution times of (a) the NSTS process and (b) the conventional solution treatment process.....	29
<b>Figure 3.1:</b> Photograph of the zircon sand mold of a 3.0L V6 engine block, with its top cover removed. (a) Front view, (b) Top view.....	39
<b>Figure 3.2:</b> Preparation and processing of the melt before casting (Cosworth Technology, 2004b).....	42
<b>Figure 3.3:</b> Closed loop feedback control system for the precise and repeatable casting process (Cosworth Technology, 2004b).....	42
<b>Figure 3.4:</b> (a) Fill level and (b) voltage profiles of the electromagnetic pump for a V6 3.0L engine block.....	44
<b>Figure 3.5:</b> The schematic of the roll over process (Cosworth Technology, 2004b).....	44
<b>Figure 3.6:</b> Comparison of the mechanical properties of the bulkheads of the V8 engine blocks produced by Montupet's SHLP process and WAP's CPSP process.....	46
<b>Figure 3.7:</b> Fishbone Diagram of the present Quality Control (QC) system at WAP.....	48
<b>Figure 3.8:</b> Standard chart for the Reduced Pressure Test (WSE-M2A-151-a2/a4 Specification).....	50
<b>Figure 3.9:</b> Cosworth Casting Process Flow Diagram (Including Quality Control test sample types and locations).....	52
<b>Figure 3.10:</b> Fishbone diagram of the Novel Plant Wide Quality Control Program.....	56
<b>Figure 4.1:</b> Flow Diagram of the novel plant wide testing and sampling program for WAP.....	60
<b>Figure 4.2:</b> The picture of the V6 engine block showing the critical locations (marked X) where the lower hardness values are expected.....	64
<b>Figure 4.3:</b> Dimensions of the UMSD cup.....	66
<b>Figure 4.4:</b> Schematic diagram explaining the Unbiased Melt Sampling Device (UMSD) sampling method.....	66
<b>Figure 4.5:</b> (a) Photograph of the UMSA test sample; (b) Dimensions in mm of the UMSA test sample.....	69
<b>Figure 4.6:</b> The locations in (a) the ingot and (b) the cylindrical permanent mold melt test bar from where the UMSA samples were machined. (c) bulkhead of a V6 block from where the UMSA test sample was excised.....	69

<b>Figure 4.7:</b> Interactive image analysis technique to quantify the morphology of the Fe rich phases present in the TA test samples.....	71
<b>Figure 4.8:</b> Schematic diagram of the thermal cycles performed during the NSTS process of the W319 alloy. Arrows present the changes in the temperature and time of the processes. The NSTS process is followed by 2 weeks of natural aging (Chen et al., 2003).....	74
<b>Figure 6.1:</b> Temperature versus. First Derivative plot of the Ingot, Melt and Engine Block Samples from April, 25, 2003.....	85
<b>Figure 6.2:</b> Temperature Vs. Fraction Solid plot of the Ingot, Melt and Block Samples from April, 25, 2003.....	86
<b>Figure 6.3:</b> Comparison of the start temperature of alloy melting ( $T_m$ ) of the ingot samples supplied by Alcoa, Alchem and Wabash.....	88
<b>Figure 6.4:</b> Two stage balanced nested design for the R&R studies.....	90
<b>Figure 6.5:</b> Percentage contribution made by each variance component to the Total variability for ALTAP and Alu-Delta.....	91
<b>Figure 6.6:</b> Run chart of the Brinell Hardness for the hit location 6 (shown in inset) of the 3.0L V6 Engine block bulkhead during the period April to June 2003.....	94
<b>Figure 6.7:</b> Run chart of the shrinkage porosity levels of bulkhead section 4 (shown in the inset) of the 3.0L V6 engine blocks during the period April to June 2003.....	94
<b>Figure 6.8:</b> Run chart of the shrinkage porosity levels of bulkhead section 7 (shown in the inset) of the 3.0L V6 engine blocks during the period April to June 2003.....	95
<b>Figure 6.9:</b> Minitab output of the process capability analysis of the bulkhead hardness data from April to June, 2003.....	95
<b>Figure 6.10:</b> Minitab output of the process capability analysis of the shrinkage porosity data of the bulkhead section 4 from April to June, 2003.....	96
<b>Figure 6.11:</b> Minitab output of the Process Capability Analysis of the shrinkage porosity data of the bulkhead section 7 from April to June, 2003.....	96
<b>Figure 6.12:</b> Tukey control chart for the Al-Si eutectic nucleation temperature.....	100
<b>Figure 6.13:</b> Representative Si structure morphologies corresponding to the AFS chart for Hypoeutectic Aluminum Silicon Alloys. (1) Fully unmodified microstructure; (2) Lamellar microstructure; (3) Partially modified microstructure;(4) Absence of the lamellar microstructure; (5) Fibrous silicon eutectic structure, (6) Very Fine Structure (Zalensas, 1993).....	101
<b>Figure 6.14:</b> Calculation of the $\Delta T$ by using the cooling curves of the unmodified and modified W319 Al alloy (IRC Brochure 2004b).....	103
<b>Figure 6.15:</b> Performance of the MLP network on the test data.....	110
<b>Figure 6.16:</b> Performance of the RBF network on the test data.....	110
<b>Figure 6.17:</b> (a) Locations of bulkhead sections 4 and 7 in a 3.0L V6 Engine block, (b) Cross section view of a bulk head section (c) X-Radiographs of bulkhead sections with porosity levels s1, s3 and s4.....	114
<b>Figure 6.18:</b> Comparison of the percentages of high and low porosity events in Group 1 and Group 4.....	119
<b>Figure 6.19:</b> Scatter Plot between Fe and Mn contents of the high and low porosity castings from north and south rollover stations. Please note the operating window for the low porosity castings.....	119
<b>Figure 6.20:</b> Shrinkage graph of the bulkhead sections 4 and 7 of the 3.0L engine blocks,	

produced in the south rollover during 2003.....	121
<b>Figure 6.21:</b> TA test samples A and B with the locations of the Image Analysis samples.....	122
<b>Figure 6.22:</b> LOM micrographs showing the microstructure of sample A: (1) Fe rich Chinese script phase, (2) Cu rich phases, (3) Unmodified flaky eutectic silicon phase.....	123
<b>Figure 6.23:</b> LOM micrographs showing the microstructure of sample B: (1) Fe rich Chinese script phase, (2) Cu rich phases, (3) Unmodified flaky eutectic silicon phase.....	123
<b>Figure 6.24:</b> Brinell Hardness (After TSR and Artificial Aging) map of the hit location 6 (shown in the inset) of the V6 3.0L engine blocks during the year 2003.....	125
<b>Figure 6.25:</b> Variations in the level of Sn during the year 2003.....	127
<b>Figure 6.26:</b> Variations in the level of Pb during the year 2003.....	127
<b>Figure 6.27:</b> Statistical relationship between the average Brinell Hardness (HB) (after the TSR and AA processes) and the start temperature of the W319 alloy melting process (T <sub>m</sub> ) for the bulkheads from the 3.0L engine blocks.....	130
<b>Figure 6.28:</b> Start temperature of the W319 alloy melting process (T <sub>m</sub> ) versus Sn level (wt.%) for WAP 3.0L engine blocks (cast using Wabash Ingots) and Alcoa as well as Alchem ingots.....	130
<b>Figure 6.29:</b> Light Optical Microscope (LOM) micrographs of the WAP 3.0L engine block bulkhead ( <b>ID: 952351</b> ) ( <b>Pb: 0.016 wt.%, Sn: 0.047 wt.%</b> ) melted and solidified three times under UMSA controlled conditions.....	132
<b>Figure 6.30:</b> Light Optical Microscope (LOM) micrographs of the WAP 3.0L engine block bulkhead subjected to the WAP TSR at 494-505°C and to AA at 257-261°C for approximately 4 hrs ( <b>ID: 952351</b> ) ( <b>Pb: 0.016 wt.%, Sn: 0.047 wt.%</b> ).....	133
<b>Figure 6.31:</b> Scanning Electron Microscopy (SEM) micrographs of the WAP 3.0L engine block bulkhead subjected to the WAP TSR at 494-505°C and to AA at 257-261°C for approximately 4 hrs each ( <b>ID: 952351</b> ) ( <b>Pb: 0.016 wt.%, Sn: 0.047 wt.%</b> ).....	134
<b>Figure 6.32:</b> Light Optical Microscope (LOM) micrographs of the WAP 3.0L engine block bulk head ( <b>ID: 952351</b> ) ( <b>Pb: 0.016 wt.%, Sn: 0.047 wt.%</b> ) remelted three times under UMSA controlled condition and subjected to the simulated TSR at 500°C and to AA at 257-261°C for approximately 4 hrs.....	135
<b>Figure 6.33:</b> Comparison of the Vickers Microhardness measurements of the “as cast” bulkhead test samples that were remelted and solidified three times using UMSA and the bulkhead test samples that were subjected to simulated TSR and Artificial Aging in UMSA.....	136
<b>Figure 6.34:</b> Photograph showing (a) a fixed ceramic insert (b) the inside of a leaked fixed ceramic insert and (c) the U-pole piece.....	141
<b>Figure 6.35:</b> Normal probability plot for the life time of the fixed ceramic insert.....	141
<b>Figure 6.36:</b> Frequency histogram of the pump failures prior to 2002.....	142
<b>Figure 6.37:</b> Exponential probability plot of the pump life time prior to 2002.....	142
<b>Figure 6.38:</b> Reliability function plot of the pump life prior to 2002.....	143
<b>Figure 6.39:</b> Frequency histogram of pump failures during the period 2002-2003.....	145
<b>Figure 6.40:</b> Extreme value probability plot of the pump life times during the period 2002-2003.....	145
<b>Figure 6.41:</b> Reliability function plot of the pump life time for the period 2002-2003..	146



<b>Figure 6.42:</b> The optimum preventive maintenance time shown in the hazard plot for the pump life time.....	148
<b>Figure 6.43:</b> Comparison of the fill Profiles of the engine blocks with low and high porosities.....	148
<b>Figure 6.44:</b> Comparison of the voltage profiles of the engine blocks with low and high porosities.....	149
<b>Figure 6.45:</b> The relationship between matrix microhardness and the area percent of Cu rich phases measured by Image Analysis (IA) on the solution treated and naturally aged UMSA test samples.....	154
<b>Figure 6.46:</b> Flow chart of the Simulated Annealing search of the NSTS Process.....	157
<b>Figure 6.47:</b> Progress of the SA search algorithm.....	158
<b>Figure 6.48:</b> Comparison between the measured values from the experiment and the predicted results by the ANN-SA model at the optimal solution treatment temperature and time.....	160
<b>Figure 7.1:</b> Grain Size measured vis-a-vis GRF calculated using the SiEQ methodology and the summation approach.....	164
<b>Figure 7.2:</b> Relationship between the $\Delta T$ undercooling parameter and the Grain Size (GS) measured on the test samples: [5-1],[5-2],[5-4], [7-2], [9-2],[9-4], and [11-4].....	166
<b>Figure 7.3:</b> The relationship between the $\Delta T$ undercooling parameter and the Growth Restriction Factor (GRF) for [5-1],[5-2],[5-4], [7-2], [9-2],[9-4], and [11-4].....	166
<b>Figure 7.4:</b> Comparison of the apparent fraction solids of the 3XX Alloys.....	169
<b>Figure 7.5:</b> Comparison of the AITAP experimental and ANN predicted (a) Temperature and (b) Fraction solid characteristics of the 7 wt.%Si 4wt.% Cu alloy.....	171
<b>Figure 7.6:</b> Comparison of the AITAP experimental and ANN predicted (a) Temperature and (b) Fraction solid characteristics of the 9 wt.%Si 1wt.% Cu alloy.....	172

## List of Tables

<b>Table 2.1:</b> Polynomial coefficients of the Al-X <sub>i</sub> systems for the calculation of Silicon Equivalency (Si <sub>EQ</sub> ), (Mitrasinovic, 2004).....	16
<b>Table 2.2:</b> Metallurgical transformations during the heating and cooling cycles of W319 alloy.....	27
<b>Table 3.1:</b> Selected thermal characteristics of ingots, melts, cast components and their processes (IRC Brochure, 2004a).....	54
<b>Table 4.1:</b> Chemical composition of the AAA standard 319 alloy (Zalensas, 1993) and the W319 alloy (Ford Engineering Material Specification WSD-M2A151-A2/A4).....	62
<b>Table 5.1:</b> Average chemical composition (wt.%) of the 3XX series of experimental Al alloys.....	77
<b>Table 6.1:</b> Comparison of the characteristic reaction temperatures (°C) and fraction solids (%) of the ingot, melt and bulkhead UMSA test samples with their Standard Deviations (SD).....	82
<b>Table 6.2:</b> Comparison of the SDAS values (µm) measured on the ingot, melt and bulkhead samples with their Standard Deviations (SD).....	83
<b>Table 6.3:</b> Comparison between the calculated SDAS values and the measured SDAS values for the ingot and melt samples.....	85
<b>Table 6.4:</b> ANOVA Table for the AITAP Data.....	90
<b>Table 6.5:</b> ANOVA Table for the Alu-Delta Data.....	90
<b>Table 6.6:</b> Tukey control limits for the TA parameters for the on-line process control of the WAP process.....	100
<b>Table 6.7:</b> Description of the input parameters of the ANN.....	105
<b>Table 6.8:</b> Architecture of the MLP neural network.....	108
<b>Table 6.9:</b> Architecture of the RBF network.....	110
<b>Table 6.10:</b> Data showing the relationship of the predicted SiML to Sr content and examples of predicted microstructure.....	111
<b>Table 6.11:</b> Mean Square Error (MSE) comparison of the neural networks with regression, and ΔT method.....	112
<b>Table 6.12:</b> Comparison of the feed-forward neural networks.....	112
<b>Table 6.13:</b> Minitab output of the 2 sample t-test for Fe in the engine blocks with low and high levels of porosity.....	116
<b>Table 6.14:</b> Minitab output of the 2 sample t-test for Mn in the engine blocks with low and high levels of porosity.....	116
<b>Table 6.15:</b> Descriptive Statistics of the Fe and Mn for low and high porosity levels...	116
<b>Table 6.16:</b> Events of low and high Porosity in the four groups with different Fe and Mn levels.....	117
<b>Table 6.17:</b> Periods of high and low porosity and the corresponding average Fe and Mn contents.....	121
<b>Table 6.18:</b> Average Fe and Mn compositions of the W319 TA test samples that were used for the image analysis.....	121
<b>Table 6.19:</b> Measurements of the morphology of the Fe based phases present in the TA samples with high and low Fe and Mn contents.....	122
<b>Table 6.20:</b> Comparison of the average characteristic reaction temperatures (°C) of an engine block with a low bulkhead hardness (Pb=0.016 wt.%, Sn=0.047 wt.%) and engine blocks with high bulkhead hardness (Pb=0.023 wt.%, Sn=0.0069 wt.%).....	129

<b>Table 6.21:</b> The revised control limits for the major and minor alloying elements.....	138
<b>Table 6.22:</b> The existing in process chemistry specification at WAP.....	138
<b>Table 6.23:</b> Comparison between the number of pump failures predicted by the extreme value distribution and the actual number of pump failures.....	146
<b>Table 6.24:</b> Architecture of the MLP neural network for modeling the NSTS Process..	152
<b>Table 6.25:</b> Comparison between the matrix microhardness and area % of Cu enriched phases predicted by the neural network and measured on the experimental test samples.....	152
<b>Table 7.1:</b> Data required for the calculation of the GRF of multicomponent hypoeutectic Al alloys, (Easton and St.John (2001)).....	163
<b>Table 7.2:</b> Comparison of the GRF values calculated Using SiEQ and the sum of $m(k-1)C_0$ method.....	163
<b>Table 7.3:</b> Characteristic temperatures and fraction solids of the 3XX series Al alloys with their Standard Deviations (SD).....	167
<b>Table 7.4:</b> Architecture of the function approximation MLP neural network for modeling the TA parameters of the 3XX Al Alloys.....	173
<b>Table 7.5:</b> Experimental data set that is used for the development of the equations given in section 7.4 for the optimization of the 3XX Al-Si alloys.....	176
<b>Table 7.6:</b> The upper and lower bounds, target values, weight and importance of the response variables.....	181
<b>Table 7.7:</b> Predicted values of the responses in the as-cast conditions and their desirabilities at the optimal levels of Si (10.65 wt.%) and Cu (2.08 wt.%).....	181
<b>Table 7.8:</b> TA parameters of the optimal Al 332 Alloy with Si (10.65 wt.%) and Cu (2.08 wt.%) predicted using Artificial Neural Networks (ANN).....	182

## List of Acronyms

- AAA:** American Aluminum Association
- AA:** Artificial Aging
- AC:** Alternating Current
- AFS:** American Foundry Society
- AIAG:** Automobile Industry Action Group
- AITAP:** Aluminum Thermal Analysis Platform
- ANN:** Artificial Neural Network
- ANOVA:** Analysis of Variance
- BSE:** Back Scattered Electron
- CACCA:** Computer Aided Cooling Curve Analysis
- CBR:** Case Based Reasoning
- CG:** Counter Gravity Process
- CPSP:** Cosworth Precision Sand Process
- DCP:** Dendrite Coherency Point
- DOE:** Design of Experiments
- DSC:** Differential Scanning Calorimeter
- DTA:** Differential Thermal Analysis
- Enviro-AITAP:** Environmental Aluminum Thermal Analysis Platform
- FB:** Fluidized Bed
- GA:** Genetic Algorithm
- GRF:** Growth Restriction Factor
- GS:** Grain Size
- HB:** Brinell Hardness
- IAS:** Image Analysis System
- IRC:** NSERC/Ford-NEMAK/University of Windsor Industrial Research Chair in Light  
Metal Casting Technology
- ISO:** International Standards Organization
- LH:** Latent Heat of Solidification
- LOM:** Light Optical Microscope

**LSL:** Lower Specification Limit  
**MLP:** Multilayer Perceptron  
**MTBF:** Mean Time Between Failures  
**NAP:** Novel Analytical Platform  
**NEC:** NEMAK Engineering Centre  
**NIST:** National Institute of Standards and Technology  
**NSTS:** Novel Solution Treatment during Solidification  
**NTQCP:** Novel Thermal Quality Control Platform  
**OES:** Optical Emission Spectroscopy  
**PCA:** Principal Component Analysis  
**PWQC:** Plant Wide Quality Control  
**QC:** Quality Control  
**R&R:** Repeatability and Reproducibility  
**RBF:** Radial Basis Function  
**RPPM:** Reduced Pressure Permanent Mold Process  
**RPS:** Reduced Pressure Sand Process  
**RPT:** Reduced Pressure Test  
**RTD:** Resistance Temperature Detector  
**SA:** Simulated Annealing  
**SD:** Standard Deviation  
**SDAS:** Secondary Dendrite Arm Spacing  
**SE:** Secondary Electron  
**SEM:** Scanning Electron Microscopy  
**SHLP:** Sand Hybrid Low Pressure Process  
**SiEQ:** Silicon Equivalency Methodology  
**SiML:** Silicon Modification Level  
**SPC:** Statistical Process Control  
**TA:** Thermal Analysis  
**TSR:** Thermal Sand Removal  
**TTT:** Time Temperature Transformation  
**UMSA:** Universal Metallurgical Simulator and Analyzer

**UMSD:** Unbiased Melt Sampling Device

**USL:** Upper Specification Limit

**UWCL:** University of Windsor Casting Laboratory

**WAP :** Windsor Aluminum Plant

# 1. Introduction

There is an ever increasing demand in the automotive and aerospace industry for aluminum castings due to the impetus for fuel economy, weight reduction and a cleaner environment. The substitution rate of aluminum for cast iron in the manufacturing of the engine blocks and cylinder heads is increasing annually. Industrial analysts forecast that by the year 2006, 60% of engine blocks, and 96% of cylinder heads in light vehicles produced in the US will be made of aluminum (Kirgin et al., 2002). Another estimate predicts that by the year 2009, the average amount of automotive cast aluminum is going to increase from 82 kg to 113 kg per vehicle (Spada, 2000). As the use of cast aluminum is increasing, it is imperative that aluminum foundries make consistent quality castings at lower manufacturing costs to stay competitive.

The NEMAK Windsor Aluminum Plant (WAP) produces aluminum engine blocks using the state of the art modified Cosworth Precision Sand Process (CPSP). Even though CPSP is a very robust process (due to quiescent bottom up low pressure precision filling using the cleanest melt from the middle of the furnace and the rollover technique), problems like sporadic outbreaks of shrink porosity and variations in engine block hardness are major concerns for WAP. Determining and analyzing the root causes of these problems are made more difficult due to the following factors: (a) The variations in the process parameters such as chemical composition, gas level, and electromagnetic pump parameters being very narrow and within the specification limits for high and low porosity, and (b) numerous independent variables and their interactions that appear to be the potential reasons for the problem at hand. Therefore, a carefully prepared synchronous dataset and an advanced statistical analysis approach are needed to zoom in on just one or two of the most significant variables. A sound knowledge of WAP processes and statistics is required for this analysis.

The reasons for the shrink porosity formation in Al-Si-Cu castings is one of the most prolific areas of research within the metal casting fraternity. This dissertation is also a contribution to this important field of study. In addition, it also addresses recent

developments such as the application of Artificial Neural Network (ANN) and optimization techniques in the metallurgy of W319 Al alloy castings.

The present WAP casting process Quality Control (QC) system was critically evaluated and areas for improvement were identified. Novel quality control tools for controlling the ingot, melt and engine block quality were developed, and tested for feasibility at the WAP. These quality control tools were developed for the W319 Al alloy presently used at WAP. However, in the final stages of this work, twelve 3XX series of Al alloys with varying silicon and copper levels were used in order to optimize the levels of Si and Cu and hence to develop a new alloy in order to improve the cast component characteristics. A novel analytical approach called Silicon Equivalency ( $Si_{EQ}$ ) has been used in this dissertation to calculate the grain Growth Restriction Factor (GRF) and hence the Grain Size (GS) and other metallurgical characteristics of the 3XX series of Al alloys.

This dissertation is divided into 8 Chapters. The first chapter is a general introduction to the dissertation. The second chapter provides the relevant literature review on the metallurgy of Al -Si alloys, Thermal Analysis (TA) of Al-Si alloys, Silicon Equivalency ( $Si_{EQ}$ ) Algorithm and its specific applications, heat treatment, and the applications of neural networks and optimization methods in materials engineering. The third chapter introduces the CPSP process used at WAP. The present Quality Control (QC) system at WAP is critically appraised and a novel Quality Control (QC) system is presented. The objectives of the project are also presented in this chapter. Chapter Four presents the experiments and measurements performed on the W319 alloy currently used by the Windsor Aluminum Plant (WAP). Chapter Five outlines the laboratory experiments performed on the 3XX series of Al alloys with varying levels of Si (5-11) wt.% and Cu (1-4) wt.%. Chapter Six presents the results and discussions from the analysis of the experimental data and measurements from Chapter Four. Chapter Six also presents the reliability studies and optimization of the preventive maintenance of the Cosworth pump. Chapter Seven describes the studies on the thermal and metallurgical characteristics of the 3XX series of Al alloys as well as the application of the  $Si_{EQ}$  algorithm. The data from the lab experiments on the 3XX Al alloys (Chapter Five) was



used to optimize the levels of Si and Cu and therefore a new alloy is obtained (Al 332) where the casting characteristics are improved while keeping the cost of the alloy low. Chapter Eight presents the Conclusions, Recommendations and Scope for Future Work.

All of the software programs and statistical models developed during this work are attached in the Appendix in a CD-ROM. In order to run these programs the user requires Matlab™ 6.5 or higher with the Neural Network Toolbox, and the Minitab™ 13 or higher installed into their computer systems.

## **2. Literature Review**

### **2.1 Metallurgy of Hypoeutectic Aluminum Silicon Alloys**

#### **2.1.1 Key Alloying and Impurity Elements**

Aluminum-Silicon alloys are the most important among the aluminum casting alloys. They make up about 85% of the cast parts produced from aluminum alloys (Gruzleski and Closset, 1990). Based on the amount of Si present, these alloys are classified into hypoeutectic (<11.7 wt.%), eutectic (11.7 wt.% to 12.6 wt.%) and hypereutectic (>12.6 wt.%) alloys (Zalensas, 1993). This literature review is mainly concentrated on the metallurgy of hypoeutectic Al-Si alloys and more specifically the Al-Si-Cu-Mg (3XX series) alloys such as Al 319. The major and minor alloying and impurity elements that are present in the Al 319 alloy are briefly outlined here:

##### **2.1.1.1 Silicon**

Silicon is the main alloying element in these alloys. The addition of silicon to aluminum improves its feeding characteristics, fluidity, lowers its solidification shrinkage and increases the hot tear resistance. The morphology of the eutectic silicon phase is “modified” using elements such as Na or Sr to improve the mechanical properties of the casting. This will be discussed in detail in section 2.1.2.2. Aluminum alloys with 5-7 wt.% Si are usually used for investment and sand castings, alloys with 7-9 wt.% Si are used for permanent mold castings and those with 8-12 wt.% Si are used for making pressure die castings (Davis, 1993). Lucas et al. (2004) have indicated that high levels of Si (~9 wt.%) refine the needle shaped brittle  $\beta$ -Al<sub>5</sub>FeSi phase in Al-Si-Cu- Mg alloys having Fe levels around 0.5 wt.% and hence increases the ductility of the alloy.

##### **2.1.1.2 Copper**

Copper is added to improve the mechanical properties by precipitation hardening after heat treatment, but, it reduces the corrosion resistance of the alloy. Moustafa et al. (2002) have reported that with the addition of up to ~3 wt.% Cu to the Sr treated Al-11.5 wt.% Si precipitation hardened alloy increases its yield strength by 57% and decreases the ductility by 33% when the Mg level is at ~0.08 wt.%. Ren (2000) has reported that for

hypoeutectic Al-Si alloys, the porosity level in the sand casting is increased when the Cu level increases from 1 wt.% to 4 wt.%. It has been suggested that this may be due to the feeding difficulties associated with high levels of Cu. This effect is more significant at slower cooling rates. Dash and Makhoulf (2001) have also reported a similar result. They have provided the following explanation to account for this effect: (1) The ternary reaction:  $liq \rightarrow \alpha-Al + Si + Al_2Cu$  occurs towards the end of solidification, when most of the casting has solidified. At high levels of Cu (~3.5 wt.%),  $Al_2Cu$  along with  $Al_5FeSi$  needles block the feeding path and cause shrink porosity. (2) Cu increases the hydrogen gas pressure associated with the dissolved hydrogen and promotes the formation of the gas pores.

### 2.1.1.3 Magnesium

According to Dasgupta et al. (1989) the addition of Mg does not have any significant effect on the mechanical properties of the Al 319 alloy either in the as cast or heat treated condition. However, Gustafsson et al. (1986) claimed that Mg additions increase the tensile strength and reduce the ductility in Al 319. Moustafa et al. (2002) have also reported that with Mg additions of up to 0.4 wt.% to the Sr treated Al-11.5 wt.% Si alloy increases its yield strength by 94% and decreases the ductility by 40% when the Cu level is at ~0.9 wt.%. In Al-Si-Mg alloys, the increase in strength during artificial aging is associated with the formation of  $\beta$  ( $Mg_2Si$ ) precipitates.

### 2.1.1.4 Iron

Iron is the most deleterious impurity element present in the secondary Al 319 alloy. The two most common forms of Fe intermetallic phases found in Al 319 are the  $\beta$ - $Al_5FeSi$  phase with “platelet” morphology and the  $\alpha$ - $Al_{15}Fe_3Si_2$  phase with “Chinese script” morphology. According to Murali et al. (1992) the presence of the  $\beta$ -phase, which appears as large platelets, decreases noticeably the ductility and the fracture toughness of the cast component. Taylor et al. (1999a) have indicated that the  $\beta$ -phase has also been shown to increase the shrinkage porosity level. Gustafsson, et al. (1986) suggested that as the Fe content increases or when the solidification rate is slower as in the case of sand castings, the length of these  $\beta$ -platelets also increases. In commercial castings the

formation of the  $\beta$ -phases is minimized by one of the following techniques: (1) rapid solidification (Narayanan, 1994), (2) the addition of transition elements such as Mn, that encourages the formation of a less harmful  $\alpha$ -Chinese script phase. This is because Mn is more readily substituted for Fe in the  $\alpha$ -phase than it is in the  $\beta$ -phase (Kozhanov et al., 1985). Mn content is usually restricted to approximately half of the Fe content (Taylor, 1995). Samuel et al. (2001), suggest that the Mn/Fe ratio must be close to 0.7 in order to achieve an effective neutralization treatment. Dinnis et al. (2004) have indicated that for Al-Si alloys with a Cu content of 3 wt.%, and an Fe content of 1wt.%, the addition of Mn does not decrease the porosity level due to the unfed solidification of the  $Al_2Cu$  at a higher fraction solid. (3) Superheating the melt from 250 to 300 °C above the liquidus temperature will result in the crystallization of the Fe in the  $\alpha$ -phase (Narayanan et al., 1994). (4) Addition of Be transforms the large Fe  $\beta$ -(beta) phases into small equiaxed shaped crystals (Sigworth et al., 1989). However the addition of Be is not practiced in the industry due to health hazards.

#### **2.1.1.5 Tin and Lead**

These are low melting point impurity elements that are found in parts per million (ppm) levels in Al-Si alloys. The work by Chagoya (2001) has shown that variations in the Pb and Sn contents affect the thermal characteristics (dendrite coherency point and Al-Si eutectic growth temperature) of the W319 Al alloy. However, the tensile and elongation properties of the engine blocks that were cast during the period of this study were unaffected. It is believed that Pb and Sn may affect the solidification kinetics of the Al-Si-Cu eutectic reaction, but further work is needed to establish the relationships. Small amounts of Sn (~0.05 wt.%) in Al-Cu alloys increase the aging response after solution treatment. Nonetheless, in the presence of small amounts of Mg the aging response is markedly reduced as Mg and Sn together form a non-coherent second phase (Davis, 1993).

#### **2.1.2 Melt Treatment and Processing**

In order to achieve sound castings with desirable properties, the molten aluminum alloy is treated prior to casting to refine its microstructure and to get rid of the dissolved hydrogen in the melt. The melt treatment techniques usually used are:

### **2.1.2.1 Grain Refinement**

It is desirable to have smaller grains in a casting than a coarse grain structure so as to enhance the feeding characteristics (Heine, 1985). There are many methods of grain refinement available, viz: agitation of the solidifying melt via mechanical or electromagnetic means, and the thermal or constitutional undercooling of the melt (Byczynki, 2002). The common practice is the constitutional undercooling by the addition of Al-Ti or Al-Ti-B master alloys as grain refiners. Aluminum dendrites nucleate on the surface of the grain refiner. For sand castings and permanent mold castings 0.15 wt.% Ti and above is suggested for good grain refinement (Sigworth and Guzowski, 1985). There are several theories on the operative mechanisms of grain refinement and still the exact mechanism is not clear. Mohanty and Gruzleski (1995) has provided a detailed review of the grain refinement theories to date.

### **2.1.2.2 Eutectic Silicon Modification**

The mechanical properties of the Al 319 alloy depend on its microstructure. The eutectic silicon during solidification usually crystallizes with an acicular platelet structure. This structure decreases the ductility of the alloy. Therefore the eutectic silicon structure is modified to a fine fibrous structure either by rapid cooling or by the addition of a chemical modifier or by superheating of the melt to  $\sim 850^{\circ}\text{C}$  (Nogita et al., 2004). The industrial practice is to modify by adding a modifier such as Na, Sr or Sb. In North America Sr is the popular modifier while in Europe Sb is widely used (Schleg, 2003). Although Na has good modification efficiency, it fades out too quickly in the melt. Therefore, it is difficult to control the modification with Na. A review of the existing theories on the mechanisms of modification is given by Makhoulf and Guthy (2001). According to the widely accepted impurity induced twinning theory proposed by Lu and Hellawell (1995), Na or Sr (modifier) is adsorbed on the growing Si crystal surfaces and thus the crystal growth is restricted. This leads to the forced twinning of the Si crystal and thus results in enhanced branching and a fibrous microstructure (See Figure 2.1 and 2.2). Although modification refines the structure and improves the tensile properties, these virtues are partly offset by the fact that modification increases the porosity in the

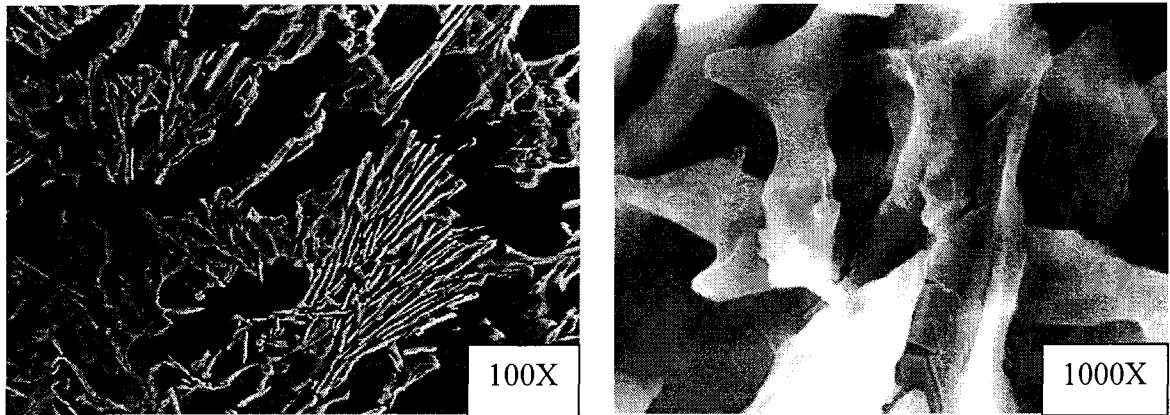


Figure 2. 1: SEM micrographs of the Si crystals in an unmodified sample of the Al 356 alloy following deep etching (Bäckerud et al., 1990).

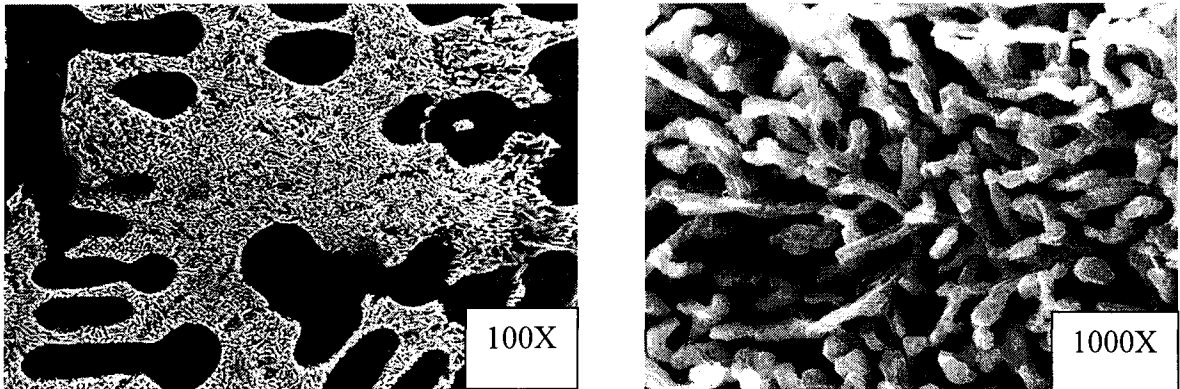


Figure 2. 2: SEM micrographs of the Si crystals in a modified sample of the Al 356 alloy following deep etching (Bäckerud et al., 1990).

casting. There has been much debate on why modification increases the porosity. Several mechanisms have been proposed such as: increase in hydrogen solubility (Denton and Spittle, 1985), reduction in interfacial surface tension (Emadi, et al., 1993), increase in the amount of oxide inclusions (Sigworth et al., 1994 and Liu et al., 2003), and the eutectic nucleation at the inter dendritic region (McDonald et al., 2000, and Nogita and Dahle, 2001). A unified theory on this phenomenon is not yet in place. It may be that each of the above mechanisms synergistically contributes to the increase in porosity depending on the alloy composition, solidification rate, hydrogen content and the inclusion levels.

### **2.1.2.3 Degassing**

Hydrogen is the only gas that has considerable solubility in liquid aluminum. The solubility of hydrogen in aluminum decreases rapidly with the temperature. The rejected hydrogen from the liquid melt will form round gas pores in the casting. Therefore the melt must be degassed before casting. The melt can be degassed by one of the following methods: (a) addition of fluxes such as chlorine to the melt, (b) bubbling purge gasses like argon or nitrogen through the melt, (c) vacuum degassing and (d) ultrasonic vibration (Zalensas, 1993). The most common method adopted in the industry is bubbling a purge gas through the melt for an extended period of time using a rotary impeller.

### **2.1.3 Porosity in Castings**

Porosity is an age old problem that began when man started to make castings. Porosity in the castings is broadly classified into gas porosity and shrinkage porosity. Gas porosity arises when the gases, mainly hydrogen, dissolved in the solidifying melt start to precipitate due to their limited solid solubility. These pores are characterized by their spherical nature, and are independent of one another.

Shrink porosity on the other hand, occurs due to insufficient feeding of the interdendritic regions. Shrink porosity has the irregular profile of the dendrites and the pores are interconnected. Although the mechanisms are distinct, in most cases, gas and shrink pores are combined together to exist as a mixed pore. The porosity in castings is a complex function that is controlled by many variables such as alloy chemical

composition, solidification rate, hydrogen content, liquid metal processing, mold design, melt cleanliness, and mold filling (turbulent or quiescent).

Campbell (1996) asserts that the origin points of porosity in castings are the double folded surface oxide films with entrapped air inside. These films get entrained inside the melt during filling and serve as progenitors of gas or shrink pores, which were demonstrated using real time x-ray radiography. Viswanathan et al.(1992) have reported that for sand castings, the porosity level increases considerably after about 80% fraction solid has formed. This means that the inability to feed the tortuous interdendritic channels that are blocked by the intermetallic phases results in the increase in porosity towards the end of solidification.

Boudreault et al. (1997) have studied the individual and combined effects of hydrogen level, melt treatment (by grain refinement and strontium modification), and solidification rate on the porosity formation of Al 319.2 sand castings. It was found that the addition of a grain refiner facilitates a round pore morphology, while the addition of strontium gives rise to an irregular pore morphology. Strontium was also seen to increase the pore density. The statistical analysis using multiple regression has shown that the hydrogen content of the melt has the highest influence on the amount of porosity present in the sand casting, followed by Dendrite Arm Spacing (DAS) , the amount of grain refiner and the interaction between the amount of grain refiner and solidification rate respectively in the decreasing order of significance. It was found that when the hydrogen level is ~0.3 ml/100g, very large pores were observed in the casting even at higher cooling rates.

Dash and Makhlof (2001) have studied the effect of key alloying elements (Si, Fe, Mg, Mn, Cu, Sr, and Ti) and the cooling rate on the feeding characteristics and porosity of Al-Si casting alloys. They used an  $L_{16}$  Taguchi orthogonal array for the experiments. The existing knowledge on the formation of the intermetallic phases in Al-Si alloys was used to select the most important two and three factor interactions from the myriad of possibilities. They concluded that the alloying elements alone do not contribute



to porosity; however, the intermetallic compounds they form, such as,  $\beta$ -iron phase,  $\text{Al}_5\text{Mg}_8\text{Cu}_2\text{Si}_6$  and  $\text{Al}_2\text{Cu}$  obstruct the interdendritic path and hinders the feeding of the liquid melt. This leads to shrinkage porosity in the casting. The statistical analysis by Analysis of Variance (ANOVA) has shown that the cooling rate is the highest contributing factor to feeding and percent porosity in the casting.

## 2.2 Thermal Analysis (TA)

In order to keep up with the high customer demand, Al foundries are compelled to manufacture castings with consistent quality, which is not possible with traditional chemical analysis quality control only. Therefore it is important to know the as cast microstructure before the casting operation and to take remedial actions for potential problems (Tuttle, 1984). The microstructure has a one-to-one relationship to the mechanical properties. Traditionally, Image Analysis with the Light Optical Microscope (LOM) is used for quantifying the microstructure of the cast component. However, this technique is time consuming and for that reason cannot be used for on-line determination of the as-cast microstructure on the foundry floor. Thermal Analysis is a quick, simple and inexpensive technique to assess the as-cast microstructure of the casting that will allow foundries to operate in the prevention mode rather than the reaction mode.

The basic idea of TA is to record the temperature changes that occur in a test sample while it is heated or cooled at a constant rate. The most well-known Thermal Analysis techniques are: (a) Cooling Curve Analysis, (b) Differential Thermal Analysis (DTA), and (c) Differential Scanning Calorimetry (DSC) (Fras et al. 1993). Both DTA, and DSC need sophisticated lab instruments that require careful sample preparation and therefore are not suitable for foundry floor applications. Cooling Curve Analysis is the most commonly used Thermal Analysis technique in foundries. The cooling curve is a time-temperature plot of the solidifying liquid melt. It is called the metallurgical “finger print” of solidification, that is unique for each alloy chemical composition. Computer Aided Cooling Curve Analysis (CACCA) allows for the rapid calculation of grain refinement (Tuttle, 1984), the Silicon Modification Level (Gallios and Sigworth, 1984), dendrite coherency point, fraction solid, and latent heat (Barlow and Stefanescu, 1997).

This helps to identify the potential problems in advance so that remedial actions can be taken to avoid producing defective cast components. Derivative cooling curve analysis can be used to accurately determine the characteristic temperatures of the metallurgical reactions that cannot be visualized on the cooling curve (Louvo, 1984).

In order to plot the fraction solid curves, the base line must be calculated first. The base line is the hypothetical first derivative curve assuming that there is no phase transformation occurring during the solidification. The literature reports that there are two procedures used for the calculation of the base line based on (a) Newtonian Analysis and (b) Fourier Analysis. The Newtonian Analysis assumes that the thermal gradient across the test sample is zero and that the heat transfer between the casting and the mold is by convection. The Fourier analysis assumes that the heat transfer occurs by conduction only. Fras et al. (1993) reported that Fourier analysis is more accurate than Newtonian because it presumes that the thermo-physical properties are temperature/time dependent. Barlow and Stefanescu (1997) also support this claim. However, Kierkus and Sokolowski (1999) have shown that if cooling curve experiments are performed under close to Newtonian cooling conditions (using a thin walled metal cup with its top and bottom insulated), which is very practical, the base line can be accurately calculated using the Newtonian method. Moreover, the Newtonian Method requires only one thermocouple at the centre of the test sample as opposed to the Fourier method where two thermocouples are required; one at the centre of the sample and the other close to the mold wall.

The cooling curve Thermal Analysis systems commercially available for Al alloys are Alu-Delta<sup>TM</sup>, TA-100<sup>TM</sup>, Meltlab<sup>TM</sup> and Thermatest<sup>TM</sup> (Morice, 1984). All of these systems measure the grain size and the modification level of the alloy only; some of them give the characteristic reaction temperatures too. The melt sampling technique used by these systems is spoon transfer, which may introduce surface oxides into the sample and hence error into the temperature measurements. Also the thermocouples and the TA system are not often calibrated and this introduces systematic error into the temperature measurements.

The NSERC/ Ford-NEMAK/ University of Windsor Industrial Research Chair (IRC) in Light Metals Casting Technology has been actively involved in the research of Thermal Analysis of Al alloys for the last decade. The Thermal Analysis Platforms developed by the IRC have enhanced capabilities of thermal characterization of the Al alloys exceeding that of commercial TA systems. The two Thermal Analysis Platforms developed by the IRC are briefly explained in the following sections.

### **2.2.1 Aluminum Thermal Analysis Platform (AITAP)**

AITAP is a cooling curve Thermal Analysis Platform developed by the IRC for Al alloys. The features that distinguish AITAP from other commercial systems are: consistent test sample mass, optimum test cups, unbiased melt sampling technique, calibrated thermocouples and data acquisition system, and minimum heat loss prior to temperature recording. There is also another form of AITAP called the Enviro-AITAP, where a Reduced Pressure Test (RPT) apparatus is customized to perform Thermal Analysis under vacuum (Mitrasinovic, 2004). The melt sampling is done using an unbiased melt sampling device which will be explained in detail in Chapter 4. AITAP is able to measure about fifty thermal and metallurgical solidification parameters. These parameters are listed below:

- The characteristic temperature, time and fraction solid of metallurgical reactions. (Refer to Appendix 2 for a detailed explanation, nomenclature and algorithms for determining these TA parameters ).
- Dendrite Coherency Point (DCP) by using single a single thermocouple signal (Jiang, et al. 1999).
- Grain Size and Silicon Modification Level.
- Volume fraction of the copper rich phases.
- Amount of dissolved hydrogen in the melt (Djurdjevic et al. 2002a).
- Latent heat of solidification.
- Apparent Fraction Solid.
- Bulk Solidification rate as well as instantaneous solidification rates at characteristic reaction temperatures.

### 2.2.2 Universal Metallurgical Simulator and Analyzer (UMSA)

Traditional Thermal Analysis systems are only designed to perform cooling curve analysis. However, the heating curve analysis is also very important for Al alloys like Al 319, where the heat treatment plays a key role in determining the mechanical properties. In this case, the heating curve analysis is imperative to establish the maximum solution treatment temperature, but safe from incipient melting. UMSA is patented under PCT/CA02/10903, Canada (Kasprzak et al., 2002). It is a Thermal Analysis platform that is able to perform heating as well as cooling curve analyses, in a continuous manner. It is also designed to perform quenching experiments at any desired stage during the solidification process. The sample can be chilled radially by blowing air around or vertically by using a chill at the bottom of the sample. In addition to measuring the solidification parameters mentioned for the ALTAP, UMSA is also able to perform the following:

- Optimization of the heat treatment parameters.
- Prediction of the segregation of alloying and impurity elements.
- Measurement of the characteristic temperatures of the heating curve.
- UMSA test samples can be used for performing mechanical properties tests.

### 2.3 Silicon Equivalency ( $Si_{EQ}$ ) Algorithm and its Applications

The Silicon Equivalency ( $Si_{EQ}$ ) algorithm is a novel analytical approach developed by the IRC for the off line quality control of ingots, melt and the cast components using the alloy chemical composition and the phase diagrams (Djurdjevic, et al., 2003a). This concept is analogous to the carbon equivalent for ferrous alloys. In  $Si_{EQ}$  algorithm, since silicon being the major alloying element for Al-Si alloys, the effect of other alloying elements is translated to their corresponding silicon equivalents. For, example, the liquidus temperature ( $T_{LIQ}$ ) of Al goes down from 660.4<sup>0</sup>C to 640<sup>0</sup>C, either by the addition of 3wt.% of Si or by 7wt.% of Cu. Therefore, the  $Si_{EQ}$  of Cu at 640<sup>0</sup>C, is 4wt.% (ie. 7-3). Using the binary phase diagrams of Al-Si and Al-Cu systems, the  $Si_{EQ}$  values for other temperatures down to the Al-Si eutectic temperature can be computed. Then the relationship between the silicon equivalency of copper and the concentration of Cu can be expressed in the form of a polynomial equation as follows:

$$\text{Si}_{\text{EQ}}^{\text{Cu}} = b_0 \cdot \text{Cu} + c_0 \cdot \text{Cu}^2 \quad (2.1)$$

where,  $\text{Si}_{\text{EQ}}^{\text{Cu}}$  is the silicon equivalency of copper;  $b_0$  and  $c_0$  are the polynomial coefficients and Cu is the concentration of copper in wt.%. Similarly, the silicon equivalencies of other alloying elements in the aluminum alloy can also be calculated using their binary aluminum phase diagrams in combination with the Al-Si phase diagram. The  $\text{Si}_{\text{EQ}}$  of the multicomponent Al-Si hypoeutectic alloy can then be written as follows:

$$\text{Si}_{\text{EQ}} = \text{Si} + \sum \text{Si}_{\text{EQ}}^{X_i} \quad (2.2)$$

where,  $\text{Si}$  is the concentration of Si in wt.% and  $\sum \text{Si}_{\text{EQ}}^{X_i}$  is the sum of the silicon

where,  $\text{Si}$  is the concentration of Si in wt.% and  $\sum \text{Si}_{\text{EQ}}^{X_i}$  is the sum of the silicon equivalencies of the individual alloying elements. The polynomial coefficients for each individual element in equation 2.2 is given in Table 2.1.

In summary, the  $\text{Si}_{\text{EQ}}$  expresses the amount of alloying and impurity elements present in the melt (including grain refiners, silicon modifiers and dissolved hydrogen) as an equivalent amount of silicon (“global” alloy chemistry). The following sections explain how the  $\text{Si}_{\text{EQ}}$  algorithm can be used to calculate the thermal characteristics of multicomponent Al-Si-Cu alloys:

### 2.3.1 Calculation of Thermal Characteristics of the 3XX Series of Al Alloys

The liquidus temperature ( $T_{\text{LIQ}}$ ), Al-Si eutectic temperature ( $T_{\text{E,NUC}}^{\text{Al-Si}}$ ) and the Al-Si-Cu eutectic temperature ( $T_{\text{E,NUC}}^{\text{Al-Cu}}$ ) can be calculated, respectively, using the silicon equivalency algorithm using the following equations (Djurdjevic et al., 2003a):

$$T_{\text{LIQ}} = 660.452 - 6.11 \text{Si}_{\text{EQ}} - 0.057 \text{Si}_{\text{EQ}}^2 \quad (2.3)$$

$$T_{\text{E,NUC}}^{\text{Al-Si}} = 660.452 - (6.11 \text{Si}_{\text{EQ}} + 11.57 \text{Si}_{\text{EQ}}^2) (12.3 / \text{Si}_{\text{EQ}}) \quad (2.4)$$

$$T_{\text{E,NUC}}^{\text{Al-Cu}} = T_{\text{LIQ}} - (6.11 \text{Si}_{\text{EQ}} + 11.57 \text{Si}_{\text{EQ}}^2) (12.3 / \text{Si}_{\text{EQ}}) \quad (2.5)$$

where,  $\text{Si}_{\text{EQ}}$  is the silicon equivalency of the alloy expressed in wt.%.

**Table 2.1: Polynomial coefficients of the Al-X<sub>i</sub> systems for the calculation of Silicon Equivalency (Si<sub>EQ</sub>), (Mitrasinovic, 2004).**

Al-X <sub>i</sub> Alloy	wt.%	
	b <sub>0</sub>	c <sub>0</sub>
Al-Cu	0.529	-0.0004
Al-Mg	0.0258	-0.0088
Al-Mn	0.8221	-0.0349
Al-Fe	0.6495	0.0003
Al-Zn	0.1227	-0.0002
Al-Sn	0.7849	-0.0313
Al-Bi	0.9076	-0.0092
Al-Pb	0.859	0.02976
Al-Sb	0.8255	-0.0327
Al-Ni	0.5644	0.0285
Al-Sr	0.7854	-0.0157
Al-Ti	-0.8159	0.00993
Al-B	0.00075	7.5 E-05

### 2.3.2 Calculation of Latent Heat of Solidification

The latent heat of solidification is a thermo physical property of a material. By definition latent heat is the energy required to solidify 1 kg of a liquid with no temperature change, expressed in kJ/kg. The mathematical modeling and computer simulation of the solidification process is inaccurate without the knowledge of the latent heat. The fluidity of the alloy also strongly depends on the amount of latent heat released during solidification. Therefore, it is worth knowing the value of the latent heat of the alloy in question in advance.

Unfortunately, there is no easy way to get the value of the latent heat of solidification of multicomponent alloys either by using measurement techniques or analytical procedures. The present practice is to measure the latent heat using the Differential Scanning Calorimeter (DSC) apparatus. Recently, Djurdjevic et al. (2003b), have shown that the  $Si_{EQ}$  can be used to calculate the latent heat of solidification of hypoeutectic Al-Si alloys. First the fraction solids of the primary aluminum ( $\alpha$ -phase) and of the secondary aluminum (aluminum in the Si eutectic) are calculated by applying the lever rule on a pseudo Al-Si binary phase diagram, where the Si concentrations are substituted by the  $Si_{EQ}$  values. The latent heat (LH) is then calculated by using the equation:

$$LH = f^{\alpha-Al}_{primary} * LH_{pure Al} + f^{\alpha-Al}_{eutectic} * LH_{pure Al} + f^{AlSi}_E * LH_{pure Si} \quad (2.6)$$

Where,  $f^{\alpha-Al}_{primary}$  is the fraction solid of the primary aluminum formed before the eutectic;  $f^{\alpha-Al}_{eutectic}$  is the fraction solid of the secondary aluminum formed after the eutectic reaction;  $f^{AlSi}_E$  is the fraction solid of the silicon eutectic;  $LH_{pure Al}$  and  $LH_{pure Si}$  are the latent heats of solidification of pure Al (390 kJ/kg) and pure Si (1800 kJ/kg), respectively.

### 2.4 Introduction to Heat Treatment

The aluminum cast components for automotive applications are often subjected to a thermal process called heat treatment which is a function of temperature and time as a post casting operation. The benefits of heat treatment are: (a) an increase in mechanical properties and corrosion resistance, (b) homogenization of the microstructure, (c)

relieving of the residual stresses and (d) improved dimensional stability of the castings (Zalensas, 1993). The heat treatment of an Al-Si-Cu alloy like Al 319 involves three basic operations: (1) Solution Treatment, (2) Quenching and (3) Natural or Artificial Aging. The temper designation of a thermally treatable alloy is denoted by 'T' (Alu-Select, 2004). The first digit after 'T' represents the heat treatment sequence. For example, temper T4 means that the specimen is solution treated and then it is naturally aged, while temper T6 means that the specimen is solution treated and then it is artificially aged (Zalensas, 1993). The basic mechanism behind the strengthening effect of heat treatment is to dissolve the constituent phases in the  $\alpha$ -Al matrix by solution treatment, then cool the specimen rapidly to get a supersaturated solid solution by quenching and precipitating the excess solutes by natural or artificial aging. These steps are explained briefly in the following sections:

#### **2.4.1 Solution Treatment**

The precipitate forming elements like Cu and Mg have limited solid solubility under ambient conditions. During solution treatment these elements are dissolved in the  $\alpha$ -Al matrix by treating them at an appropriately higher temperature for a sufficient amount of time. The solution treatment temperature and time are dependent on the alloy chemical composition, modification level, and the casting technique (Zalensas, 1993 and Major and Apelian, 2003). The solution temperature should be high enough to allow for the maximum diffusion rate of the constituent elements into the solvent. However, the solution temperature should not exceed the incipient melting temperature, where the nonequilibrium eutectic colonies start melting. This will result in poor mechanical properties. Another effect of the solution treatment is the spheroidization of the constituents like eutectic Si that do not dissolve during solution treatment. A chemically modified Al356 (Al-Si-Mg) alloy spheroidizes much better than an unmodified alloy in a shorter time during solution treatment. Also the particle size of the Si particles increases by Ostwald ripening (Major and Apelian, 2003). In Al 319 the iron intermetallic phases such as  $\text{Al}_3\text{FeMg}_3\text{Si}_6$  and  $\beta\text{-Al}_5\text{FeSi}$  do not dissolve or undergo any morphological changes during solution treatment (Crepeau, 1995). However, Narayanan and Samuel (1995) reported that for the Al 319 alloy with an Fe content of 1wt.%, the dissolution of the Fe intermetallic phases increases with the increase in solution temperature and is



decreased by the addition of Mn. The third aim of solution treatment is to homogenize the microstructure. This eliminates the effects of both micro and macro segregation by evenly distributing the precipitating elements.

### **2.4.2. Quenching**

Quenching is defined as the controlled extraction of heat from the casting. After the solution treatment Al castings are immediately quenched to get a supersaturated solid solution. A delay in quenching or quenching with a slow cooling rate (slack quench) will result in the precipitation of the phases at an inappropriate time. The most common quenching media used are water at 65<sup>0</sup>C -100<sup>0</sup>C, a blast of air or a polymer solution (Major and Apelian, 2003, and MacKenzie, 2003). Higher quenching rates will significantly improve most mechanical properties; however, it will cause high residual stresses which in turn may distort the casting.

According to MacKenzie (2003) the mechanism of quenching using a liquid medium takes place in 3 stages consecutively: (1) Vapour stage: A “vapour blanket” covers the test specimen. The heat transfer mechanism at this stage is mainly by radiation and the rate is very slow. In order to avoid this film formation, the quenching medium temperature is kept close to 100<sup>0</sup>C and it is agitated (Major and Apelian, 2003). (2) Boiling stage: During this stage the test specimen comes in direct contact with the quenching liquid and bubbles of boiling liquid are emanated from its surface. This stage has the fastest heat transfer rate by conduction and continues until the temperature of the surface of the specimen is below the boiling point of the liquid. (3) Convection stage: Heat transfer during this stage is mainly by convection and has the slowest heat transfer rate. MacKenzie (2003) also suggests that a polyalkylene glycol based polymer quenchant significantly reduces the residual stress and associated distortion (typical of water quenching) without affecting the mechanical properties. Cloás et al.(1998) have shown that as the cooling rate of quenching decreases, the hardness of the casting also decreases.

### 2.4.3 Aging

During the aging process, the precipitation of the solute atoms from the supersaturated solid solution occurs due to their limited solid solubility at lower temperatures. This process is very slow under the ambient conditions but the precipitation rate increases when the casting is brought to a higher temperature but much lower than the solution temperature. This is called Artificial Aging (AA). Figure 2.3 shows the effect of aging time and temperature on the hardness of Al-4Cu alloy.

It can be seen that for a given temperature, the hardness increases with time and reaches a maximum value and then decreases. The process of aging the casting beyond the time to attain the maximum hardness is termed as over aging. Although over aging decreases the tensile properties a little, it improves the ductility, dimensional stability, and resistance to stress corrosion cracking (Zalensas, 1993). The mechanisms of strengthening and metallurgical transformations of precipitation hardening are well documented in the literature (Zalensas, 1993 and ASM International, 1992). In summary, the formation of coherent Guiner Preston (GP) zones, nucleation of the semi-coherent intermediate precipitates, transformation to a stable incoherent precipitate and finally the coarsening of the precipitates by Ostwald ripening occur successively during the aging process. These events are schematically shown in Figure 2.4. The increase in the hardness with the increase in aging time in Figure 2.3 can be attributed to the resistance offered by the GP zones and the transformation precipitates to the movement of dislocation defects. The decrease in hardness during over aging is due to the coarsening of the  $Al_2Cu$  precipitate. The dislocations can then easily bypass the widely spaced coarse precipitates by Orowan looping (Zalensas, 1993). Figure 2.3 also shows that a lower aging temperature provides higher hardness. However, the time required to achieve this hardness is also much higher which in turn means higher costs and energy from the industry perspective.

Lumely et al. (2003) have reported secondary precipitation between  $25^{\circ}C$  and  $65^{\circ}C$  in the Al 357 casting alloy and in many wrought Al alloys. A modified aging treatment which is termed as “interrupted aging” has been suggested for these alloys. In this method, following the conventional aging treatment the specimen is quenched again to  $20^{\circ}C$ , and aged at a lower temperature ( $25^{\circ}C$  -  $65^{\circ}C$ ) for a sufficient period of time.

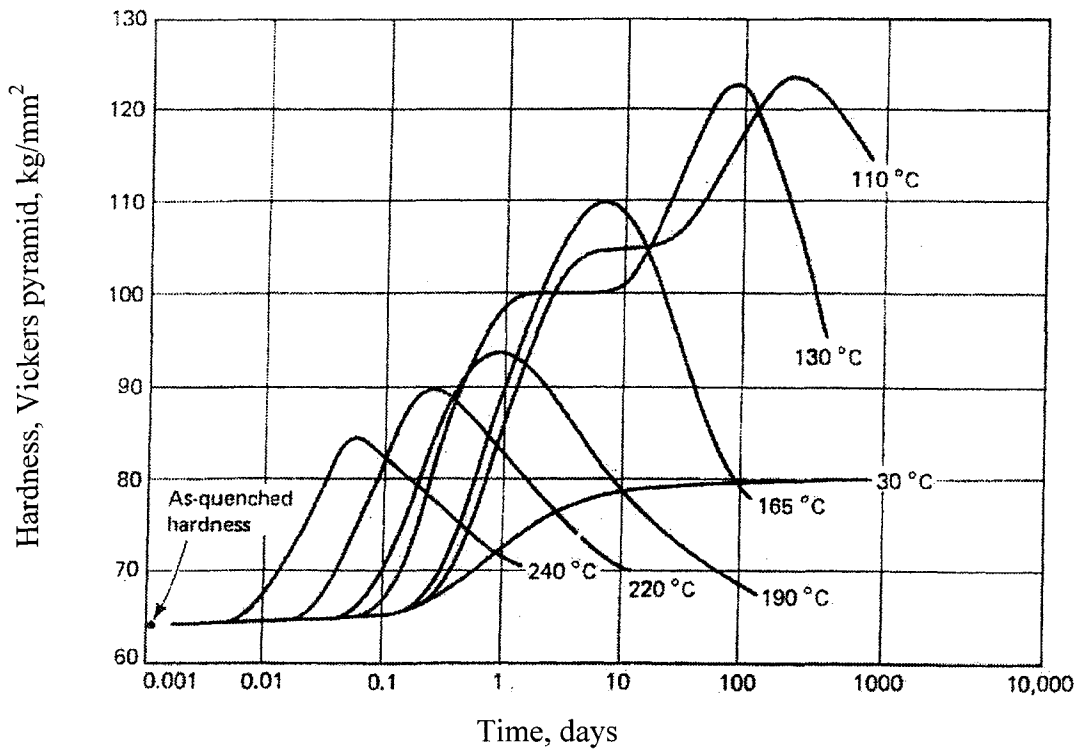


Figure 2.3: Hardness as a function of aging time and temperature for the Al-4Cu Alloy. This alloy was solution treated for 48 hours at 520°C, then water quenched to 25°C (ASM International, 1992).

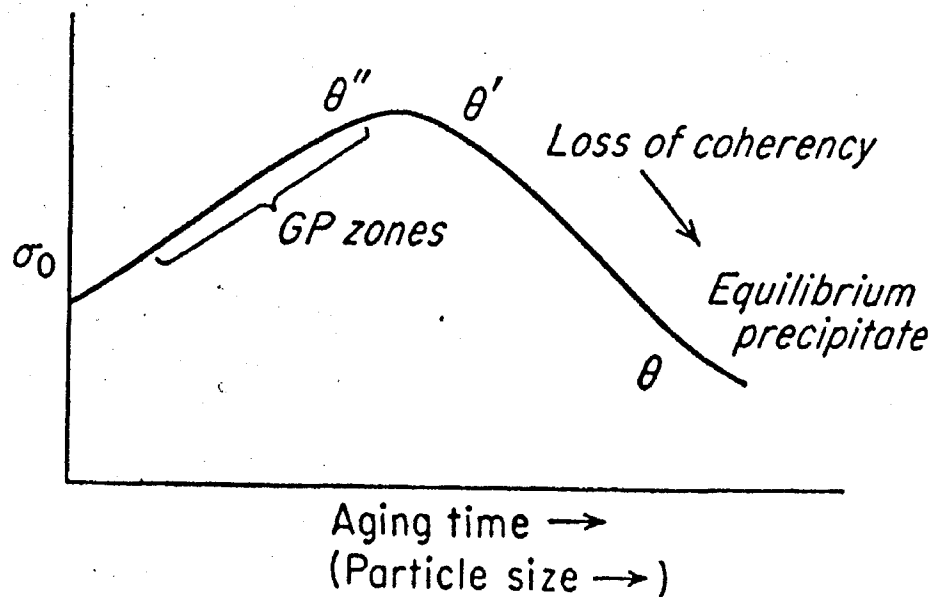


Figure 2.4: Variation of the yield stress, and formation of precipitates with aging time (schematic drawing) (Dieter, 1976).

#### 2.4.4 Literature Review on the Heat Treatment of the Al 319 alloy

The heat treatment of the Al319 and Al356 alloys was investigated in depth due to their widespread consumption in making automobile engine blocks and cylinder heads. Sablonnière and Samuel (1996a, and 1996b) have studied the effect of chemical composition, solution temperature, solution time and aging temperature on tensile properties and the microstructure of the Al319 alloy. Two variants of Al 319 with low and high levels of Fe, Mn and Cr were used in these studies. The level of Mg in these alloys was increased from 0.09 to 0.5 wt.%. The addition of Mg up to ~0.5 wt. % resulted in the partial transformation of the  $\beta$ -Al<sub>5</sub>FeSi phase to Al<sub>8</sub>Mg<sub>3</sub>FeSi<sub>6</sub>, precipitation of the Mg<sub>2</sub>Si phase and precipitation of an Al<sub>5</sub>Mg<sub>8</sub>Cu<sub>2</sub>Si<sub>6</sub> phase. The addition of 0.1wt.% Mg gives an ~5% improvement in alloy strength and an ~3% improvement in ductility. For the Al 319 alloy with low levels of Mg and intermetallics, a two stage solution treatment consisting of 12 hours at 510<sup>0</sup>C (to dissolve all the copper phases) followed by 12 hours at 540<sup>0</sup>C (to dissolve the  $\beta$ -Al<sub>5</sub>Fe Si needle phases and to globularize the eutectic Si) is recommended. In the two-step solution treatment the castings were first heated to just below the melting point of the copper rich phases to dissolve them and then they were safely heated to the final solution temperature to dissolve the additional hardening elements and to achieve a greater degree of homogenization. For the Al 319 alloy with Mg ~0.5 wt.%, a single stage solution treatment at 510<sup>0</sup>C for 12 hours was proposed, as solution treatment above this temperature will result in the incipient melting of the copper phases. Sablonnière and Samuel (1996a) suggested an aging temperature of 158<sup>0</sup>C for 5 hours for the Al 319 alloy. These aging parameters were recommended based on the tensile properties; however, in order to restrict the dimensional growth during service over aging may have been required.

Sokolowski et al. (1995) compared the mechanical properties of the cast Al 319 alloy after the traditional one-step and a two-step solution treatment followed by artificial aging. It was found that the two-step solution treated test samples had higher mechanical properties (tensile strength, hardness and impact energy) compared to their one-step solution treated counter parts. The higher mechanical properties were attributed to the higher degree of dissolution and homogenization of the Cu rich phases during the two-step process. Sokolowski et al. (1995) also proposed a new method to quantify the matrix

homogeneity as a function of the variability in the micro hardness across the sample. This investigation recommended a first step solution treatment of 8 hours at 495<sup>0</sup>C followed by a second stage of 2 hours at 520<sup>0</sup>C, water quenching and artificial aging of 5 hours at 250<sup>0</sup>C for the W319 alloy. Sokolowski et al. (2001) further examined the parameters of the two-step solution process in order to optimize the solution treatment time, temperature, and the aging time and temperature. For the 319 alloy with 20 ppm of Sr the optimum temper for mechanical properties and homogeneity was: solution treatment 2h at 495<sup>0</sup>C; ramp time (20 min) to 515<sup>0</sup>C for 4 h; followed by water quench to 74<sup>0</sup>C ; artificial aging:3 h at 250<sup>0</sup>C. It can be seen that compared to the optimum treatment time reported by Sablonnière and Samuel (1996b) (15 hours), the new optimum treatment time is much shorter (9 hours) and achieves almost similar mechanical properties.

Wang et al. (2003a) studied the solution treatment of Al11Si(1-4)Cu0.3Mg alloys using a Differential Scanning Calorimeter (DSC). It was found that for alloys with less than 2 wt. % Cu, it was possible to complete the solution treatment in a single step at 535<sup>0</sup>C while for alloys having more than 2wt.% Cu, a two-stage solution treatment was required. This was because lower amounts of copper would form a very small amount of Cu precipitates to dissolve during the solution treatment. It was also noted that higher solidification rates reduce the amount of precipitates formed and decrease the dendrite arm spacing. This would lessen the diffusion distances of the precipitates which in turn would decrease the solution treatment time. The energy (area) of the endothermic peaks of the Cu reactions obtained by calorimetry could be related to the amount of Cu enriched phases dissolved in the  $\alpha$ -Al matrix. The obtained results were in agreement with the metallographic measurements (Lasa and Rodriguez-Ibabe, 2002, and Djurdjevic et al., 2001a). Lasa and Rodriguez-Ibabe (2002) indicated that DSC analysis could be used to optimize the solution treatment parameters of the Al alloys instead of the conventional time consuming metallographic analysis.

Recently, in order to reduce the long cycle times of heat treatment (6-30 hours) of Al castings, Fluidized Beds (FB), instead of conventional furnaces, were proposed. FB have more rapid and efficient heat transfer and offer more uniform distribution of the temperature than conventional furnaces. Studies on the A356 alloy have shown that the kinetics of the metallurgical transformations (spheroidization and coarsening of Si and

Mg<sub>2</sub>Si phases) was much faster with FB reactor. In fact, for the A356 alloy, FB could yield the similar mechanical properties as in conventional furnaces in as short as 30 minutes (Makhlouf et al. 2003, Keist and Bergman 2003, and Chaudhury et al., 2003). However, currently there is no literature available on the heat treatment of Al 319 alloys using FB.

#### **2.4.5 Heat Treatment of the W319 Alloy at the Windsor Aluminum Plant (WAP)**

Presently, at WAP the solution treatment is integrated with the Thermal Sand Removal Process (TSR). Inside the TSR furnace, heat and air decomposes the resin so that the zircon sand strips away from the casting. About 95% of the zircon sand is recycled. The TSR is designed to maintain a steady temperature over the entire cycle (5 hours). The furnace manufacturer claimed that effective TSR and solution treatment could be performed in the same cycle. However, the Industrial Research Chair (IRC) found that this was not feasible for macro segregated copper rich phases in the W319 casting (especially in the bulkhead section) when the transfer temperature was dropped below the solution temperature. In 1993, the IRC optimized the solution temperature (500<sup>0</sup>C) for the W319 alloy castings in order to avoid the detrimental incipient melting of AlCuMgSi rich phases. The time/temperature profile studies indicated that the breakdown of the sand mold and the core required a minimum of 3.5 hours, leaving 1.5 hours for the solution treatment. This time was insufficient to dissolve the AlCuMgSi segregated phases. The castings coming out of the TSR furnace were immediately quenched. The castings were then transported to B&W Heat Treating, Kitchener, Ontario, for artificial aging.

The type of heat treatment depends on the size of the engine block. 2.5L, 3.0L and 3.9L engine blocks are given a T5 heat treatment which means heating to the solution treatment temperature for a time period sufficient to remove all the sand, air quenched and then artificially over aged. This is a deviation from the T5 heat treatment, because by definition the T5 heat treatment implies only artificial aging without any prior solution treatment, but in this case the blocks are partially solution treated in the TSR process. These engine blocks have cast-in liners where the cylinder liners are placed in the mold assembly before the casting operation. The 4.6L engine blocks are given a T7 heat treatment: Solution treated during TSR, air quenched and artificially over aged. These

blocks have press-in liners where the cylinder liners are press fitted into the block at the engine plant (Burford, 2004).

Since TSR, Solution, and Artificial Aging treatments of the engine blocks represent a high percentage of WAP's total manufacturing costs, there is a need to develop new technologies and optimize them to reduce production costs and to improve productivity. It can be seen clearly that if an alternative heat treatment method can produce the same mechanical properties as the present methods in a much shorter time, then costs can be minimized and energy savings can be maximized. The Novel Solution Treatment during Solidification (NSTS) can be carried out to achieve this objective.

#### **2.4.6. Introduction to Novel Solution Treatment during Solidification Process(NSTS)**

Traditionally, heat treatment is a post solidification or post casting process. The main idea behind the NSTS process is to integrate the heat treatment with the solidification process and hence to minimize the heat treatment time. This can be achieved by isothermal holding of the solidifying casting at a desired temperature for a sufficient period of time. This method was reported in 1999 in a United States Patent (No. 5,922,147) as a "simplified heat treatment method to harden aluminum castings made from heat treatable aluminum alloys with a copper content of up to 5wt.% such as 3XX-T6 series" (Valtierra et al., 1999). This patent presented a concept that is generally applicable to all 3XX Al alloys.

The IRC at the University of Windsor developed the specific NSTS process for the W319 alloy (containing >3.3 wt.% of Cu), and studied its effect on the structure and mechanical properties of the cast components (Chen, 2003). The isothermal holding temperatures for this study were established by cooling and heating curve analysis of the W319 alloy. Figure 2.5 shows the heating, cooling curves and the first derivative of the W319 alloy. It can be seen from Figure 2.5 that the melting of the Cu enriched phases begins at 505<sup>0</sup>C and ends at 521<sup>0</sup>C. Therefore the isothermal holding solution temperatures of the optimum NSTS must be above 500<sup>0</sup>C. Table 2.2 provides the metallurgical transformations and the corresponding temperatures during heating and

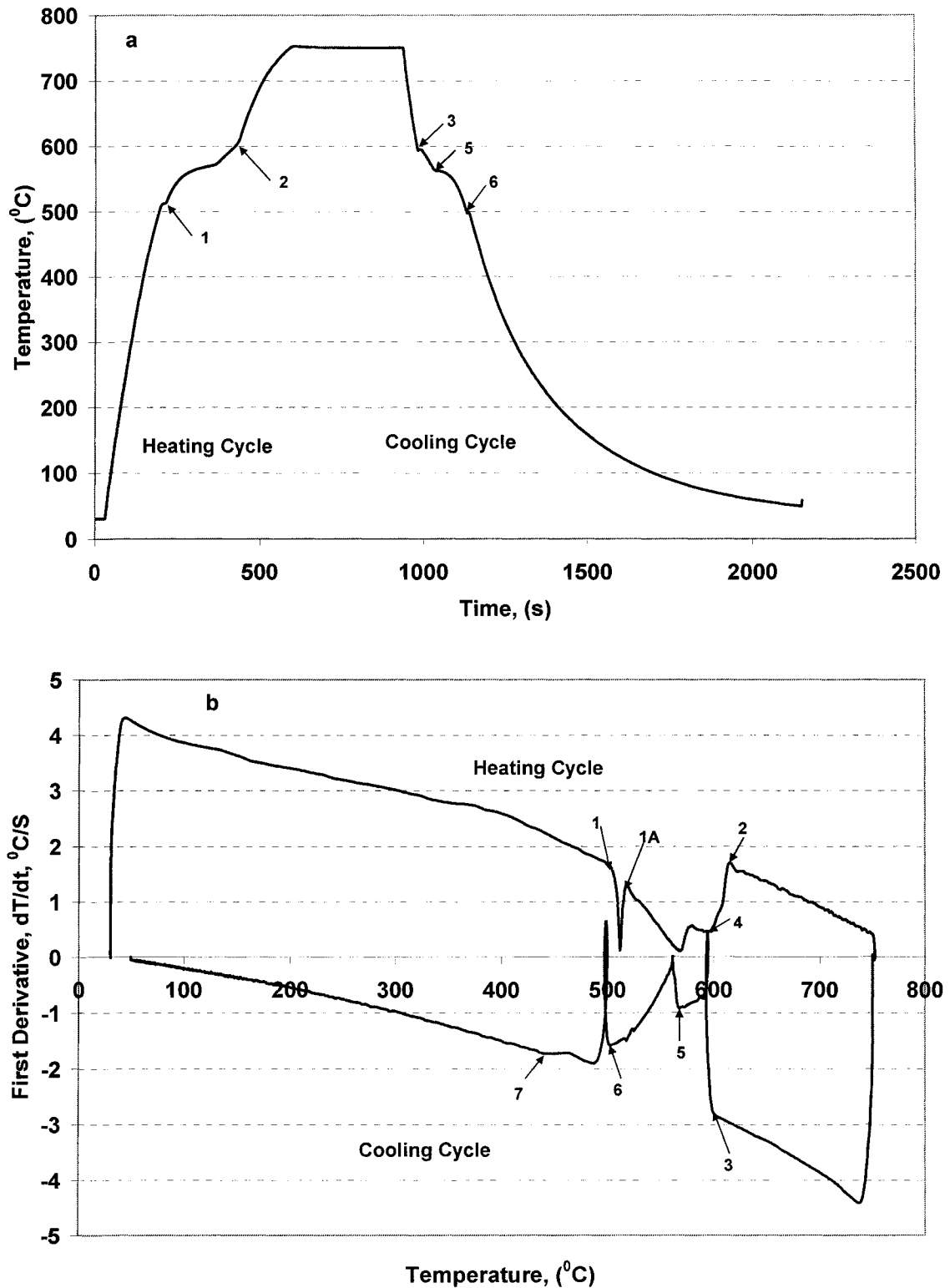


Figure 2.5: (a) Heating and cooling curves of the W319 alloy; (b) First Derivative versus Temperature curve.



**Table 2.2: Metallurgical transformations during the heating and cooling cycles of the W319 alloy**

Reaction Number in Figure 2.5(b)	Heating		Solidification	
	Reaction Name	Reaction Temperature (°C)	Reaction Name	Reaction Temperature (°C)
1	beginning of the alloy melting	505		
1A	end of dissolution of the Cu phases	521.6		
2	end of alloy melting process	616.5		
3			beginning of the nucleation of the Al dendrites	598.9
4			Dendrite coherency point	594.5
5			beginning of the nucleation of the Al-Si eutectic	565.1
6			beginning of the nucleation of the Cu enriched phases	501.4
7			end of the alloy solidification	440.5

cooling cycles of the W319 alloy.

The major objective of the solution treatment of Al319 alloy is to dissolve the maximum amount of Cu phases in the aluminum matrix. The effectiveness of the solution treatment can be quantified by measuring the area percent of the Cu enriched phases that is left undissolved after solution and aging treatments using Image Analysis. The matrix microhardness measurements also reflect on the performance of the solution and aging treatments because the microhardness increases as the concentration of the precipitates in the  $\alpha$ -Aluminum increases. The temperature and time of isothermal holding are the critical parameters of the NSTS process. Design and analysis of the experiments by varying the isothermal holding temperatures and times have revealed that the matrix microhardness is maximum when the isothermal holding temperature is in the range of 510<sup>0</sup>C-520<sup>0</sup>C (Chen, 2003 and Chen et al., 2003). This means that for this temperature range, during isothermal holding, most of the Cu atoms dissolve in the  $\alpha$ -Aluminum without forming the Cu based phases. From Figure 2.5a it can be seen that this temperature range is within the start and end melting temperatures of the Cu phases in the heating cycle. It was found that isothermal holding above 520<sup>0</sup>C is not effective as it is far above the nucleation temperature of the Cu enriched phases. Also holding temperatures below 500<sup>0</sup>C are not advised because this does not maximize the diffusion of Cu into the Al matrix. As the isothermal holding time increases, the matrix microhardness also increases irrespective of the holding temperature. However, holding time must be minimized from the energy and cost point of view (Kasprzak, et al., 2001).

A comparison of the tensile properties of the heat treated (solution treated and artificially aged) V6 3.0 L engine blocks and NSTS treated samples are given in Figure 2.6. It can be seen that NSTS treated test samples result in similar or even higher mechanical properties. The NSTS process provides these properties in a much shorter (250%) solution time than the conventional solution treatment. This is shown in Figure 2.7.

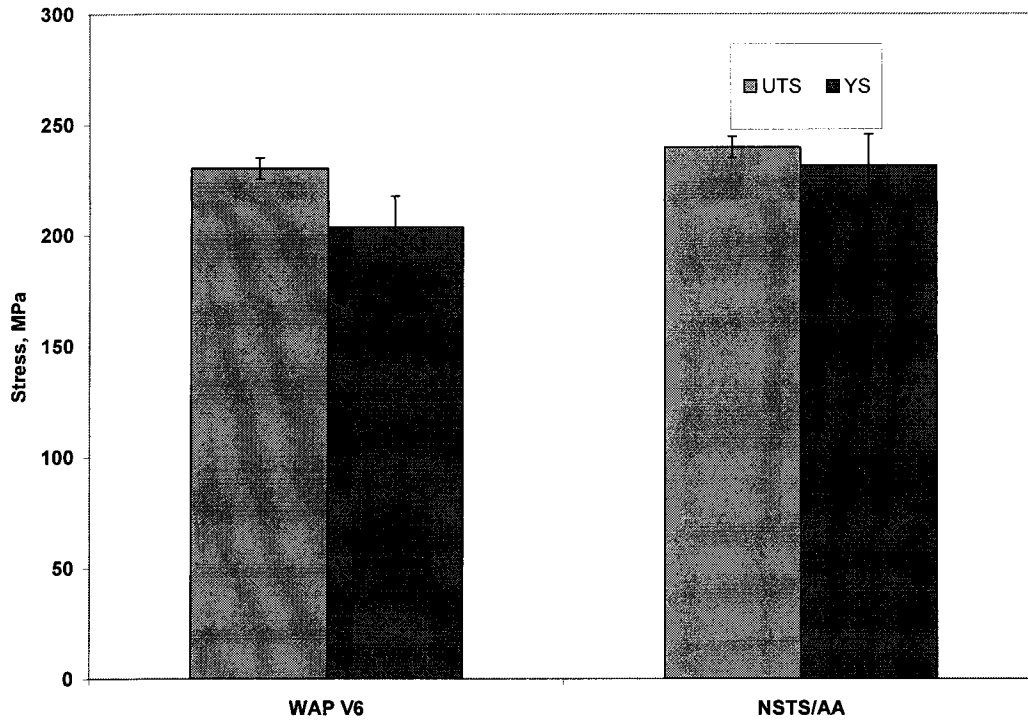


Figure 2.6: Comparison of the tensile properties of the heat treated WAP V6 3.0L engine blocks and test samples after the NSTS process at 510°C for 30 minutes followed by Artificial Aging (AA) at 200°C for 2 hours (Chen, 2003).

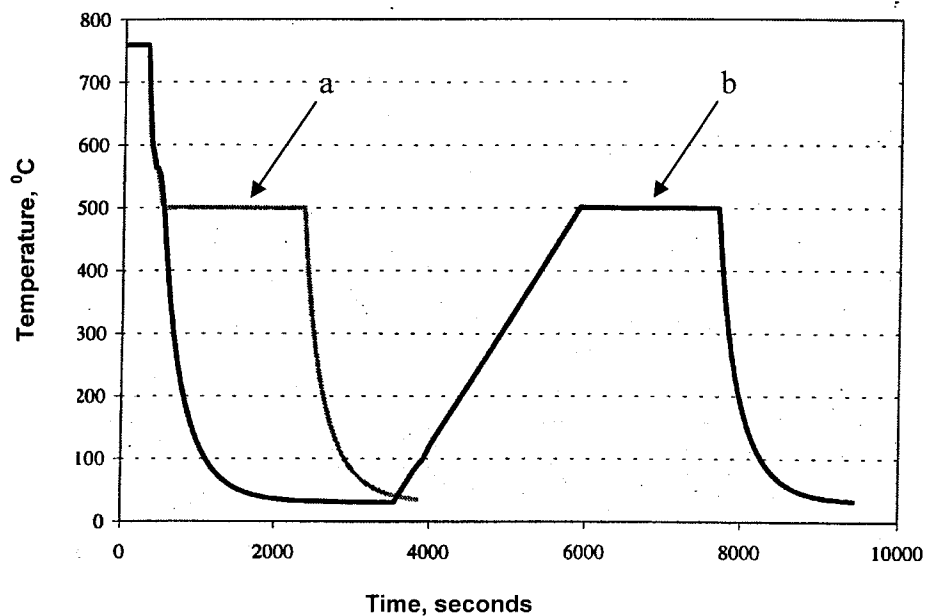


Figure 2.7: Comparison between the solution times of (a) the NSTS process and (b) the conventional Solution Treatment process.

## 2.5 Artificial Intelligence Applications in the Metal Casting Industry

In recent years the casting industry has seen the extensive usage of artificial intelligence techniques such as expert systems, fuzzy logic, case based reasoning, genetic algorithm and neural networks in the areas of diagnostics, design, planning, monitoring and prediction (Sillèn, 2002 ). Cooling curve Thermal Analysis is an area where artificial intelligence techniques can be incorporated for the prediction of the microstructure and mechanical properties of the castings. Although there are many Thermal Analysis systems available only a few are reported to have artificial intelligence systems incorporated. ATAS<sup>®</sup> is an artificial intelligence based commercial Thermal Analysis system developed for cast iron foundries (Novacast, 2004). This system employs a rule based expert system (that makes use of if-then rules) to interpret the cooling curve characteristics and hence to predict the quality of the melt. The cooling curve characteristics are estimated by using a Case Based Reasoning (CBR) system. The CBR system has examples of cooling curves with known characteristic outcomes stored in its database. When a new cooling curve is presented, the system searches its database using a similarity index to find the most similar case and the associated characteristics are presented as the predicted outcome (Sillèn, 1996). Li et al. (1999) have developed two back propagation neural network models to predict the chemical composition and the mechanical properties of grey cast iron using Thermal Analysis parameters as inputs. These results show that neural network give more accurate predictions than a multiple regression models.

Chagoya (2001) developed a knowledge based Thermal Analysis system to predict the casting characteristics of the W319 alloy using a CBR system. The cooling curve Thermal Analysis was performed by the software of the Aluminum Thermal Analysis Platform (ALTAP) and the parameters (time, temperature and fraction solid) of the characteristic reactions were passed on to the CBR system that uses the 18 cases stored in its library to predict the casting characteristics. The Thermal Analysis experiments and the casting microstructure and mechanical properties data for the development of this system were obtained from WAP. Wang et al. (2003b) used neural networks and the parameters of the cooling curve, (viz: liquidus under cooling

temperature, liquidus arrest temperature, and liquidus under cooling time), to predict the Grain Size of Ti and B refined Al-7wt.% Si alloys. Since this dissertation also utilized neural networks for modeling the Silicon Modification Level (SiML) of the W319 alloy, a detailed literature review on application of neural networks in materials science is presented below.

### 2.5.1 Artificial Neural Network (ANN)

ANN consists of simple synchronous processing elements that are inspired by biological nervous systems (Calcaterra et al., 2000). They solve a problem by means of learning rather than by specific programming based on well-defined rules (Lehr et al., 1994, and Beale et al., 2002). The input and output data are linked using a particular set of nonlinear basis functions. The basic unit of the ANN is the *neuron*. Neurons are connected to each other by links known as *synapses*; associated with each synapse there is a *weight factor*. Usually neural networks are *trained* so that a particular set of inputs produces, as nearly as possible, a specific set of target outputs (Malinov et al., 2001). In feed-forward ANN the information is processed in one direction - from input to output - and the neurons are arranged in layers. The number of input and output parameters determines the number of neurons in the input layer and in the output layer, respectively.

ANN can be employed to model complex, nonlinear processes due to the following reasons:

1. ANN has adaptive learning algorithms and a trained neural network can generalize well on the test data. In other words ANN has self-learning and self-tuning capacity, and the output of the ANN approach successively the desired output during training (Pospichal et al., 1997 and Chen et al. 2002).
2. ANN can capture the interactions between the inputs because the hidden units are non-linear. The nature of the interactions is implicit in the values of the connection weights (Bhadeshia, 1999).
3. Modeling using ANN has been extensively used in the field of Materials Science and Engineering; Approximately 90 papers were found published in this area in the last decade. Some of the selected examples reported in the literature are given below:

Perzyk and Kochanski (2001) developed a multilayer perceptron backpropagation neural network to predict the hardness, tensile strength and elongation of ductile cast iron using the chemical composition, spheroidization and pouring temperatures as the inputs. Yarlagadda and Chiang (1999) predicted the injection time of the high pressure die casting process using the melt temperature, die temperature, casting weight and the injection pressure as inputs. They found that the Levenberg-Marquardt training algorithm gives smaller mean square errors for the testing data when compared to other training algorithms. Kusiak and Kuziak (2002) used the austenite grain size, and the solidification rate as inputs to predict the proeutectoid ferrite, Widmanstätten ferrite and perlite fractions as well as the ferrite grain size of steel. They also developed a second neural network model to estimate the mechanical properties (yield strength and ultimate tensile strength) of steel from the chemical composition. The model was later validated using industrial data. Malinov and Sha (2004) developed a neural network model to predict the Time Temperature Transformation (TTT) diagrams of titanium alloys from its chemical composition. They further developed another neural network model to estimate the mechanical properties of titanium alloys using the chemical composition, heat treatment parameters and work temperature as inputs.

Neural network modeling involves the following steps:

- a. **Database collection:** The input-output sets (dataset) are gathered by experimentation, literature, or from industry data.
- b. **Analysis and preprocessing of the data:** This step involves the splitting of the data set into training and testing sets. The training dataset is randomized before the training phase.
- c. **Training of the Neural Network:** The process of fitting the network to the experimental data is called *training*. It consists of adjusting the weight of each connection (*synapse*) between neurons. The weight of a synapse multiplied by the strength of the signal on that synapse gives the contribution of that synapse to the *activation* of the neuron for which it is an input. The total activation of a neuron is then the sum of the activations of all of its inputs and this defines the value of the

output signal for that neuron, via a *transfer function*. Transfer functions are generally s-shaped (sigmoid) curves, with the output value confined within the limits such as (0,1) or (-1/2,1/2). The most popular transfer functions are hard limit, linear, log sigmoid, and hyperbolic tangent sigmoid and radial basis function (Malinov et al., 2001).

By adjusting the values of synaptic weights throughout the network, the outputs of the ANN for any given set of inputs can be altered. During the training the weights are adjusted until the network correctly simulates the behaviour of the system to be modeled. The simulation will rarely be exact; training is usually aimed at minimizing the sum of squares of the differences between predicted and measured values of the outputs.

- d. **Testing of the trained network:** The trained network is simulated with unseen input data that is not used for training and the obtained outputs are compared with the target outputs to assess the generalizing ability of the neural network.

## 2.6. Literature Review on the Application of Optimization Methods in Materials Science

Traditionally and still sometimes, optimization is a time consuming and expensive trial and error routine in materials science. However, with the current advances in software engineering, many statistical, simulation and optimization software packages are available for use. These softwares are very user friendly and contain all the standard algorithms and techniques that the engineer may require. Using the available literature data, computer simulations can predict the effect of varying the design variables on the response variables. This largely eliminates the time consuming trial and error experimentation. Experimentation is necessary only to verify the optimal outcome (Schmidt, 2001). A review of the literature of the application of optimization methods in materials science has revealed that generally speaking there are three approaches that are employed for optimization.

The first approach is mainly used for optimal alloy selection and for deciding the compositions of constituent elements in the alloy. This approach can be called the “metallurgical paradigm” of optimization. It makes use of the phase diagrams and

thermodynamic calculations to predict the microstructure and phases that will result for different compositions of the alloy. Commercial metallurgical software packages like Chem-Sage®, Thermo-Calc™, and CALPHAD™ are able to predict the phase diagrams and the phases formed from multicomponent alloys. A composition that will give a microstructure, which in turn improves the mechanical properties, will be the optimal composition. Waldner et al. (1995) used this approach to optimize the levels of Chromium (Cr) and Tungsten (W) in a cobalt (Co) based alloy for wear and corrosion resistance applications at elevated temperatures. Zhu et al. (2002) proposed a streamlined method for the design of a creep resistant Al-Cu-Mg-X wrought alloy that is age hardenable using the phase diagrams. According to them “in order to optimize a given property one must determine the necessary ideal microstructural components, which are dictated by alloy composition and processing from solidification through final manufacture”. Tagiev et al. (1996) also stressed the importance of the investigation of the multicomponent phase diagrams, and structure-property relationships to optimize the composition of high strength casting aluminum alloys.

The second approach uses statistical Design of Experiments (DOE) and Taguchi Methods™. Park et al. (2001) determined the optimal process parameters (Si content of the alloy, sintering time and temperature) of the powder forging process for an aluminum piston alloy using DOE. Major et al. (2000) used a fractional factorial design ( $2^{8-4}$ ) to optimize the composition of the AA512 alloy permanent mold casting so as to improve its ductility by the formation of a fine ternary eutectic microstructure. Sokolowski et al. (2001) optimized the heat treatment parameters (Solution Treatment, quenching and Artificial Aging) of the Al 319 aluminum alloy using a ( $2^{6-3}$ ) fractional factorial design. Taguchi Methods™ use highly fractionated factorial designs called orthogonal arrays and are widely used by quality practitioners due to their simplicity (Ross, 1988). Syrcos (2003) used the Taguchi Methods™ to determine the optimal process parameters (piston velocity, metal temperature, filling time and hydraulic pressure) of the die casting process of the Al9Si13Cu alloy that would improve the casting density. In DOE and Taguchi Methods™, the Analysis of Variance (ANOVA) of the experimental data provides the critical parameters and interactions influencing the response. However, a two level



experiment is unable to provide information about the nonlinearity of the process. Therefore they can only be used as screening experiments.

The third approach consists of modeling the process using the data from the experiments and then searching for the optimal process parameters using a search method. The modeling of the process is usually performed by using Artificial Neural Network (ANN) or Regression Models. The search methods normally used are calculus based techniques or guided random search methods like genetic algorithms and simulated annealing (Sadagopan and Pitchumani, 1998). This approach has been utilized in this dissertation. Song and Zhang (2001a and 2001b) and Song et al. (1995) determined the optimal percentage of plastic deformation for hot and cold work, as well as the optimal Solution Treatment and aging time of the 7175 wrought aluminum alloy using ANN and genetic algorithms. Geng et al. (1998) optimized the chemical composition and the tempering temperature of the steels used in space crafts for high strength and high fracture toughness, by using ANN and simulated annealing algorithm. They recommended this method for multiobjective problems where no analytical expression relating inputs and outputs was available. The machining parameters of the high speed milling of SKD 61 tool steels were optimized to obtain the minimum production cost by the application of polynomial networks (a variant of the neural network) and simulated annealing (Juan et al., 2003). Chakraborty and Mukherjee (2000), compared the performances of genetic algorithm, simulated annealing and the steepest descent method in optimizing the casting parameters such as negative strip time, flux pool depth and vitrification ratio to obtain the maximum casting speed in the continuous casting of steel billets. The steepest descent algorithm failed to converge, while the genetic algorithm found a solution that is closer to the values practiced in the industry than that of simulated annealing.

It is also noteworthy to mention the interesting work by Ashby (2000) on the multiobjective optimization in material design and selection. In a multiobjective optimization material selection problem with conflicting objectives, Ashby suggested the creation of a “trade off surface” that identifies a set of solutions that offers the best

compromise between the objectives. He also proposed the formulation of a composite objective function called “value function” (V) and the minimum value of ‘V’ will be the over all optimum.

### **3. Introduction to the Cosworth Casting Process and the Quality Control System at Windsor Aluminum Plant (WAP)**

#### **3.1 Quiescent Mold Filling Techniques for Aluminum Cast Components**

The aluminum casting industry use variations of the low pressure pouring method for quiescent mold filling. In this method, the metal is introduced into the mold from the bottom or side at low pouring rates. The metal is drawn into the mold by either vacuum or is pushed in by air pressure, centrifugal force, or by a pump (Gouwens and Gouwens, 2004). These methods fill the mold with a minimum turbulence to the melt and hence this minimizes the formation of entrapped oxides and hydrogen as opposed to the gravity pouring process. The main low pressure filling methods are Reduced Pressure Permanent Mold (RPPM), Reduced Pressure Sand (RPS) and Counter Gravity (CG) casting processes (Mackay, 2003). Recently, Montupet S.A in Quebec has patented a process called the Sand Hybrid Low Pressure (SHLP) process; the highlights of which are (a) usage of green sand molds, (b) gating system and risers on the deck area of the block, (d) roll over after filling and (c) rapid cooling of the thick bulkhead sections by means of chills to improve the fatigue properties of these critical sections (Meyer and Plumail, 2002). Computer simulations and radiographic analysis of the investment castings have shown that mold filling systems with controlled bottom filling have a quiescent metal flow and fill the test bars evenly (Jolly et al., 2002). The castings are manufactured at the Windsor Aluminum Plant (WAP) by a technique known as the Cosworth Precision Sand Process (CPSP) (Kanicki, 1994).

#### **3.2 Description of the Cosworth Precision Sand Process (CPSP)**

Based on the original concept of Dr. J. Campbell, the Cosworth process was developed in the 1970s by Cosworth Technology Ltd., Worcester, England, to meet the need for highly specialized cast components for Formula One race car engines. In 1989, the Windsor Aluminum Plant, which is the largest engine block foundry in the world, obtained a license to cast parts using the Cosworth process. This process was significantly improved and tailor made by Ford engineers and the IRC who converted it into a high volume production process for consumer vehicles, so that the casting yield was increased

by 85%. This is because the filling time of the pump for a mold is only 30 seconds and after rollover (rotating the mold by 180°) the rest of the liquid metal feeding during solidification was done through risers and not by the pump. Alternatively, in the original Cosworth Process the pump pressure was maintained throughout the solidification. This considerably reduces the yield.

The following sections describe the steps involved in the CPSP.

### 3.2.1 Mold and Core Making

The Cosworth process uses cores made of zircon sand (Cosworth Technology, 2004a). The cores are interlocked to form the mold into which the molten aluminum is pumped (See Figure 3.1). The advantages of using zircon sand over silica sand are:

- It has a similar specific gravity as molten aluminum, therefore the core does not move or float in the aluminum.
- It has a low thermal coefficient of expansion which provides exceptional accuracy and minimal core distortion (less than 0.05%).
- It has high conductivity and provides a higher solidification rate of the cast component.
- It is chemically inert to Al alloys at normal casting temperatures.
- It has a stable grain structure which enables thermal reclamation with minimal losses. Though zircon sand is more expensive than silica sand, some of the cost difference is offset as 95% of the Zircon sand can be reclaimed.

The binder system (ISOCURE™ system from Ashland Chemical Company) uses the cold box process. This process does not require heat to cure the core but instead uses a catalyst gas (Tri Ethyl Amine). The ISOCURE™ system is a modification of the Phenolic-Urethane cold box system invented by Ashland (Foti, 1999). Two parts of the resin (phenol-formaldehyde resin and poly methylene bis-phenylisocyanate) are mixed in the ratio 55/45 and then added to the sand. These are blended together to achieve uniform coating of sand grains. The mixed sand is introduced into the core making machine. The core box cavities are filled with the sand-resin mixture by blowing compressed air into the machine. The catalyst gas is then passed through the core to cure it instantly.

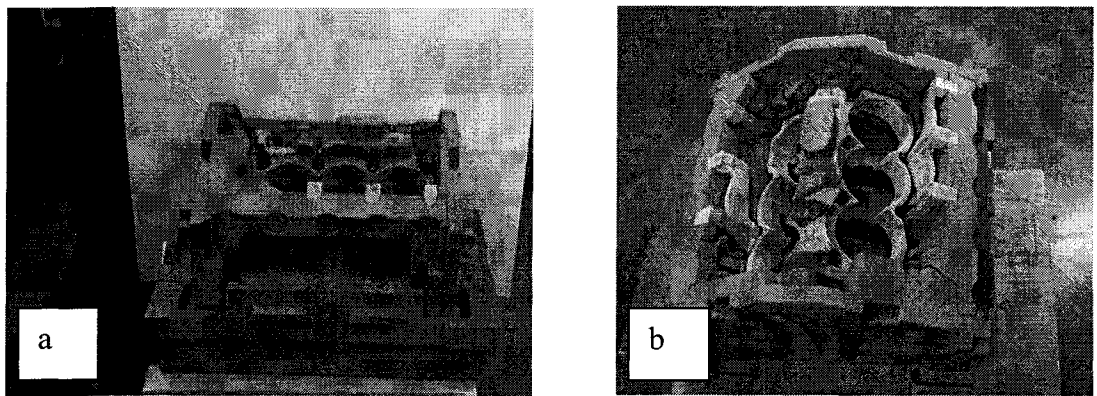
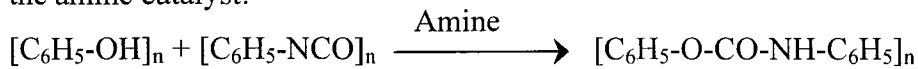


Figure 3.1: Photograph of the zircon sand mold of a 3.0L V6 engine block, with its top cover removed. (a) Front view, (b) Top view.

During curing the following addition polymerization reaction occurs in the presence of the amine catalyst:



The hydroxyl groups of phenolic resin reacts with the isocyanate groups of the poly isocyanate to form the poly urethane resin. It is the polyurethane resin that bonds the sand particles together (Ashland, 1994).

The cores are then assembled by robots to form the mold. The sand molds are vented to remove the gases trapped during casting. The completed core package is then transported by the monorail system to the melt area, where the cast-in cast iron liners are pre heated to reduce the chilling effect of the iron on the molten aluminum during fill. This is called the Tocco Process. The package is then transferred to a carousel rollover system that moves it into the place for casting.

### 3.2.2 Melting of Ingots, Scrap Blocks and Cut off Risers

The W319 ingots, the cut off risers from the engine blocks and the scrap blocks after removing the cylinder liners are melted in a jet melting furnace and the melt is then transferred to a Reverb Furnace. The charge materials are preheated inside the jet melter before introducing them into the molten liquid melt bath.

### 3.2.3 Liquid Melt Processing

The liquid melt processing consists of radiant electrical heating of the melt, use of an inert nitrogen atmosphere, continuous degassing of the melt and a large holding furnace.

The use of radiant electrical heating minimizes the convection currents induced into the melt. This helps the oxides such as Alumina ( $\text{Al}_2\text{O}_3$ ), Magnesia ( $\text{MgO}$ ) and Magnesium Aluminate Spinel ( $\text{MgAl}_2\text{O}_4$ ) as well as impurities (eroded molding materials and refractories) to settle at the top or bottom of the melt at a constant melt temperature. An inert atmosphere of nitrogen gas blanket is used to cover the melt and this prevents further oxidation of the melt. The level of hydrogen in the melt is reduced by degassing where argon gas is passed into the melt using a rotary impeller. As the gas bubbles move up through the bath, hydrogen diffuses in to the bubbles due to the difference in its in the

partial pressure in the bath and its partial pressure in the bubbles. The rotary impeller produces very small bubbles that rise very slowly to the surface of the melt. This allows more hydrogen to diffuse in the bubble. Also the rotary impeller produces lesser turbulence in the melt than the graphite lance (Zalensas, 1993). The gas bubbles also help some of the oxides to float to the surface of the melt.

Aluminum reacts with oxygen to form oxides, which are entrained in the melt. These oxides nucleate pores and limit the fatigue life of the casting. Some of the oxides can be prevented from entering the mold by using filters. The melt is filtered after degassing and also at the entrance of the pump duct using ceramic foam filters. In addition to this, WAP uses a large holding furnace with a long residence time to clean the melt. The oxides float to the surface and the gentle filling of the mold prevents the oxides from entering the mold.

The W319 alloy used at WAP is not grain refined since the Ti residual jams the pump orifice (Sokolowski et al., 2000). Sr is no longer used to modify the melt because it leads to the formation of stable oxide residues that also clogs the pump nozzle (Sokolowski et al., 2003). A mixture of nitrogen and chlorine (up to 5wt.%) was used for degassing; however chloride residues causes the blockage of the electromagnetic pump. Therefore, presently at WAP degassing is done using an inert argon gas as per the recommendations of the IRC (Sokolowski et al., 2003). Figure 3.2 shows the preparation and processing of the melt before casting.

#### **3.2.4 Casting/Pouring**

The sand molds are placed in a carousel rolover system that moves it into place for filling. The mold is filled vertically as the feed tube from the electromagnetic pump is connected to the main side sprue of the mold. The metal is drawn from the middle of the holding furnace. This ensures that the cleanest metal enters the mold. The feeding pressure is provided by the electromagnetic pump which is permanently immersed in the large volume of metal in the holding furnace. The electromagnetic pump has a closed loop control system as shown in Figure 3.3. The feedback is provided by an antenna, that measures the height of the aluminum in the mold. The antenna uses the principle of

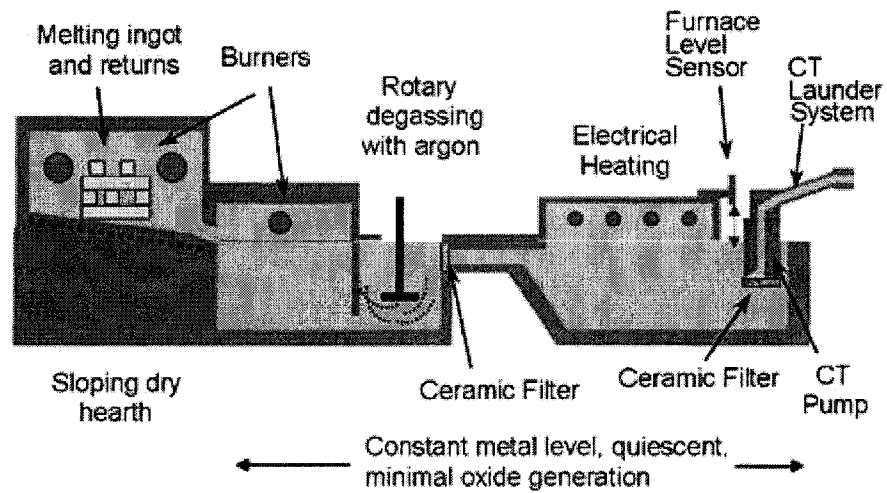


Figure 3.2: Preparation and processing of the melt before casting (Cosworth Technology, 2004b).

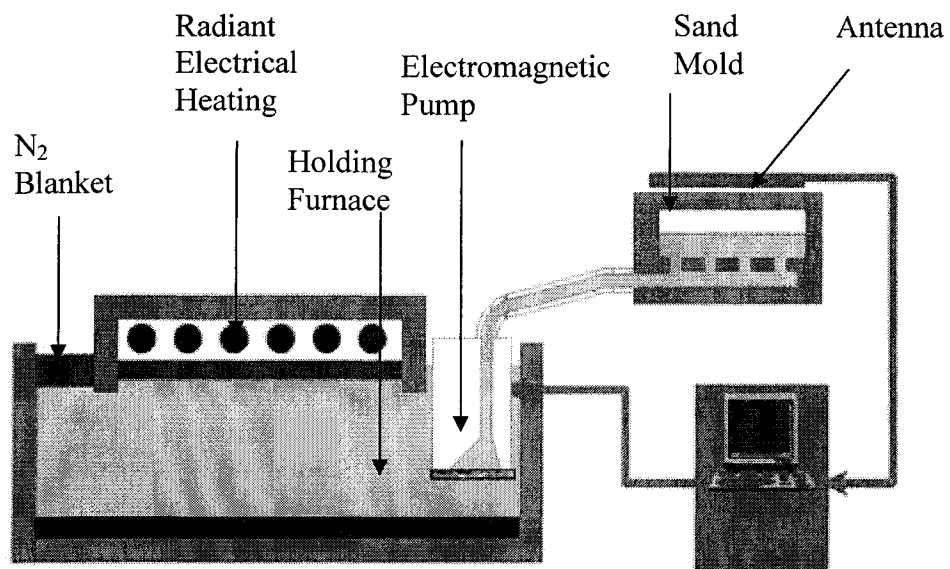


Figure 3.3: Closed loop feedback control system for the precise and repeatable casting process (Cosworth Technology, 2004b).



parallel plate capacitor where one side of the capacitor is the antenna and the other side is the aluminum in the mold. As the mold fills, the distance between the plates changes and thus the value of the capacitance is changed. The relative height of aluminum in the mold is measured as a function of the capacitance. The pump uses a preprogrammed fill profile to fill the mold. Fill profile is a program that contains information such as mold height at various times, the voltage applied to the pump, the allowable trim value for the voltage and the time for the roll over to start.

The filling process starts when the computer increases the voltage on the pump. The aluminum will start to flow into the mold. The voltage is changed incrementally as the casting continues to fill. If the mold height measured by the antenna lags or leads the pre-programmed value at any point of time, the computer will trim the voltage on the pump to compensate. This provides a very accurate and repeatable filling process. All the measured values are stored every half a second (See Figure 3.4). Following the low pressure fill, the mold is rotated 180° (called roll over) and is moved away from the furnace. The metal in the feed tube then drains back into the holding furnace to prevent metal spill. During the roll over process pump pressure is maintained on the mold. This keeps up the metal feed to the solidifying casting. Feeding then continues through the risers without the need of the pump pressure. This procedure allows for a very high level of productivity. After roll over the hottest metal present in the risers feeds the bulkheads (the critical section of the block that solidifies last). Roll over also minimizes the convection currents in the solidifying melt because the hottest metal is on the top of the mold. The roll over technique is illustrated in Figure 3.5.

### **3.2.5 Thermal Sand Removal (TSR) and Air Quenching**

After the mold is filled, it is transferred to the Thermal Sand Removal (TSR) furnace. The TSR furnace has indirect gas fired tubes. The sand mold with the casting is transported through the furnace on a moving conveyor and is subjected to a temperature of 495°C to 500°C for a sufficient period of time (5 hours). (This TSR time and temperature has been optimized by the IRC). During this time, heat together with a high volume of air breaks down the chemical bond formed between the resin and sand so that the sand strips off from the casting. The sand then falls down to a conveyor at the bottom

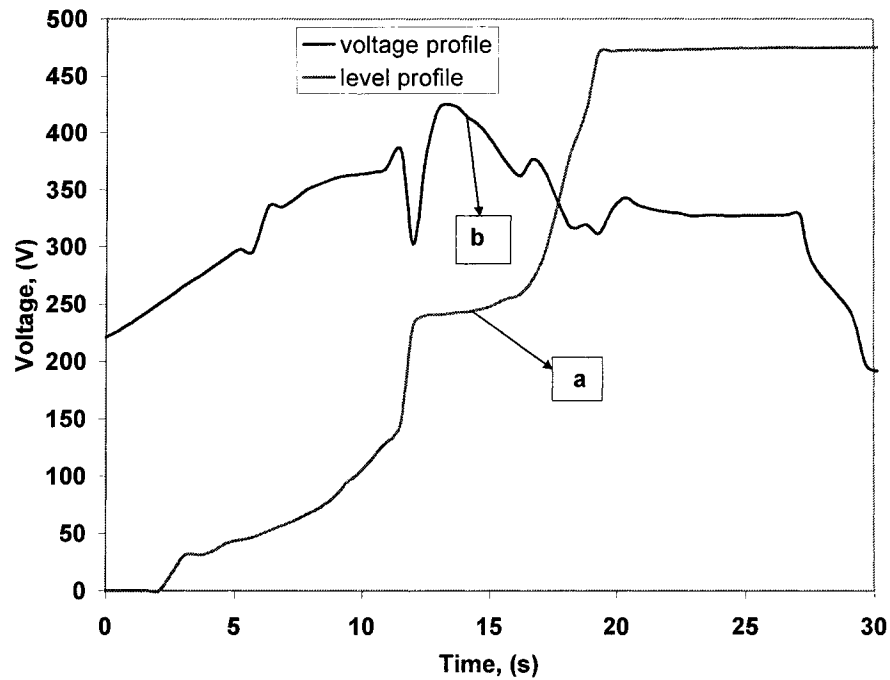


Figure 3.4: (a) Fill level and (b) voltage profiles of the electromagnetic pump for a V6 3.0L engine block.

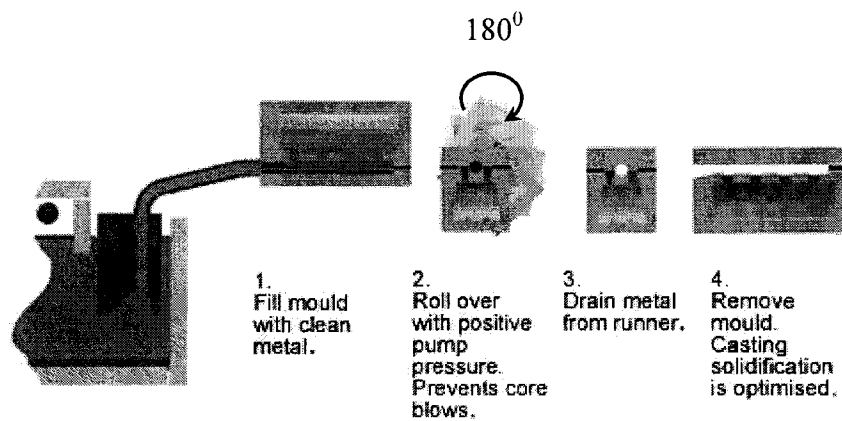


Figure 3.5: The schematic of the roll over process (Cosworth Technology, 2004b).

of the TSR unit and is returned for recycling and reuse. The castings are also partially solution treated during the TSR process. This thermal treatment is followed by an air quench reducing the casting temperature from 505<sup>0</sup>C to 250<sup>0</sup>C in about 4.5 minutes. The air quenching ensures that there are no harmful residual stresses are present in the casting. The internal stresses produced by air quenching are negligible to those produced by water quenching.

Therefore, the main purposes of the TSR process are:

- Cleans the casting by removing the sand
- Reclaims the sand for later reuse
- Partially solution treats (ST) the casting for better mechanical properties

Apelian et al. (1996) has summarized the advantages of the Cosworth casting process over other sand casting technologies:

- The cleaning and finishing operations are minimized as the Cosworth process leaves very little flash.
- It eliminates the shortcomings of dry sand cores and green sand molds.
- Produces an 85% higher yield and 10-12% lighter castings.
- Castings with excellent mechanical properties without any grain refinement or modification.
- Lower machining costs and machining allowances in the 1.5-2mm range can be specified.

The mechanical properties of the bulkheads of the V8 engine blocks produced by using the CPSP process at WAP and the SHLP process used by Montupet S.A. (mentioned in Section 3.1), are compared using a histogram in Figure 3.6. It can be seen that the mechanical properties of the bulkheads produced using the SHLP process are significantly higher than those of the CPSP bulkheads. This is because the Secondary Dendrite Arm Spacing (SDAS) values of the SHLP bulkheads ( $26.8 \pm 4.9 \mu\text{m}$ ) are considerably lower than those of the CPSP bulkheads ( $47.3 \pm 8.8 \mu\text{m}$ ). The reduction in the SDAS values in the SHLP process were achieved by the chilling of the bulkhead during the solidification process. It must be noted that both CPSP and SHLP processes use the Al 319 alloy to make V8 engine blocks.

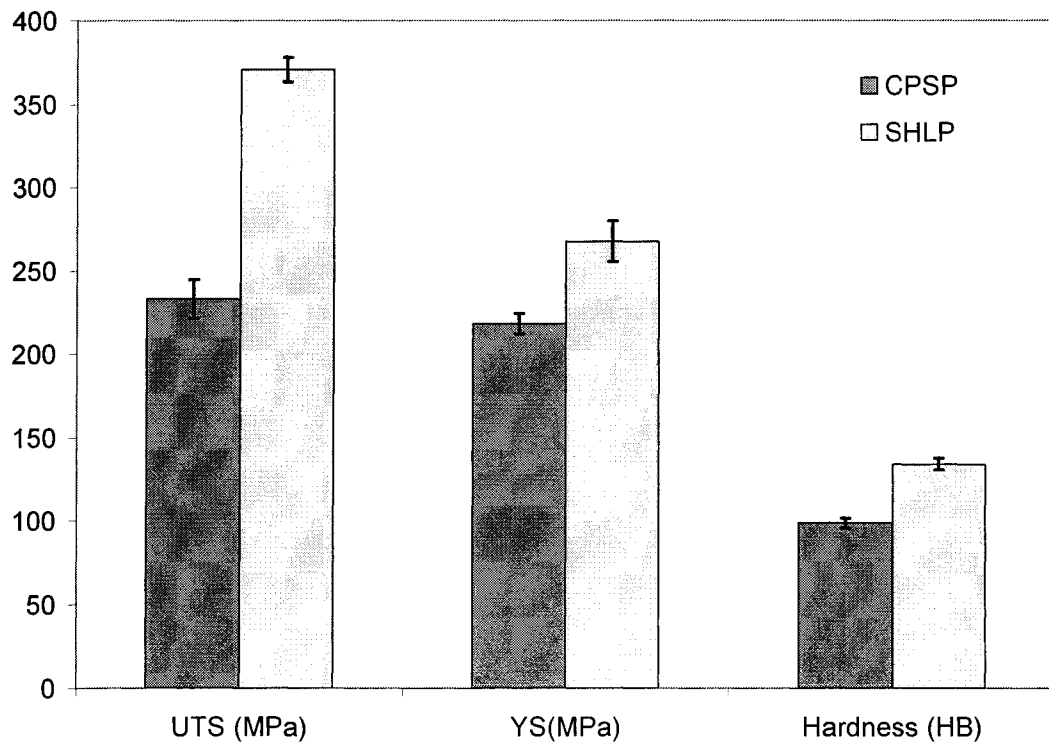


Figure 3.6: Comparison of the mechanical properties of the bulkheads of the V8 engine blocks produced by Montupet's SHLP process and WAP's CPSP process. (UTS: Ultimate Tensile Strength, YS: Yield Strength, HB: Brinell Hardness)

### **3.3 Analysis of the Present Quality Control System at WAP**

#### **3.3.1 Fishbone Diagram of the Present Quality Control (QC) System**

The fishbone diagram which is also called the Cause and Effect Diagram or the Ishikawa Diagram was developed by K. Ishikawa in 1943. This is a tool to analyze the process and to identify the essential performance measures of the process that are to be monitored for Quality Control (QC). It also helps to create a better understanding of the interrelationships that exist in the process (Mitra, 1993). The fishbone diagram of the present QC system for the Cosworth process at WAP is given in Figure 3.7. The components of the Cosworth process are the bones of this diagram. The presently available measures to control the quality of each bone are shown as its branches in the diagram. Each bone and its branches are discussed in detail in the following sections.

#### **3.3.2 Quality Control of the W319 Ingots**

Each ingot supplier tests the chemical composition of the samples using Optical Emission Spectroscopy (OES) from the supply of ingots at their lab ahead of shipping and ensures that the compositions of individual elements are within the composition specification that is provided by NEMAK. The details regarding the procedure and standards for chemical composition analysis using the OES is given in Chapter Four. When the supply enters WAP, the laboratory confirms that the chemical composition is within the specification limits as specified in WSE-M2A151-A2/A4 by testing a representative test sample provided by the ingot supplier. If the chemistry of the test sample is within the specifications, the supply of ingots is accepted and are stored under controlled humidity and temperature.

The OES chemistry results are archived and then graphically analyzed to study the variations in the alloy chemistry using the “Chemistry Viewer” software developed and implemented by the IRC. The software is able to make time series plots for individual elements so that the effect of their variations on the cast component characteristics can be studied. It is also able to calculate the Silicon Equivalency ( $Si_{EQ}$ ) and hence the thermal and structural characteristics of the alloy can be predicted. The software also has a Statistical Process Control (SPC) module to assist the process engineers in making

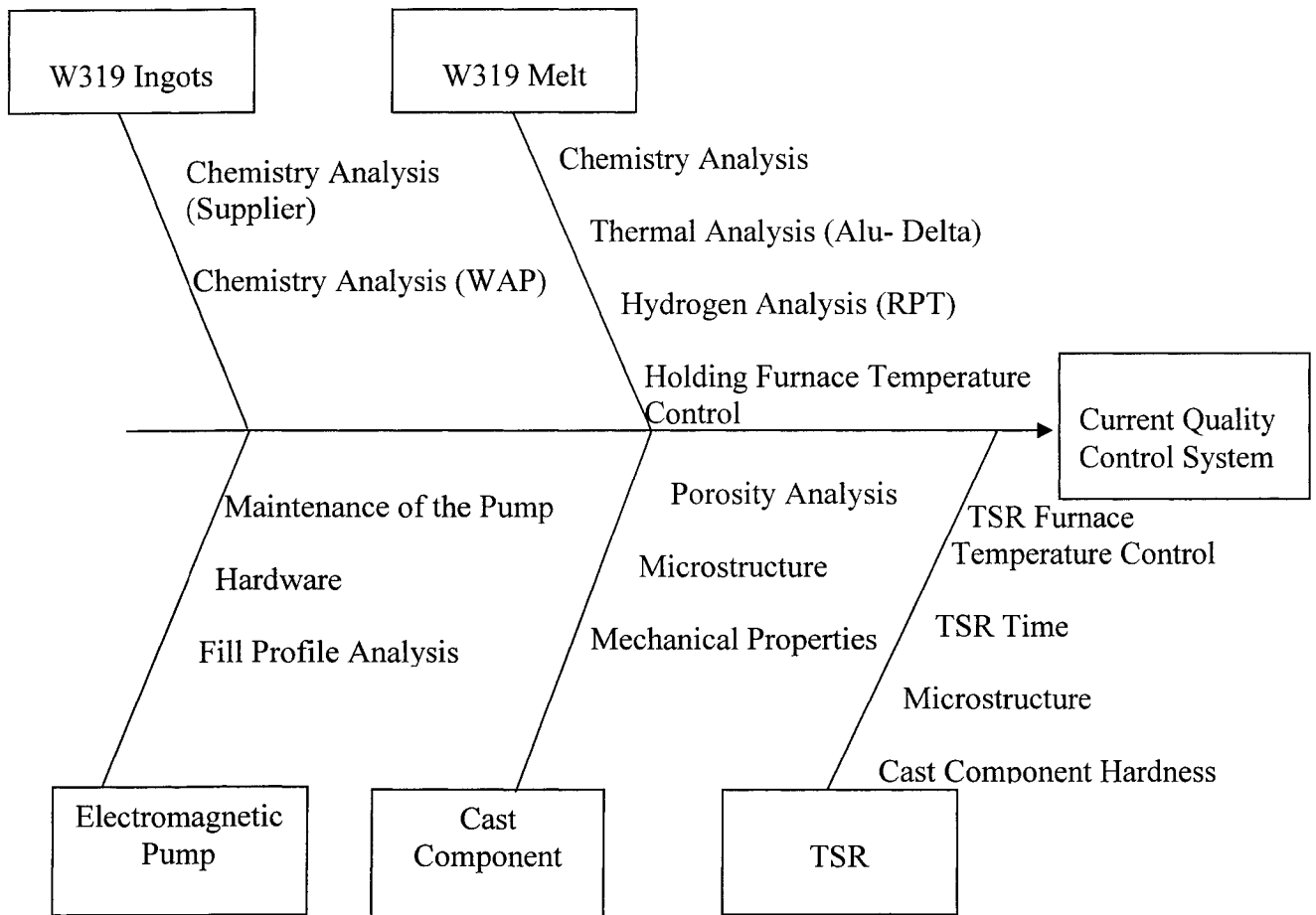


Figure 3.7: Fishbone diagram of the present Quality Control (QC) system at WAP

TSR : Thermal Sand Removal Process

RPT: Reduced Pressure Test

decisions regarding process control. The development of the “Chemistry Viewer” is part of the Master’s Thesis work of Mr. Dilon Yousif.

### **3.3.3 Quality Control of the W319 Melt**

The melt quality is ensured before casting by testing a sample of the melt from the holding furnace for chemical composition and hydrogen content. The in-process melt chemistry specifications and the chemistry specifications for the incoming W319 ingots (before processing) have the same control limits. The comparative hydrogen level is measured using the Reduced Pressure Test (Straube-Pfeiffer Test) (Zalensas, 1993). The gas porosity level is determined by comparing a longitudinal cross section of the test sample with a standard chart (See Figure 3.8). If the porosity level is less than 7, the melt is acknowledged for casting. The abovementioned tests are carried out twice for each 8 hour shift. In addition to this, Thermal Analysis (TA) of the melt sample is also performed using the Alu-Delta TA system. Alu-Delta measures the relative Grain Size and Silicon Modification Level of the melt. However, presently the melt used is neither grain refined nor chemically modified.

### **3.3.4 Quality Control of the Engine Blocks**

Random samples of blocks (2) are drawn from each shifts production and the bulkhead integrity of the blocks is checked by destructive X-Ray radiographic analysis as per the ASTM E-155 standard. The gas and shrinkage porosity levels of each bulkhead section are determined. The inner bulkheads have more porosity than the outer ones due to their slower solidification rate. If the porosity levels of all the bulkheads are less than s4 and g4 level the batch is accepted. Otherwise, the batch is hold for more inspection and investigation.

The Brinell Hardness (HB) of the engine blocks is measured at various locations as per the Ford Engineering Specification WSE-M2A-151-A2/A4. The hardness at every specified location should be between 85-115 HB. The softest locations are the intersections of the inner bulkheads with the risers. In addition to these tests, a comprehensive metallurgical and mechanical evaluation of a sample engine block

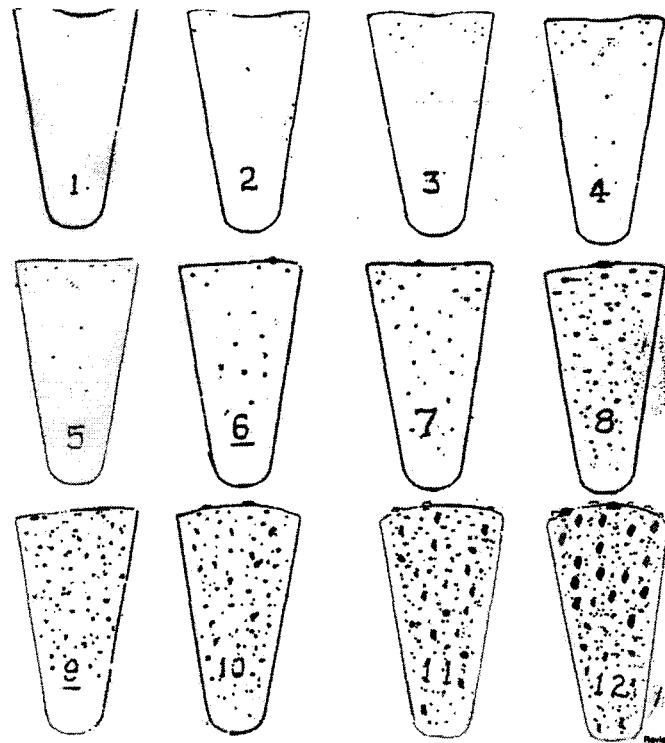


Figure 3.8: Standard chart for the Reduced Pressure Test (WSE-M2A-151-A2/A4 Specification)



is conducted once every six months at an external lab (Climax Research Services Inc., Michigan) as per engineering material specification WSE-M2A151-A2/A4. The mechanical properties measured at the external lab are Ultimate Tensile Strength, Yield Strength, Shear Strength, Elongation (%), and hardness (HB). The metallurgical characteristics measured are Secondary Dendrite Arm Spacing, Grain Size, Volume Fraction of Porosity and the maximum Pore Size.

### 3.3.5 Quality Control of the Cosworth Pump

The Cosworth pump is an electromagnetic pump whose working principle is the Flemings Left Hand 3 Finger Rule. This rule gives the direction of the resulting force acting on a conductor of electricity when the electric current and magnetic field are applied on it at right angles to each other. When the thumb, forefinger and middle finger of the left hand are positioned at right angles to each other, the thumb gives the direction of the resulting force where the forefinger and the middle finger are the current and magnetic field directions respectively. The Alternating Current (AC) is used to supply the current as well as to create the magnetic field on the pole pieces. When they are applied at right angles to each other the molten aluminum is carried through a high temperature ceramic duct to the zircon sand mold (CMI Novacast, 2004).

The Cosworth pump is a crucial component of the Cosworth process: pump failure would lead to casting defects and loss of production. The hardware of the pump is periodically maintained. The newly built pumps are “recirculated” (the detailed explanation is given in Section 6.6.1) at the NEMAK Engineering Centre (NEC) for 5000 cycles and thereafter are installed into the regular production at WAP. The pump nozzle is cleaned (“rodded”) every 2 hours to clear the clogs, if any, during the production shift. After completing 40,000 cycles in the regular production at WAP, the pumps are recalled for preventive maintenance. The used *fixed inserts* (a ceramic component of the pump through which the melt is delivered to the mold) are replaced with new ones and the pump is rebuilt.

Figure 3.9 shows the Cosworth Casting Process flow diagram at WAP together with the locations of the test samples.

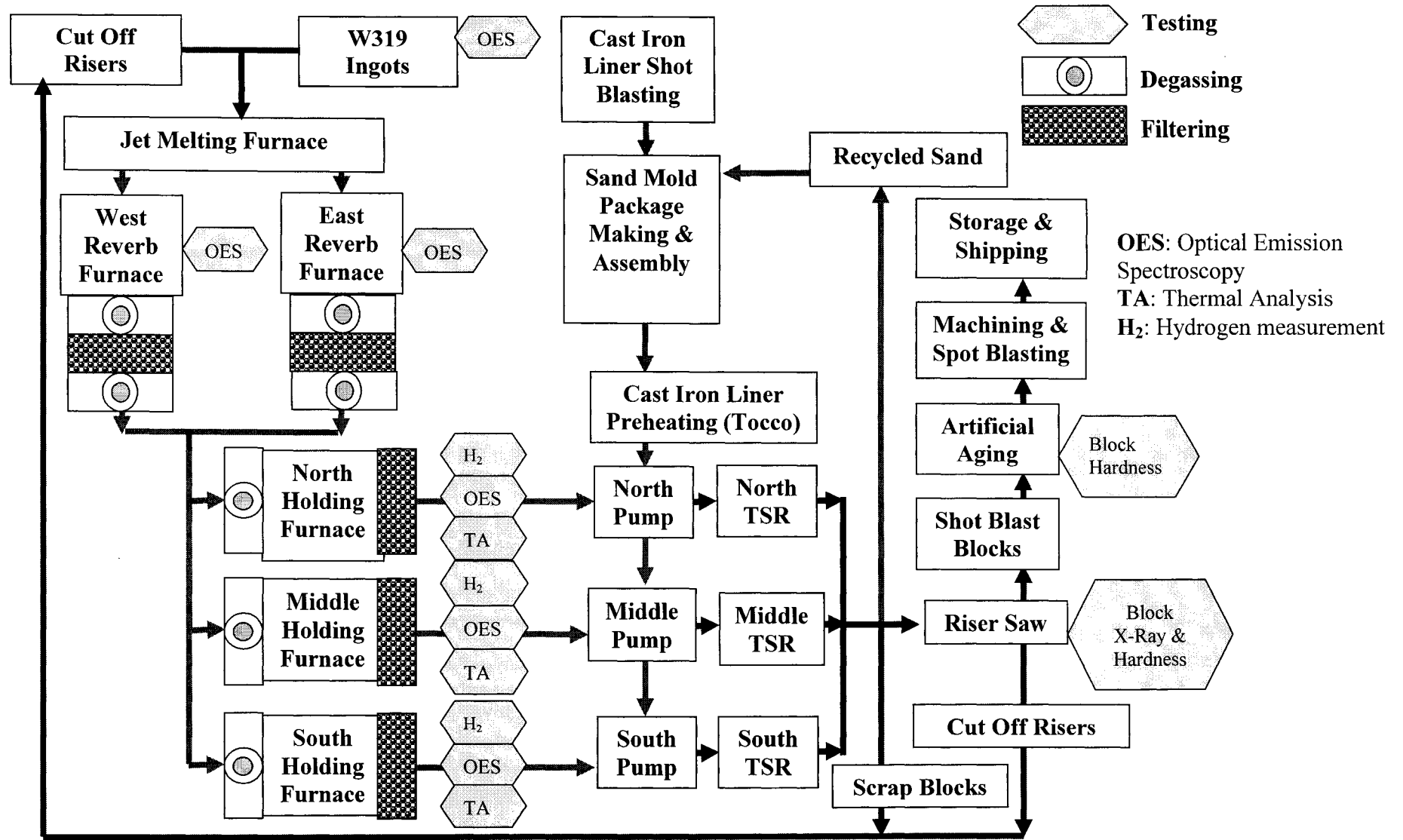


Figure 3.9: Cosworth Casting Process Flow Diagram (Including Quality Control test sample types and locations)

### 3.4 Assessment and Critique of the Present QC System at WAP

WAP was the first casting plant in the world to obtain ISO14000 certification in 1997. A critical assessment of the present Quality Control system at WAP was performed and the following inferences were drawn:

1. WAP uses many advanced techniques such as OES and X-Ray radiography to measure and control the casting quality. However, it does not utilize the full potential of Thermal Analysis as a Quality Control tool. Thermal characteristics can be used as a common denominator linking the materials, processes and cast components together. Table 3.1 summarizes the selected thermal characteristics of aluminum alloys and their processes. The present Thermal Analysis (TA) system at WAP (Alu-Delta) is neither precise nor accurate. This has been confirmed by the Repeatability & Reproducibility studies described in Chapter 6. Alu-Delta uses ladling and spoon transfer for sampling of the melt. This introduces gaseous contaminants (resulting in oxides, hydrogen etc.) into the melt (Sokolowski et al., 2003) and hence it is not able to render unbiased sampling. Therefore, Alu-Delta has to be replaced by a more robust TA system coupled with an unbiased sampling device.
2. The variations in chemical composition, even though they are within the specification limits, may have an influence on the cast component properties (eg. porosity, hardness etc). For example, IRC research helped WAP to reduce the level of Sr to residual levels (~20 ppm) and thereby reduced the shrink porosity levels significantly in the engine block bulkhead sections. However, a more detailed statistical analysis is necessary to identify other elements whose variations within the specification limits may have an influence on the cast component characteristics. This will help WAP to revise the control limits for these elements and thus ensure more consistent quality.
3. The electromagnetic pump maintenance data provides a wealth of useful information about the average pump life time and the failure modes of the pump. However, this

**Table 3.1 Selected thermal characteristics of ingots, melts, cast components and their processes (IRC Brochure, 2004a)**

Thermal Characteristics	Ingots	Melts and their Processes	Cast Components		
			Solidification	Thermal Sand Removal	Heat Treatment
Liquidus Temperature	x	x	x		
Ai-Si Eutectic Nucleation Temperature	x	x	x		
Solidus Temperature	x	x	x		
Start Temperature of the dissolution of the soluble phase(s)	x			x	x
Beginning of Alloy Melting Temperature	x	x	x	x	x
End of Alloy Melting Temperature	x	x			
Fraction Solid and Liquid	x	x	x		
Melt Superheat	x	x			

data has not been analyzed to date using advanced reliability analysis techniques to determine the life distributions and mean failure times. Also the preventive maintenance time of the pump is established based on experience and heuristics rather than statistics.

4. Presently, at WAP, the Thermal Sand Removal (TSR) and partial Solution Treatment (ST) are carried out simultaneously at 495-500<sup>0</sup>C for 5 hours. This process consumes large amount of energy and time and thereby increases the production costs. The Artificial Aging (AA) process is done at 250<sup>0</sup>C for 4 hours at B&W Heat Treating Ltd., Kitchener, Ontario. These processes have to be modified and substituted by a novel energy efficient Solution Treatment method that has a much shorter duration and still yields similar casting properties as the conventional Solution Treatment and the Artificial Aging method.
5. The W319 alloy currently used by WAP has its own inherent limitations. For example, WSE-M2A151-A2 requires that the high cycle fatigue stress of the V8 engine block must be at least 65 MPa. However, the engine blocks produced from the W319 alloy have a mean fatigue stress of only 53.8 ± 3 MPa, which is less than the requirement (Mackay, 2003). Therefore, the levels of major alloying elements (*ie.* Si and Cu) in the W319 alloy should be optimized to improve cast component characteristics.

### **3.5 Proposed Novel Plant Wide Quality Control (PWQC) System for WAP**

Based on the critical analysis of the present Quality Control system a novel Plant Wide Quality Control system has been proposed for WAP. The fish bone diagram of the novel system is shown in Figure 3.10. A special feature of the Novel QC system is that the thermal characteristics are used as a common denominator linking the materials, processes and the cast components. The thermal characterization of materials and simulation of the metallurgical processes is performed by the Universal Metallurgical Simulator and Analyzer (UMSA). Complex WAP processes can be dissected and the root causes of casting failures can be determined by the novel Quality Control platform. The

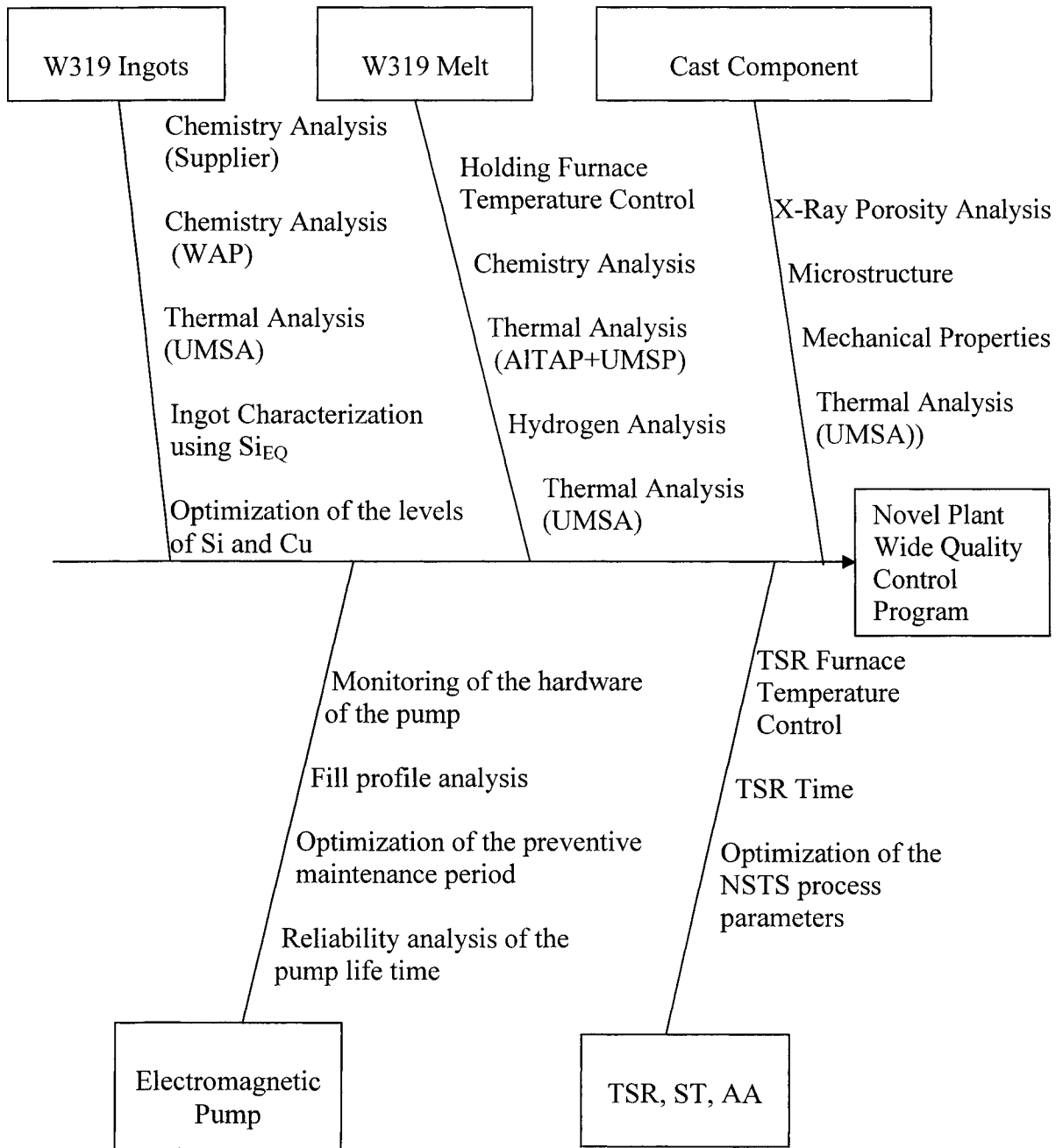


Figure 3.10: Fishbone diagram of the Novel Plant Wide Quality Control Program

- UMSA: Universal Metallurgical Simulator and Analyzer
- AITAP: Aluminum Thermal Analysis Platform
- UMSP: Unbiased Melt Sampling Platform
- TSR: Thermal Sand Removal Process
- ST: Solution Treatment
- AA: Artificial Aging
- NSTS: Novel Solution Treatment during the Solidification Process
- Si<sub>EQ</sub>: Silicon Equivalency Methodology

material and cast component sampling and Thermal Analysis (TA) data are unbiased and are traceable to National Institute of Standards and Technology (NIST) standards. The Novel Analytical Platform (NAP) that is incorporated into the Optical Emission Spectroscopy (OES) routine at WAP can also be used for thermal characterization. The NAP procedures use the Silicon Equivalency ( $Si_{EQ}$ ) algorithm, which numerically expresses the amount of alloying and impurity elements (including hydrogen) present in the aluminum melt as an equivalent amount of silicon.

The other important features of the proposed novel PWQC system are:

- An Aluminum Thermal Analysis Platform with a Melt Sampling Device for the unbiased thermal characterization of the WAP melt.
- Statistical analysis of the inter relationships between the cast component characteristics and the alloy chemical composition.
- Reliability analysis of the electromagnetic pump maintenance data that leads to the optimization of the preventive maintenance period of the pump.
- Optimization of the solution treatment parameters (time and temperature) of the Novel Solution Treatment during Solidification (NSTS) process.
- Optimization of the levels of the major alloying elements (Si and Cu) of the W319 alloy so as to develop a new alloy and hence improve the cast component characteristics.

### **3.6 Project Objectives**

The main objective and hence the integrating theme of this dissertation is the Quality Control and improvement of the W319 Al alloy castings produced at WAP through the implementation of a novel Plant Wide Quality Control system. In order to achieve this objective the entire casting process consisting of materials, processes and cast components has been considered and the following secondary objectives have been identified:

1. Develop a Novel Thermal Quality Control Platform (NTQCP) for the grading of ingot suppliers and for the thermal characterization of the ingot, melt and engine block samples resulting in consistent engine block characteristics.

2. Evaluate the sensitivity of the Unbiased Melt Sampling Device (UMSD) in combination with the Aluminum Thermal Analysis Platform (ALTAP) as a Quality Control tool in detecting the daily process shifts in comparison with the existing Alu-Delta Thermal Analysis system used at WAP.
3. Enhance the present capabilities of the ALTAP by the development of an Artificial Neural Network (ANN) model for the on-line prediction of the Silicon Modification Level (SiML) of the melt from Thermal Analysis parameters.
4. Investigate the effect of melt chemistry on casting porosity and engine block hardness and thereby revise the chemical composition specifications for the W319 alloy.
5. Improve the Reliability of the Electromagnetic Pump by optimizing its Preventive Maintenance Time.
6. Optimize the Solution Treatment parameters (Time and Temperature) of the Novel Solution Treatment during Solidification (NSTS) process for the W319 alloy that will result in a reduction in production costs and an increase in energy savings.
7. Develop a new alloy by optimizing the levels of Si and Cu present in the 3XX series of hypoeutectic Al-Si alloys (Si (5-11 wt.%) and Cu (1-4 wt.%)), and thereby improve the casting characteristics of the WAP engine blocks.

It must be emphasized that the overall academic objectives of this project go beyond the scope of WAP and aim at making significant contributions to the entire aluminum casting industry and to metallurgical science. For, example, WAP is presently using an unmodified melt with residual levels of Sr to make the engine blocks. However, the software for the on-line prediction of the Silicon Modification Level (SiML) was developed for Al casting plants around the world who still employs modification of the melt to achieve desirable mechanical properties of the cast component. It is worthwhile for these casting facilities to know the modification level of the melt on-line prior to the casting operation.



## **4. Experiments and Measurements Involving the W319 alloy Used at the Windsor Aluminum Plant**

### **4.1 Introduction**

The experiments and data collection for this dissertation were carried out in two stages. The first stage consists of the experiments and measurements conducted on the W319 alloy used at the Windsor Aluminum Plant (WAP). In the second stage, experiments and measurements were expanded to the 3XX series of Al-Si alloys. This was done to find an alternative optimum alloy for W319 that will improve the cast component integrity and related properties while lowering the ingot price. These experiments are outlined in the next chapter. The chemical composition of W319 falls within the range of composition that is covered by the 3XX series of Al-Si alloys.

The following sections of this dissertation explain the measurements and experiments done at WAP. The latter sections describe experiments performed in the University of Windsor Casting Laboratory (UWCL) on the W319 alloy test samples collected from WAP. These include ingot, melt and engine block samples.

The flow diagram in Figure 4.1 depicts the testing and sampling program for the plant wide quality control at WAP. A special feature of this program is that samples can be analyzed at different stages (ingots, melts and engine blocks) using the Universal Metallurgical Simulator and Analyzer (UMSA) under the same experimental conditions. The major advantages of using UMSA are the following:

- Replication and analysis of actual WAP metallurgical processes including simulation of TSR and heat treatment processes.
- Provides thermal characteristics and porosity free mechanical test samples.

This project evaluates the entire casting process at different stages starting with the incoming ingots, through the melt treatment and finishing with the as cast and heat treated engine blocks.

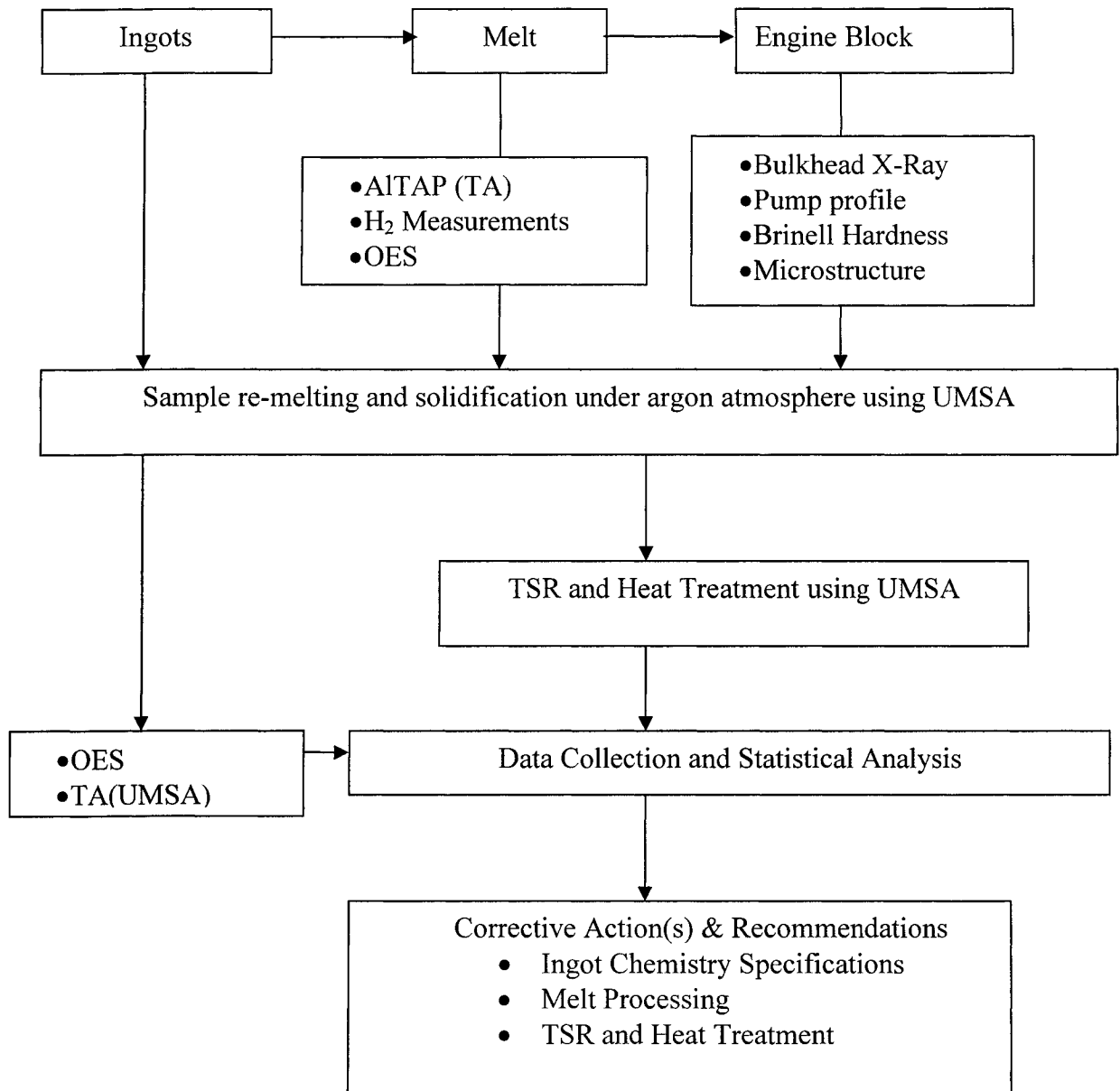


Figure 4.1: Flow Diagram of the novel plant wide testing and sampling program for WAP.

## **4.2 Chemical Composition and Specifications of the W319 Alloy**

Aluminum casting alloys are numbered according to a three digit (plus decimal) system adopted in 1954 by the American Aluminum Association (AAA) and approved by the American National Standards Institute in 1957 (ANSI H35.1) (Zalensas, 1993). The standard AA319 alloy is used for making sand castings as well as permanent mold castings. The W319 alloy used at WAP has a different chemical composition than that of the AA319 alloy. The W319 alloy has higher levels of Si and Mg and lower levels of Fe. The amount of Sr in the W319 alloy is <0.002 wt. %, which means that no chemical modification is applied to the melt. (Refer to Table 4.1).

## **4.3 Windsor Aluminum Plant Data**

### **4.3.1 Chemical Composition of the W319 Alloy**

The chemical composition of the W319 alloy is measured on a daily basis using an Optical Emission Spectrometer (OES) as per the ASTM E1251 specification. The collected melt sample is allowed to solidify in a custom die cast steel mold to insure fast solidification with minimum segregation. The analytical surface finish is prepared by either carbide (most common) or diamond machining. The spark analysis is repeated at least three times at three different random locations of the sample to ensure the repeatability of the measurements. The OES analysis software automatically archives the results in a database for further analysis and comparison with the chemical composition control limits. Chemical analysis is conducted for each holding furnace, reverb furnace, and on the ingot shipments received.

### **4.3.2 Hydrogen Measurements of the Melt**

The hydrogen levels in the melt are measured before and after degassing using the AISCAN Hydrogen Analyzer. It must be noted that, for the regular production at WAP, the comparative hydrogen level in the melt is measured using the Reduced Pressure Test (RPT). AISCAN measurements were performed specifically for this project only. The thermocouple of the AISCAN unit is immersed into the liquid melt to read the melt

**Table 4.1: Chemical composition of the AAA standard 319 alloy (Zalensas, 1993) and the W319 alloy (Ford Engineering Material Specification WSD-M2A151-A2/A4)**

Alloy	Chemical Composition, (wt.%)				
	Si	Fe	Cu	Mn	Mg
AA319	5.5-6.5	1.0 Max	3.0-4.0	0.50 Max	0.10 Max
W319	7-7.8	0.4 Max	3.3-3.7	0.2-0.3	0.25-0.35

**Table 4.1: Continued....**

Alloy	Chemical Composition, (wt.%)							
	Zn	Ti	Pb	Sn	Sr	Cr	Ni	Other Elements
AA319	1.0 Max	0.25 Max	N/A	N/A	N/A	N/A	N/A	0.50 Max
W319	0.25 Max	0.1-1.5	0.1 Max	0.1 Max	0.002 Max	0.1 Max	0.1 Max	0.05 Max

N/A: Not Available

temperature ( $760 \pm 0.5^{\circ}\text{C}$ ). The nitrogen gas is purged into the liquid melt through the probe of the AlSCAN unit. As the nitrogen circulates through the bath, it picks up hydrogen, and eventually the hydrogen in the melt and in nitrogen reaches equilibrium. The hydrogen content is determined by measuring the thermal conductivity of the hydrogen – nitrogen mixture (Zalensas, 1993). The unit of hydrogen measurement is ml of  $\text{H}_2$ / 100g of Al. The average of three measurements is taken as the hydrogen level.

#### **4.3.3 Brinell Hardness of the Cast Component**

Brinell hardness measurements are performed at several locations on the engine block after Thermal Sand Removal (TSR), Solution Treatment and Artificial Aging as specified in the Ford Engineering Specification WSE-M2A-151-A1. However, the critical locations are the intersections of the inner bulkheads with the risers where the cooling rate is the slowest. (See Figure 4.2). These sections have lower hardness than the outer bulkhead sections which solidifies faster. The measurements are performed according to the ASTM E-10 specification. Measurements are comprised of the average of 5 random indentations. The specific condition of the Brinell Hardness Test is that a load of 500kg is applied on the sample surface for 15 seconds.

#### **4.3.4 Casting Porosity by X-Ray Radiographic Analysis**

The porosity analysis is conducted using X-Ray testing of the machined bulkhead section. The most critical sections are the inner bulkheads due to their slower solidification rate compared to the remaining casting sections. Two blocks are selected from the daily production for X-Ray destructive testing. The engine block is sliced in 1” thick slices and shot blasted for final cleaning before X-Ray Analysis is conducted. The X-Ray images obtained from the test are printed on standard X-Ray film paper and are digitally stored in the computer system. The results are compared with ASTM E-155 standard for evaluating casting gas and shrinkage porosity levels in Al castings. These porosity rating results are archived in a database for further analysis.

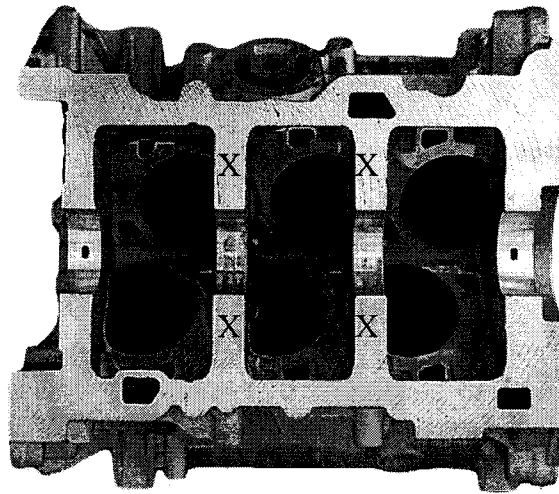


Figure 4.2 The picture of the V6 engine block showing the critical locations (marked X) where the lower hardness values are expected.

#### **4.3.5 Cosworth Pump Profile and Pump Maintenance Records**

The Cosworth pump is an electromagnetic pump that delivers the molten aluminum into the sand mold. A Programmable Logic Control (PLC) system controls the fill rate of the molten metal into the mold with the use of a feed back system. The fill profile provides the liquid metal height in the mold during filling, the pump voltage, and the maximum allowable voltage for each point in the fill profile. (Refer to Section 3.2.4). The pump maintenance records were obtained during the period 1999-2003. They contain information such as: the roll over at which the pump was installed, the date of installation, the date at which the pump was removed from the roll over for overhauling, the number of castings produced by using the pump and the reason for pump failure. This data is a good source for life distribution studies and therefore to establish the preventive maintenance times of the pump.

#### **4.4 Experiments at the Windsor Aluminum Plant**

##### **4.4.1 Thermal Analysis Using the Unbiased Melt Sampling Device (UMSD) and the Aluminum Thermal Analysis Platform (AITAP)**

Thermal Analysis (TA) experiments were conducted at the middle holding furnace at WAP during April 2003 and June 2003. The temperature of the melt at the holding furnace is kept at  $760 \pm 5$  °C. The TA test samples were taken using the Unbiased Melt Sampling Device (UMSD), which was designed and built for this dissertation and is currently undergoing patenting. The UMSD main advantages are:

- It can potentially extract a representative unbiased melt sample without the introduction of additional oxides and gases during sampling.
- It enables safe, simple, and easy industrial operation and maintenance.
- Low cost for equipment and the sampling cup can be reused.

The thermal analysis sample mass is 400g  $\pm$  10 g and the dimensions of the sampling cup are shown in Figure 4.3. The mass of the cup is 400g . The test sample cooling rate is  $0.16 \pm 0.025$  °C/sec. The UMSD was used during April and June of 2003 to collect 30 days of thermal analysis data. The procedure for conducting the TA experiments using the UMSD (See Figure 4.4) is explained as follows:

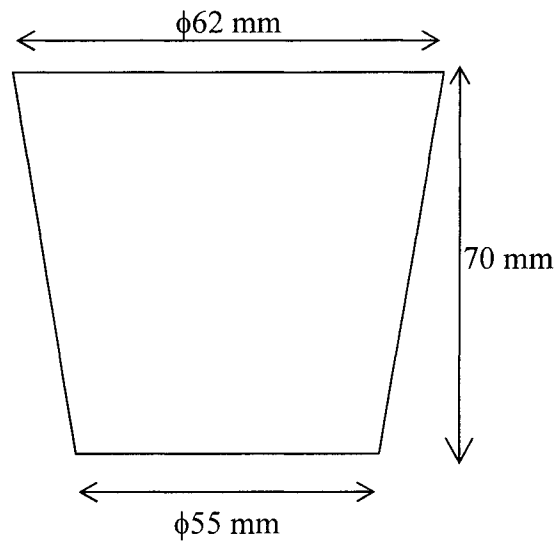


Figure 4.3 Dimensions of the UMSD cup

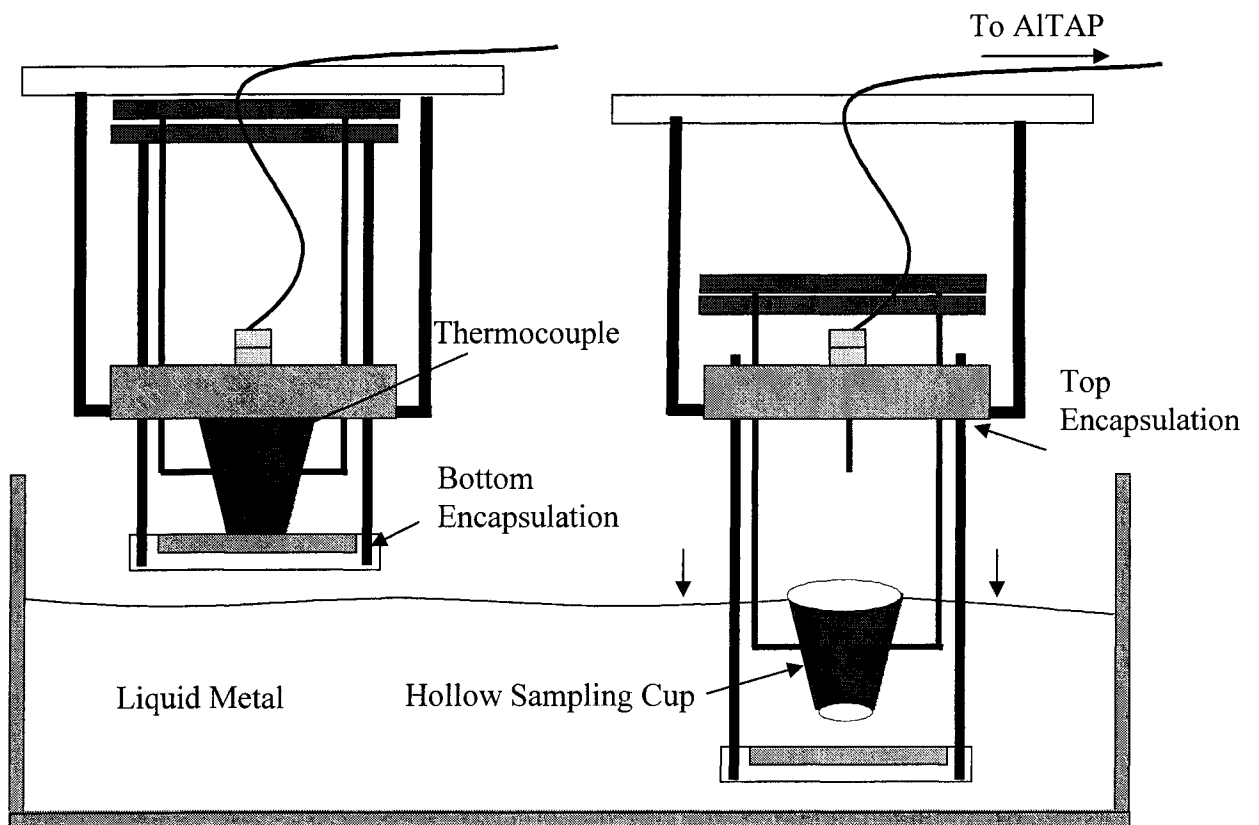


Figure 4.4: Schematic diagram explaining the Unbiased Melt Sampling Method.



The sampling cup is coated with graphite or boron nitride solution and is preheated at 200<sup>0</sup>C for 10 minutes. The dross surface of the melt in the holding furnace is skimmed off using a preheated sprouted steel ladle. The bottom cup encapsulation section of the device is submerged into the melt to a depth of 1 foot below the surface. The hollow sampling cup is then immersed into the melt until it is in full contact with the bottom cup encapsulation section that is already inside the melt. The bottom cup encapsulation and sampling cup unit together is then lifted until it is above the melt surface, so that the top cup insulation is in firm contact with the top of the cup. The firm contact between the sampling cup and the bottom encapsulation prevents the leakage of the liquid metal. A shielded K-type thermocouple is introduced into the center of the solidifying sample through the top encapsulation. The temperature of the solidifying sample is recorded at a rate of 5 readings/second using a high speed data acquisition system (National Instrument 16 MIO) with a resolution of 16 bits. The data acquisition system is connected to the Aluminum Thermal Analysis Platform (AITAP) software. This software is capable of recording the temperature data, filtering, and performing cooling curve analysis. The obtained results are archived for further analysis. It should be noted that the AITAP system and the data acquisition system are calibrated prior to the Thermal Analysis experiments using a procedure developed by the author of this dissertation (Francis et al., 2001). This procedure is explained in Appendix 1. This ensures that the temperatures measured by the AITAP are traceable to National Institute of Standards and Technology (NIST) standards.

## **4.5 Experiments and Measurements Performed at the University of Windsor Casting Laboratory (UWCL)**

This section describes the experiments and measurements carried out using the ingot, melt and engine block samples collected from the Windsor Aluminum Plant.

### **4.5.1 Thermal Analysis Using the Universal Metallurgical Simulator and Analyzer (UMSA)**

UMSA can perform metallurgical simulations of heating and cooling processes at different heating and cooling rates on macro test samples. (Kasprzak et al., 2002). The

diameter of the test sample is  $\Phi=14$  mm and the length is  $l=18$  mm. The test sample has a predrilled hole having a diameter of  $\Phi=1.5$  mm to allow for the insertion of the thermocouple (see Figure 4.5). The average mass of the test sample is  $7.5\pm 0.2$  gm. In this project heating and cooling curve analysis using UMSA (1 KW power output) was performed on the following type of samples obtained from the Windsor Aluminum Plant (WAP):

- (a) Samples obtained from the ingots.
- (b) Permanent mold cast cylindrical block samples collected from the melt. These samples were cast by pouring the melt from the middle holding furnace around  $\sim 760^{\circ}\text{C}$  to a preheated permanent mold.
- (c) Samples excised from the bulkheads of the V6 engine blocks.

Figures 4.6 (a & c) show the locations of the ingot and engine block from where the UMSA test samples were extracted. Figure 4.6 (b) shows the permanent mold cast cylindrical block from which the melt UMSA test sample is machined. The procedure for thermal analysis is described as follows:

The test sample was heated (at 80% of the maximum output power) up to  $750\pm 0.5^{\circ}\text{C}$  in 15 minutes. The sample reached the set temperature ( $750^{\circ}\text{C}$ ) in 8-10 minutes and then stabilized around it. The sample was then cooled to  $100^{\circ}\text{C}$  under natural cooling conditions. This cycle was repeated 3 times for each sample. The first heating and cooling cycle is for the creation of good contact between the sample and the thermocouple that allows for unbiased temperature measurements. The temperatures during heating and cooling were recorded at a frequency of 5 samples/second using low thermal mass thermocouples. These thermocouples were connected to a National Instruments data acquisition system which is a part of the UMSA computer controlled system. The UMSA system along with the data acquisition system was calibrated before the experiments were conducted using the procedure discussed in Appendix 1 and developed by the author (Francis et al., 2001).

#### **4.5.2 Metallographic Analysis of the Test Samples**

Light Optical Microscopy (LOM) was used for the phase identification of selected TA test samples. This analysis was done using the Leica Q550IW Image Analysis system at the University of Windsor. The samples for Image Analysis were prepared using

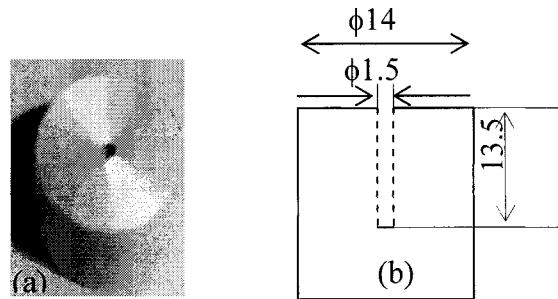


Figure 4.5: (a) Photograph of the UMSA test sample; (b) Dimensions in mm of the UMSA test sample

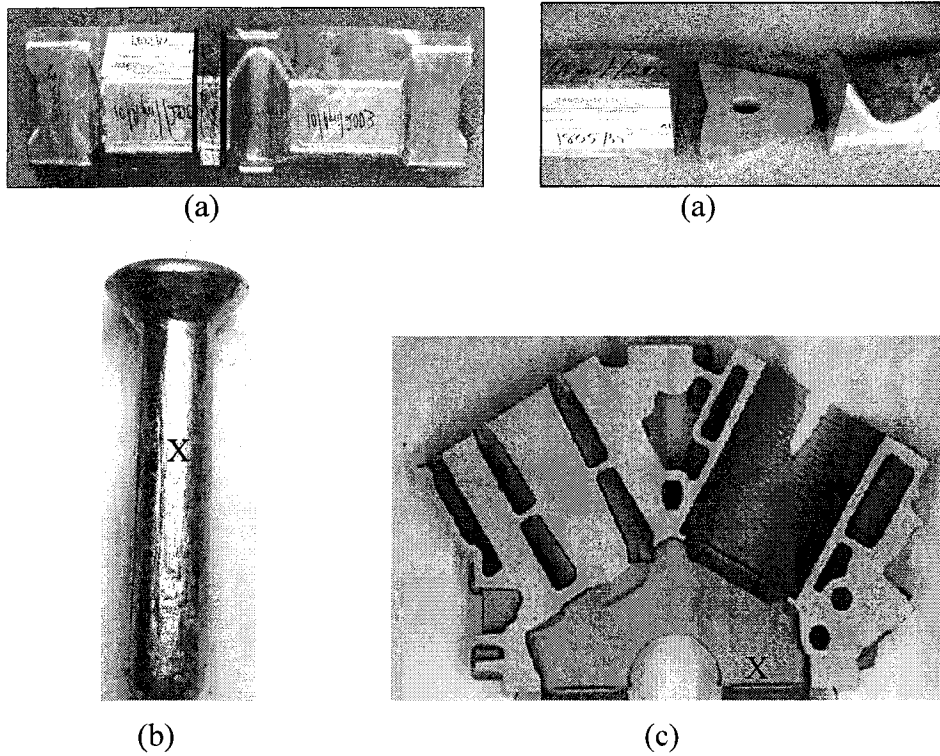


Figure 4.6: The locations in (a) the ingot and (b) the cylindrical permanent mold melt test bar from where the UMSA samples were machined. (c) bulkhead of a V6 block from where the UMSA test sample was excised (Marked as 'X').

standard metallographic sample preparation and polishing procedures in a semiautomatic BUEHLER polishing machine. The final polishing was done using 0.05  $\mu\text{m}$  slurry. The phases present in the microstructure were identified by comparing the micrographs obtained from the polished test samples with the existing Atlases for the 3XX series of Al Alloys (Bäckerud et al.,1990).

The Fe rich phases present in selected TA test samples were analyzed using a JEOL JSM 5800 Scanning Electron Microscope (SEM). Twenty images were obtained from each test sample under 100x magnification. The SEM was used in order to get a high resolution image so as to clearly distinguish between the Fe rich phases and the Cu rich phases. These images were then loaded into the Leica QWin Image Analysis system and the system was calibrated using the calibration standard. The Fe phases present in the image were selected by the user through an interactive image analysis technique (See Figure 4.7). The phase morphology of the Fe rich phases (area and perimeter) were quantified using a program developed by the IRC.

SEM observations were also performed on the fractured surfaces of TA test samples with high levels of Sn (~400 ppm) and Pb (~350 ppm). The samples for analysis were prepared by immersing a 0.25" thick test sample in liquid nitrogen and then fracturing the brittle sample. The fracture surface was analyzed for phase constituents in Secondary Electron (SE) and Back Scattered Electron (BSE) modes under magnifications ranging from 800x to 3000x.

#### **4. 6 Previous IRC Experiments**

The novel tools for the on-line evaluation of the Silicon Modification Level (SiML) and the optimization of the Solution Treatment of the W319 alloy are two important original contributions of this dissertation to the aluminum casting industry. These tools were developed using the complementary data that is obtained from the past IRC experiments. For the purpose of this dissertation, these experiments are discussed briefly in the following sections.

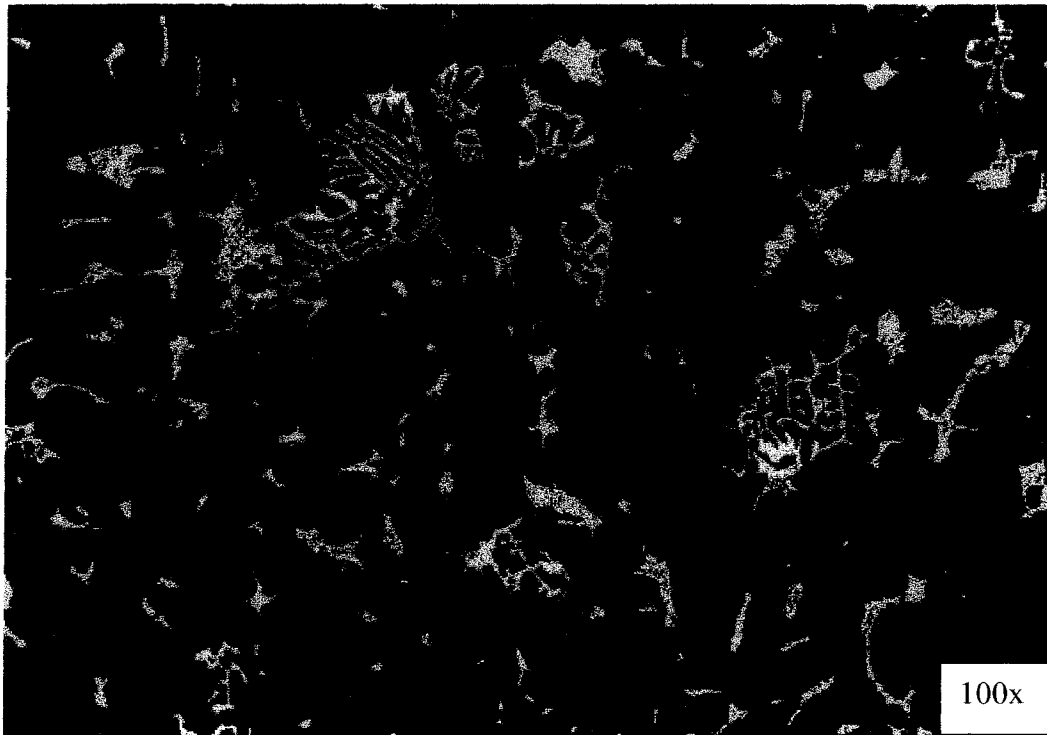


Figure 4.7: Interactive image analysis technique to quantify the morphology of the Fe rich phases present in the TA test samples. The Fe rich phases are detected by the user and are shown in green by the image analysis software. The interactive technique means that the detection of the features of interest is done manually while the image analysis is automated.

#### **4. 6.1 Thermal Analysis Experiments for the On-line Prediction of the Silicon Modification Level (SiML) of the W319 alloy**

A total of 10 kg of W319 alloy ingots were melted in an electric resistance furnace kept at a temperature of  $735 \pm 5$  °C. Degassing was done for 15 minutes using an argon rotary degasser. The melt was modified through the addition of master alloy (Al-10 -wt% Sr). An incubation time of 15 minutes was allowed after the strontium addition. The strontium level was varied between 8 and 96 ppm (1 ppm=0.0001 wt%). Thermal Analysis (TA) was conducted using the Aluminum Thermal Analysis Platform (ALTAP) developed at the University of Windsor. This system records the temperature history of a  $160 \pm 10$  g test sample of molten alloy as it cools down from  $\sim 730$ °C to 400° C. The TA test samples were taken by submerging a cylindrical graphite cup (40 mm diameter, 50 mm deep) into the melt. The cup was kept submerged in the melt for 20s after which it was placed on the stand. Two K-type thermocouples, sheathed in stainless steel, were introduced into the cup to measure the temperature of the melt as it is cooled. The data for TA was collected using a high-speed data acquisition system linked to a personal computer.

Specimens for Image Analysis (IA) were cut from the test samples close to the tips of the thermocouples. The cross-sections of the specimens were ground and polished using standard metallographic procedures. The final polish was done using OP-U on microcloth. A Leica Q5501W Image Analysis System (IAS) was used to assess the Silicon Modification Level (SiML) of the polished test samples. Forty seven cooling curves (data sets) are obtained from the TA experiments with different levels of strontium ranging from 8 ppm (unmodified) to 96 ppm (fully modified) (Djurdjevic et al., 2001b).

#### **4.6.2 Novel Solution Treatment during Solidification (NSTS) Experiments of the W319 Alloy**

The laboratory experiments were performed using cylindrical specimens with a diameter of  $\phi = 14$ mm and a length of  $l = 18$ mm (See Figure 4.5b). All test samples were machined from an unmodified W319 alloy in order to simulate the WAP production conditions. The UMSA Advanced Thermal Analysis was performed in order to identify the metallurgical reactions during the melting and solidification cycles. The information

from the heating cycle was used to further design heat treatment operations. The heating rate during the heating cycle was kept at 0.2 °C/s. The Solution Treatment by isothermal holding was performed at 500 °C, 510 °C, 520 °C, 530 °C and 540°C for 30, 60, 120 and 240 minutes followed by air quenching at 1 °C/s. All the test samples were then naturally aged for a period of two weeks. The schematic of the experiments is shown in Figure 4.8. Each solution treatment experiment was repeated 5 times.

Samples for metallographic observations and metal matrix microhardness measurements were prepared using standard metallographic procedures and the BUEHLER automated equipment. The area fraction of the Cu enriched phases (this is the area of the Cu phases undissolved in the matrix after the temper) in the samples was evaluated using a LEICA QW-550 automated Image Analysis System (IAS) linked to a Leica DMR Light Optical Microscope (LOM). Additional metallographic observations were made using a JEOL JSM 5800 Scanning Electron Microscope (SEM) in the Back Scattered Electron (BSE) mode. Twenty-five (25) analytical fields were measured for each specimen and the average value and standard deviation were calculated. The matrix Vickers Microhardness was measured using a BUEHLER microhardness tester under a 25g load for 15s (HV25). Twenty measurements were taken per sample and the average microhardness and standard deviation were determined. Metal matrix microhardness measurements were chosen in place of overall macrohardness measurements to evaluate the dissolution of Cu enriched phases and other structural constituents on the solid solution strengthening effect (Chen, 2003).

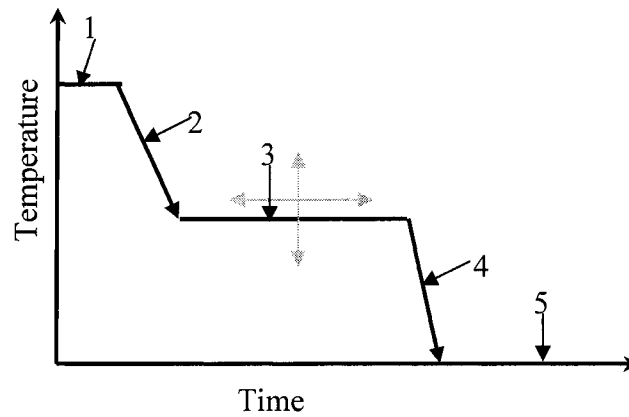


Figure 4.8 : Schematic diagram of the thermal cycles performed during the NSTS process of the W319 alloy. Arrows present the changes in the temperature and time of the processes. The NSTS process is followed by 2 weeks of natural aging (Chen et al., 2003)

1. Melt superheat temperature, 750<sup>0</sup>C.
2. Solidification process of the UMSA test sample.
3. Solution treatment.
4. Quenching.
5. Natural Aging.



## **5. Experiments and Measurements Involving the 3XX Series of Al Alloys**

### **5.1 Introduction**

The experiments and measurements presented in the previous chapter were primarily conducted to develop novel quality control tools for minimizing the variability in the casting characteristics at WAP. However, as mentioned in Section 3.4, the presently used W319 alloy has its innate limitations. The casting characteristics can be improved by developing a new alloy by optimizing the levels of Si and Cu present in hypoeutectic Al-Si alloys. The research at IRC has made great progress in this direction in the recent years (Ren, 2000 and Mackay, 2003). This work has been expanded in this dissertation by considering the entire 3XX family of hypoeutectic Al-Si alloys.

The experimental work described in this Chapter consists of the Thermal Analysis (TA) of the 3XX series of Al-Si alloys using the ALTAP. The microstructure characterization (Dendrite Arm Spacing and Grain Size) and Brinell Hardness of the TA test samples were also performed. The main objective of these experiments and measurements was to optimize the levels of Si and Cu in the hypoeutectic 3XX alloys and to develop a new alloy as a replacement for the W319 alloy.

### **5.2 Preparation of the 3XX Series of Al Alloys and their Chemical Compositions**

The 3XX series of Al alloys are Al and (Si-Mg) or (Si-Cu) or (Si-Mg-Cu) alloys (Zalensas, 1993). In this work Al-Si-Cu alloys are considered. The experimental alloys were designed and prepared in the IRC metal casting laboratory, by mixing 99.99% Pure Al and two master alloys viz. Al50%Si and Al55%Cu, in 1.5 kg capacity, ceramic bottom pour siphon crucibles. No grain refining agents or modifiers were added to these alloys. This was done to minimize the cost and to avoid the increase in the porosity level associated with the modification. The samples were prepared and held overnight (12 hours) in a Lindberg<sup>TM</sup> resistance furnace set at  $740 \pm 5$  °C. The furnace was filled with argon gas throughout the time the melt was held in the furnace. Before casting the melt surface was carefully skimmed and the melt was thoroughly mixed to ensure uniform

composition of the cast samples. It should be noted that the composition of W319 (7 wt% Si and 4wt% Cu) falls within the range of composition covered by these alloys. A total of 12 synthetic alloys were prepared and their chemistries were analyzed by Optical Emission Spectroscopy (OES) as per the ASTM E1251 specification. The chemical compositions of these alloys are given in Table 5.1. The levels of elements like Fe and Mn were kept low for the experimental alloys as the main interest was to evaluate the effect of changing Si and Cu.

### **5.3. Thermal Analysis (TA) of the 3XX Series of Al Alloys Using ALTAP**

TA experiments were conducted using the Aluminum Thermal Analysis Platform (ALTAP) developed at the University of Windsor. This system records the temperature history of a  $300 \pm 5$ g test sample of the molten alloy as it cools down from  $\sim 730^{\circ}\text{C}$  to  $400^{\circ}\text{C}$ . The TA test samples were taken by pouring the molten alloy in the ceramic crucible into a 0.025 mm thick stainless steel foil cup (50 mm diameter, 60 mm deep) from the Lindberg<sup>TM</sup> furnace. A low thermal mass thermocouple (K-Type) was introduced into the cup to measure the temperature of the melt as it cooled. The cup was insulated at the top and bottom to allow only Newtonian heat transfer. The data for TA were collected using a high-speed Data Acquisition System (5 readings/second) linked to a personal computer. The TA experiments were repeated three times for each alloy composition (24 samples).

### **5.4 Measurements and Metallurgical Characterization of the 3XX Series of Alloys**

#### **5.4.1 Secondary Dendrite Arm Spacing (SDAS)**

The ALTAP thermal analysis tests samples (12 samples), were cut longitudinally and were prepared for microstructure analysis using the standard metallographic grinding and polishing procedures. The SDAS measurements were carried out as described in the Ford Engineering Materials Specification WSE-M2A151-A3 (also ASTM E-3). Micrographs of magnification 100X are prepared from the polished sample. Several were

**Table 5.1: Average chemical composition (wt.%) of the 3XX series of experimental Al alloys.**

Alloy ID	Si	Cu	Fe	Mg	Mn	Zn	Ti	Sr	Ni	Al
[5;1]	4.85	1.03	0.09	0.14	0.01	0.01	0.057	0.001	0.009	Bal
[5;2]	5.01	2.06	0.1	0.15	0.01	0.01	0.062	0.001	0.009	Bal
[5;4]	4.89	3.85	0.09	0.16	0.01	0.01	0.057	0.003	0.009	Bal
[7;1]	7.13	0.96	0.12	0.28	0.01	0.01	0.098	0.003	0.008	Bal
[7;2]	7.05	1.98	0.13	0.28	0.01	0.01	0.094	0.003	0.009	Bal
[7;4]	6.75	4.38	0.12	0.29	0.01	0.01	0.091	0.003	0.009	Bal
[9;1]	9.17	1.05	0.12	0.31	0.01	0.01	0.100	0.002	0.007	Bal
[9;2]	9.02	2.44	0.12	0.31	0.01	0.01	0.096	0.003	0.007	Bal
[9;4]	8.95	4.38	0.14	0.27	0.01	0.01	0.090	0.003	0.009	Bal
[11;1]	10.84	0.94	0.11	0.19	0.01	0.01	0.062	0.003	0.009	Bal
[11;2]	10.67	1.95	0.10	0.16	0.01	0.01	0.060	0.002	0.011	Bal
[11;4]	10.55	4.36	0.13	0.17	0.01	0.01	0.056	0.003	0.010	Bal

lines were drawn over the secondary dendrite arms in a perpendicular direction. The length of the line and the number of intersecting secondary dendrite arms were measured and the average SDAS was calculated. A total of 3 micrographs were prepared for each sample and 10 measurements were done for each micrograph.

#### **5.4.2 Grain Size**

The Grain Size of the samples was measured by the linear intercept method as described by the ASTM E-112-96 standard. The measurements were made by drawing straight lines in an arbitrary direction on the micrograph of the structure. The size distribution of the grains was calculated from the lengths of their intercepts. The average Grain Size was the total length of the lines divided by the number of grains intercepted by the lines (N). Grains lying at the ends of the test line were counted as half a grain. All whole grains intercepted were counted as one. Grains tangent to the test line were not counted. The chemical delineation of the grains at higher Si and Cu levels in the test samples, made it difficult to obtain good etching. Therefore, it was possible to measure the grain sizes of only 7 test samples. However, this work has shown that by using the Growth Restriction Factor (GRF) technique described in Chapter 7, the Grain Sizes of 3XX series of Al-Si alloys could be accurately predicted.

#### **5.4.3 Brinell Hardness**

The Brinell Hardness of the AITAP thermal analysis test samples (12 samples) was measured using the same procedure described in Section 4.3.3. The measurements were performed according to the ASTM E-10 specification. The test samples were sectioned in the longitudinal direction and machined to get an even surface. The average of 5 random indentations was computed. The specific conditions for the Brinell Hardness Test were a load of 500kg was applied on the sample surface for 15 seconds.

#### **5.4.4 Latent Heat of Solidification**

The latent heat of solidification of the test samples was measured by using a NETZSCH Pegasus 404C Differential Scanning Calorimeter (DSC) apparatus. In order to obtain an unbiased microstructure and repeatable results, the DSC specimens were

“rapidly quenched” by a massive copper chill and machined to a thickness of 0.5mm and a diameter of 5mm (average mass was  $\sim 20\text{mg}$ ). The samples were cleaned using propanol solution and placed into an alumina crucible. The experiments were performed at the same heating and cooling rate of  $0.1^\circ\text{C/s}$ . High purity Argon as a protective gas was used during the experiments. The DSC apparatus was calibrated using a sapphire standard test sample. Starting at room temperature ( $25^\circ\text{C}$ ), the DSC samples were heated to  $800^\circ\text{C}$ , held at this temperature for 10 minutes and then cooled down to room temperature. Each DSC experiment for each particular alloy was repeated twice and an average value for latent heat was computed.

## **6. Results and Discussions of the Experiments and Measurements Involving the W319 Al Alloy Used at WAP**

### **6.1 Introduction**

This chapter presents the results and discussions regarding the experiments performed on the W319 Alloy.

The test samples collected from different stages (ingot, melt and block) of the WAP process were characterized by Thermal Analysis in order to compare the TA characteristics. The sensitivities of the presently used Thermal Analysis system (i.e. Alu-Delta) and AITAP were compared by Repeatability and Reproducibility (R&R) Studies. Process capability analysis of the WAP process was performed using the hardness and shrinkage porosity data that was obtained during the period of Thermal Analysis experiments at WAP. The Tukey control chart limits for the key TA parameters were established for the statistical process control of the WAP process by means of TA. Although WAP presently does not use chemical modification of the eutectic silicon, this has been very much in practice in NEMAK's Essex Aluminum Plant (EAP) as well as other aluminum foundries and research laboratories. Therefore a novel method for the on-line evaluation of the Silicon Modification Level (SiML) using Thermal Analysis and Artificial Neural Network was developed in the scope of this dissertation.

The WAP melt chemical composition was statistically analyzed to find the link between the elements and casting porosity as well as Brinell Hardness. The reliability studies on the electromagnetic pump are also presented. Finally, this Chapter introduces a method to optimize the solution treatment parameters of the Novel Solution Treatment during Solidification (NSTS) for the W319 Alloy.

### **6.2 Thermal Characterization of the Ingot, Melt and Engine Block Bulkhead Samples using the UMSA**

Heating and Cooling curve analysis of the test samples of the ingot, melt and bulkhead of engine block samples were performed by using the UMSA Thermal Analysis platform. This allows for the comparison of the thermal characteristics of the material at

different stages of the process as shown in Table 6.1. The values presented in the Table are the average values (number of samples=3) of the TA parameters of the test samples collected over three days; April 10, 17, and 25, 2003. Table 6.1 shows that the liquidus temperature (reaction 4) of the bulkhead samples is approximately 7 to 8<sup>0</sup>C higher than that of the ingot and the melt samples. Also the fraction solid of the block bulkhead samples at the aluminum silicon eutectic nucleation reaction is 6% higher than the corresponding average values of the ingot and the melt. This may be explained as follows: The engine block is a complex casting having many sections with varying thicknesses. As a result the thinner sections solidify faster than the thicker sections. The engine block test sample was extracted from the thickest section of the casting (i.e. the bulkhead), which solidifies at the end. Therefore, there is enough time for the macro and micro segregation of the alloying elements like copper, which is almost 4 times denser than aluminum and hence the bulkhead chemistry will be slightly different from the rest of the casting. Secondly, the engine block was sampled right after the TSR process and air quenching. So the full homogenization heat treatment is yet to be completed.

The above mentioned hypothesis has been confirmed by measuring the Secondary Dendrite Arm Spacing (SDAS) values of the ingot, melt and block UMSA samples. Since the mass of these test samples is the same (7.5±0.2 gm) and the samples were solidified under identical solidification conditions, the effect of solidification rate on the SDAS is the same for all the samples. Therefore, if the SDAS of these samples differ from each other, it is due to the difference in their chemical composition. The SDAS values of the ingot, melt and block samples are presented in Table 6.2. It can be seen from Table 6.2 that the average SDAS of the block sample is ~6 μm higher than that of the ingot and melt samples. This means that the block sample has a different chemistry than the ingot and melt samples.

The author of this work has developed a novel equation to calculate the SDAS of the hypoeutectic 3XX Al alloys as a function of their solidification rate and the alloy chemical composition (Djurdjevic et al., 2004a).

**Table 6.1: Comparison of the characteristic reaction temperatures ( $^{\circ}\text{C}$ ) and fraction solids (%) of the ingot, melt and bulkhead UMSA test samples with their Standard Deviations (SD) (Cooling Rate =  $\sim 0.83^{\circ}\text{C}/\text{Sec}$ ).**

Reaction Number	Name of the Reaction	Ingot ( $^{\circ}\text{C}$ )	Melt ( $^{\circ}\text{C}$ )	Block ( $^{\circ}\text{C}$ )
		SD	SD	SD
1	Beginning of the alloy melting	504.7	504.5	505.6
		1.7	0.9	0.5
2	End of dissolution of the Cu phases	521.6	522.5	521.4
		2.2	1.5	2.0
3	End of the alloy melting process	616.6	618.4	625.1
		2.1	2.7	3.9
4	Beginning of the nucleation of the Al dendrites	602.3	600.9	608.7
		1.1	0.7	0.3
5	Dendrite Coherency Point	596.1	595.5	602.9
		0.7	0.9	0.7
	Fraction Solid at the Dendrite Coherency Point (%)	7.8	8.4	9.9
		0.1	0.4	0.5
6	Beginning of the nucleation of the Al-Si eutectic	567.7	567.4	568.2
		0.9	1.2	0.4
	Fraction solid at the beginning of the nucleation of the Al-Si eutectic(%)	32.6	33.0	39.0
		0.6	0.5	0.5
7	Beginning of the nucleation of the Cu enriched phases	501.9	502.3	499.8
		1.1	1.7	0.5
	Fraction solid at the beginning of the nucleation of the Cu enriched phases (%)	93.4	93.5	94.8
		0.2	0.4	0.2
8	End of the alloy solidification	443.5	441.8	442.0
		6.3	3.6	2.9



**Table 6.2: Comparison of the SDAS values ( $\mu\text{m}$ ) measured on the ingot, melt and bulkhead samples with their Standard Deviations (SD)**

	<b>SDAS (<math>\mu\text{m}</math>)</b>	<b>Standard Deviation (<math>\mu\text{m}</math>)</b>
<b>Ingot</b>	34.9	9.4
<b>Melt</b>	35.4	9.1
<b>Block</b>	40.7	10.3

This equation is given by :

$$\text{SDAS} = -22.86 - 89.73R + 35.29\text{Si} - 2.90\text{Cu} + 20.12R^2 - 2.41\text{Si}^2 \quad (R^2=0.80) \quad (6.1)$$

where R is the solidification rate ( $^{\circ}\text{C}/\text{sec}$ ), and Si and Cu are the silicon and copper contents in wt.%, respectively. The accuracy of this equation has been verified using the SDAS measurements of the ingot and melt samples. These results are presented in Table 6.3. It can be seen that the calculated and measured values of the SDAS are very close to each other.

Another application of the thermal characterization is that the severity of macro-segregation of the “low melting point phases” including CuAlMgSi, Sn, and Pb can be compared between the samples. For example, the Temperature Vs. First Derivative plot of the ingot, melt and bulkhead samples from April, 25, 2003 is shown in Figure 6.1. When there is no segregation, all the curves should match perfectly with each other. However in this case, the peak for the low melting point phases of the block sample show a significantly different peak height and convolution level from the corresponding peaks for the ingot and the melt. This indicates the presence of macro-segregation of the low melting point phases in the block sample.

The Temperature – Fraction solid plots of the ingot, melt and engine block samples are given in Figure 6.2 . It can be seen that the fraction solid plots of the ingot and melt samples are identical while that of the block sample has a different profile. This again confirms that the chemistry of the bulkhead sample is different from that of the ingot and the melt samples.

### 6.2.1 Grading of the Ingot Suppliers for Consistent Casting Properties

Presently, the ingot quality is controlled at WAP by chemical composition analysis only. If the chemistry of the supplied ingots falls between the specification limits, the ingot is certified for production. However, this method does not allow for the grading of the ingot suppliers in terms of the overall metallurgical quality of the supplied ingots. This work presents a novel approach for benchmarking the ingot suppliers by heating curve analysis. UMSA test samples were machined from the ingots delivered by three ingot suppliers, viz: A, B and C. Thermal Analysis experiments (heating and

**Table 6.3: Comparison between the calculated SDAS values and the measured SDAS values for the ingot and melt samples.**

Type of Sample	Composition in wt.%		Average Solidification Rate ( $^{\circ}\text{C}/\text{Sec}$ )	Average SDAS ( $\mu\text{m}$ )	
	Si	Cu		Calculated	Measured
Ingot	7.38	3.41	0.84	35.1	34.9
Melt	7.52	3.51	0.83	35.7	35.4

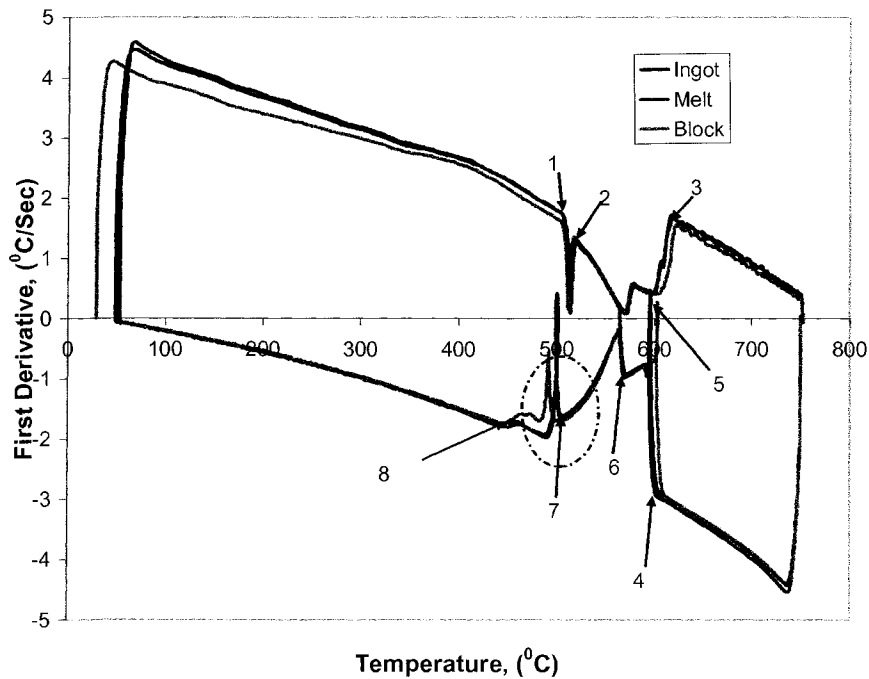


Figure 6.1: Temperature versus First Derivative plot of the Ingot, Melt and Engine Block Samples taken on April, 25, 2003. The nucleation of the Cu rich phases is shown in the circle.

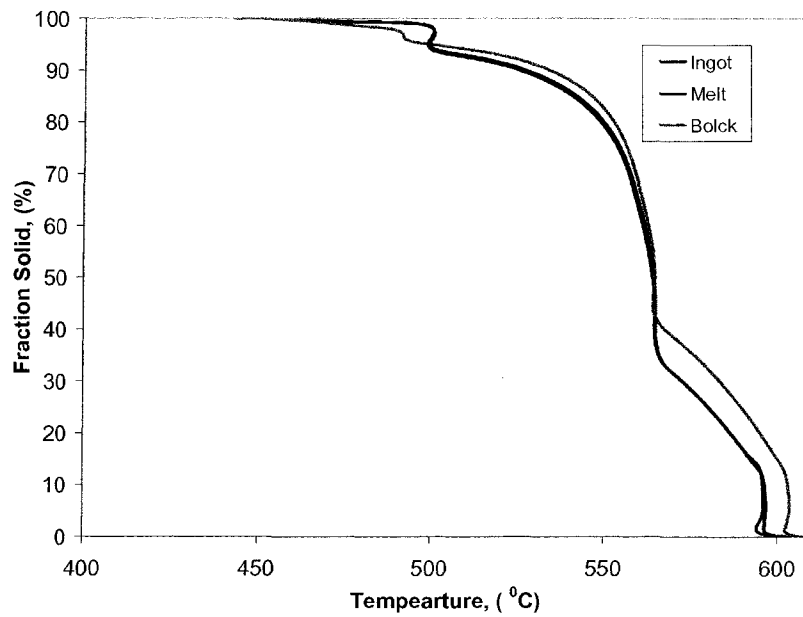


Figure 6.2: Temperature versus Fraction Solid plot of the Ingot, Melt and Block Samples taken on April, 25, 2003.

cooling) of the ingot samples were performed on these samples using UMSA and as explained in Section 4.5.1 of this dissertation. Using the derivative heating curve analysis, the start temperature of alloy melting ( $T_m$ , reaction #1 in Figure 6.1) of the test samples was calculated. These results are plotted in Figure 6.3 for comparison. Figure 6.3 shows that the value of  $T_m$  is maximum for the ingots supplied by supplier A. This is a highly desirable situation because this allows for the maximum dissolution of the copper rich phases in the shortest time and a higher TSR temperature can be used. On the other hand the values of  $T_m$  of the ingots from supplier C are 4<sup>0</sup>C lower than the TSR temperature. This could potentially result in the detrimental incipient melting of the low melting point phases and lower mechanical properties such as hardness. Therefore, heating curve analysis using UMSA is recommended as a tool for the selection of ingot suppliers. Further research has shown that the  $T_m$  is controlled by the amount of low melting point elements like Pb and Sn present in the alloy. This will be discussed in detail in Section 6.5.2.2.

### **6.3 Thermal Analysis of the WAP Melt**

In this Section the Repeatability and Reproducibility (R&R) studies of the AITAP and Alu-Delta are discussed at the outset. The results of this study provide the justification for using AITAP for further Thermal Analysis of the melt at WAP. The results of the Thermal Analysis is discussed in Section 6.3.2.

#### **6.3.1 Repeatability and Reproducibility (R&R) Studies of AITAP and Alu-Delta**

Repeatability is defined as the variation observed when the same operator measures the same sample repeatedly with the same device. Reproducibility is defined as the variation observed when different operators measure the same samples using the same device (Minitab, 2000). Repeatability measures the variation due to the gage whereas reproducibility measures the variation due to the operators. The studies by Chagoya (2001) using isoplots have shown that temperature TA parameters are the most robust for industrial measurements, because time and fraction solid parameters are dependent on the cooling rate and mass of the test sample. Therefore, the silicon eutectic growth

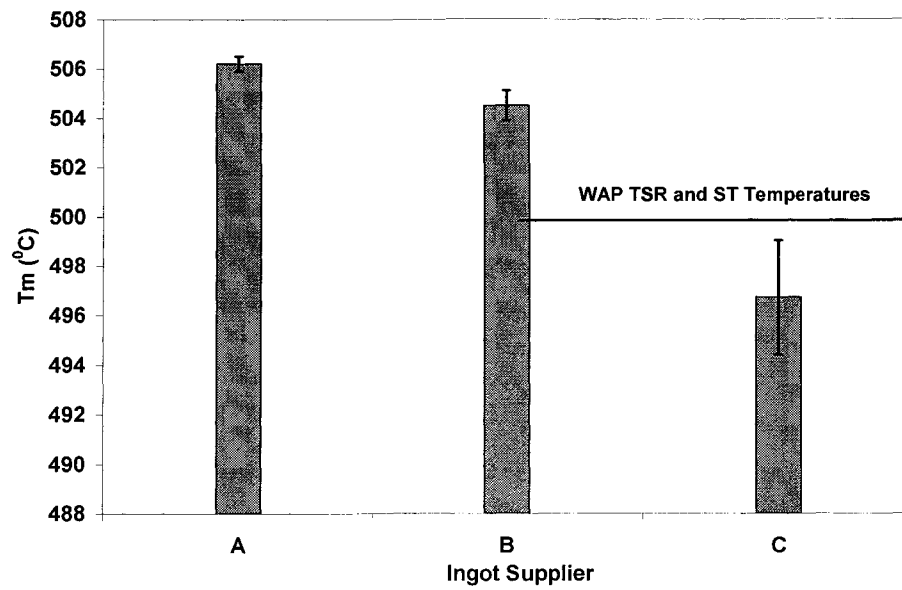


Figure 6.3: Comparison of the start temperature of alloy melting ( $T_m$ ) of the ingot samples supplied by ingot suppliers A, B, and C.

temperature ( $T_{E,G}^{AlSi}$ ) was chosen as the TA parameter for comparison between AITAP and Alu-Delta.

The objective of the R&R studies was to compare which among the 2 TA systems was more sensitive to the day to day changes in the WAP melt. If a TA system is insensitive to small daily changes in the process, it cannot give early warning signals to potential problems. 18 measurements of  $T_{E,G}^{AlSi}$  taken over 6 days (3 per day), were obtained from AITAP as well as Alu-Delta. Since each operator measured distinct samples, the nested Gage R&R model was used for the analysis (Mintab, 2000). The general linear statistical model for this two stage nested design is given by (Montgomery, 2001):

$$y_{ijk} = \mu + O_i + S_{j(i)} + \varepsilon_{(ij)k} \quad \left\{ \begin{array}{l} i=1,2 \\ j=1,2,3 \\ k=1,2,3 \end{array} \right. \quad (6.2)$$

where,  $y_{ijk}$  is the observation for the  $i^{\text{th}}$  operator,  $j^{\text{th}}$  sample and  $k^{\text{th}}$  replication,  $\mu$  is the overall mean of the measurements,  $O_i$  is the effect of the operator 'i',  $S_{j(i)}$  is the effect of the sample 'j' that is nested within the operator 'i' and  $\varepsilon_{(ij)k}$  is the random error between repeated measurements. This balanced nested design is shown in Figure 6.4. The nested Analysis of Variance (ANOVA) Tables for AITAP and Alu-Delta are given in Tables 6.4 and 6.5 respectively. These analyses were performed by using the Minitab<sup>TM</sup> statistical software.

Table 6.4 shows that the main source of variability in the case of AITAP is the sample to sample variation within the operators (p-value<0.05). This means that AITAP is sensitive to the variations in the samples from one day to another. This is a very favourable condition. Meanwhile, Table 6.5 shows that in the case of Alu-Delta neither the operator nor the sample to sample variation are the main sources of variability. Hence the main source of variability must be the measurement system itself. This is an unfavourable situation. The percentage contribution made by each variance component to the overall variability is plotted in Figure 6.5. This plot again is the graphical visualization of the ANOVA results, which shows that in the case of Alu-Delta the total Gage R&R contributes up to 90% of the variability, while in the case of AITAP the sample to sample variation adds up to 81% of the overall variability. The parameters of

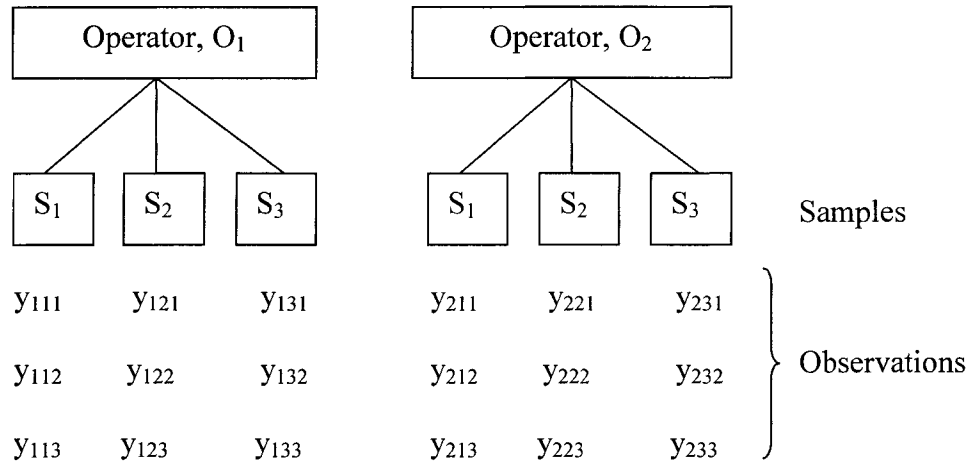


Figure 6.4: Two stage balanced nested design for the R&R studies.

**Table 6.4: ANOVA Table for the AITAP Data**

Source of Variability	Degree of Freedom	Sum of Squares (SS)	Mean Square (MS)	F-value	p-value
operator	1	0.82911	0.82911	0.8749	0.40256
sample (operator)	4	3.79079	0.947698	13.7771	<b>0.00019</b>
Error (Repeatability)	12	0.82546	0.068788		
Total	17	5.44536			

**Table 6.5: ANOVA Table for the Alu-Delta Data**

Source of Variability	Degree of Freedom	Sum of Squares (SS)	Mean Square (MS)	F-value	p-value
operator	1	3.5556	3.55556	2.88939	0.16439
sample (operator)	4	4.9222	1.23056	1.42995	0.28327
Error (Repeatability)	12	10.3267	0.86056		
Total	17	18.8044			



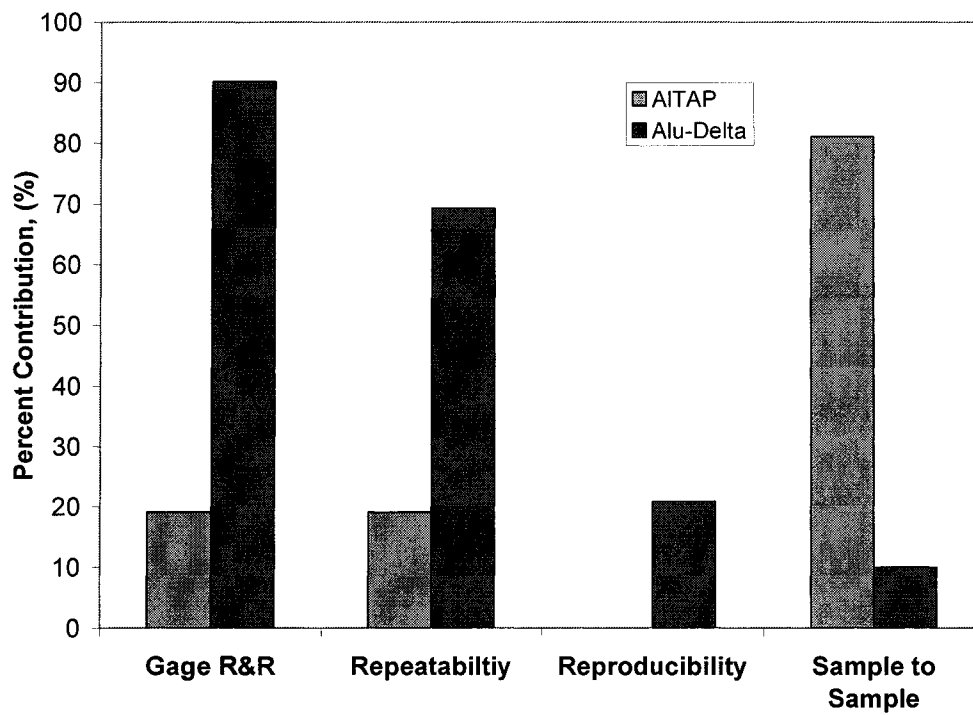


Figure 6.5: Percentage contribution made by each variance component to the total variability for AITAP and Alu-Delta. Note that the percentage contribution of Reproducibility of AITAP to the total variability is zero.

the R&R studies can be calculated by substituting the Mean Square (MS) values from the ANOVA Tables (6.4 & 6.5) in the formulas given below (Minitab, 2004a).

$$\sigma^2_{\text{Repeatability}} = \text{MS Error} \quad (6.3)$$

$$\sigma^2_{\text{Reproducibility}} = b * (\text{MS sample}(\text{operator})) / a \quad (6.4)$$

$$\sigma^2_{\text{Total Gage R\&R}} = \sigma^2_{\text{Repeatability}} + \sigma^2_{\text{Reproducibility}} \quad (6.5)$$

$$\sigma^2_{\text{Sample}} = (\text{MS sample}(\text{operator}) - \text{MS Error}) / n \quad (6.6)$$

$$\sigma^2_{\text{Total variability}} = \sigma^2_{\text{Total Gage R\&R}} + \sigma^2_{\text{Sample}} \quad (6.7)$$

where, a is the number of samples (i.e.,6), b is the number of operators(i.e.,2), and n is the number of replications (i.e.,3).

Another parameter to measure the performance of a measurement system that can be derived from the R&R parameters is the “number of distinct categories” (D), (Wheeler and Lyday, 1989). The equation for the calculation of the D is given by:

$$D = \sqrt{\frac{2 * \sigma^2_{\text{Sample}}}{\sigma^2_{\text{Total Gage R\&R}}}} \quad (\text{rounded to the nearest integer}). \quad (6.8)$$

The physical meaning of the value of D is that it is the number of distinct samples that the measurement system can distinguish from one another. For example in this case, since there are 6 different samples, it would be ideal if the value of D is 6. The lower the value of D, the lesser the precision of the gage. The values of D for AITAP and Alu-Delta were calculated to be 3 and 0 respectively. This means that Alu-Delta is unable to distinguish between the test samples from one day to another. This again is a confirmation of the results of the ANOVA studies. According to the Automobile Industry Action Group (AIAG) when the value of D is less than 2, the measurement system should not be used for process quality control. Studies by Kierkus et al. (2002) have reported substantial errors in the measurements of TA parameters by Alu-Delta. The liquidus temperature measured by the Alu-Delta was found to be 11<sup>0</sup>C above that which is measured by AITAP, calculated by Si<sub>EQ</sub> (Silicon Equivalency), and also reported in the literature. The Aluminum Copper eutectic nucleation reaction temperature measured by Alu-Delta and AITAP differs by about 5<sup>0</sup>C, AITAP measurements being closer to the theoretical values predicted by the Si<sub>EQ</sub>.

Based on the above discussion it is highly recommended that Alu-Delta be replaced by AlTAP for WAP melt process control.

### **6.3.2 Thermal Analysis of the WAP Melt Using AlTAP**

The Thermal Analysis of the melt at the middle holding furnace was carried out using AlTAP and the Unbiased Melt Sampling Device (UMSD) during the months of April and June 2003 as described in Section 4.4.1. The variations in the bulkhead Brinell Hardness (HB) and the variations in the shrinkage porosity level in the critical bulkhead Sections 4 and 7 during this period are plotted in Figures 6.6, 6.7 and 6.8. It can be seen from these Figures that during the period under consideration, the WAP process was in a state of statistical control, which means that the only source of variation in the process was due to the chance causes that were inherent to any process. In other words there were no assignable causes that would warrant an out of control situation, during the period of the Thermal Analysis experiments. Therefore, the shrinkage porosity and the hardness data during this period could be used for process capability analysis (Mitra, 1993).

#### **6.3.2.1 Process Capability Analysis of the WAP process**

The process capability analysis measures the variability of the process that is caused by chance causes when the process is in the state of statistical control. Process capability is a measure of the ability of the process to consistently manufacture products (in this case, engine blocks) with quality characteristics that meet the specifications. In order to perform the process capability analysis, the distribution of the quality characteristics of interest (in this case hardness and porosity) must be determined as a first step. The normality assumption of the quality characteristics was checked using a probability plot and was found satisfactory. The Minitab™ outputs of the process capability analyses of the bulkhead hardness data, and shrink porosities of bulkhead Sections 4 & 7 are given in Figures 6.9, 6.10, and 6.11.

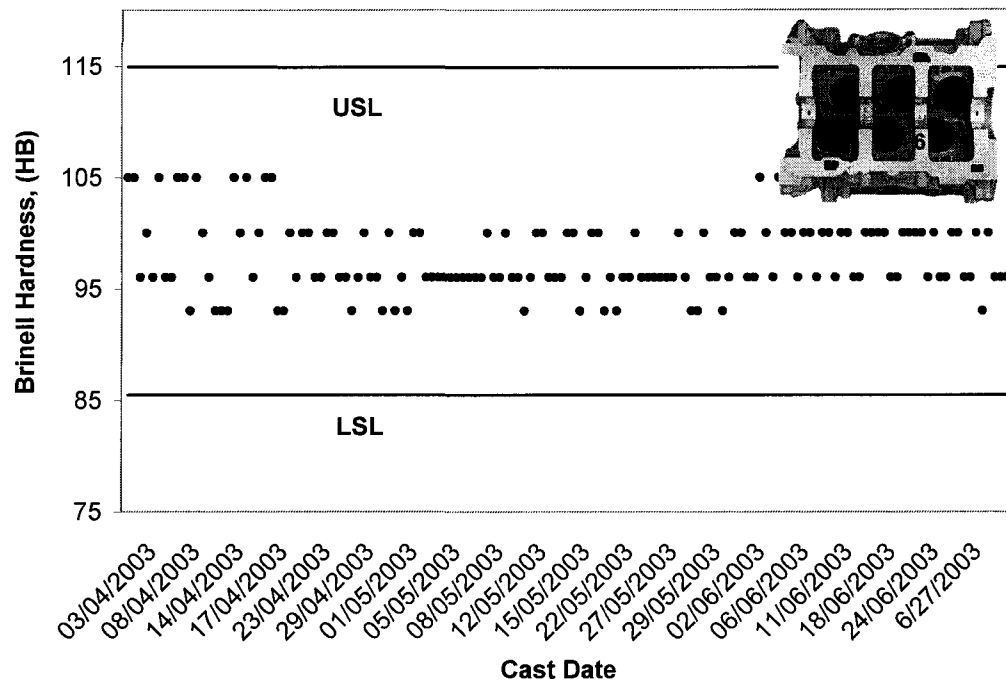


Figure 6.6: Run chart of the Brinell Hardness for the hit location 6 (shown in inset) of the 3.0L V6 engine block bulkhead during the period from April 2003 to June 2003. (USL and LSL are the upper and lower specification levels).

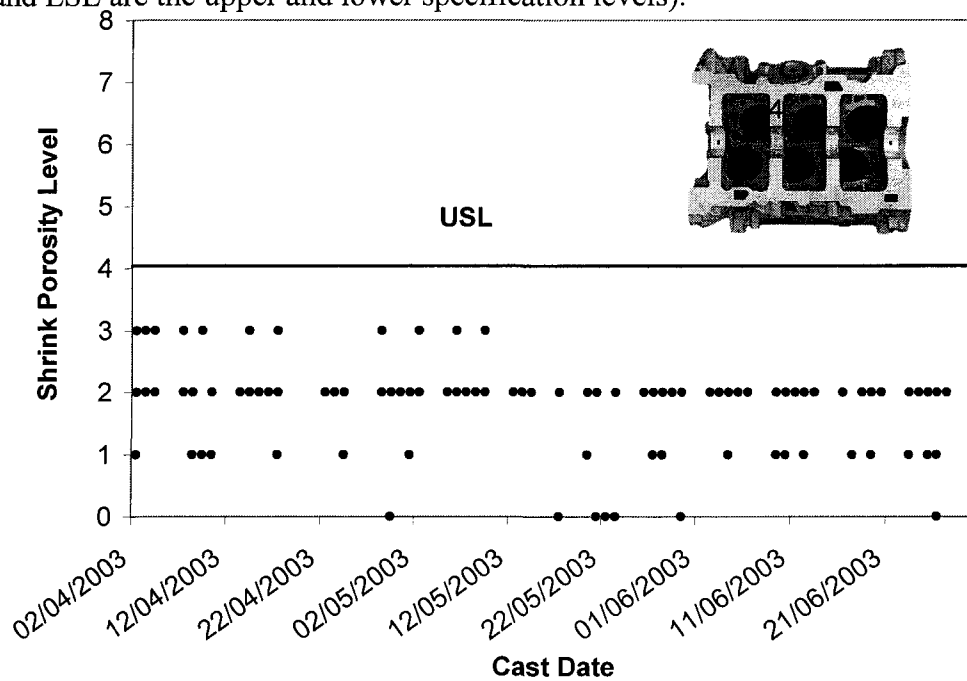


Figure 6.7 : Run chart of the shrinkage porosity levels of bulkhead Section 4 (shown in the inset) of the 3.0L V6 engine blocks during the period from April 2003 to June 2003. The maximum level on the Y axis is eight, because as per the ASTM E-155 standard, shrink porosity is classified into 8 levels.

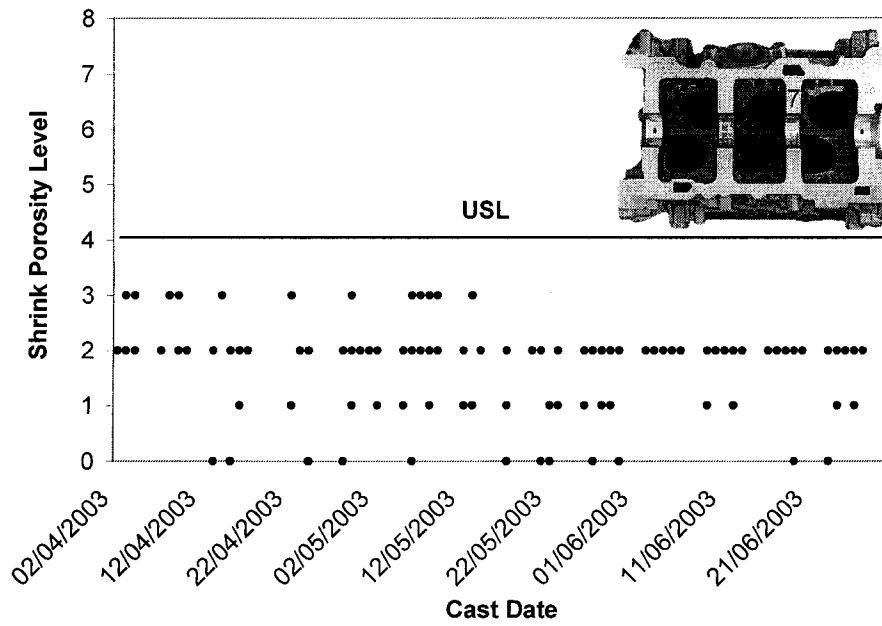


Figure 6.8: Run chart of the shrinkage porosity levels of bulkhead Section 7 (shown in the inset) of the 3.0L V6 engine blocks during the period from April 2003 to June 2003.

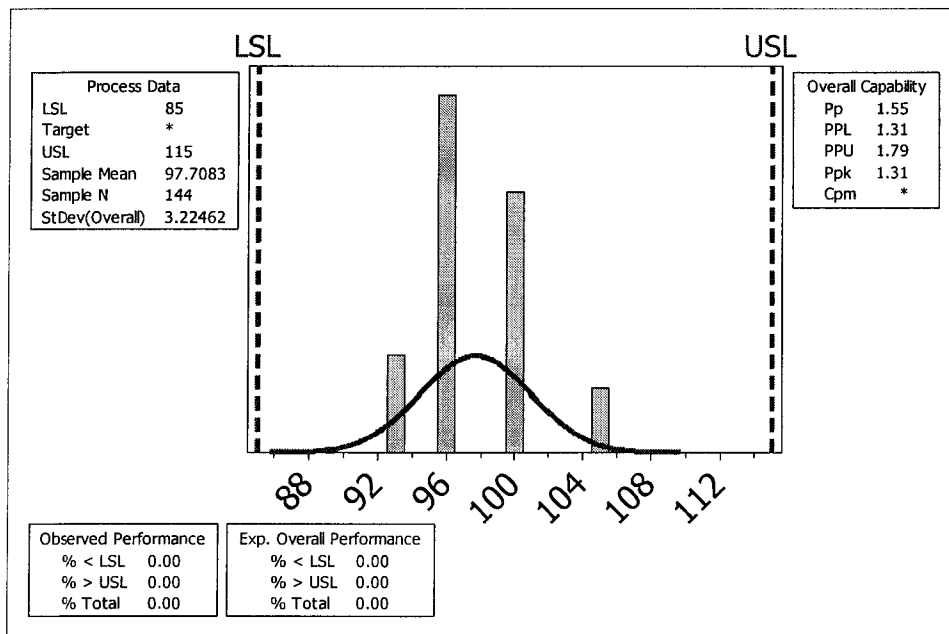


Figure 6.9: Minitab output of the process capability analysis of the bulkhead hardness data from April 2003 to June, 2003.

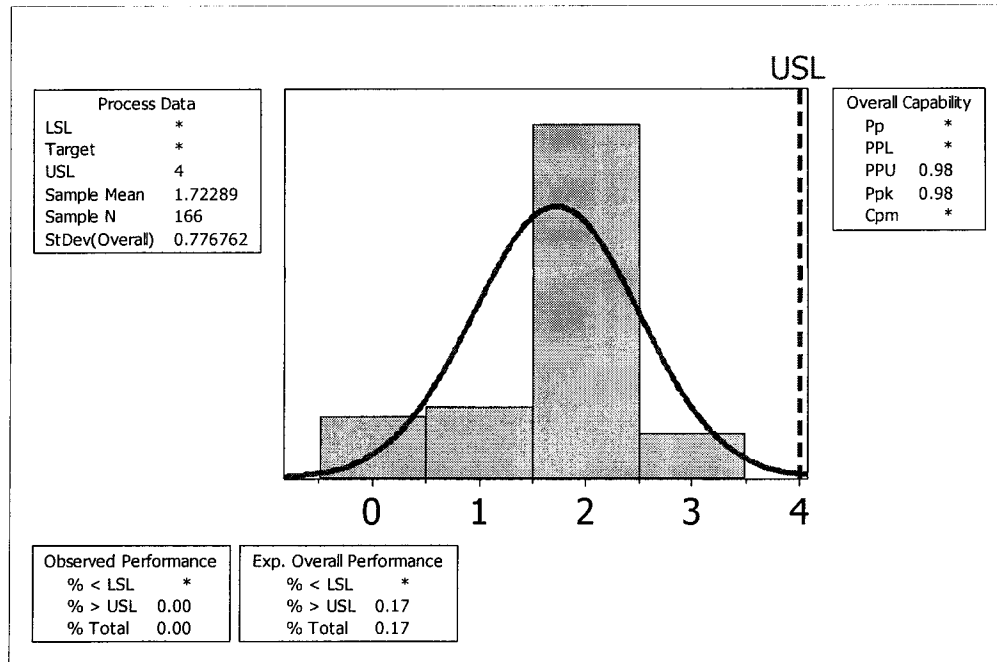


Figure 6.10: Minitab output of the process capability analysis of the shrinkage porosity data of bulkhead Section 4 from April 2003 to June, 2003.

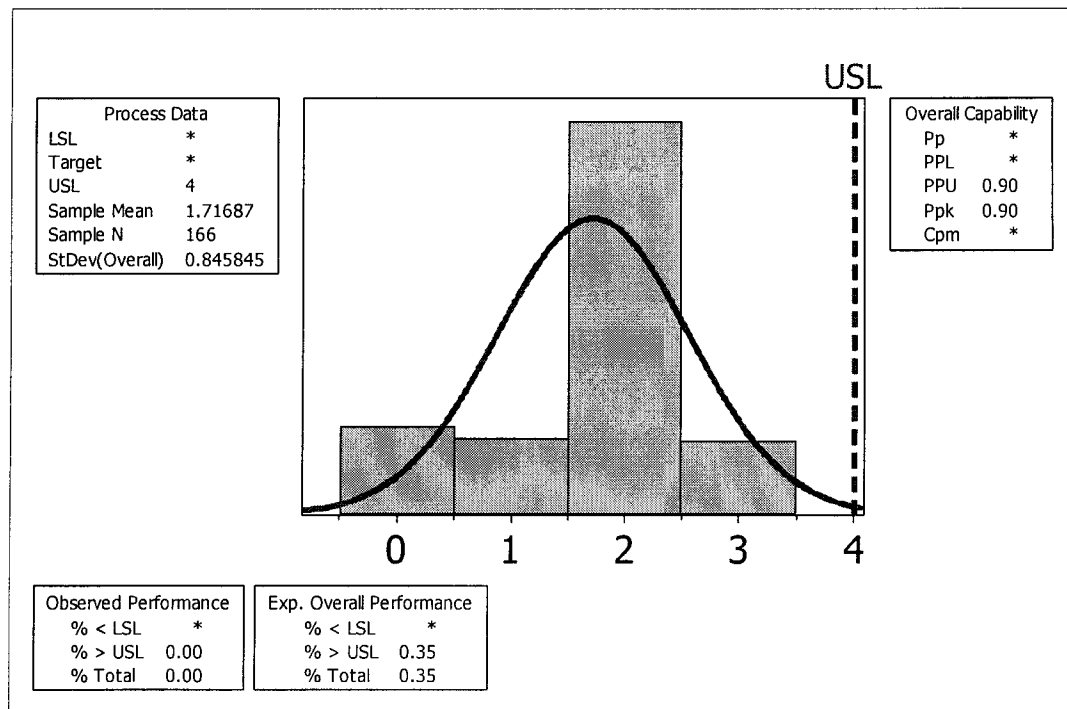


Figure 6.11: Minitab output of the Process Capability Analysis of the shrinkage porosity data of bulkhead Section 7 from April 2003 to June, 2003.

The indices of the process capability are calculated using the following equations (Mitra, 1993):

$$\text{Process Performance Ratio (Pp)} = \frac{\text{USL} - \text{LSL}}{6\sigma} \quad (6.9)$$

$$\text{Process Performance Lower index (PPL)} = \frac{\mu - \text{LSL}}{3\sigma} \quad (6.10)$$

$$\text{Process Performance Upper index (PPU)} = \frac{\mu - \text{LSL}}{3\sigma} \quad (6.11)$$

$$\text{Process Performance Index (Ppk)} = \text{Min (PPL, PPU)} \quad (6.12)$$

where USL is the upper specification limit, LSL is the lower specification limit,  $\mu$  is the process mean and  $\sigma$  is the process standard deviation. The process capability indices are calculated by using the sample estimates of the process mean and process standard deviation. It must be noted that there are no calculations using the LSL, that are involved in the process capability analysis with the shrinkage porosity data. This is because the most desirable value for porosity is zero, where it is at a minimum.

The process capability analysis shows that the WAP process with its current process parameters is able to produce engine blocks that meet the hardness specifications 100% of the time (Ppk=1.31).

The process capability analysis of the shrinkage porosity data shows that the present WAP process parameters are barely capable of meeting the specification (Ppk=0.98 & 0.9) requirements for porosity. This is because the present inherent process variations are more than the maximum allowable variation as far as shrink porosity is concerned. The analysis predicts that with the present process parameters, 0.35% of the 3.0LV6 engine blocks will have porosity levels higher than s4 in bulkhead Section 7 and 0.17% will have porosity levels higher than s4 in bulkhead Section 4. Therefore, a more detailed investigation is required to identify the root causes behind the variations in shrinkage porosity so that corrective actions can be recommended to reduce these variations. This analysis has been presented in Section 6.5.1.

### 6.3.2.2 Development of the Tukey Control limits of the TA Parameters for the Statistical Process Control at WAP

The WAP process was in a state of statistical control during the period when the Thermal Analysis experiments were performed. In Section 6.3.1, the R&R studies revealed that the AITAP TA parameter is so sensitive that it detects the small day to day changes in the WAP process. Therefore, the Thermal Analysis parameters obtained from the Computer Aided Cooling Curve Analysis of the TA data from WAP can be used to establish the control limits for the quality control charts, which in turn, can be used to control the WAP process. Since these control limits were established using the data when the process was in statistical control, if an out of control condition occurs after the implementation of the control chart, it will be plotted as a point that lies outside its control limits. The assignable cause for this out of control point must be investigated and corrective actions should be taken to bring the process back into control state. Thus the control chart helps the process engineers to distinguish between the variations in the process due to chance causes that are innate with the process and the variation due to assignable causes that shows a “*real*” shift in the process (Mitra, 1993).

The control limits for the TA parameters were calculated using the Tukey’s Method and therefore the corresponding control charts are called Tukey Charts. When the sample size is small, observations are independent of each other and the data is continuous and numerical, one can use either the Tukey chart or a Moving Average Chart to control the process. The Tukey chart was preferred over the Moving Average Chart for the following reasons (George Mason University, 2004a):

- (1) Tukey control limits are tighter than the moving average control limits
- (2) The control limit calculations are easier and hence it is easier to maintain a Tukey Chart.
- (3) The Tukey limits are calculated using the median, and therefore it is more robust to outliers in the data.

The equations for the calculation of the Tukey control limits are given as (George Mason University, 2004b):



$$\text{LCL} = \text{Lower Fourth} - 1.5 * \text{Fourth Spread} \quad (6.13)$$

$$\text{UCL} = \text{Upper Fourth} + 1.5 * \text{Fourth Spread} \quad (6.14)$$

where, the Lower Fourth is the median of the lowest 50% of the data, data from the smallest number till (or including) the median, the Upper Fourth is the median of the top 50% of the data, data from (or including) median of the full data set to the highest value and the Fourth Spread is the difference between the upper and lower fourths.

The Tukey control limits for the key TA parameters are given in Table 6.6, and the Tukey control chart for the Al-Si eutectic nucleation temperature is shown in Figure 6.12. It is recommended that these control charts be implemented at WAP for the on-line process control of the WAP process.

## **6.4 Development of a Novel Methodology for the On-line Prediction of the Melt Silicon Modification Level (SiML) Using Artificial Neural Networks and Thermal Analysis**

### **6.4.1 Introduction**

The on-line prediction of the Silicon Modification Level (SiML) is very important to the Quality Control of the W319 aluminum alloy castings. Conventionally, SiML is estimated by destructive sampling and manual microscopic analysis of the casting structure. The structure is compared with the American Foundry Society (AFS) chart for Microstructure Control in Hypoeutectic Alloys. In this chart the entire range of the modification level is divided into six classes based on the structure of the eutectic silicon particles. Fully modified structures fall into class 5 and 6, partially modified into 2 to 4 and unmodified into class 1. Refer to Figure 6.13. Based on visual comparison, the specimen is assigned a modification level, where the structure of the specimen is closest to the AFS chart. This method is subjective and hence inaccurate. Djurdjevic et al., (2001b) modified this method by using the perimeter of the eutectic silicon as the classifying criterion. The SiML calculated as outlined in equation 6.15.

**Table 6.6: Tukey control limits for the TA parameters for on-line process control of the WAP process.** (The algorithms to determine these TA parameters are given in Appendix 2.)

TA Parameter	Lower Control Limit (LCL)	Upper Control Limit (UCL)
Liquidus Temperature ( $T_{LIQ}$ )	593	601
Al-Si eutectic nucleation temperature ( $T^{Al-Si}_{E,NUC}$ )	566	571
Fraction solid at the Al-Si eutectic nucleation temperature ( $fs^{Al-Si}_{E,NUC}$ )	30	38
Al-Cu eutectic nucleation temperature ( $T^{Al-Cu}_{E,NUC}$ )	498	510
Solidus Temperature ( $T_{SOL}$ )	448	477

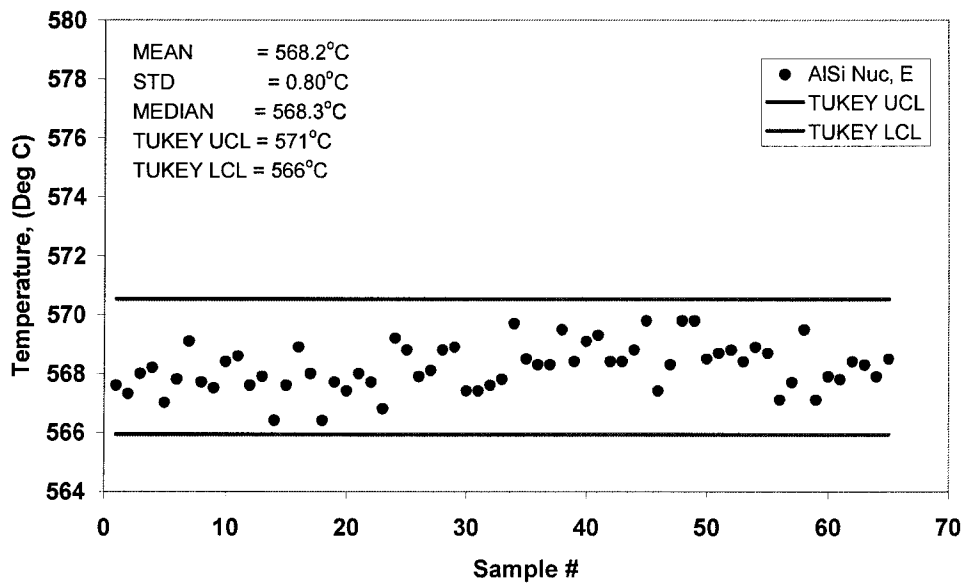


Figure 6.12: Tukey control chart for the Al-Si eutectic nucleation temperature.

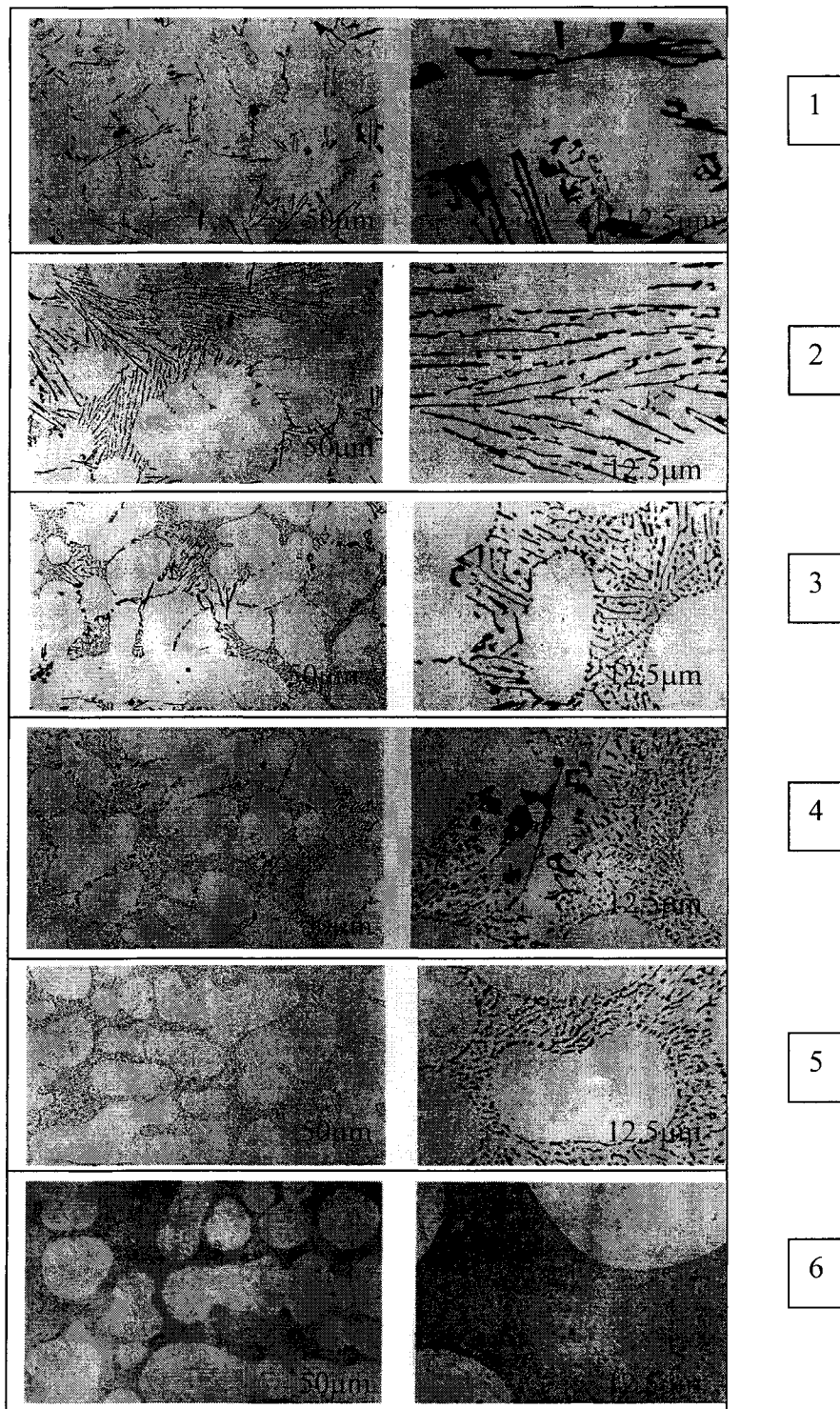


Figure 6.13. Representative Si structure morphologies corresponding to the AFS chart for Hypoeutectic Aluminum Silicon Alloys. (1) Fully unmodified microstructure; (2) Lamellar microstructure; (3) Partially modified microstructure; (4) Absence of the lamellar microstructure; (5) Fibrous silicon eutectic structure; (6) Very Fine Structure (Zalensas, 1993).

$$\text{SiML} = (1\text{x}\text{a}\%) + (2\text{x}\text{b}\%) + (3\text{x}\text{c}\%) + (4\text{x}\text{d}\%) + (5\text{x}\text{e}\%) + (6\text{x}\text{f}\%) \quad (6.15)$$

where a% - f% are the percentages for classes 1-6, respectively, present in the specimen. This technique is objective and accurate. However it is expensive and time consuming. Also the microscope is not suitable for use in the foundry environment as an online method to predict the SiML. Djurdjevic et al. (2001b) presented another method to assess the SiML using the Thermal Analysis (TA) technique. In this method the  $\Delta T$  parameter of the cooling curve was correlated to the SiML and estimated via Image Analysis (IA). See Figure 6.14. The  $\Delta T$  parameter is the difference in the Al-Si eutectic growth temperature between the unmodified and modified alloys. The  $\Delta T$  parameter can be obtained from the cooling curve using equation 6.16.

$$\Delta T = T_{E,G,UNMODIFIED}^{Al-Si} - T_{E,G,MODIFIED}^{Al-Si} \quad (6.16)$$

where:  $T_{E,G,UNMODIFIED}^{Al-Si}$  is the aluminum-silicon eutectic growth unmodified temperature as the maximum temperature achieved during the recalescence of the melt from the nucleation temperature without any addition of modifiers or with a residual level of modifiers (8 ppm Sr), and  $T_{E,G,MODIFIED}^{Al-Si}$  is the aluminum-silicon eutectic growth modified temperature as the maximum temperature that is achieved during the recalescence of the solidifying melt. From the knowledge of the  $\Delta T$  parameter, the SiML can be calculated using equation 6.17 (Djurdjevic et al., 2001b).

$$\text{SiML} = \frac{-17.0741}{\{1 + \exp[(\Delta T - 13.42472)] / 2.04788\}} + 18.06746 \quad (6.17)$$

This method improves the precision and accuracy of the SiML assessment because it eliminates the operator bias and subjectivity. This method gives a digital criterion for the assessment of SiML and can be used as an online method for the estimation of SiML. The cooling curve is very sensitive to the changes in the concentration of alloying elements even at ppm (parts per million) levels (Djurdjevic et al., 2002a). Recent studies on the 3XX series of Al alloys with different levels of Si (5-11 wt.%) and Cu (1-4 wt.%) revealed the influence of the concentration of chemical elements on the cooling curve parameters (Djurdjevic et al., 2002b).

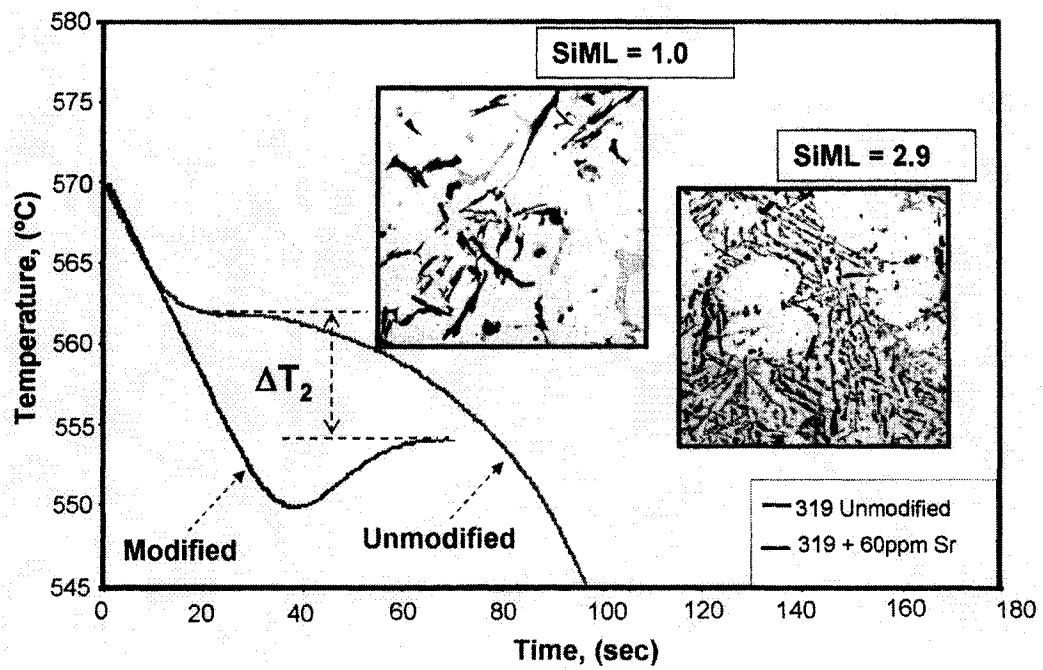


Figure 6.14: Calculation of the  $\Delta T$  using the cooling curves of the unmodified and modified W319 Al alloy (IRC Brochure 2004b).

In this work, Neural Network modeling was attempted to predict the SiML using the TA parameters as inputs. The on-line prediction of SiML is important for control of the casting microstructure and hence control of the casting properties. It has already been shown that TA can be used to predict the SiML. But the existing method also needs information about the unmodified alloy cooling curve characteristics. Heusler and Schneider (2002) have discussed the problems in determining the unmodified silicon eutectic temperature: (1) it requires Thermal Analysis of the unmodified melt which is time consuming and (2) sometimes the supplied ingots are premodified which makes this measurement impossible. Therefore, it would be worthwhile to develop a novel model to assess the SiML, by just using TA parameters of the cooling curve of the melt under investigation. Artificial Neural Network (ANN) has the potential to develop such a model due to the reasons described in Section 2.5.1. The experiments and the procedure for the collection of the database for the development of the ANN model are presented in Section 4.6.1. The remaining steps involved in the Artificial Neural Network modeling are presented below.

#### **6.4.2 Selection of the Input Parameters of the ANN**

The input parameters of the ANN were selected from the cooling curve parameters. The cooling curves were processed and the TA parameters (time, temperature, and fraction solid) were computed. The input parameters for the ANN were selected from the computed TA parameters by using Stepwise Regression Analysis. The symbols of the selected TA parameters, their description, metallurgical meaning, and p-values are shown in Table 6.7. The algorithms for detecting these TA parameters are given in Appendix 2. The p-value for a parameter indicates whether the effect of that parameter is significant on the response (SiML). If p-value is less than or equal to the  $\alpha$ -level (0.05) selected, then the effect of the parameter is significant. If p-value is larger than the  $\alpha$ -level, the effect is not significant (Devore, 1999). The selection of the input parameters is a very important aspect of ANN modeling. Usually the choice is based on the physical background of the process. All relevant input parameters must be included as inputs of the ANN. However those parameters that are linearly dependent should not be included as inputs.

**Table 6.7. Description of the input parameters of the ANN**

Symbol of the TA Parameter	Description	Metallurgical Meaning	p-value
$T_{COH}^{DEN}$	Temperature at the Dendrite Coherency Point (DCP)	At this point the dendrite tips of neighbouring grains come in contact and become fixed at their locations forming a skeleton throughout the sample. This point marks the transition from mass feeding to interdendritic feeding.	0
$f_{COH}^{DEN}$	Fraction Solid at the Dendrite Coherency Point (DCP)		0.012
$T_{E,NUC}^{Al-Si}$	Temperature at the Al-Si Eutectic Nucleation	As dendrites nucleate in the samples, the composition of the remaining liquid reaches the eutectic composition and the Al-Si eutectic begins to nucleate and grow.	0
$T_{E,G}^{Al-Si}$	Temperature at the Al-Si Eutectic Growth	Point at which considerable eutectic growth occurs. These parameters are used to gauge the morphology of the Al-Si structure.	0
$f_{E,NUC}^{Al-Cu}$	Fraction solid at the Al-Cu Eutectic Nucleation	Start of the formation of the Al-Cu eutectic as the remaining liquid becomes enriched with Cu and Si. The temperature and duration of this phenomenon can be used to establish adequate solution treatment parameters.	0.016
$f_{E,MIN}^{Al-Cu}$	Fraction solid at the Al-Cu Eutectic Minimum	Point after stable co-precipitation of Al and Cu when latent heat generation equals the heat loss of the sample and appears as a minimum in the Al-Si region of the cooling curve.	0

### 6.4.2.1 Analysis and Pre-processing of the Data

The relationship between SiML and the input cooling curve parameters was established by performing a Multiple Linear Regression analysis. The regression equation and the  $R^2$  value are given in equation 6.18.

$$\begin{aligned} \text{SiML} = & 520 - 29.4\text{fs}^{\text{DEN}}_{\text{COH}} - 0.645\text{T}^{\text{DEN}}_{\text{COH}} + 0.165\text{T}^{\text{Al-Si}}_{\text{E,NUC}} - 0.238\text{T}^{\text{Al-Si}}_{\text{E,G}} \\ & - 49.9\text{fs}^{\text{Al-Cu}}_{\text{E,NUC}} - 45.3\text{fs}^{\text{Al-Cu}}_{\text{E,MIN}} \quad R^2=0.872 \quad (6.18) \end{aligned}$$

A high  $R^2$  value indicates a good fit between input parameters and SiML. The experimental data set is divided into the training and testing sets. Approximately 15% of the experimental data was used for testing the model. The test data set was chosen to represent all the modification levels of the experimental data set (1 to 5). The training program was written in such a way that each time the program is run it starts with a different random distribution of the training data (Malinov et al., 2001). Prior to training, the data set is subjected to Principal Component Analysis (PCA), which eliminates the highly correlated (redundant) input variables from the data (Beale and Demuth, 2001).

### 6.4.3 Neural Network Training

In this research, two alternative neural networks were developed to predict the SiML. They are: the (a) Multilayer Perceptron (MLP) Neural Network and (b) the Radial Basis Function (RBF) Neural Network.

#### 6.4.3.1 Multilayer Perceptron Neural Network (MLP)

MLP is a feed-forward network composed of an input layer, an output layer, and a number of hidden layers. The most popular algorithm for training of the MLP is backpropagation. In this algorithm, initially a random set of weights are assigned to the network. Input data is then presented and the output of the network is compared to the desired output. The network adjusts the weights of the *synapses* so as to reduce the difference between the network output and the desired output (error). This procedure is repeated until an acceptably low value of error is achieved (Malinov et al., 2001). In this



work the MLP is trained using the Levenberg-Marquardt backpropagation (Beale et al. 2002) algorithm, which is based on a standard numerical optimization technique. When a network is able to perform as well on a test set as on a training set, the network is said to generalize well. In this work the generalizability of the MLP network has been attempted by means of regularization (Foresee and Hagan, 1997). Different network architectures have been investigated to determine the network, which takes less time for training and corresponds to a minimum generalization error. This means that the network parameters are determined by the trial and error method. Only those parameter values were selected which give a minimum error on the test data set and also take less time for training. The architecture of the selected MLP network is given in Table 6.8.

#### 6.4.3.2 Radial Basis Function Networks (RBF)

This network was introduced to solve multivariable interpolation problems. The Radial Basis Function (RBF) network consists of one input layer, one hidden layer and one output layer. The neurons in the hidden layer do not use the weighted sum of inputs and sigmoid transfer functions, which are typical of MLP networks. Instead, the vector distance between the input weight vector and input vector determines the outputs of the hidden layer radial basis neurons. The output layer consists of linear neurons and produces a weighted sum of the outputs of the hidden layer (Beale and Demuth, 2001). The neurons in the RBF network have localized receptive fields, whereas the sigmoid transfer function of the standard Multilayer Perceptron (MLP) network creates a global response (Campos-Velho et al., 1999). The RBF network trains faster than multilayer networks, but requires many neurons for high-dimensional input spaces (Beale et al., 2002). The transfer function for a radial basis neuron is given in equation 6.19:

$$\mathbf{radbas}(n) = e^{-n^2} \quad (6.19)$$

where  $n$  is the net input to the radial basis transfer function which is the vector distance between the input weight vector and the input vector, multiplied by the bias vector. The training of RBF consists of deciding the number of hidden neurons, and the centers and spread of the transfer function and then training the output layer (Campos-Velho et al., 1999). These decisions are made empirically by examining the vectors in the training data (Old Dominion University, 2002).

**Table 6.8. Architecture of the MLP neural network**

Number of hidden layers	Number of neurons in the hidden layer(s)	Number of neurons in the output layer	Transfer function of the hidden layers	Transfer function of the output layer	Training algorithm
2	6 in each layer	1	log sigmoid	linear	Bayesian regularization in combination with Levenberg-Marquardt training

The output layer weights are then trained using backpropagation (Campos-Velho et al., 1999). Radial basis networks tend to have many more neurons than a comparable MLP feed-forward network with sigmoid neurons in the hidden layer. The architecture of the developed RBF network is given in Table 6.9. It can be seen that the number of neurons in the hidden layer of RBF networks is much larger than that of the MLP.

#### 6.4.4. Testing of the Trained Neural Network

The performance of the MLP network on the test data set has been evaluated. The network was found to generalize well with the test data. Figure 6.15 shows the performance of the MLP on the test data set. The Target SiML is the modification level calculated using equation 6.15. The Predicted SiML is the modification level given by the Neural Network. The RBF network is also found to generalize well with the test data set. Performance of the RBF neural network on the test data set is shown in Figure 6.16. The data showing the levels of Strontium (Sr) in the test data set samples, the SiML predicted by the ANN models, the target SiML, and the corresponding microstructures are given in Table 6.10.

The Mean Square Error (MSE) of the test data set is the criterion used to evaluate the accuracy of the Neural Network. Lower levels of MSE imply higher accuracy. MSE is calculated using equation 6.20:

$$\text{MSE} = \frac{1}{N} \sum_{i=1}^N (t_i - a_i)^2 \quad (6.20)$$

where:

$N$  = size of the test data set.

$t_i$  = desired output value for the  $i^{\text{th}}$  input data.

$a_i$  = predicted output value for the  $i^{\text{th}}$  input data by the model.

The MSEs of the MLP and RBF Neural Networks on the test data set have been compared with those obtained for the  $\Delta T$  method and for Multiple Linear Regression. These results are shown in Table 6.11. It can be seen that the Mean Square Error is the

**Table 6.9. Architecture of the RBF network**

Number of hidden layers	Number of neurons in the hidden layer	Number of neurons in the output layer	Transfer function of the hidden layers	Transfer function of the output layer	Spread Constant
1	38	1	Radial Basis	Linear	2.3

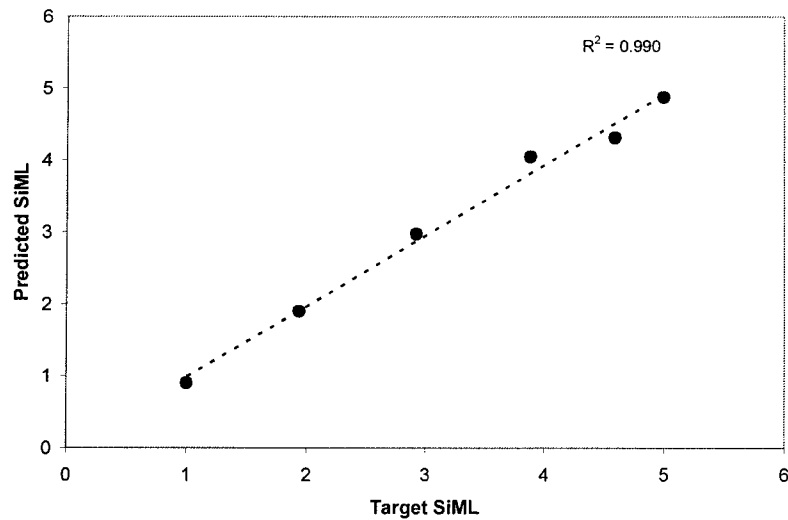


Figure 6.15.: Performance of the MLP network on the test data.

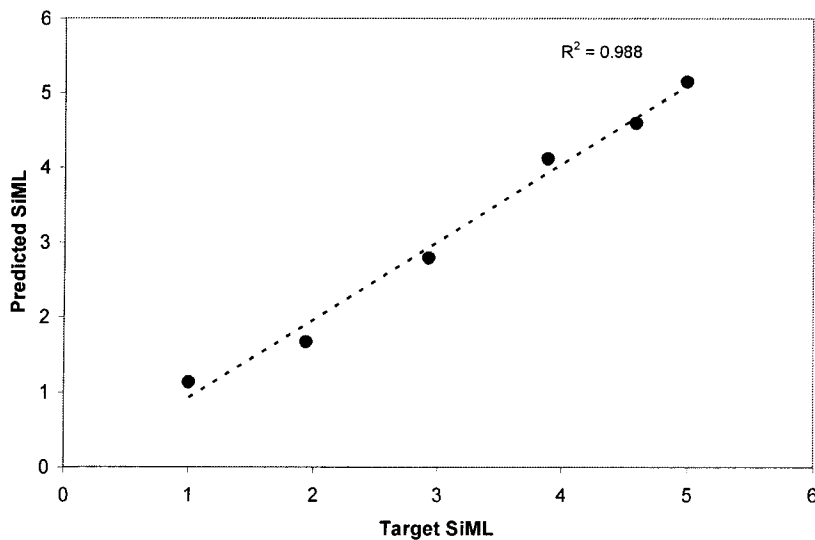


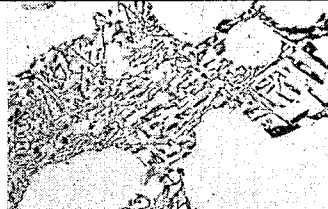
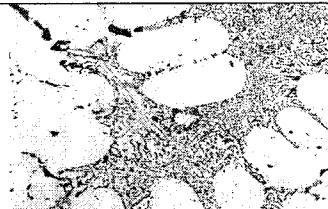
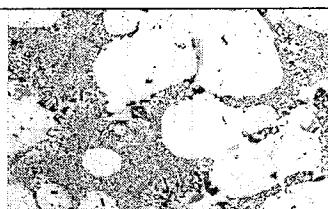


Figure: 6.16. Performance of the RBF network on the test data.

**Table 6.10. Data showing the relationship of the predicted SiML to Sr content and examples of predicted microstructure. (Average Solidification Rate of the test samples = 0.43 +/- 0.057 °C/Sec)**

Sr Level (ppm)	Predicted SiML (MLP)	Predicted SiML (RBF)	Target SiML	Microstructure Magnification: 200x	
8	0.9	1.13	1.0	Fully unmodified microstructure	
38	1.9	1.67	1.94	Lamellar microstructure	
56	2.97	2.79	2.92	Partially modified microstructure	
72	4.04	4.11	3.88	Modified microstructure	
96	4.87	5.15	5.0	Very fine microstructure	

**Table 6.11. Mean Square Error (MSE) comparison of the neural networks with the Multiple Linear Regression and the  $\Delta T$  method.**

	Multilayer Perceptron	Radial Basis Function	Multiple Linear Regression	$\Delta T$ method
MSE	0.02	0.03	0.12	0.002

**Table 6.12. Comparison of the feed-forward neural networks.**

Neural Network	MSE	Training Time (Seconds)
Multilayer Perceptron	0.02	20.77
Radial Basis Function	0.03	2.38

least for the  $\Delta T$  method. However, this method requires information about eutectic growth temperature of the unmodified alloy. The advantage of the ANN approach is that it only requires the TA parameters and does not require any other information. It still provides very high accuracy. This shows that the ANN in conjunction with cooling curve TA software can be used as an on-line quality control tool at the casting plant. The software will act as an advisory system for the foundry men to control the morphology of the eutectic silicon particles. The two feed-forward neural networks developed in this work were compared in terms of the MSE on the test data and the training time. Refer to Table 6.12. It can be seen that the MLP gives the lowest MSE. The training time of the RBF network is much lower than that of the MLP network.

## 6.5 Analysis of the WAP Melt Chemistry

The process capability analysis discussed in Section 6.3.2.1 has shown that with the present level of inherent variations, the WAP process is not capable of producing engine blocks with porosity levels less than s4 (see Figure 6.17 c) 100% of the time. Given the efficiency of degassing process at WAP, and the repeatability of the fill profile of the pump, one major source for the variations in the shrink porosity level could be within the specification variations in the chemical composition. However, the W319 alloy has as many as 24 elements, and the variations of most of the constituent elements were found only at the 2<sup>nd</sup> or 3<sup>rd</sup> decimal point. Therefore, powerful data mining and analysis techniques are needed to identify the elements whose variations significantly influence the variations in the shrinkage porosity level of the engine block bulkhead.

### 6.5.1 The Effect of Melt Chemistry on Casting Porosity

Porosity was measured on bulkhead Sections 4 and 7 of the V6 3.0L engine block was chosen for this analysis (See Figure 6.17). These are the Sections having the highest porosity in the engine block. The X-ray radiography results data file of the south and north rollovers from 2002-03 were filtered to obtain two categories of porosity, i.e., low and high. The porosity level s0 (when both bulkhead Sections 4 &7 have s0 porosity) was assigned to be the low level and the s3 level (when both bulkhead Sections 4&7 have s3 or higher porosity) was assigned to be the high level. The magnitudes of porosity for the

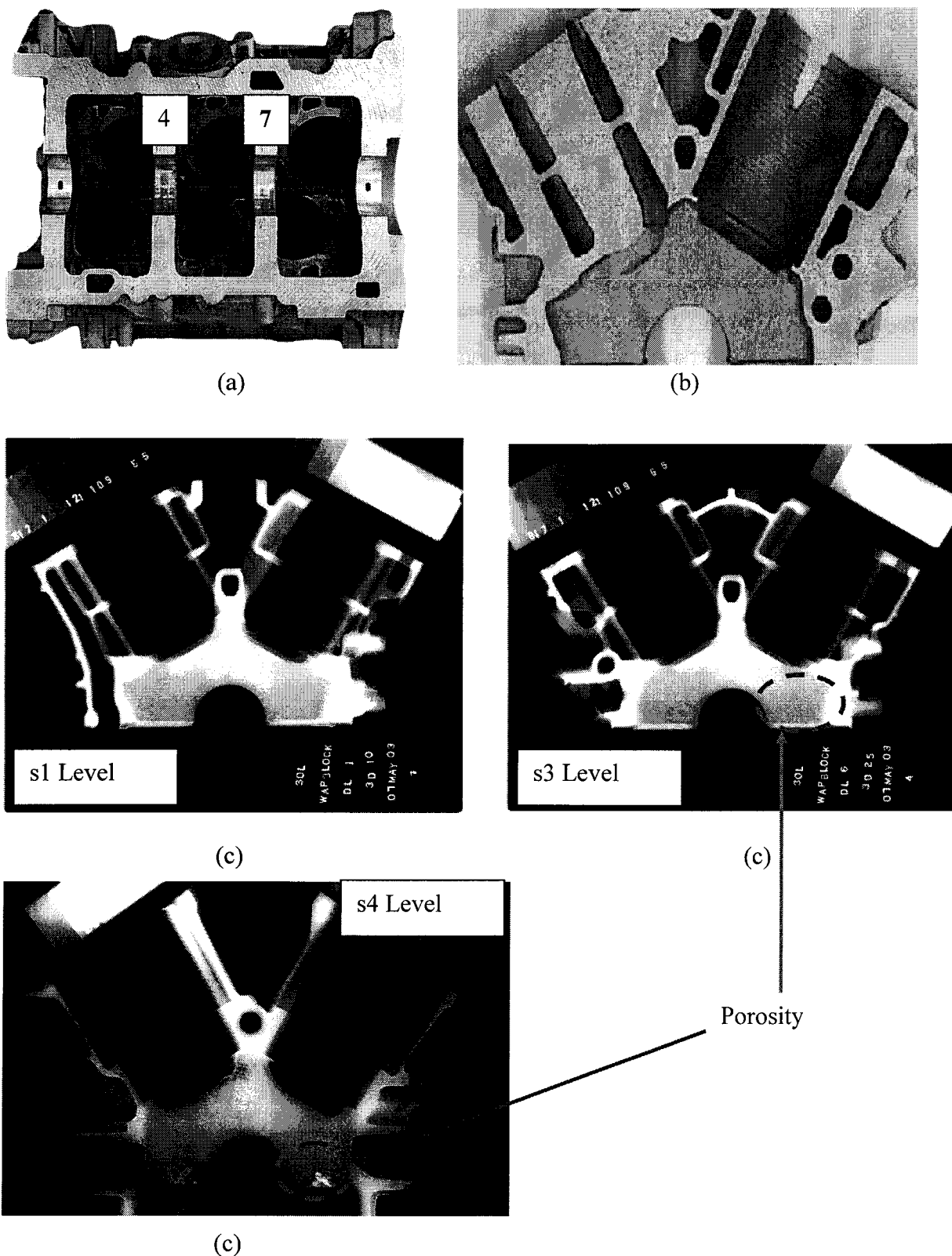


Figure 6.17 : (a) Locations of bulkhead Sections 4 and 7 in the 3.0L V6 engine block, (b) Cross Section view of a bulkhead Section (c) X-Ray Radiographs of bulkhead Sections with porosity levels s1, s3 and s4.



low and high levels were clearly distinct; therefore the effect of chemistry could be quantified.

The time, date of casting, and rollover station of casting of the engine block having a porosity level of either s3 or s0 were then obtained from the pump voltage profile file. This was achieved by matching the serial number of the engine block in the X-ray file with the serial number in the voltage profile file. The chemistry measurement that is closest to the time of casting of the engine block is then assigned as the melt chemistry of the engine block in question. The melt chemistries of the engine blocks with low and high porosity levels were then tested using the 2 sample student t-test to determine if their sample means were significantly different from each other. (For example, are the sample means of the silicon levels of the engine blocks with low and high porosity levels significantly different from each other?). The null hypothesis of the test is that the sample means are equal. The 2 sample student t-test for each element in the W319 Al alloy showed that Fe and Mn are the only 2 elements whose sample means are significantly different from each other under low and high porosity conditions. The results of the 2 sample t-test for Fe and Mn are outlined in Tables 6.13 and 6.14, respectively. It can be seen that the 95% confidence interval of the sample mean differences does not include zero. This means that there is a significant difference between the sample means of Fe and Mn in the low and high porosity levels.

To further investigate the effect of Fe and Mn, the descriptive statistics of the Fe and Mn data were computed. This is shown in Table 6.15. The literature (Dash and Makhlof, 2001 and Lucas et al., 2004) reported that in Aluminum-Silicon alloys there exists a very strong interaction between Fe and Mn and they form an intermetallic compound  $Al_{15}(MnFe)_3Si_2$  together. To study the effect of this interaction on porosity, the data was split into four groups and the frequency of the high and low porosity events in each case was counted. The counting was accomplished by using the multiple condition filtering technique in Excel®. The boundary points for the separation between the four groups were established using the  $Q_1$  and  $Q_3$  limits for Fe and Mn (see Table 6.15). The results are tabulated in Table 6.16. The Table shows that when the Fe level is  $>0.358$  wt.%, the number of events of low porosity are more than that of high porosity. On the other hand, when the Fe level  $<0.358$  wt.%, the trend is exactly the opposite.

**Table 6.13: Minitab output of the 2 sample t-test for Fe in the engine blocks with low and high levels of porosity**

	Number of Samples	Mean	Standard Deviation	Standard Error of the Mean
Fe (low porosity)	49	0.3639	0.0104	0.0015
Fe (high porosity)	55	0.3536	0.0101	0.0014

$H_0: \mu_1 = \mu_2$ ; where  $\mu_1$  and  $\mu_2$  are the sample means of the composition of Fe in engine blocks with high and low levels of porosity.

95% Confidence Interval for  $(\mu_1 - \mu_2)$ : (-0.01429, -0.00631)

**p-value = 0**, Degree of Freedom = 102

**Table 6.14: Minitab output of the 2 sample t-test for Mn in the engine blocks with low and high levels of porosity**

	Number of Samples	Mean	Standard Deviation	Standard Error of the Mean
Mn (low porosity)	49	0.24647	0.00665	0.00095
Mn (high porosity)	55	0.24165	0.00802	0.0011

$H_0: \mu_1 = \mu_2$ ; where  $\mu_1$  and  $\mu_2$  are the sample means of the composition of Mn in engine blocks with high and low levels of porosity.

95% Confidence Interval for  $(\mu_1 - \mu_2)$ : (-0.00771, -0.00193)

**p-value = 0.001**, Degree of Freedom = 102

**Table 6.15: Descriptive Statistics of the Fe and Mn for low and high porosity levels**

	Number of Samples	Mean	Median	Standard Deviation	Minimum	Maximum	Q1	Q3
Fe (low porosity)	49	0.3639	0.3640	0.0104	0.3411	0.3898	0.3582	0.3701
Fe (high porosity)	55	0.35362	0.35350	0.01012	0.33300	0.38770	0.34780	0.35780
Mn (low porosity)	49	0.24647	0.24580	0.00665	0.2312	0.2605	0.24250	0.25080
Mn (high porosity)	55	0.24165	0.24120	0.00802	0.21700	0.25750	0.23640	0.24560

Q1 and Q3 are the first and third quartiles of the data . 50% of the data lie between the Q1 and Q3 (interquartile range).

**Table 6.16: Events of low and high Porosity in the four groups with different Fe and Mn levels.**

<b>Group 1</b>		<b>Group 2</b>	
Fe > 0.358 wt.% Mn > 0.245 wt.%	High Porosity Events:9	Fe > 0.358 wt.% Mn < 0.245 wt.%	High Porosity Events:3
	Low Porosity Events:24		Low Porosity Events:13
<b>Group 3</b>		<b>Group 4</b>	
Fe < 0.358 wt.% Mn > 0.245 wt.%	High Porosity Events:6	Fe < 0.358 wt.% Mn < 0.245 wt.%	High Porosity Events:37
	Low Porosity Events:4		Low Porosity Events:8

It is well known from the literature that high Fe levels increase the porosity in the casting (Samuel et al., 2001, Dash and Makhlof, 2001, and Lucas et al., 2004). However, the present work shows that the number of events of high porosity also increases when the Fe level is  $<0.358$  wt%. This indicates the possibility that there could be an optimum Fe level where porosity will be at a minimum. This finding is consistent with that as reported by Taylor et al. (1999a), who proposed a model for Fe related porosity formation in Al-5Si0.5Mg1Cu castings. It has been suggested that at low Fe contents the Si eutectic forms ahead of the  $\beta$ -Al<sub>5</sub>FeSi. At high iron concentrations,  $\beta$ -Al<sub>5</sub>FeSi forms first and then the Si eutectic nucleates on these large platelets blocking the feeding of the interdendritic regions. Between these low and high Fe contents, there exists a “critical Fe level” where the porosity is at a minimum. At the critical Fe level many small eutectic grains nucleate on small  $\beta$ -Al<sub>5</sub>FeSi platelets and thereby the most permeable semisolid structure is obtained.

It should be mentioned that *by high Fe level* the literature means Fe concentrations greater than 0.9 wt%. There are no studies reported in the literature that deal with such a narrow range of Fe concentrations as studied in this dissertation. Group 1 and Group 4 are compared through a bar graph in Figure 6.18. For Group 1, (When Fe  $>0.358$  wt.% and Mn  $>0.245$  wt.%), 73% of the total number of events are low porosity events. Conversely, for Group 4, (When Fe  $<0.358$  wt.% and Mn  $<0.245$  wt.%), 82% of the total number of events are high porosity events. This means that if the melt has a Group 1 chemistry of Fe and Mn, there is a probability of 0.73 that it will give a low porosity casting, whereas, if the melt has a Group 4 chemistry there is a probability of 0.82 that it will result in a high porosity casting. Therefore, Group 1 is a safer zone to operate in, while Group 4 is a greater risk. This study demonstrated that even very small scale changes in the Fe content will bring about significant changes in the porosity level of the casting. The effect of Mn on its own is not significant, but the interaction between Mn and Fe is significant. This agrees with what has been reported in the literature. It should also be kept in mind that the bulkhead chemistry may be to some extent different from the melt chemistry (OES) due to the segregation effects during the solidification process.

The Fe and Mn contents of the castings with high and low porosity are plotted in a scatter plot in Figure 6.19. This plot enables the creation of an operating window of low

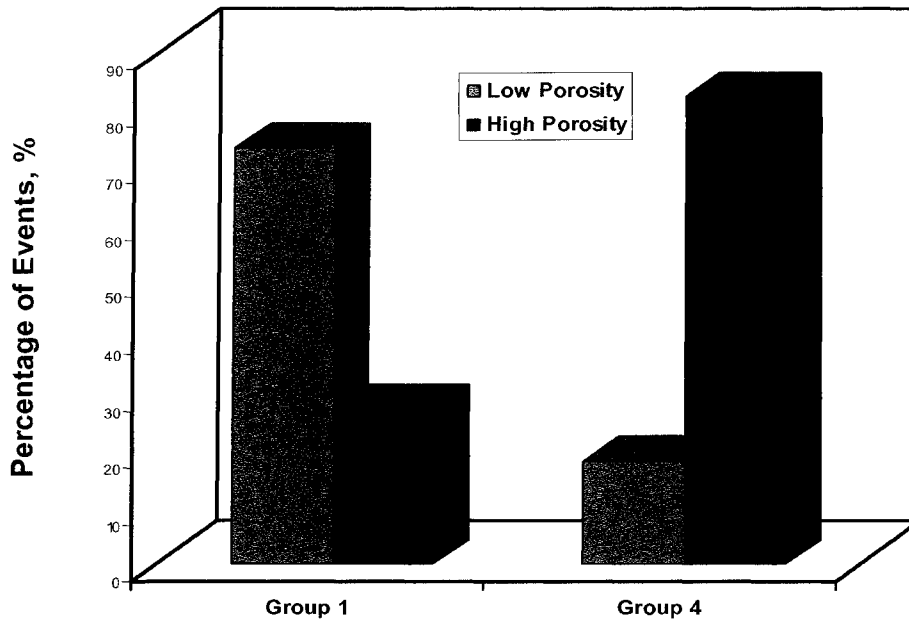


Figure 6.18: Comparison of the percentages of high and low porosity events in Group 1 and Group 4.

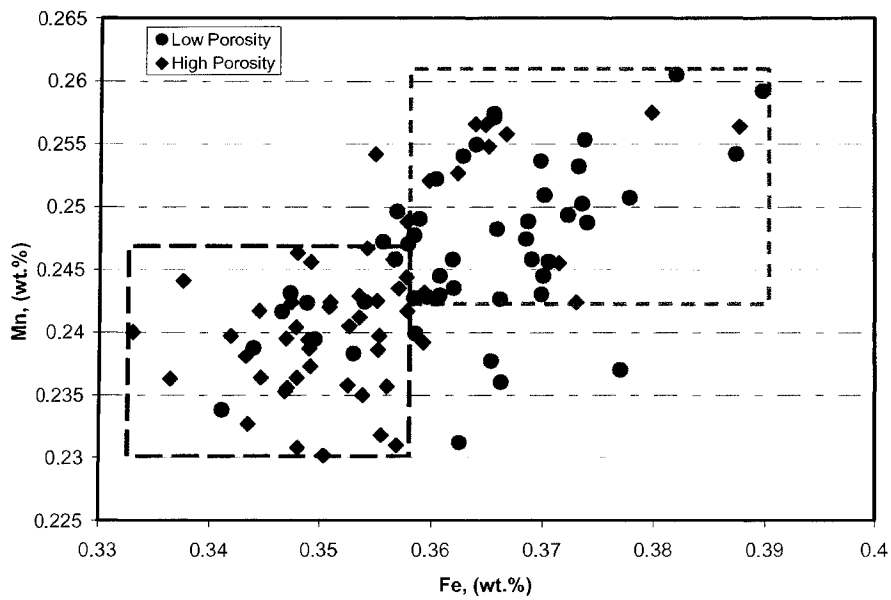


Figure 6.19 : Scatter Plot between Fe and Mn contents of the high and low porosity castings from the north and south rolover stations. Please note the operating window for the low porosity castings.

porosity so that the aim will be to set up the control limits of the melt chemistry (for Fe and Mn) during the production at WAP. The operating window of low porosity for Fe is from 0.36 to 0.39 wt.% and for Mn is from 0.24 to 0.26 wt.%. There exists a certain degree of overlap between scatter points in the high and low porosity regions. This may be due to the fact that other factors such as degassing, filling, and melt cleanliness could also be influential on the shrink porosity. In addition to this some adherent uncertainties of the X-Ray data could also be a factor.

In order to confirm the above results, periods of high and low porosity were selected from the shrinkage graph of the south rollover for 2003 (See Figure 6.20). The average Fe and Mn contents for these periods are given in Table 6.17. It can be seen from Table 6.17 that when the shrink porosity levels are lower, the average chemistry of Fe and Mn falls within the levels specified by the operating window for low porosity in Figure 6.19. On the other hand, when the porosity levels are high, the average Fe and Mn levels are within the region for high porosity in Figure 6.19. The maximum Fe level encountered in this study was 0.39 wt.%. However, according to Taylor et al. (1999b) the optimum Fe content for an Al alloy, with a Si content similar to that of the W319, the critical Fe content is ~0.5 wt.%. Therefore, more investigation is required in order to determine the optimum level of Fe and Mn in the W319 alloy that will potentially result in low porosity castings.

#### **6.5.1.1 Image Analysis of the TA Samples with High and Low Levels of Fe and Mn**

Image Analysis using LOM and SEM was performed on two W319 TA test samples with high and low levels of Fe and Mn. The average compositions of Fe and Mn present in these samples are given in Table 6.18. The photographs of these samples with the locations of the samples for Image Analysis are shown in Figure 6.21. The morphology of the Fe based phases were measured (refer to Section 4.5.2) for both the samples and the summary of these measurements is presented in Table 6.19. It can be seen from Table 6.19 that the area and perimeter of the Fe based phases of sample A are 35.8% and 35.3%, respectively, higher than that of sample B. This is expected as the Fe content of sample A (0.41 wt%) is higher compared to sample B (0.35 wt.%). The LOM micrographs representative of the microstructures of samples A and B are shown in Figure 6.22 and Figure 6.23.

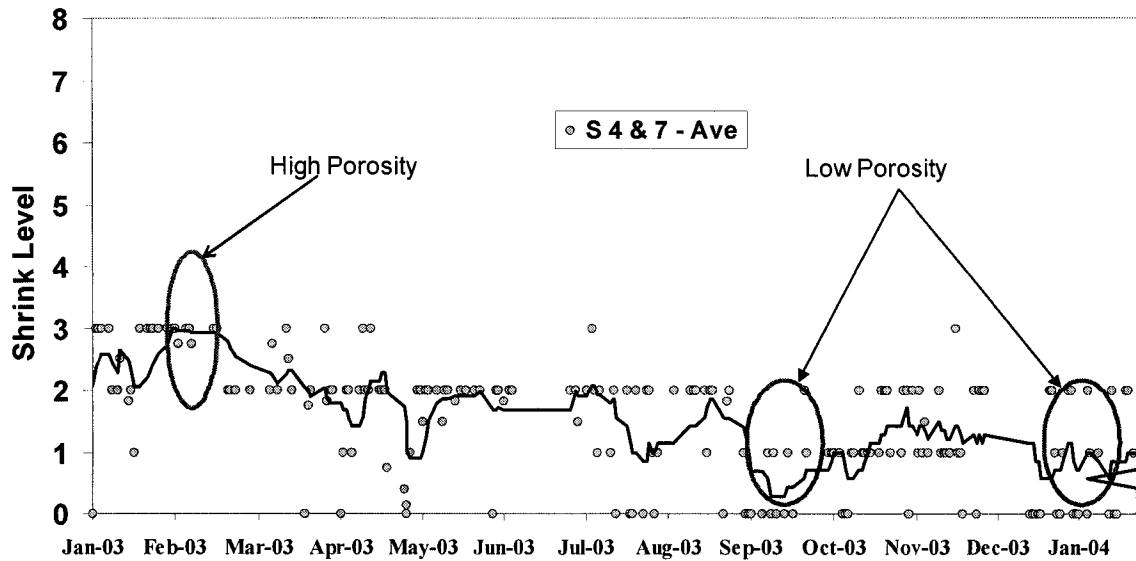


Figure 6.20: Shrinkage graph of bulkhead Sections 4 and 7 of the 3.0L engine blocks, produced in the south rolover during 2003.

**Table 6.17: Periods of high and low porosity and the corresponding average Fe and Mn contents.**

Period	Porosity Level	Average Fe, (wt.%)	Average Mn, (wt.%)
February 17-28, 2003	High	0.3512	0.2460
September 15-30, 2003	Low	0.3665	0.2489
January 1-20, 2004		0.3657	0.2431

**Table 6.18: Average Fe and Mn compositions of the W319 TA test samples that were used for Image Analysis.**

Sample	Fe, (wt.%)	Mn, (wt.%)
A	0.41	0.27
B	0.35	0.24

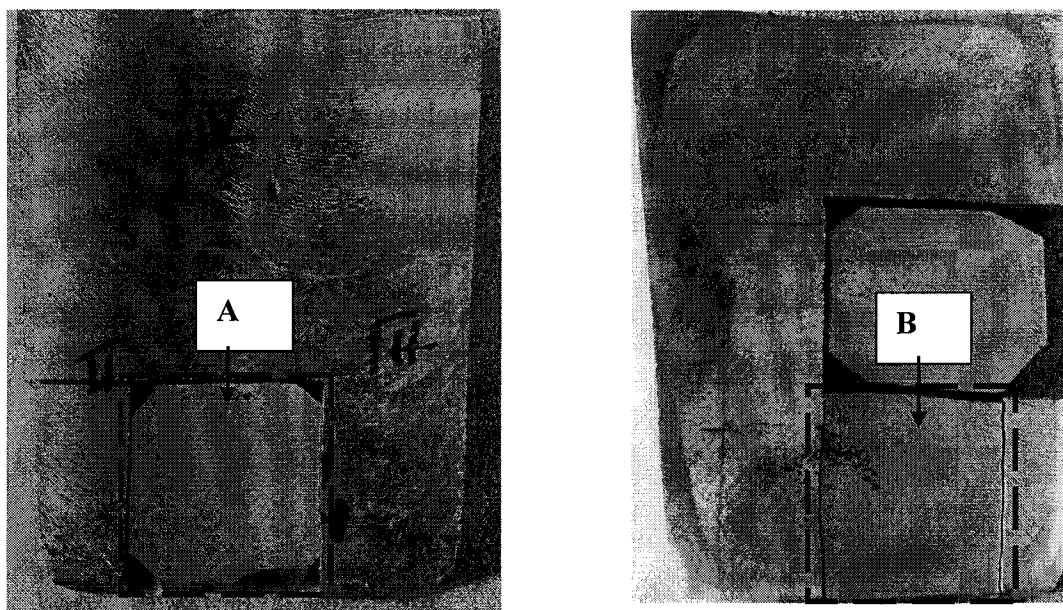


Figure 6.21: TA test samples A and B with the locations of the Image Analysis samples. The Image Analysis samples are shown within in the dashed lines and are taken from identical locations in samples A and B.

**Table 6.19: Measurements of the morphology of the Fe based phases present in the TA samples with high (A) and low (B) Fe and Mn contents.**

Sample ID		Area ( $\mu\text{m}^2$ )	Perimeter ( $\mu\text{m}$ )
A	Average	8942.88	4126.78
	Standard Deviation	3147.82	1426.04
B	Average	6585.12	3048.12
	Standard Deviation	2859.74	1322.92



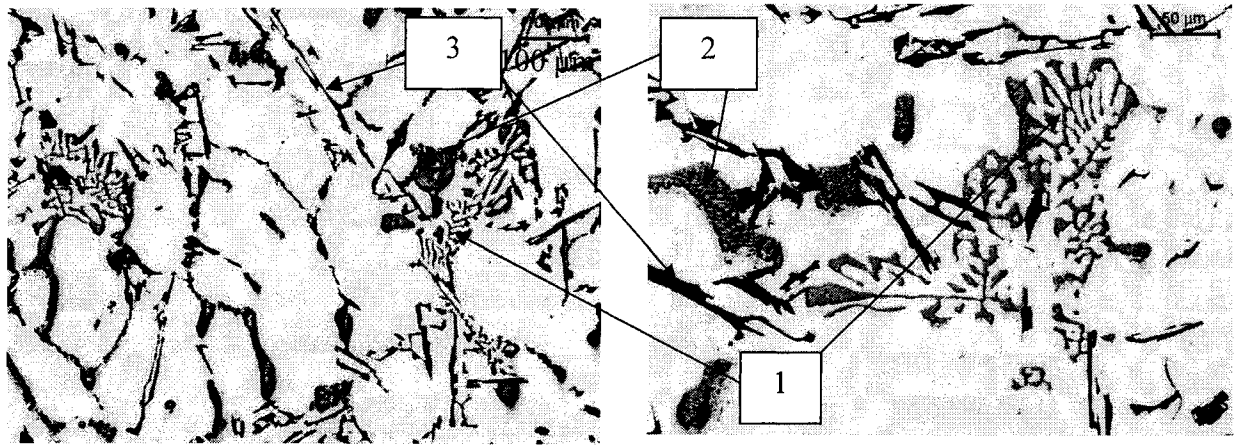


Figure 6.22: LOM micrographs showing the microstructure of Sample A (Fe=0.41 wt.% and Mn=0.27 wt.%): (1) Fe rich Chinese script phases, (2) Cu rich phases, (3) Unmodified flaky eutectic silicon phase.

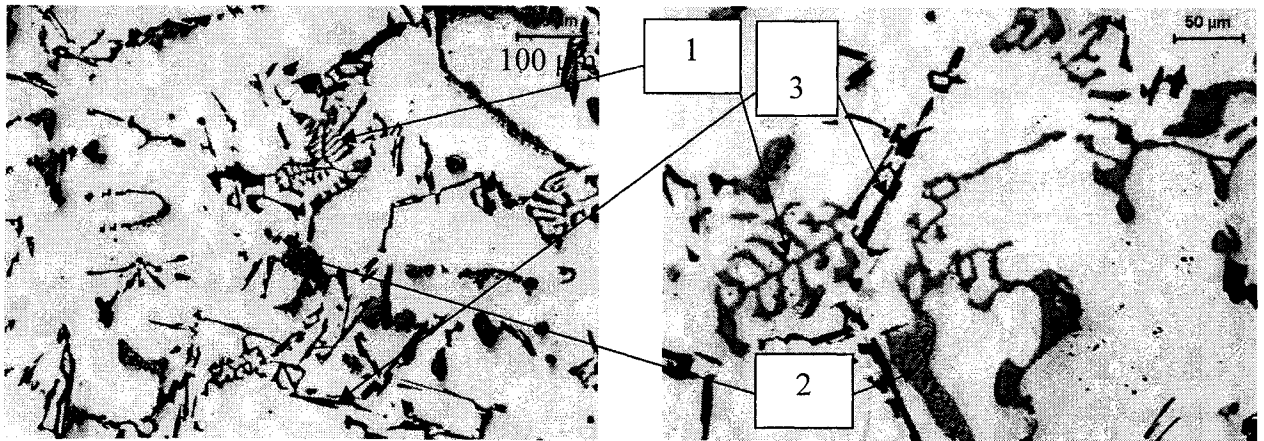


Figure 6.23: LOM micrographs showing the microstructure of Sample B (Fe=0.35 wt.% and Mn=0.24 wt.%): (1) Fe rich Chinese script phases, (2) Cu rich phases, (3) Unmodified flaky eutectic silicon phase.

### **6.5.2 Effect of Melt Chemistry on the Hardness and Heat Treatability of the Engine Block**

The Brinell Hardness (HB) values after TSR and Artificial Aging of the bulkheads for the V6 3.0L engine block produced at WAP during the month of October 2003 were below the lower limit of specification (85 HB). These engine blocks were called “soft blocks” (see Figure 6.24). The major objectives of this study were (1) to determine the root cause of the low hardness problem and to relate it to WAP’s TSR and Artificial Aging (AA) processes and (2) to provide WAP management with corrective actions to be taken that will render the required casting characteristics under Ford’s Engineering specifications. In order to achieve these goals and to solve this problem the following methodology was adopted.

1. Statistical Analysis of the relationship between WAP melt chemistry and the block hardness after the TSR and Artificial Aging Treatments.
2. Extensive Thermal Analysis (heating and cooling curve) runs of the test samples extracted from the bulkhead of the soft engine blocks and establishment of the relationship between the start temperature of alloy melting ( $T_m$ ) to the alloy chemical composition.
3. Simulations of the TSR and Artificial Aging processes at WAP using UMSA in order to understand the effect of these treatments on soft engine block samples.
4. Image Analysis of the UMSA test samples and test samples from WAP after TSR and Artificial Aging.
5. Matrix Micro hardness measurements for the as cast UMSA test samples as well as for the simulated TSR and Artificially Aged UMSA test samples.

#### **6.5.2.1 Statistical Analysis of the Relationship between Engine Block Bulkhead Hardness and the Chemical Composition**

The statistical analysis was then performed to identify those elements that have the strongest influence on the bulkhead hardness after TSR and Artificial Aging. Stepwise Regression was used for this analysis. This procedure iteratively adds or removes variables at each step of the regression. The criterion for adding or removing variables at any step is done by the partial F-test (Montgomery, 1999). This analysis was performed

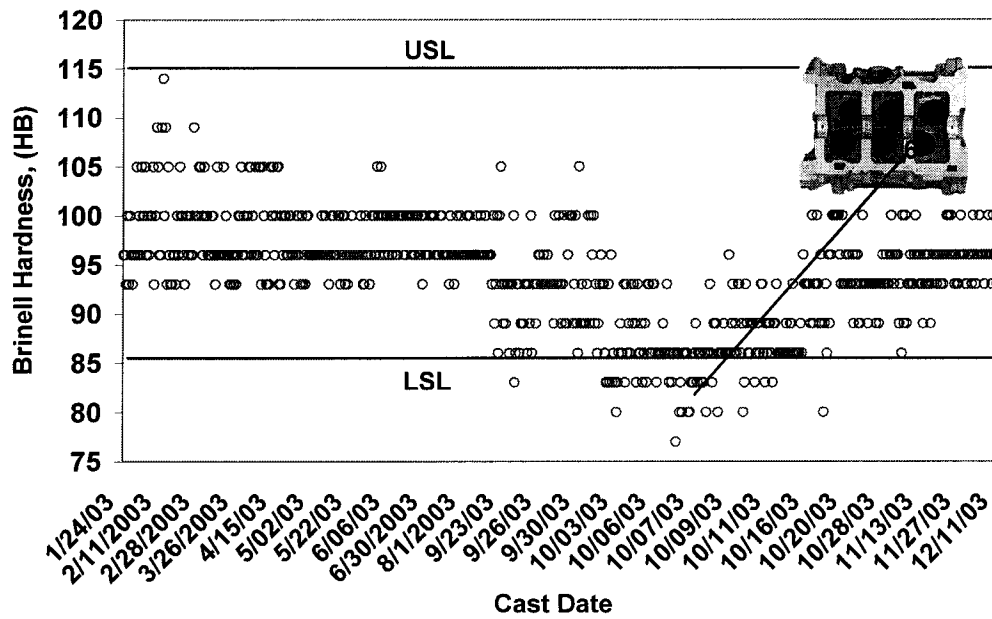


Figure 6.24: Brinell Hardness (After TSR and Artificial Aging) map of the hit location 6 (shown in the inset) of the V6 3.0L engine blocks during 2003. LSL and USL are the upper and lower specification limits of the hardness respectively.

using the Minitab Statistical Software. Average chemistries from 24 days and the corresponding average daily bulkhead Brinell Hardness after TSR and Artificial Aging were used for this analysis. The analysis shows that Sn ( $p$ -value=0) and Pb ( $p$ -value=0.003) are the two elements that have a significant effect on the Brinell Hardness. The time series plots of the Sn and Pb levels of the W319 alloy during 2003 are shown in Figures 6.25 and 6.26 respectively. It can be seen from these time series plots and from Figure 6.24 that the Sn and Pb were at elevated levels during the period when the soft blocks problem occurred. The relationship between Sn, Pb and hardness value after TSR and Artificial Aging was established using the Multiple Linear Regression analysis.

$$\mathbf{HB=97.52-134.44Pb-204.60Sn} \quad \mathbf{R^2=0.77} \quad \mathbf{(6.21)}$$

According to the above equation, for the lowest levels of Sn (0.0019 wt.%) and Pb (0.0111 wt.%), HB=95.6, while for the highest analyzed levels of these impurity elements (Sn=0.0388 wt.% and Pb=0.0297 wt.%), HB=85.7. This is in excellent agreement with the WAP measured HB data.

Another technique to combine the effects of Pb and Sn, is by the use of Silicon Equivalency ( $Si_{EQ}$ ). The Silicon Equivalency of Sn and Pb was calculated using the formula as given below:

$$\mathbf{Si_{EQ}(Pb \& Sn)=0.859Pb+0.0297Pb^2+0.7849Sn -0.0313Sn^2} \quad \mathbf{(6.22)}$$

The relationship between the  $Si_{EQ}$  (Pb&Sn) and the average Brinell Hardness measured on the engine blocks after TSR and Artificial Aging is written as follows:

$$\mathbf{HB=-250.16Si_{EQ} (Pb\&Sn)+99.301} \quad \mathbf{(R^2=0.75)} \quad \mathbf{(6.23)}$$

The statistical analysis has shown that variation in the Sn content has the strongest influence on engine block hardness. The regression equation considering the effect of Sn alone is written as follows:

$$\mathbf{HB =94.254-197.54Sn;} \quad \mathbf{R^2=0.73} \quad \mathbf{(6.24)}$$

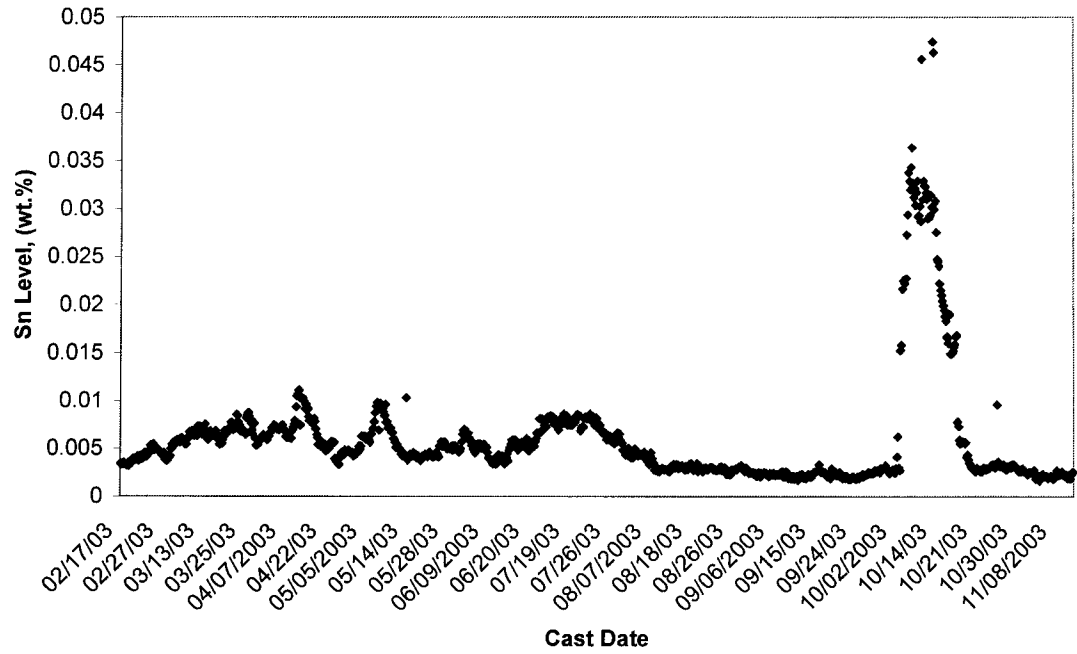


Figure 6.25: Variations in the level of Sn during 2003.

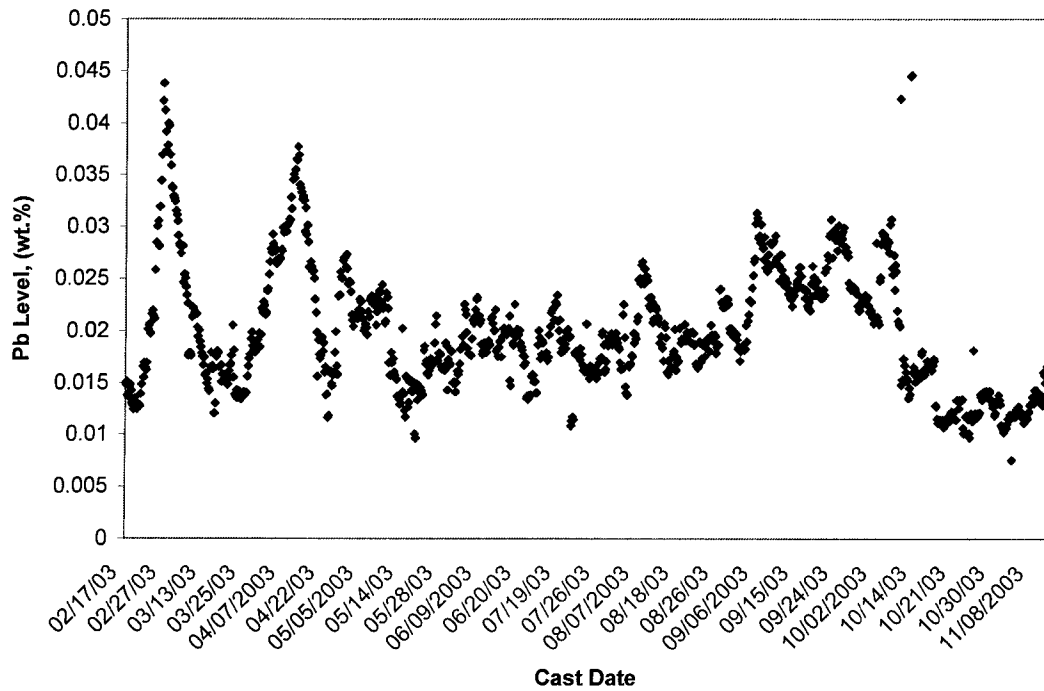


Figure 6.26: Variations in the level of Pb during 2003.

### **6.5.2.2 Thermal Characterization of the Soft Engine Block Samples**

UMSA heating and cooling curve runs were performed on the soft block bulkhead samples under controlled conditions as explained in Section 4.5.1, and the thermal characteristics were computed. Table 6.20 compares the average thermal characteristics of the block samples from Table 6.1, with an average bulkhead hardness value of 98.75 HB (standard deviation=3.65), and the thermal characteristics of a soft block sample with a bulkhead hardness value of 80 HB. It can be seen from Table 6.20 that the thermal characteristics of the blocks with high and low hardness are significantly different from each other. This has demonstrated the ability of the UMSA TA system to identify potential problems.

The relationship between the start temperature of the alloy melting ( $T_m$ ) and the Brinell Hardness of the bulkheads at different Sn levels are plotted in Figure 6.27. It can be seen that high levels of Sn lowers both  $T_m$  as well as the Brinell Hardness of the bulkheads. This result has a direct implication on the WAP TSR process where the temperature is kept at 500<sup>0</sup>C. At higher Sn levels, the WAP TSR process will not render the required minimum hardness of 85 HB.

In connection with the discussion in Section 6.2.1, the start temperature of alloy melting of the ingot samples supplied by suppliers A, B and engine blocks cast using the ingots from supplier C are plotted against their Sn contents (Refer to Figure 6.28). It can be seen the  $T_m$  of the engine blocks cast using the ingots from supplier C is ~4 <sup>0</sup>C below the TSR temperature. Subsequently, the supplier C was contacted to reduce the Sn levels in the alloy to less than 0.0050 wt.%.

### **6.5.2.3 Image Analysis of the WAP Soft Engine Block Bulkhead Samples**

Image Analysis was performed using Light Optical Microscope (LOM) and the Scanning Electron Microscope (SEM) on the following samples having elevated levels of Sn and Pb: (a) Bulkhead samples after TSR and Artificial Aging from WAP, (b) UMSA samples extracted from the bulkhead of the engine block that are remelted and solidified 3 times under controlled conditions (c) Bulkhead samples following simulated

**Table 6.20: Comparison of the average characteristic reaction temperatures ( $^{\circ}\text{C}$ ) of an engine block with low bulkhead hardness (Pb=0.016 wt.%, Sn=0.047 wt.%) and engine blocks with high bulkhead hardness (Pb=0.023 wt.%, Sn=0.0069 wt.%).**

Reaction Number	Name of the Reaction	Block with High Hardness	Block with Low Hardness
		Std Dev	Std Dev
1	Beginning of the alloy melting, ( $T_m$ )	505.6	495.06
		0.5	0.6
2	End of alloy melting process	625.1	609.8
		3.9	0.6
3	Beginning of the nucleation of the Al dendrites	608.7	597.4
		0.3	0.3
4	Dendrite Coherency Point (DCP)	602.9	592.4
		0.7	0.9
5	Beginning of the nucleation of the Al-Si eutectic	568.2	563.1
		0.4	0.4
6	Beginning of the nucleation of the Cu enriched phases	499.8	494.9
		0.5	0.9
7	End of the alloy solidification	442.0	436
		2.9	2.4

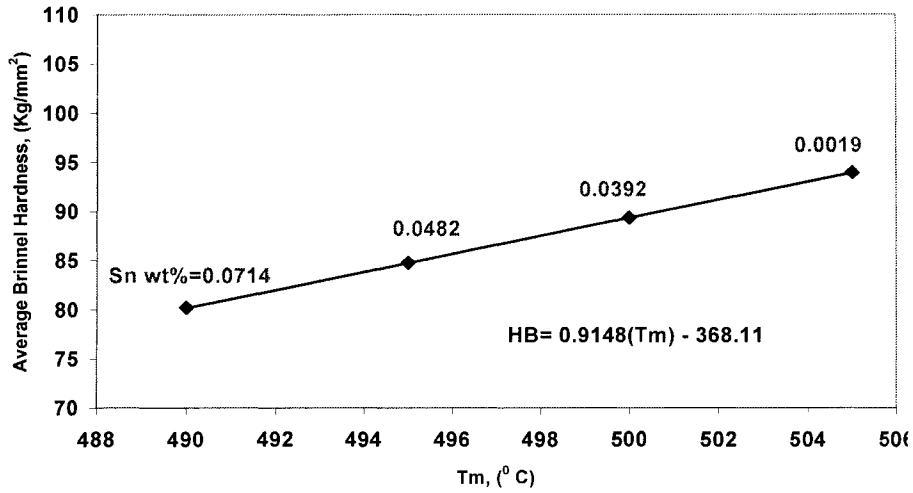


Figure 6.27: Statistical relationship between the average Brinell Hardness (HB) (after the TSR and AA processes) and the start temperature of the W319 alloy melting process (Tm) for the bulkheads from the 3.0L engine blocks.

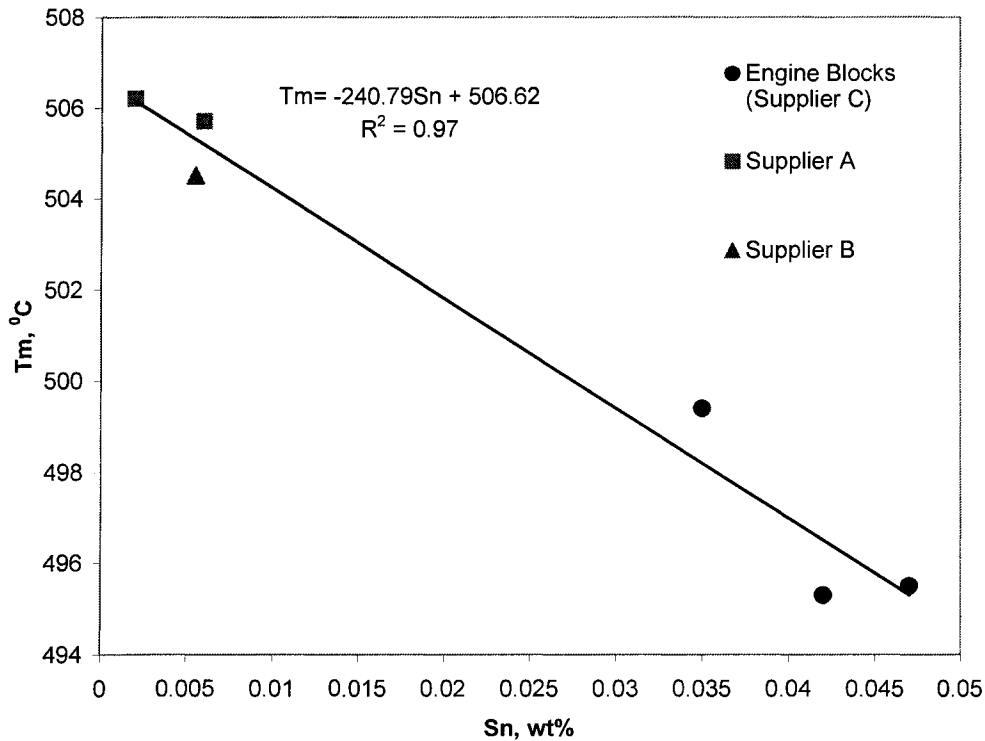


Figure 6.28: Start temperature of the W319 alloy melting process (Tm) versus Sn level (wt.%) for WAP 3.0L engine blocks (cast using Ingots from supplier C) and supplier A as well as supplier B.



TSR and Artificial Aging in UMSA. These samples were solution treated for 4 hours at 500<sup>0</sup>C and then artificially aged at 257-261<sup>0</sup>C for four hours using UMSA. This was done to emulate the WAP TSR and Artificial Aging process at B&W Heat Treating, Kitchener, Ontario.

The micrographs of these samples are shown in Figures 6.29 to 6.32. The as cast bulkhead UMSA sample that is used just for the TA runs (remelted and solidified 3 times) has an unmodified silicon eutectic structure (Figure 6.29). Figure 6.30 shows that there is considerable amount of coarse undissolved Cu based phases having a diameter up to 50  $\mu\text{m}$  in the sample that is obtained from WAP after TSR and Artificial Aging. The eutectic Si present in this sample has an unmodified flaky structure because the alloy has residual amount of Sr only. The SEM micrograph of this sample in Figure 6.31 shows the presence of a droplet of Pb and Sn inside a cavity of 45 $\mu\text{m}$ . Figure 6.32 shows that the sample that was subjected to the simulated TSR and Artificial Aging in UMSA has a partially modified eutectic Si structure. This suggests that the higher levels of Sn enhance the thermal modification of Si. The microstructure in Figure 6.32 shows that most of the Cu based phases dissolved in the matrix after Solution Treatment and Artificial Aging. The undissolved copper phases are present as semi-globular particles. This is a direct contrast to the sample that underwent the actual TSR and Artificial Aging operations at WAP as shown in Figure 6.30. This is due to the fact that, since the UMSA samples are in direct contact with the heat for a longer period of time; therefore a better heat transfer and Solution Treatment was obtained in comparison with the sample from the actual TSR process.

#### **6.5.2.4 Matrix Microhardness Measurements of the Engine Block Samples with Elevated Levels of Sn and Pb**

The matrix microhardness measurements (HV 25) were made on the simulated TSR , Artificially Aged samples as well as on the as cast samples used for the TA runs in UMSA. The results are plotted in Figure 6.33. The following observations were made from this graph:

1. The matrix microhardness of the as cast test samples with elevated levels of Sn and Pb are similar to that of a W319 casting with a residual amount of Sn and Pb

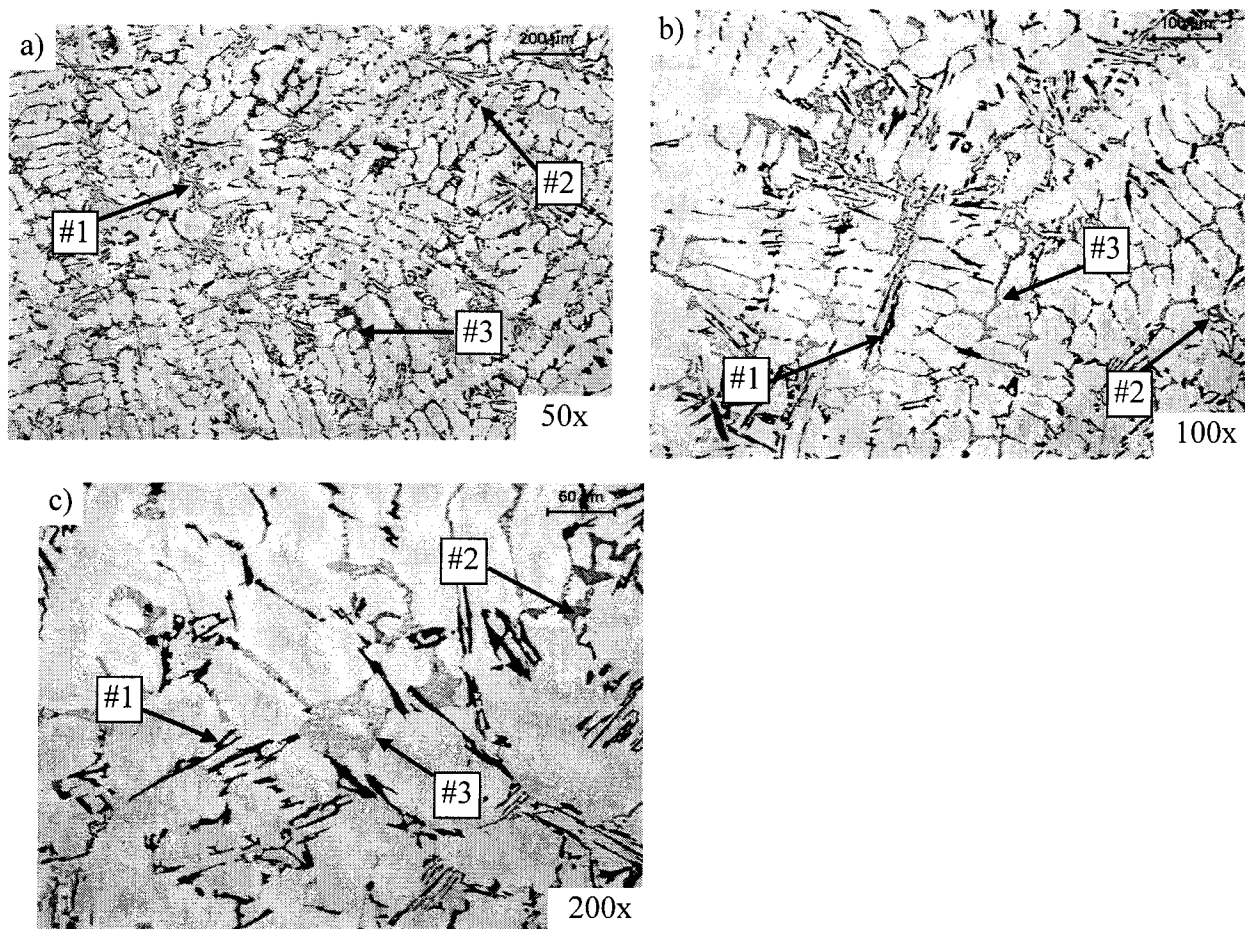


Figure 6.29. Light Optical Microscope (LOM) micrographs of the WAP 3.0L engine block bulkhead (ID: 952351) (Pb: 0.016 wt.%, Sn: 0.047 wt.%) melted and solidified three times under UMISA controlled conditions. The cooling rate during solidification was 0.75°C/s.

a, b, c) As cast unmodified microstructures. Note: Si phase (#1), Fe based phase (#2) and fine Cu rich phase (#3).

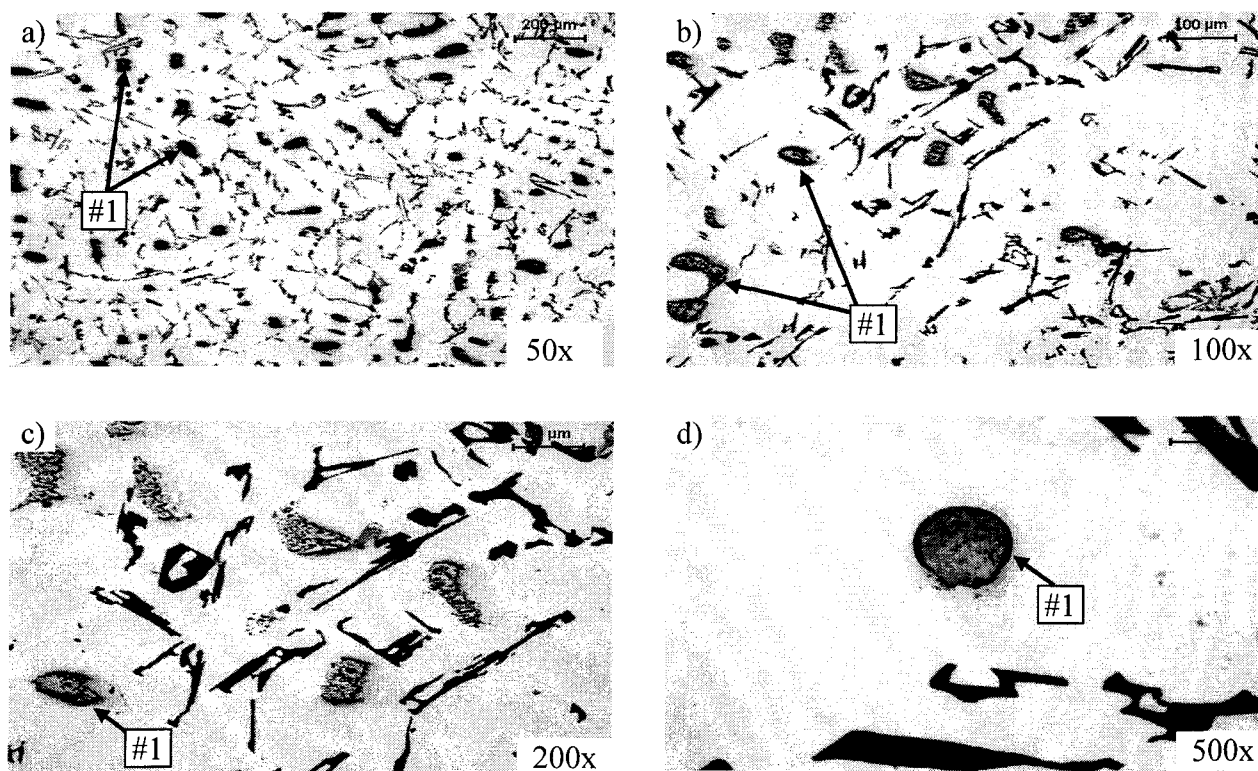


Figure 6.30. Light Optical Microscope (LOM) micrographs of the WAP 3.0L engine block bulkhead subjected to WAP TSR at 494-505°C and to AA at 257-261°C for approximately 4 hrs (ID: 952351) (Pb: 0.016 wt.%, Sn: 0.047 wt.%).

- a) A considerably large volume fraction of undissolved Cu rich phases (#1).
- b, c) Higher magnifications revealed “dendritic-like” structure of the Cu rich phases (#1). In some areas dissolution of the Cu rich phases is in progress and is visible.
- d) A higher magnification of the single globular Cu rich phase (#1) up to 20µm in diameter.

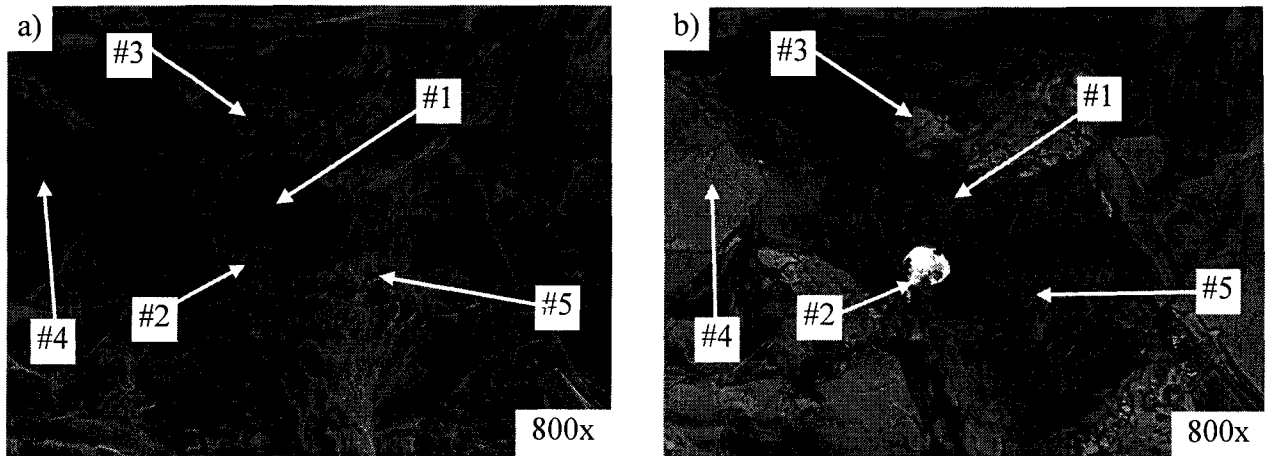


Figure 6.31. Scanning Electron Microscopy (SEM) micrographs of the WAP 3.0L engine block bulkhead subjected to the WAP TSR at 494-505°C and to AA at 257-261°C for approximately 4 hrs each (ID: 952351) (Pb: 0.016 wt.%, Sn: 0.047 wt.%).

Note: Void (#1) approximately 45 $\mu$ m in diameter containing Pb and Sn based particles (#2) approximately 15 $\mu$ m in diameter. The void was most likely caused by microscopic incipient melting of the Cu rich phases during the WAP TSR process. The void is surrounded by Cu rich phases (#3), Fe based phases (#4) and the Al matrix (#5).

- a) Secondary Electron Image (SE).
- b) Back Scattered Electron Image (BSE).

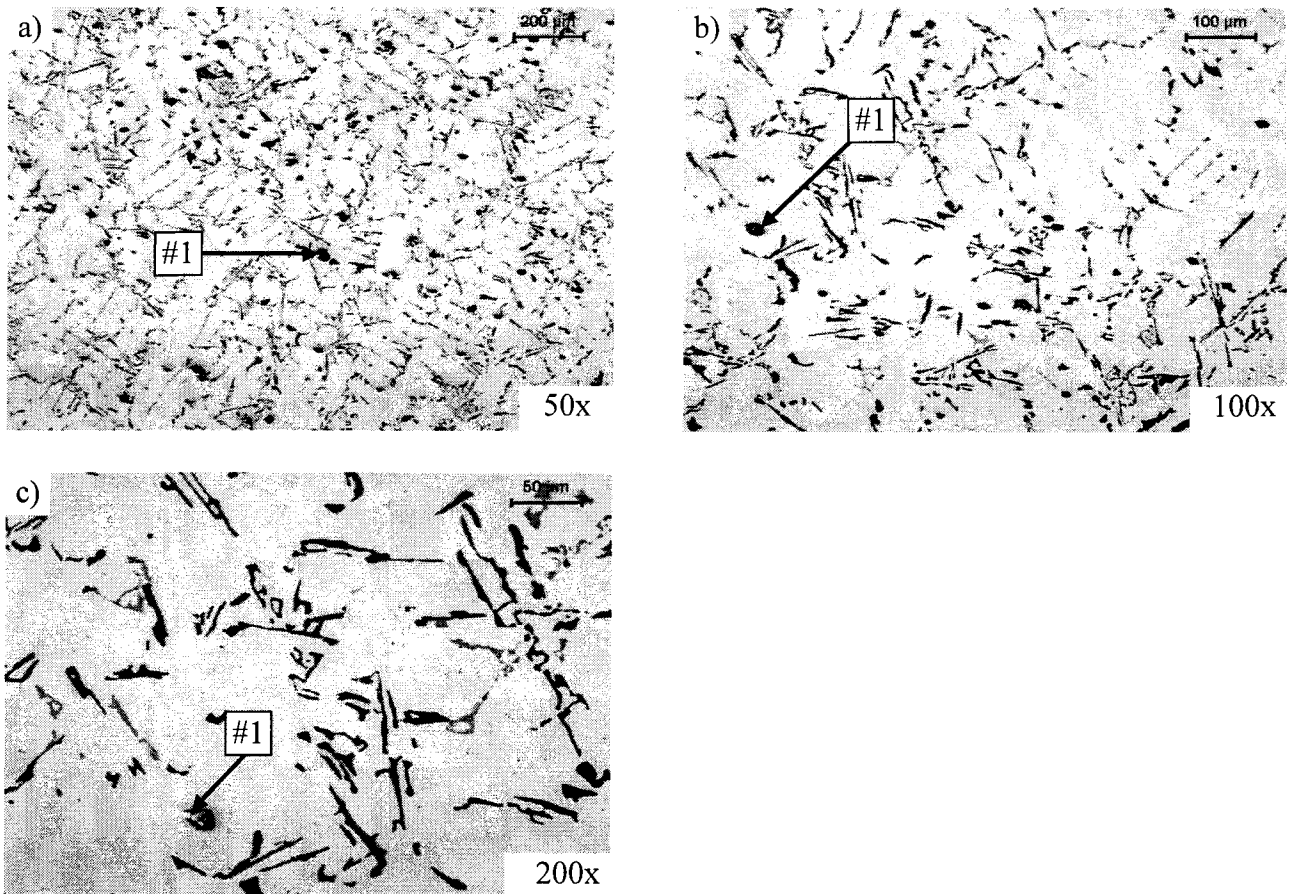


Figure 6.32: Light Optical Microscope (LOM) micrographs of the WAP 3.0L engine block bulkhead (ID: 952351) (Pb: 0.016 wt.%, Sn: 0.047 wt.%) remelted three times under UMSA controlled conditions and subjected to the simulated TSR at 500°C and to AA at 257-261°C for approximately 4 hrs.

- a) Numerous Cu rich phases with globular shapes (#1) are evident.
- b, c) A higher magnification of the remelted Cu rich phases during the simulated TSR process (#1).

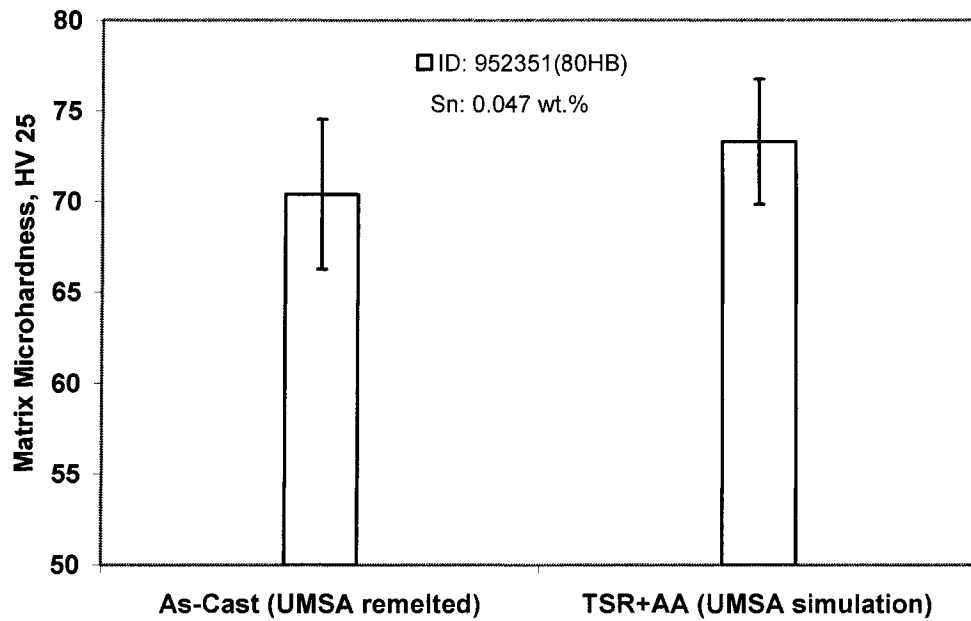


Figure 6.33: Comparison of the Vickers Microhardness measurements of the as cast bulkhead test samples that were remelted and solidified three times using UMSA and the bulkhead test samples that were subjected to simulated TSR and Artificial Aging using UMSA .

( $64.5 \pm 6.5 \mu\text{HV}$ ). The measurements of the matrix microhardness of W319 alloy with residual amounts of Sn and Pb are given by Chen (2003).

2. The matrix microhardness increases by approximately 15% after the simulated TSR and Artificial Aging treatments.

Chen (2003) reported that in the case of the W319 alloy having residual amounts of Sn (40 ppm) and Pb (150 ppm), Solution Treatment followed by two weeks of natural aging increased the matrix microhardness by about 63%. Meanwhile, the present work showed that with elevated levels of Sn and Pb the matrix microhardness increased by only 15% after Solution Treatment and Artificial Aging. Since Cu dissolved well during the Solution Treatment, Sn may be adversely affecting the formation of Cu strengthening precipitates and therefore the hardness has not increased as expected. Saga and Kikuchi (2004) studied the effect of adding small amounts of Sn on the aging response of 1.2%Mg<sub>2</sub>Si-0.5%Si alloy. They noted that the addition of Sn suppresses the precipitation during aging. Sn interacts more strongly with the vacancies than Cu due to its higher diffusion coefficient and occupies the vacancy positions. This delays the diffusion of other solute atoms and thereby suppresses the precipitation during aging.

In the light of the above discussion it is evident that the present chemical composition specification limits are too lax and even within the specification variation would result in changes in hardness and porosity levels. Therefore, there is a need to revise the existing control limits for the major and minor alloying elements in the W319 alloy used at WAP. These limits were revised using 120 chemical compositions corresponding to sound castings with required HB from the regular production at WAP. These upper and lower control limits (3 sigma limits) were calculated using the equations for the control chart for the mean (Mitra, 1993).

The revised control limits for the major and minor alloying elements are given in Table 6.21. The existing in process chemistry specification at WAP is given in Table 6.22. Table 6.22 shows that the existing specification would tolerate up to 1000ppm of Sn and Pb, but it can be seen that when the Sn and Pb levels were around 400 ppm and 250 ppm, the bulkhead hardness of the engine blocks were reduced considerably. In the case of Sn and Pb, the revised control limits suggest a maximum Sn content of 50 ppm and a

**Table. 6.21: The revised control limits for the major and minor alloying elements**

Element	Si	Cu	Fe	Mn	Mg	Zn	Ni	Pb	Sn
UCL	7.7	3.6	.4	.26	.31	<.17	<.03	<.02	<.0047
LCL	7.4	3.4	.36	.24	.27				

UCL: Upper Control Limit

LCL: Lower Control Limit

**Table:6.22:The existing in process chemistry specification at WAP**

Element	Si	Cu	Fe	Mn	Mg	Zn	Ni	Pb	Sn
UCL	7.8	3.7	<.4	.3	.35	<.25	<.1	<.1	<.1
LCL	7.0	3.3		.2	.25				



Pb content of 200 ppm. This would result in a HB of 93 according to equation 6.21. This is 8 divisions above the lower limit for HB (ie. 85). The existing specification allows for any Fe level less than 0.4 wt.% since Fe is considered as an impurity element. However, the results from Section 6.5.1 have shown that the number of events of high porosity increases when the Fe content goes below 0.358 wt.%. Therefore, the revised control limits suggests a LCL of 0.36 wt.% for Fe.

## **6.6 Analysis of the Electromagnetic Pump Performance and Reliability**

### **6.6.1 Reliability Studies of the Pump**

Reliability by definition is the “probability of a product performing its intended function for a stated period of time under certain specified conditions” (Mitra, 1993). The IRC, since its inception, was actively involved in improving the performance and reliability of the electromagnetic pump. For instance, in 1999, WAP eliminated the pump clogging problem after successfully implementing the following IRC recommendations:

- (a) Reduction of the Ti levels in the alloy to a maximum of 0.1 wt.%, which avoided the precipitation of insoluble Al-Ti-Si crystals in the pump nozzle (Sokolowski et al., 2000).
- (b) Elimination of chlorine degassing and Sr master alloy addition procedures so that the formation of chlorine rich compounds and oxides of Sr was minimized. Most of the pump residue resulted from the formation of these two compounds (Sokolowski et al., 2003). As a result, the lives of the pumps were increased from 6,000 castings sometimes even up to a maximum of 88,000 castings.

The main objectives of the reliability studies of the pump were (a) to identify the statistical distribution that the pump life time follows and (b) to optimize the preventive maintenance time of the pump based on the Mean Time Between Failures (MTBF) calculated for the assumed life distribution. MTBF is the mean expected time between two successive failures of a repairable system. The data from the pump maintenance file from 1999 to 2003 was used for this analysis. Until the end of 2001, WAP was following a reactive maintenance policy, where the pumps were replaced only after they went defunct. The life of the pump was unpredictable. They could last anywhere from 1 minute

up to 3 to 4 months, sometimes installing 2 or 3 in a row until the one that worked was found. One of the frequent failure modes of the pump was the leaking of the melt through the fixed insert into the magnetic U-pole pieces and so causing their damage. A fixed insert is a ceramic component of the pump through which the aluminum enters the sand mold (See Figure 6.34). U-pole pieces are magnetic parts of the electromagnetic pump that serve as carriers of the magnetic flux. Each U-pole piece costs \$23,586. In a year WAP used to lose an average of 10 U-pole pieces due to bleeding through the fixed inserts. The life of the fixed ceramic insert is normally distributed with a mean life of about 50,000 castings. The normal probability plot for the life of the fixed insert is shown in Figure 6.35. The failed pumps are rebuilt in the pump room by replacing their damaged parts with new ones.

Before 2002, the pumps were rebuilt with the used fixed inserts if these inserts were not damaged last time. If the fixed insert had already been consumed to make say, 42,000 castings with the previous pump, the probability of a catastrophic failure of this insert increases exponentially after 8,000 castings were made with the new pump. This will considerably shorten the life of the newly rebuilt pump. The pump life times were found to be exponentially distributed with an MTBF of 19,055 castings during this period. The frequency histogram of pump failures, exponential probability plot and the reliability function plots of the pump life before 2002 are shown in Figures 6.36, 6.37 and 6.38 respectively.

Since the beginning of 2002, the maintenance policy of the pump was changed to preventive maintenance. According to this policy, the pumps were always rebuilt with new ceramic fixed inserts. After rebuilding, the new pumps were recirculated 5,000 times at the Nematik Engineering Centre (NEC). Recirculation means just pumping aluminum for “seasoning” the new fixed insert. This was done to avoid the increased level of head deck porosity that is common with new fixed inserts. The pumps are then installed into regular production at WAP. They are recalled for preventive maintenance after 40,000 castings were made, regardless of whether they failed or not. Thus the pumps have pumped aluminum 45,000 times before being sent for rebuilding. After preventive maintenance the pump life times were found to follow an extreme value distribution with an MTBF of 43,094 castings. The histogram of pump failures, the extreme value

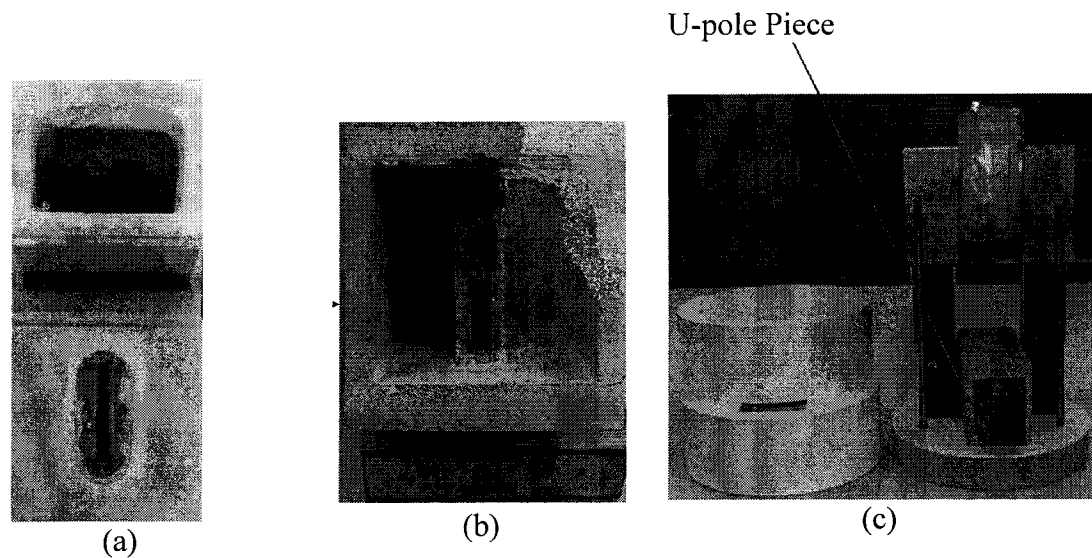


Figure 6.34: Photograph showing (a) a fixed ceramic insert (b)the inside of a leaked fixed ceramic insert and (c) the U-pole piece positioned inside the fixed ceramic insert.

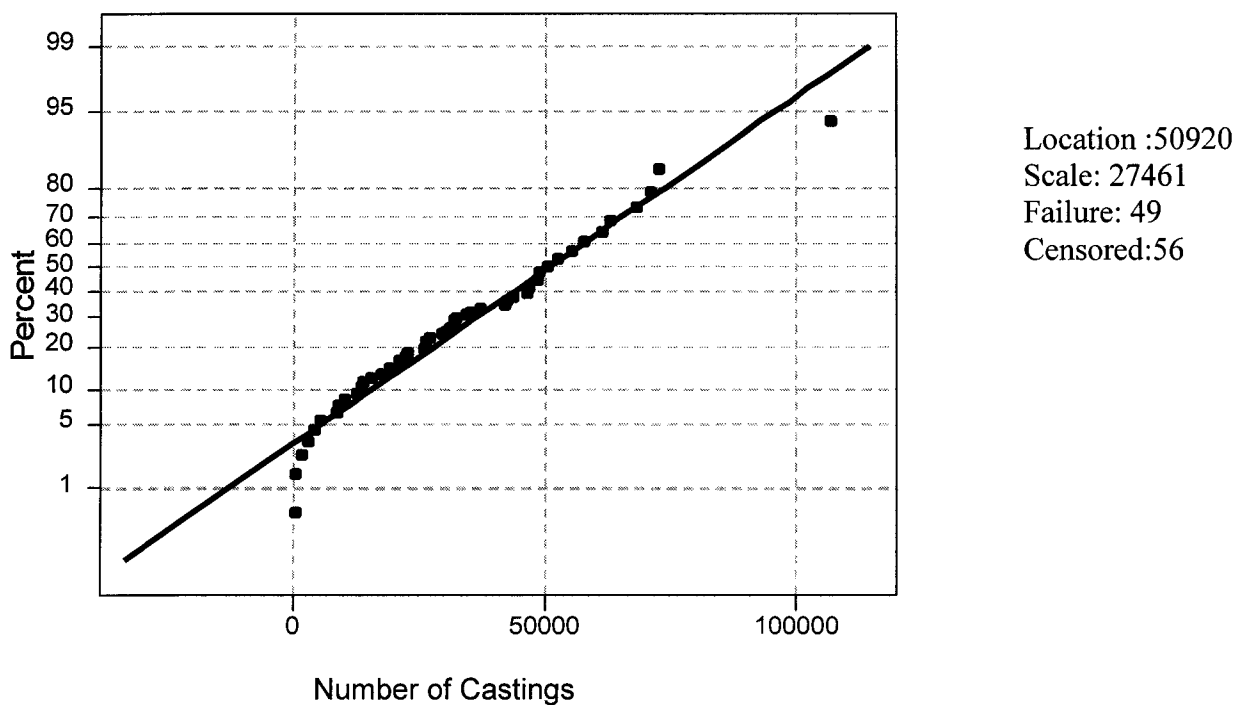


Figure 6.35: Normal probability plot for the life time of the fixed ceramic insert.

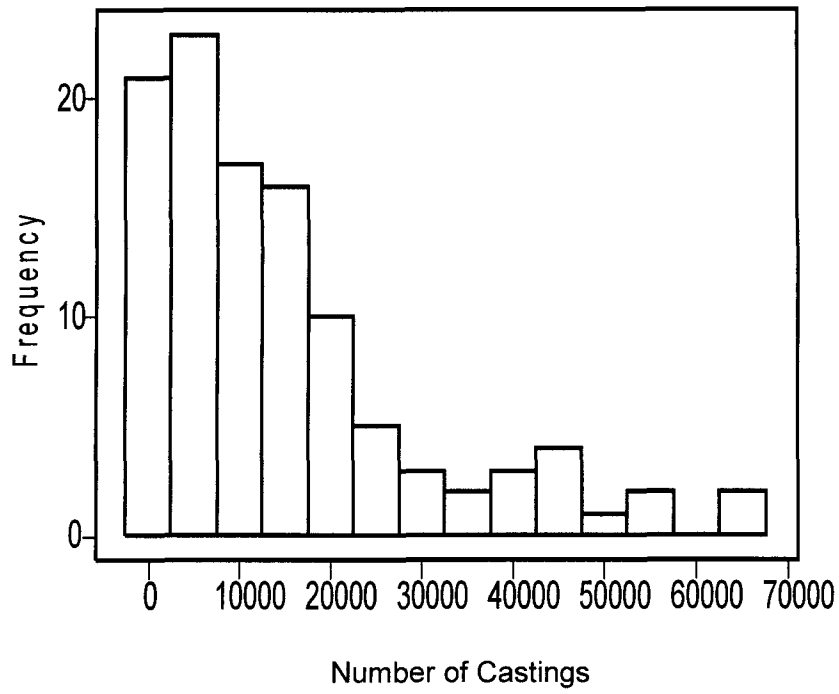


Figure 6.36: Frequency histogram of the pump failures prior to 2002.

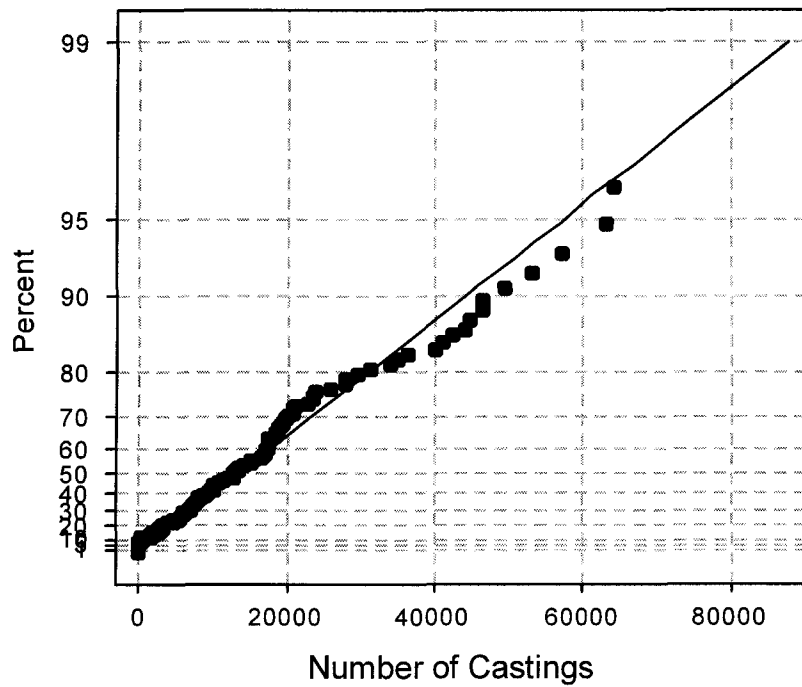


Figure 6.37: Exponential probability plot of the pump life time prior to 2002.

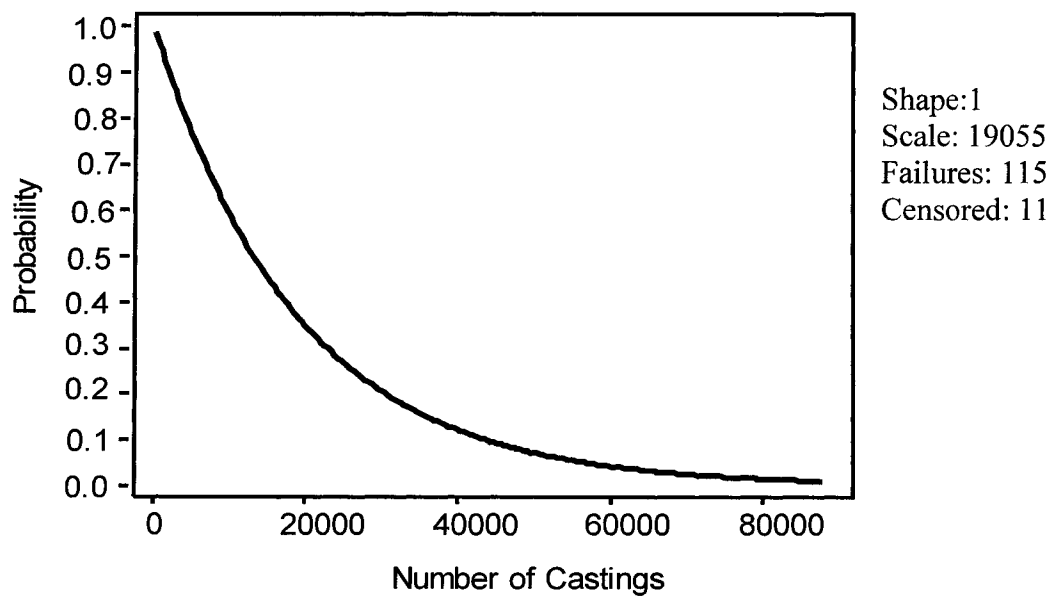


Figure 6.38: Reliability function plot of the pump life prior to 2002.

probability plot and the reliability function plot of the pump life during the period 2002-2003 are plotted in Figures 6.39, 6.40 and 6.41 respectively. It can be seen that as a result of the new preventive maintenance policy the MTBF of the pumps increased from 19,505 to 43,904 castings (a 225% increase) and the reliability of the pumps at MTBF increased from 0.37 to 0.57. Consequently, the total number of pumps could be reduced from 15 to 6.

#### **6.6.1.1 Calculation of the Cost Savings as a Result of Preventive Maintenance**

The cost of losing 10 U-pole pieces in an year = \$235,860.

WAP makes on an average 800,000 castings in a year.

The average number of fixed inserts that would be required without the preventive maintenance policy for 3 rollovers =  $(800,000/50,000) * 3 = 48$ .

The average number of fixed inserts that would be required with the preventive maintenance policy for 3 rollovers =  $(800,000/40,000) * 3 = 60$ .

The additional cost of the fixed inserts for preventive maintenance =

$(60 - 48) * \$1254.38 = \$15,052.56$ , where, the amount \$1,254.38 is the price of a fixed insert.

Therefore, the net savings per annum =  $\$235,860 - \$15,052.56 = \$220,807.44$ / year.

#### **6.6.1.2 Optimization of the Preventive Maintenance Time of the Pump**

According to the present preventive maintenance routine, the pump pumps the melt 45,000 times before going for maintenance (40,000 times in production and 5,000 times during recirculation). However, it can be seen from the reliability analysis that the MTBF of the pump is only 43,904 castings. This means that the present preventive maintenance time exceeds the MTBF of the pump. In order to verify if the number of pump failures increases after the MTBF, the number of pumps failed between specific intervals were counted. Also the number of pump failures predicted by the extreme value distribution for the same intervals was calculated. The results are presented in Table 6.23.

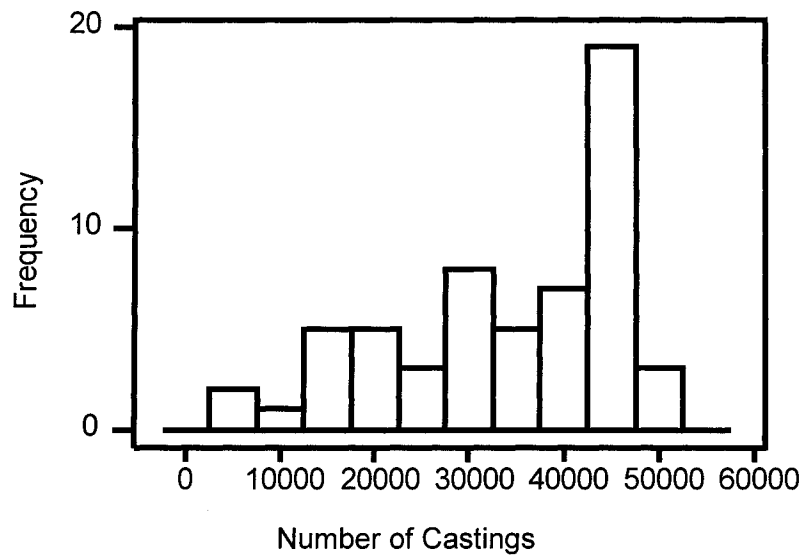


Figure 6.39: Frequency histogram of pump failures during the period 2002-2003.

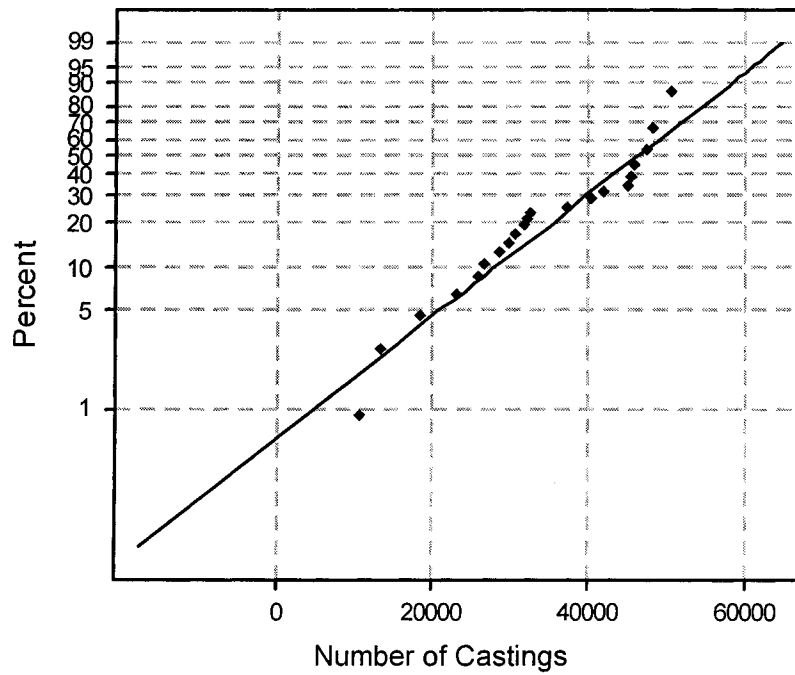


Figure 6.40: Extreme value probability plot of the pump life times during the period 2002-2003.

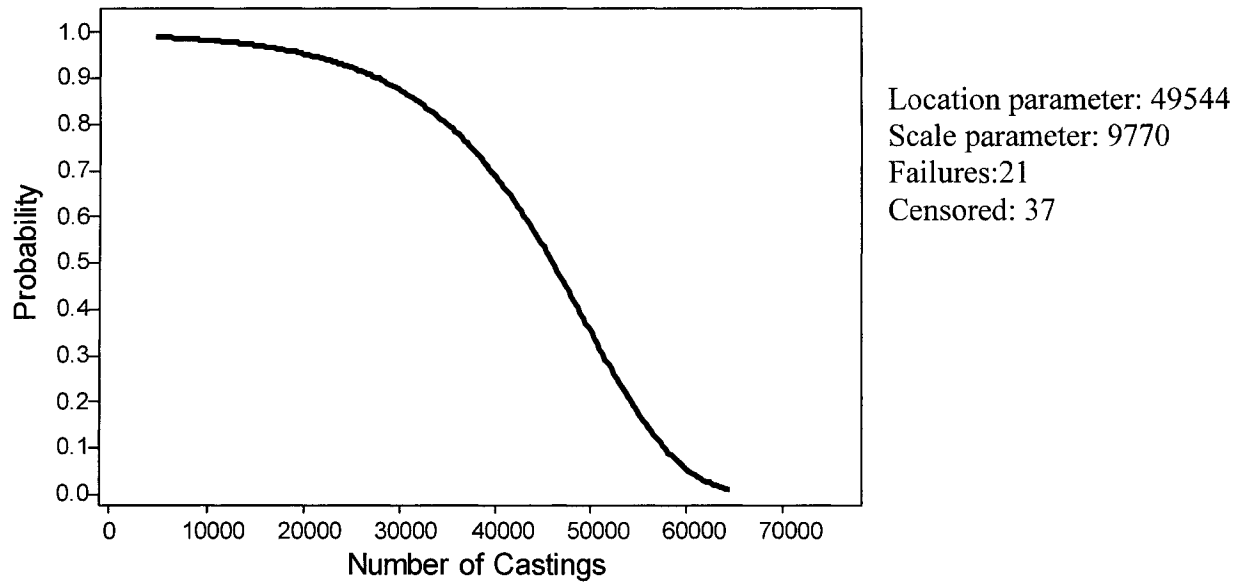


Figure 6.41: Reliability function plot of the pump life time for the period 2002-2003.

**Table 6.23: Comparison between the number of pump failures predicted by the extreme value distribution and the actual number of pump failures.**

Interval (Castings)	Number of Failures Predicted by the model	Actual Number of Failures
0-43000	7	10
43000-45000	3	5
45000-50000	6	6



It can be seen that the number of pump failures increases exponentially after the MTBF. Therefore, the present preventive maintenance time has been revised so that pump will be sent for maintenance after it has pumped the melt 43,000 times (38,000 times in production and 5,000 times during recirculation). The revised preventive maintenance time is optimum because, it is lesser than the MTBF, but at the same time it is not too far from it so that the frequency of maintenance is minimized. The optimum preventive maintenance time is shown in the hazard plot in Figure 6.42.

### **6.6.2 Analysis of the Voltage and Fill Profiles of the Pump**

The voltage and fill profiles of the high and low porosity engine blocks discussed in Section 6.5.1 were compared to find if the filling has any effect on porosity. Figure 6.43 and Figure 6.44 show the fill and voltage profiles of the high and low porosity castings, respectively, subplotted above and below for comparison. No appreciable differences are observed between the high and low porosity profiles in both the Figures. Therefore, it can be concluded that if filling has any effect at all on porosity, that effect is similar on both high and low porosity castings.

## **6.7 Optimization of the Solution Treatment Parameters of the Novel Solution Treatment During Solidification Process Using Artificial Neural Networks and Simulated Annealing Algorithm**

### **6.7.1 Introduction**

The problem of finding the optimal Solution Treatment temperature and time for the NSTS process (see section 2.4.6) is a complex one, because the solution time should be minimized while maximizing the matrix microhardness that is accomplished by minimizing the area percent of undissolved Cu enriched phases. Currently, the optimal parameters are chosen from the available design of experiments (Section 4.6.2). However the experiments were performed at discrete temperatures and times that are spaced relatively far from each other. For example, the Solution Treatment experiments were done at 60 minutes for different discrete temperatures and the next set of Solution Treatment experiments were performed at 120 minutes. There is no information about the in-between times. Although performing more experiments at the in between times, say at

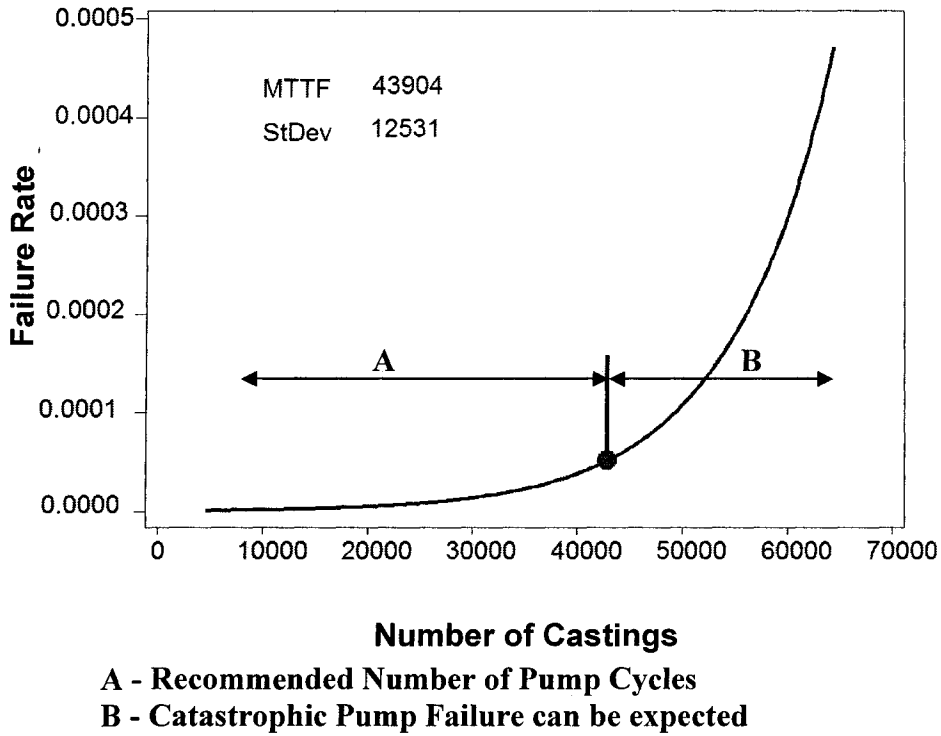


Figure 6.42: The optimum preventive maintenance time shown in the hazard plot for the pump life time.

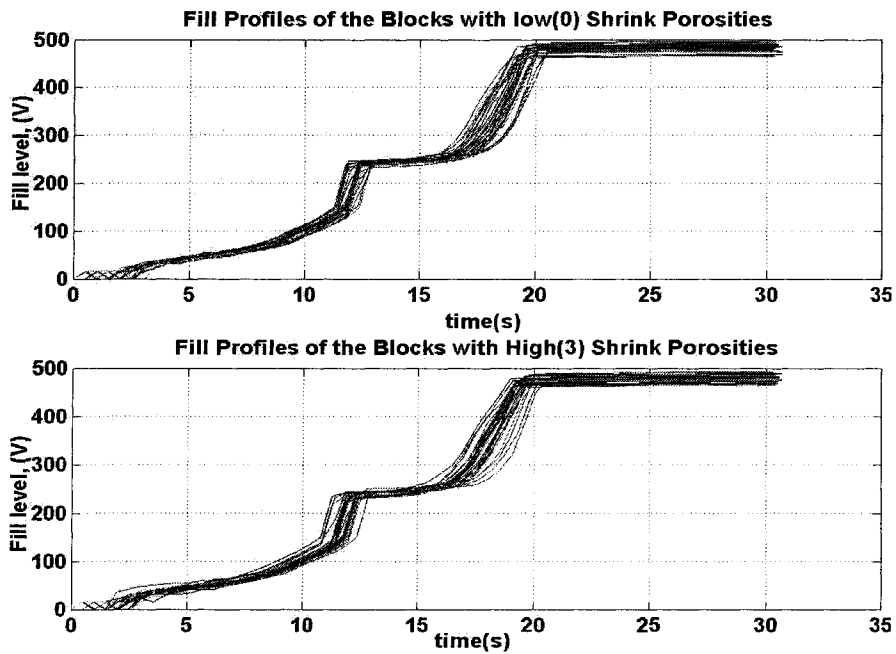


Figure 6.43: Comparison of the fill Profiles of the engine blocks with low and high porosities.

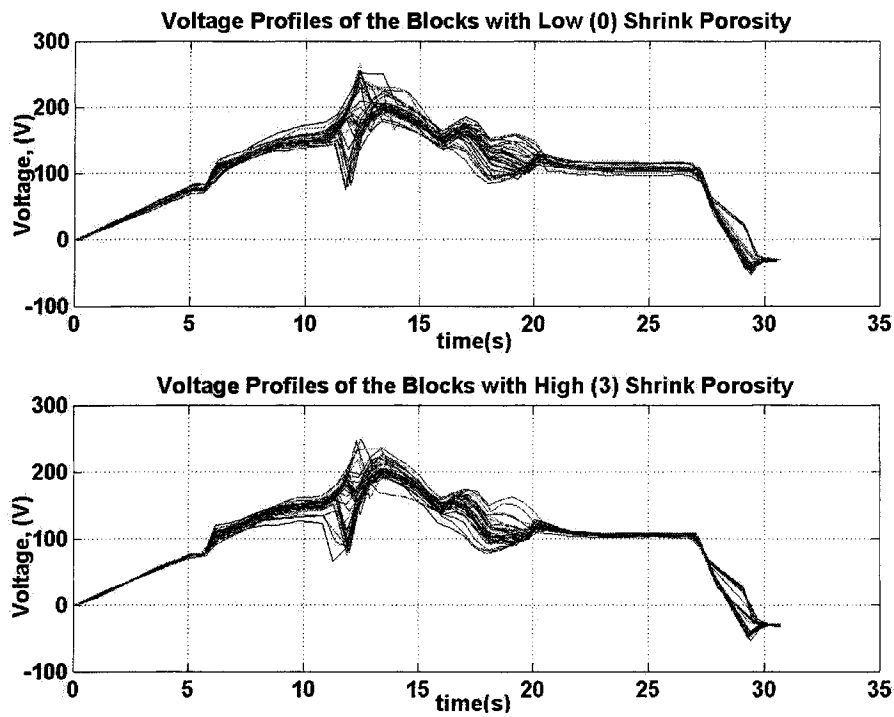


Figure 6.44: Comparison of the voltage profiles of the engine blocks with low and high porosities.

90 minutes, will give more accurate and precise information about the NSTS process, it is not possible from the resources, cost and time perspectives. Another cost effective alternative is to model the NSTS process using the available experimental results so that the microhardness, and area percent of the copper phases at any point within the limits of the experiments can be predicted with minimum error. The Artificial Neural Network (ANN) is one such technique that is used to model nonlinear processes like heat treatment. Modeling the process will provide a continuous solution space. Then a suitable optimization method can be used to search this solution space and to find the optimum solution satisfying the objectives.

### **6.7.2. Steps for the Optimization of the NSTS Process**

The optimization of the NSTS process consists of the following four steps:

1. Experiments for Database Collection.
2. Modeling of the NSTS process using Artificial Neural Networks.
3. Searching for the optimal NSTS parameters using Simulated Annealing Algorithm.
4. Verification of the Optimal NSTS Parameters.

These steps are explained in detail in the following sections:

#### **6.7.2.1 Experiments for the Database Collection**

The experimental procedures for database collection for the development of the neural network model and for the optimization of the Solution Treatment parameters of the NSTS process are presented in Section 4.6.2.

#### **6.7.2.2 Modeling of the NSTS Process Using the Artificial Neural Networks (ANN)**

In order to model the NSTS process, a Multilayer Perceptron (MLP) neural network has been employed (Refer to Section 6.4.3.1). The architecture of the selected MLP network is given in Table 6.24. In this problem, the inputs to the MLP neural network are the time (t) and the temperature (T) of the NSTS process. The outputs of the MLP are the matrix microhardness (HV25) and the area fraction of the Cu enriched

phases of the heat treated specimens. The generalizing ability of the neural network was determined by simulating the network with an unseen dataset (testing set) that is not used for training. The predicted values are compared with the average values measured on the experimental test samples. These values are tabulated in Table 6.25. It can be seen that the Neural Network is able to model the NSTS process accurately.

### **6.7.2.3 Searching for an Optimal Solution Using Simulated Annealing (SA) Algorithm**

The MLP feed forward neural network used here is only able to map the relationship between the input space and the output space. There is another Neural Network model called the Hopfield Network that is used for solving the optimization problems. The MLP neuron and the Hopfield neuron differ from each other in their functional structures (Pharm and Karaboga, 2000). Therefore, in order to find the optimum NSTS parameters, the MLP Network has to be linked to a search algorithm such as Simulated Annealing (SA). The optimum NSTS were found by formulating an objective function and then searching for the minimum value of the objective function using Simulated Annealing algorithm. During the search, the SA algorithm continuously calls up the neural network model to obtain the values of the matrix microhardness and the area percent of the copper based phases, in order to calculate the value of the objective function. The search cannot be progressed further without the neural network providing these values. In other words, the role of the neural network here is that of a constant supplier of matrix microhardness and area percent copper phase values for any random combination of the Solution Treatment temperature and treatment time that are requested by the SA algorithm.

In SA search, it is not required to calculate the gradient unlike traditional nonlinear optimization algorithms. In other words, the function need not be differentiable for the SA search. SA algorithm can escape the local minimum and can reach the global

**Table 6.24: Architecture of the MLP neural network for modeling of the NSTS**

Number of hidden layers	Number of neurons in the hidden layer	Number of neurons in the output layer	Transfer function of the hidden layers	Transfer function of the output layer	Training algorithm
1	6	2	tangent sigmoid	linear	Levenberg-Marquardt

**Table 6.25: Comparison between the matrix microhardness and Area % of Cu Enriched Phases predicted by the neural network and measured on the experimental test samples**

Solution Temperature (°C)	Solution Time (min)	measured Matrix Microhardness (HV 25)	Predicted Matrix Microhardness (HV 25)	Measured Area % of Cu Enriched Phases	Predicted Area % of Cu Enriched Phases
510	240	115.5	117.7	0.26	0.20
540	30	104.0	102.7	0.83	0.81

minimum irrespective of the initial search conditions (Juan et al.,1993, and Tang and Chung, 1995). Also in SA, the solutions need not be converted into binary digits as in Genetic Algorithm (GA). Because of these attractive properties the SA algorithm is employed in this problem to find out the optimal Solution Treatment conditions for the NSTS process.

An objective function has been formulated to achieve the following objectives:

1. The matrix Microhardness of the solution treated and naturally aged specimens is maximized.
2. The area percent of undissolved Cu phases present in the solution treated and naturally aged specimens must be minimum.
3. The Solution Treatment time must be minimized.

This is a multiobjective optimization problem involving three objectives. When more Cu is dissolved in the  $\alpha$ -Al matrix the matrix microhardness increases. The relationship between matrix microhardness and the area fractions of the Cu rich phases obtained from Image Analysis (IA) is shown in Figure 6.45.

The relationship shown in Figure 6.45 is given in equation 6.25:

$$Cu_A (\%) = 0.04796 * e^{-2.389 * Z_{HV}} + 0.322 ; \quad R^2=0.96 \quad (6.25)$$

where,  $Cu_A$  (%) is the area percent of the undissolved Cu enriched phases after the Solution Treatment and natural aging and  $Z_{HV}$  is the standard normal deviate of the Matrix Micro Hardness with a mean value of 109.6 and a standard deviation of 4.324.

It can be seen that as the  $Cu_A$  (%) decreases, matrix micro hardness increases. This relationship has been mapped by the ANN model. The objective function of the problem is constructed using the penalty method to transform a constrained optimization problem into an unconstrained one (Brahma et al., 1998, and Chakraborty and Mukherjee, 2000).

The objective function for the problem can be written as:

$$E = w_1 C\bar{u}_A + w_2 \bar{t} - w_3 \mu \overline{HV} \quad (6.26)$$

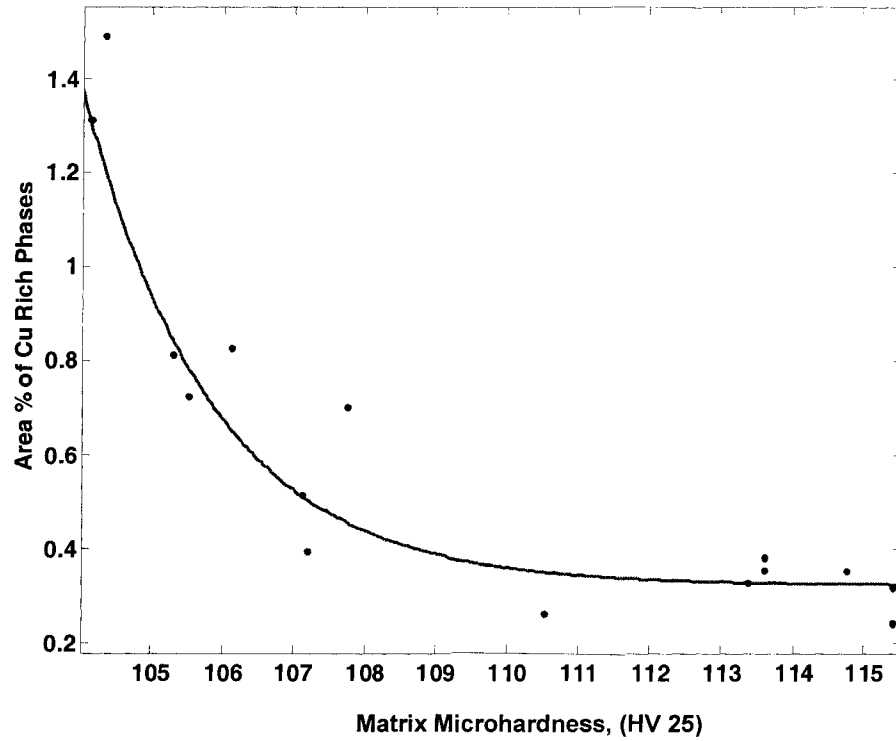


Figure 6.45: The relationship between matrix microhardness and the Area Percent of Cu Rich Phases measured by Image Analysis (IA) on the solution treated and naturally aged UMSA test samples.



where,  $\overline{Cu}_A$ ,  $\bar{t}$ , and  $\overline{\mu HV}$  are the area percent of the Cu phases, Solution Treatment time and the matrix microhardness, respectively, all normalized to be in the range [0-1];  $w_1$ ,  $w_2$ , and  $w_3$  are the corresponding weights. The normalization was done by dividing each value in the column vector by the maximum value of the vector. The weights of  $\overline{\mu HV}$  and  $\overline{Cu}_A$  ( $w_1$  and  $w_3$ ) are assumed to be equal and are set to 1 since they are equally important and complementary to each other. The value of  $w_2$  is fixed by trial and error to be 1. If the Solution Treatment time ( $t$ ) needs to be reduced further, a higher value can be assigned to  $w_2$ . But this may change the values of  $\overline{\mu HV}$  and  $\overline{Cu}_A$ %, accordingly. Note that the time factor is added as a penalty in the objective function to minimize the Solution Treatment time.

The origins of the SA algorithm date back to 1953, when Metropolis et al. (1953), proposed a mathematical model to simulate the movement of the solids from one energy state to another while they are cooling. Suppose the solid is at temperature,  $T$ , with an energy level  $E_1$ . A small random agitation is applied to this solid to create a new perturbation energy state  $E_2$ . If the energy level of the new state ( $E_2$ ) is lower than that of the current state ( $E_1$ ), the solid rearranges itself to the new energy state. If  $E_2$  is higher than  $E_1$ , the solid will move to  $E_2$ , but with a probability as given in equation 6.27.

$$P(E) = e^{\left(\frac{-\Delta E}{k_B T}\right)} \quad (6.27)$$

where,  $\Delta E = E_2 - E_1$ ,  $k_B$  is Boltzman's Constant (Metropolis et al., 1953), and  $T$  is the temperature. equation 6.27 is known as the Metropolis Criterion. In 1983, Kirkpatrick et al (1983) developed an algorithm using the Metropolis Criterion to solve combinatorial optimization problems. This algorithm is called Simulated Annealing (SA). In SA, the objective function of the optimization problem is the energy level in the Metropolis criterion. Basically, SA algorithm involves a series of Metropolis evaluations with the decrease of the temperature. At the beginning, since the temperature is high, the probability of accepting higher energy states is also high. Later, as the optimization progresses, the temperature decreases slowly, as a result the probability of moving to a higher energy state (objective function) also decreases as per equation 6.27. This means

that after a series of evaluations the algorithm will settle down for the lowest energy level, in other words, it reaches the optimal solution. Figure 6.46 shows the flow diagram of the SA algorithm for this problem.

The initial annealing temperature was determined by randomly generating 10 solutions and using equation 6.28:

$$T_a = \frac{-(E_{\max} - E_{\min})}{\log(0.5)} \quad (6.28)$$

where  $E_{\max}$  and  $E_{\min}$ , respectively, are the maximum and minimum values of the objective function obtained from the 10 generated solutions and  $T_a$  is the annealing temperature. This equation has been derived from the Metropolis criterion in equation 6.27.

This is done to ensure that the probability of accepting uphill moves during the initial iterations is high. The neighbouring solutions are created from the current solutions using a random number generator according to the equations 6.29 and 6.30:

$$T_{\text{new}} = T_{\text{current}} + (\text{rand} * 5) \quad (6.29)$$

$$t_{\text{new}} = t_{\text{current}} + (\text{rand} * 5) \quad (6.30)$$

where,  $T_{\text{new}}$  is the new Solution Treatment temperature,  $T_{\text{current}}$  is the current Solution Treatment temperature,  $t_{\text{new}}$  is the new Solution Treatment time,  $t_{\text{current}}$  is the current Solution Treatment time and *rand* is a random number between 0 and 1, respectively. Each temperature and time generated is passed on to the neural network model to give the matrix micro hardness and the area fraction of Cu phases (see Figure 6.46). The objective function is then calculated using equation 6.26. After every 100 iterations, the annealing temperature was reduced according to the equation 6.31:

$$(T_a)_{\text{new}} = (T_a)_{\text{current}} * 0.9 \quad (6.31)$$

where,  $(T_a)_{\text{new}}$  is the new annealing temperature, and  $(T_a)_{\text{current}}$  is the current annealing temperature. Slow cooling is done to escape from local minima. The program is terminated when  $T_f = T_a < 0.0001$ . The SA search program is written using the Matlab<sup>TM</sup> language. The progress of the SA search is shown in Figure 6.47.

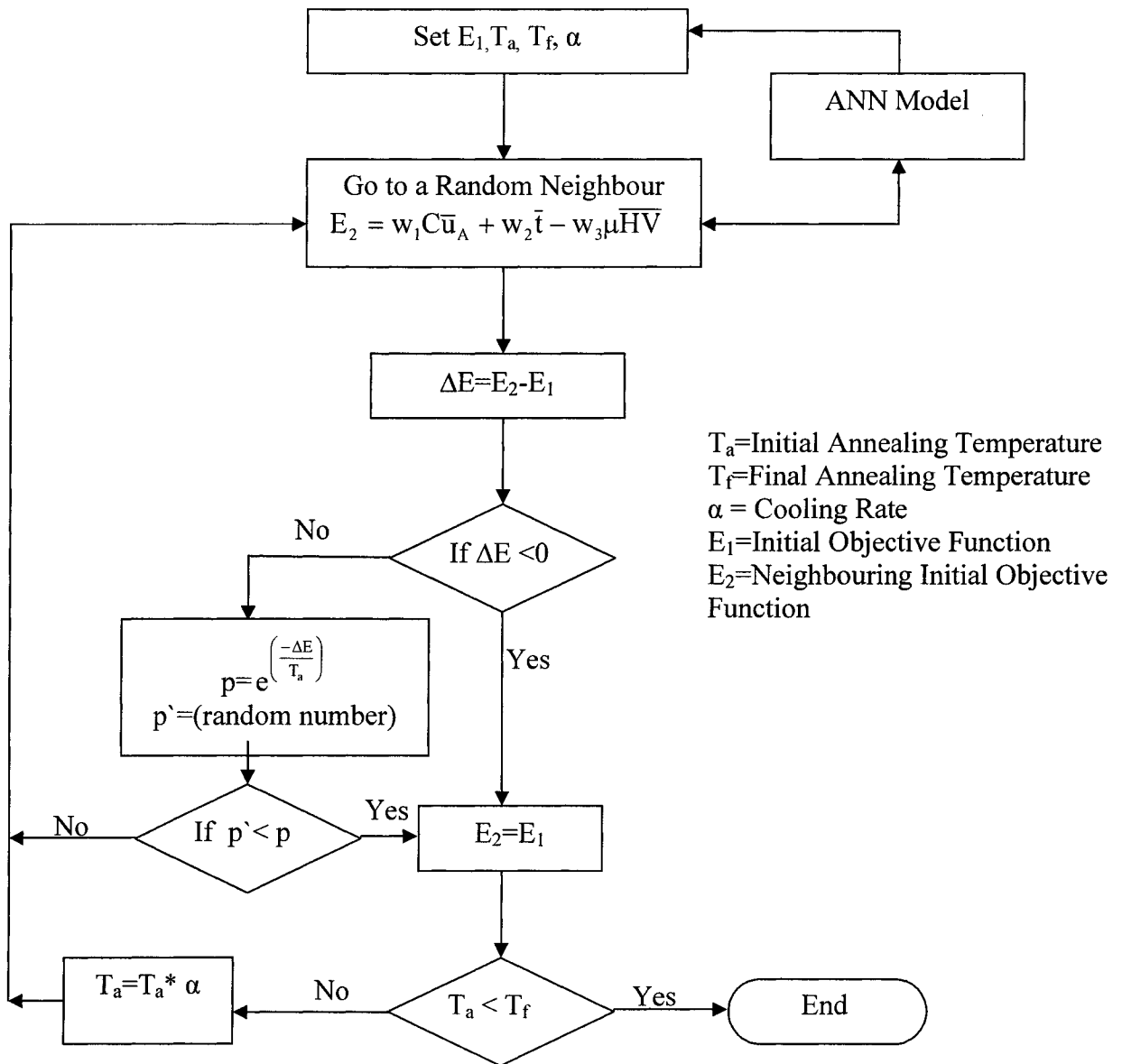


Figure 6.46: Flow chart of the Simulated Annealing search of the NSTS Process.

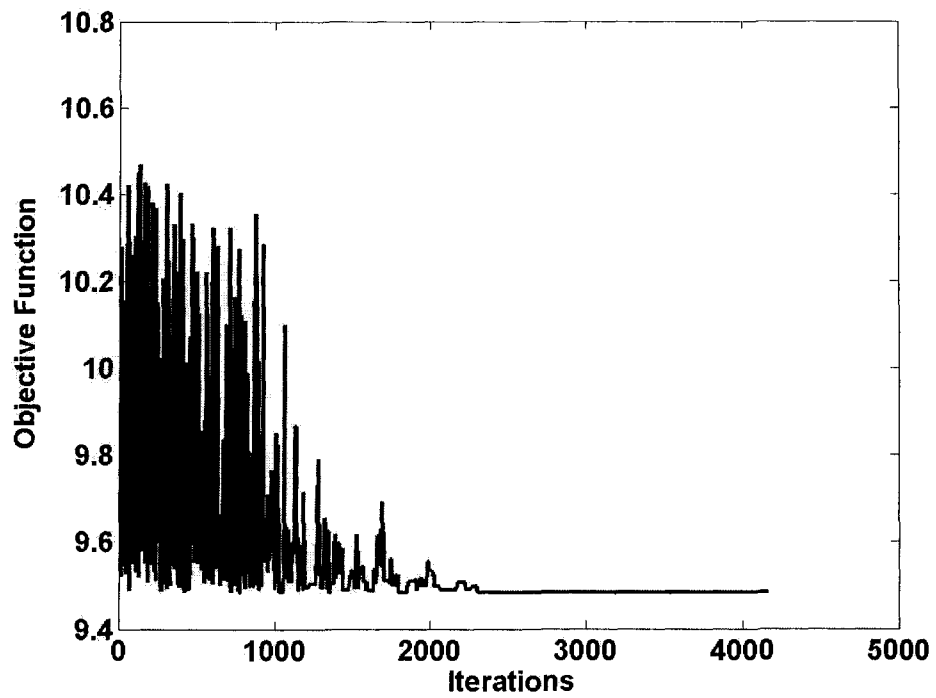


Figure 6.47: Progress of the SA search algorithm.

#### **6.7.2.4 Verification of the Optimal Solution Treatment Parameters by Experimentation**

The verification experiment was performed at the the optimal heat treatment conditions (516<sup>0</sup>C and 66 minutes). The matrix micro hardness and the area percent of Cu enriched phases were measured after naturally aging the test specimen for two weeks. The averages of the results measured from the experimental and predicted values by the model are shown in Figure 6.48. It can be seen that the predicted results are very close to the results obtained from the experiments at the optimum conditions.

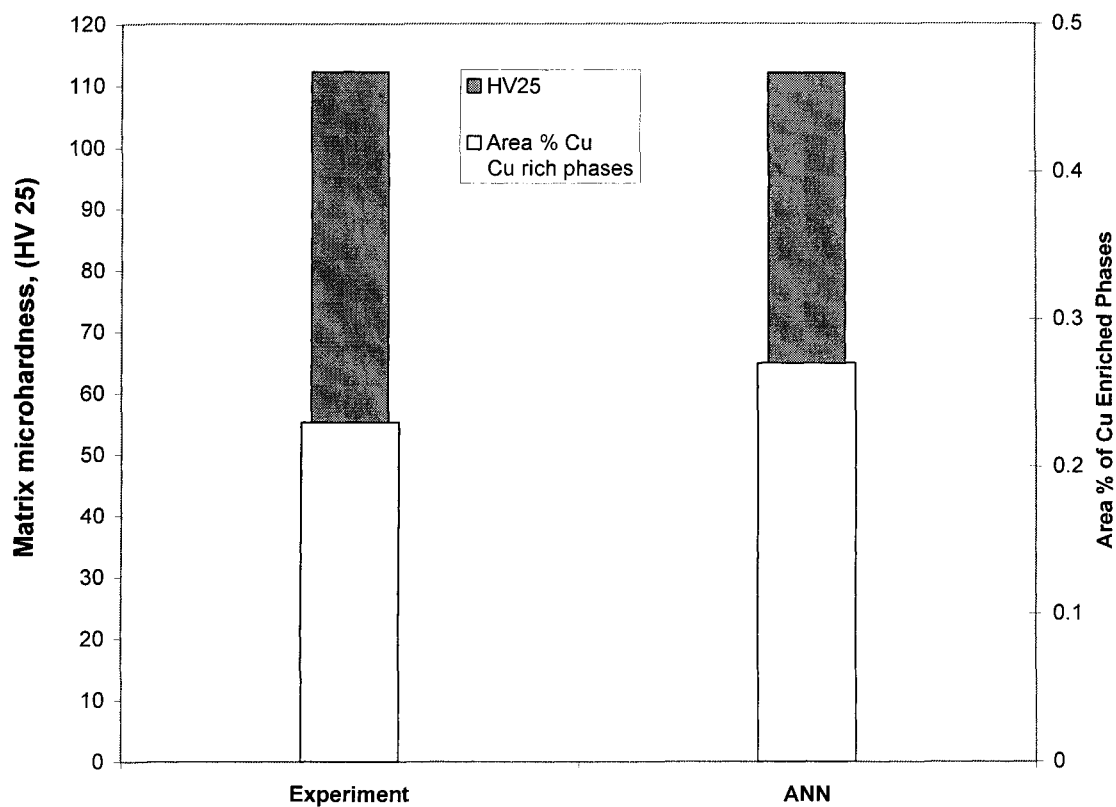


Figure 6.48: Comparison between the measured values from the experiment and the predicted results by the ANN-SA model at the optimal Solution Treatment temperature and time.

## **7. Optimization of the Si and Cu Levels of the 3XX Al Alloys for the Future Generation of Engine Blocks**

### **7.1 Introduction**

This chapter presents the results and discussions from the experiments, measurements and calculations conducted on the 3XX series of Al alloys described in Chapter Five. A novel algorithm using the Silicon Equivalency ( $Si_{EQ}$ ) to predict the grain Growth Restriction Factor (GRF) and the Grain Size of the 3XX alloys is introduced. An analytical platform using Artificial Neural Network (ANN) to predict the characteristic TA parameters of the 3XX Al alloys is discussed. The various inter-relationships between the Thermal Analysis parameters, Si and Cu contents, SDAS, Grain Size, latent heat and Brinell Hardness are established using multiple linear regression analysis as well as the response surface method. These relationships were then utilized to optimize the level of Si and Cu in the 3XX Al alloys and hence to develop a new alloy. The results presented in this Chapter have been disseminated by the author in two recent publications (Byczynski et al., 2003, Djurdjevic et al., 2004b).

### **7.2 Novel Algorithm for the Prediction of the Grain Growth Restriction Factor (GRF) and the Grain Size (GS) of Multicomponent Al-Si Alloys Using the Silicon Equivalency ( $Si_{EQ}$ ) Algorithm.**

The GRF calculations were performed for very slow cooling rate conditions ( $\sim 0.13^{\circ}C/s$ ), which can be approximated to be close to equilibrium solidification conditions. The casting structure and integrity are adversely affected by the slow equilibrium solidification conditions due to the formation of a coarse microstructure and due to the increased propensity for porosity formation. The bulkhead of the engine block has also close to equilibrium solidification conditions and therefore these calculations could be applied to estimate the bulkhead metallurgical properties. In this work the Grain Size was measured in order to establish its relationship with the GRF. It must be noted that the experimental alloys contained the same level of impurities in as are present in the secondary alloys used by the aluminum casting industry.

Bäckerud (1983) has introduced the Growth Restriction Factor (GRF) as a measure of the growth restricting effect of solute elements on new grains at the solid liquid interface as they grow into the melt. The GRF is calculated as:

$$\text{GRF} = \sum_{i=1}^n m_i C_i (k_i - 1) \quad (7.1)$$

where,  $n$  is the number of elements present in the alloy,  $m_i$  is the slope of the liquidus line of the  $i^{\text{th}}$  element,  $C_i$  is the concentration of the  $i^{\text{th}}$  element and  $k_i$  is the partitioning coefficient for the  $i^{\text{th}}$  element. Table 7.1 presents the values of  $k$ ,  $m$  and  $m(k-1)$  for the common Al-X binary alloy systems.

This work presents a novel method for the calculation of the GRF for the multicomponent alloys using the  $\text{Si}_{\text{EQ}}$ . The novel equation for the GRF of the multicomponent Al-Si alloy is estimated by considering the alloy as a pseudo binary Al- $\text{Si}_{\text{EQ}}$  alloy:

$$\text{GRF} = m (k-1) \text{Si}_{\text{EQ}} \quad (7.2)$$

where,  $m$  is the slope of the liquidus line of the Al-Si binary phase diagram,  $\text{Si}_{\text{EQ}}$  is the Silicon Equivalency and  $k$  is the partition coefficient for the Al-Si binary phase diagram.

Table 7.2 summarizes the values of the GRF calculated for the 3XX series of Al alloys using equations 7.1 and 7.2. Table 7.2 shows that the GRF calculated by  $\text{Si}_{\text{EQ}}$  is much lower than that calculated using the summation approach. The reason being, in the  $\text{Si}_{\text{EQ}}$  approach, the interaction between three elements (Al-Si and  $X_i$ ) is incorporated. The interactions are becoming more significant at higher solute concentrations. Easton and StJohn (2001) have observed a similar trend when they compared the GRF value of Al Si7Mg0.3Ti0.02 alloy using Thermocalc<sup>TM</sup> solidification software (GRF=43.1 °C) and the traditional summation approach (GRF =47.1 °C). According to the  $\text{Si}_{\text{EQ}}$  method the GRF of this alloy is calculated to be 40.7 °C.

Figure 7.1 shows the relationship between the Grain Sizes of 3XX alloys and their GRF's calculated using equations 7.1 and 7.2. The GRF is found to be highly correlated ( $R^2=0.99$ ) and is linearly increasing with the increase in the Grain Size. As previously mentioned there is a transition point at 3 wt.% Si after which the Grain Size increases with the increase in the Si content in the alloy. All the 3XX aluminum alloys analyzed in this work had Si contents greater than 3 wt.%.

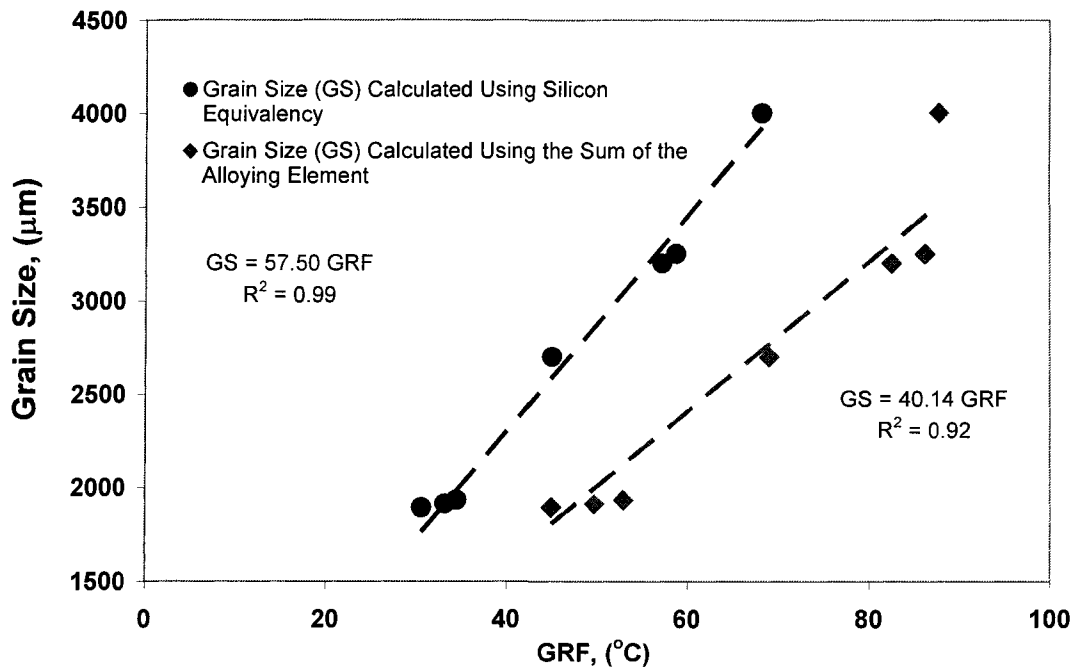


**Table 7.1: Data required for the calculation of the GRF of multicomponent hypoeutectic Al alloys, (Easton and StJohn (2001)).**

Al- $X_i$ Alloy	k	m	$m(k-1)$
Al-Si	0.11	-6.6	5.9
Al-Cu	0.17	-3.4	2.8
Al-Mg	0.51	-6.2	3
Al-Mn	0.94	-1.6	0.1
Al-Fe	0.02	-3	2.9
Al-Zn	0.88	-2.97	0.3
Al-V	4	10	30
Al-Mo	2.5	5	7.5
Al-Nb	1.5	13.3	6.6
Al-Ge	0.10	-4.66	-4.2
Al-Li	0.56	-8.06	3.8
Al-Ni	0.007	-3.3	3.3
Al-Cr	2	3.5	3.5
Al-Ti	7.8	33.3	220
Al-B	0.067	1.015	3.2

**Table 7.2: Comparison of the GRF values calculated Using  $Si_{EQ}$  and the sum of  $m(k-1)C_0$  method**

Alloy	$Si_{EQ}$ (wt.%)	GRF by $Si_{EQ}$	GRF by $\sum k(m-1)C_0$
[5-1]	5.21	30.58	44.94
[5-2]	5.64	33.16	49.71
[5-4]	5.87	34.45	52.92
[7-1]	7.46	43.81	67.51
[7-2]	7.66	45.01	69.04
[7-4]	7.79	45.74	73.33
[9-1]	9.51	55.89	80.27
[9-2]	9.73	57.18	82.45
[9-4]	10.00	58.18	82.45
[11-1]	11.18	65.69	81.12
[11-2]	11.28	66.26	82.61
[11-4]	11.62	68.24	87.66

Figure 7.1: Grain Size measured vis-a-vis the GRF calculated using the  $Si_{EQ}$  methodology and the summation approach.

The  $\Delta T$  undercooling parameter ( $\Delta T = T_G^{\text{aDEN}} - T_{\text{MIN}}^{\text{aDEN}}$ , refer to Appendix 2) has been used in the Thermal Analysis literature to measure the Grain Size (Zalensas, 1993). Larger  $\Delta T$  parameter indicates a coarse grain structure and a smaller  $\Delta T$  parameter, refers to a finer grain structure. The plot between the  $\Delta T$  parameter and the Grain Size measured for the experimental alloys is shown in Figure 7.2. It can be seen from Figure 7.2 that the relationship between  $\Delta T$  and Grain Size is in agreement with that which has been published in the literature. A higher value of  $\Delta T$  implies that the larger undercooling was required to generate sufficient number of nuclei for stable crystal growth. On the other hand, a smaller value of  $\Delta T$  means that adequate number of nuclei are generated in the liquid with a smaller degree of undercooling and the latent heat released from these nuclei are sufficient to balance the heat extraction from the mold. Since there was no grain refiner added to the experimental alloys and the solidification conditions were close to equilibrium solidification, Figure 7.2 shows the effect of increasing the levels of Si and Cu in the 3XX alloy on the Grain Size. This will be discussed in detail in Section 7.4.1.

The plot between GRF and the  $\Delta T$  is given in Figure 7.3. This positive correlation is expected given the strong correlation between the GRF and Grain Size ( $R^2=0.99$ ) as shown in Figure 7.1.

### 7.3 Thermal Analysis (TA) of the 3XX Al Alloys

The TA parameters of the 3XX series aluminum alloys were computed using the advanced Computer Aided Cooling Curve Analysis algorithms. The characteristic TA parameters (temperature and fraction solid) and the corresponding standard deviations of the 3XX alloys are tabulated in Table 7.3.

Mackay (2003) has suggested that the apparent fraction solid parameters could be used as a measure of the propensity for porosity formation in the 3XX Al alloys. The equations to calculate the apparent fraction solid parameters are given below:

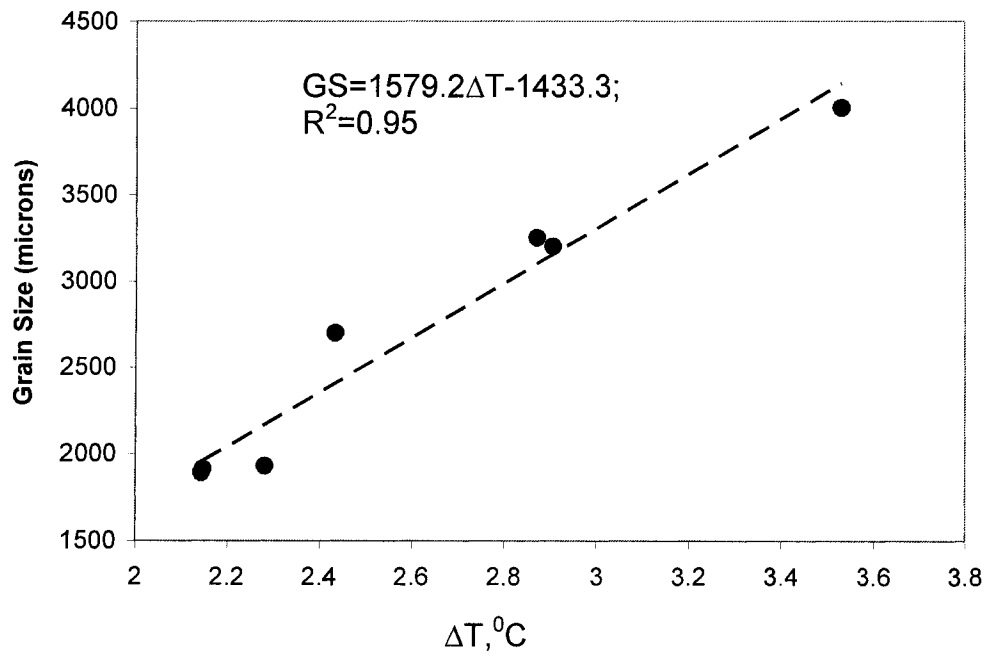


Figure 7.2 : Relationship between the  $\Delta T$  undercooling parameter and the Grain Size (GS) measured for the test samples: [5-1],[5-2],[5-4], [7-2], [9-2],[9-4], and [11-4].

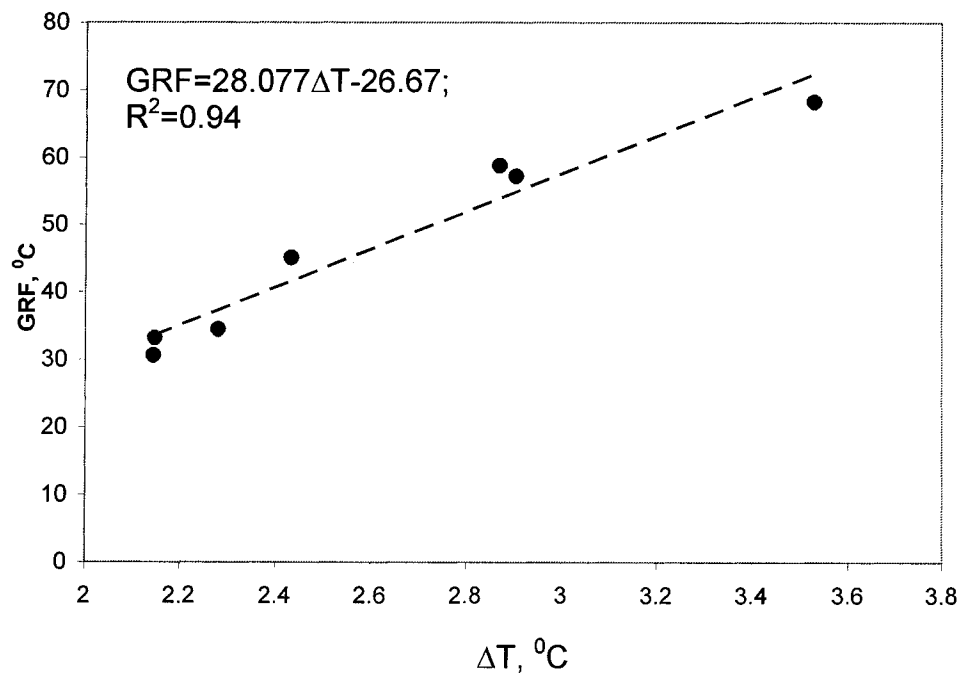


Figure 7.3: The relationship between the  $\Delta T$  undercooling parameter and the Growth Restriction Factor (GRF) for the test samples: [5-1],[5-2],[5-4], [7-2], [9-2],[9-4], and [11-4].

**Table 7.3: Characteristic temperatures and fraction solids of the 3XX series of Al alloys with their Standard Deviations (SD). (Djurdjevic and Kierkus, 2000)**

Alloy	$T_{LIQ}$ /SD	$T_{COH}^{\alpha DEN}$ /SD	$fs_{COH}^{\alpha DEN}$ /SD	$T_{E,NUC}^{Al-Si}$ /SD	$fs_{E,NUC}^{Al-Si}$ /SD	$T_{E,NUC}^{Al-Cu}$ /SD	$fs_{E,NUC}^{Al-Cu}$ /SD	$T_{SOL}$ /SD
[5-1]	627.27	625.53	8.10	573.00	61.37	544.93	94.77	479.97
	1.23	0.98	0.17	0.50	0.81	0.90	0.59	0.97
[5-2]	622.83	621.37	7.58	567.20	59.93	534.50	93.10	477.93
	0.45	0.68	0.37	0.40	0.78	1.35	0.30	0.64
[5-4]	618.30	616.57	7.13	552.23	58.37	512.03	91.50	482.63
	0.10	0.49	0.21	0.67	0.71	0.57	0.26	1.59
[7-1]	613.27	610.57	6.50	570.03	43.60	526.03	97.10	485.30
	1.56	0.23	0.95	0.67	0.36	0.75	0.10	0.89
[7-2]	610.03	607.13	6.90	569.03	41.43	508.50	96.13	480.37
	0.70	1.72	0.61	0.20	1.97	0.82	0.23	0.85
[7-4]	604.58	601.50	5.88	558.53	40.30	509.58	90.80	481.83
	1.57	0.41	0.48	0.74	0.59	0.31	0.37	0.92
[9-1]	597.28	594.53	6.15	568.48	28.15	526.30	96.70	485.03
	1.49	1.62	2.00	0.64	0.24	0.77	0.08	0.99
[9-2]	589.90	587.60	7.75	564.58	26.25	506.50	95.23	480.05
	0.47	0.42	0.66	0.56	0.42	0.70	0.13	0.88
[9-4]	583.50	580.95	7.78	562.88	21.73	508.08	91.53	480.23
	0.64	0.90	0.57	1.90	0.85	0.93	0.15	0.46
[11-1]	579.37	579.43	5.97	574.57	10.57	519.73	98.20	480.70
	1.38	1.16	0.25	1.19	0.99	0.95	0.10	0.78
[11-2]	576.23	576.27	5.93	575.53	8.73	501.67	97.40	476.53
	0.57	0.23	0.70	0.21	0.49	0.15	0.17	0.25
[11-4]	566.97	567.17	2.87	568.50	4.60	513.73	92.73	481.93
	0.67	0.31	0.57	0.46	0.44	0.15	0.21	1.12

$$af_s^{\alpha-DEN} = fs_{E,NUC}^{Al-Si} \quad (7.3)$$

$$af_s^{Al-Si} = fs_{E,NUC}^{Al-Cu} - fs_{E,NUC}^{Al-Si} \quad (7.4)$$

$$af_s^{Al-Cu} = 100 - fs_{E,NUC}^{Al-Cu} \quad (7.5)$$

where,  $af_s^{\alpha-DEN}$  is the apparent fraction solid of the  $\alpha$ -Al dendrites,  $fs_{E,NUC}^{Al-Si}$  is the fraction solid at the Al-Si eutectic nucleation,  $af_s^{Al-Si}$  is the apparent fraction solid of the Al-Si eutectic,  $fs_{E,NUC}^{Al-Si}$  is the fraction solid at the Al-Si-Cu eutectic nucleation reaction and  $af_s^{Al-Cu}$  is the apparent fraction solid of the Cu rich eutectic. Please refer to Appendix 2 to see the locations of these parameters in the fraction solid curve.

Mackay (2003) has proposed that in order for the 3XX Al alloy to have a lower propensity for pore nucleation and growth, it should have a smaller value for the  $af_s^{\alpha-DEN}$  and a larger fraction solid value for the  $af_s^{Al-Si}$ . When the  $af_s^{\alpha-DEN}$  is smaller, the volume fraction of the  $\alpha$ -Al dendrites formed will be smaller and a high  $af_s^{Al-Si}$  means that the volume fraction of the Al-Si eutectic will be larger. When the volume fraction of the  $\alpha$ -Al dendrites are smaller, the hydrostatic stress or the shrinkage pressure exerted on the liquid melt will be less. Therefore, the alloy with a lower  $af_s^{\alpha-DEN}$  will have a lower tendency for pore nucleation (Mackay, 2003). The apparent fraction solid of the 3XX Al alloys are compared by using a stacked histogram in Figure 7.4. It can be seen from this Figure that the  $af_s^{\alpha-DEN}$  decreases when moving from alloy composition 5 wt.% Si-1 wt.% Cu to 11 wt.% Si-4 wt.% Cu. A similar trend in the decrease of the Secondary Dendrite Arm Spacing (SDAS) values was also observed. This has been explained in the Section 7.4.1. Therefore, the tendency for porosity formation in 3XX Al alloys with higher levels of Si (9-11 wt.%) is expected to be lower compared to 3XX Al alloys with lower levels of Si (Ren, 2000, Mackay, 2003).

Another important result that is obtained from the analysis of the cooling curve parameters is that the latent heat of solidification of the 3XX aluminum alloys was found to have a negative linear relationship with the fraction solid parameter at the Al-Si eutectic nucleation temperature ( $fs_{E,NUC}^{Al-Si}$ ). This relationship can be expressed in the form of an analytical expression given in equation 7.6.

$$\text{Latent Heat} = -1.3701 (fs_{E,NUC}^{Al-Si}) + 496.48 \quad (R^2=0.96) \quad (7.6)$$

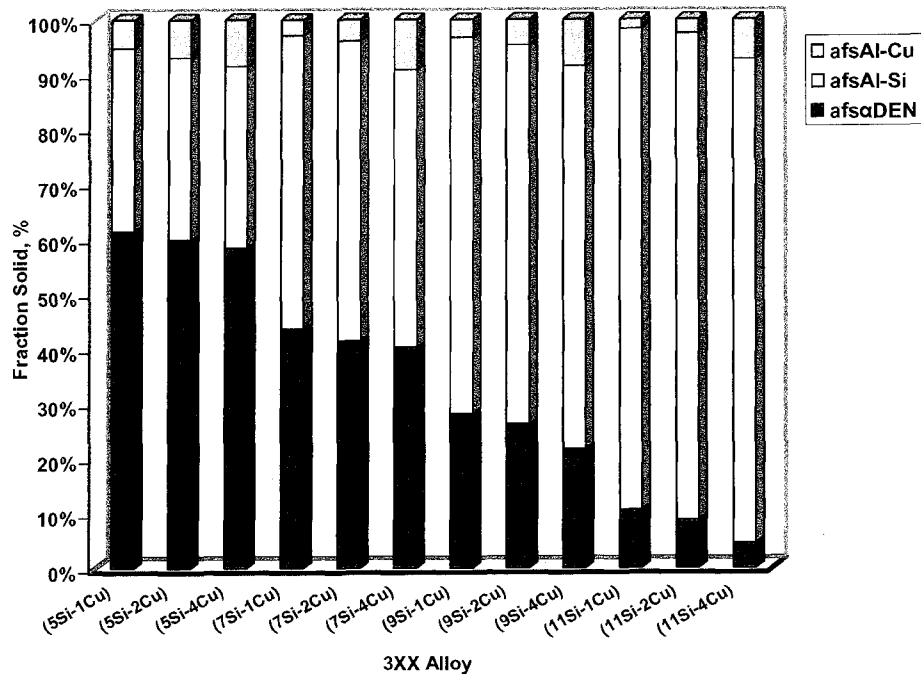


Figure 7.4: Comparison of the apparent fraction solids of the 3XX Alloys.

The above mentioned relationship may be reasoned as follows: The latent heat of pure Si is 1800 kJ/kg while that of pure Al is only 390 kJ/kg. So when Si is added to the Al alloy the latent heat of the resultant alloy increases. In the meantime the chemical composition of the alloy is also moving closer to the eutectic composition (12.3 wt.% Si) by the addition of Si. For that reason the fraction solid at which the Al-Si eutectic reaction commences is decreased.  $f_{S_{E,NUC}}^{Al-Si}$  can also be viewed as the amount of  $\alpha$ -Al formed before the beginning of the eutectic reaction. equation 7.6 provides an easier and inexpensive way to calculate the latent heat of solidification of 3XX aluminum alloys when compared to the Differential Scanning Calorimetry technique. The latent heat parameter is very essential for the mathematical modeling and computer simulation of the solidification process of the alloys. Also the fluidity of the alloy is directly proportional to its latent heat. Note that equation 7.6 is valid for only slow cooling rates ( $\sim 0.1$  °C/s) approaching equilibrium solidification conditions.

### 7.3.1 Prediction of the TA Parameters Using Artificial Neural Network (ANN)

It is known from the previous IRC research that the characteristic temperature parameters of the 3XX alloys can be calculated using the Silicon Equivalency ( $Si_{EQ}$ ) analytical methodology. However, the  $Si_{EQ}$  approach is not able to predict the characteristic fraction solid parameters. Therefore, a novel approach using ANN was used in this work to predict the characteristic temperature as well as the fraction solid parameters of the 3XX alloys.

The neural network was trained with 11 datasets and then tested with an unseen 12<sup>th</sup> dataset to evaluate its generalizing ability. Figure 7.5 and Figure 7.6 compare the predicted TA parameters of the 7wt.% Si-4wt.% Cu alloy and 9wt.% Si-1wt.% Cu alloy by ANN against those parameters measured by AITAP for the same alloys. It can be seen from Figure 7.5 and Figure 7.6 that the ANN predicted values are very closely matching the values measured by the AITAP. The inputs to the neural network are the silicon and copper contents of the alloy and the outputs are the characteristic temperature and fraction solids. The architecture of the MLP neural network for the prediction of the characteristic TA parameters of the 3XX alloys is given in Table 7.4.



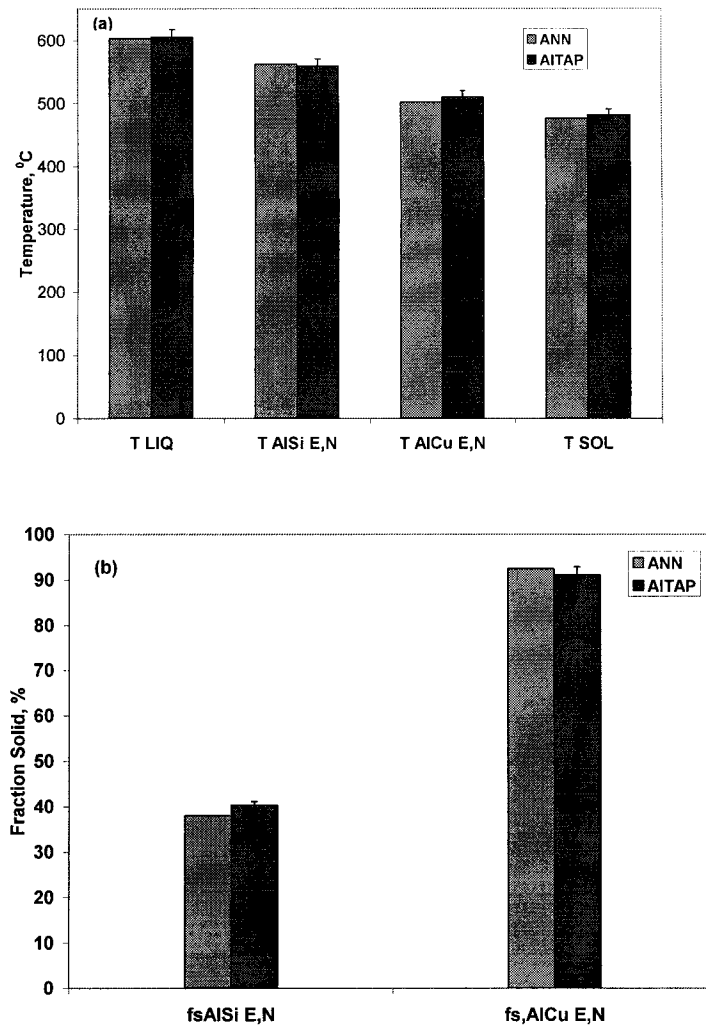


Figure 7.5: Comparison of the AITAP experimental and ANN predicted (a) Temperature and (b) Fraction Solid characteristics of the 7 wt.%Si-4wt.% Cu alloy.

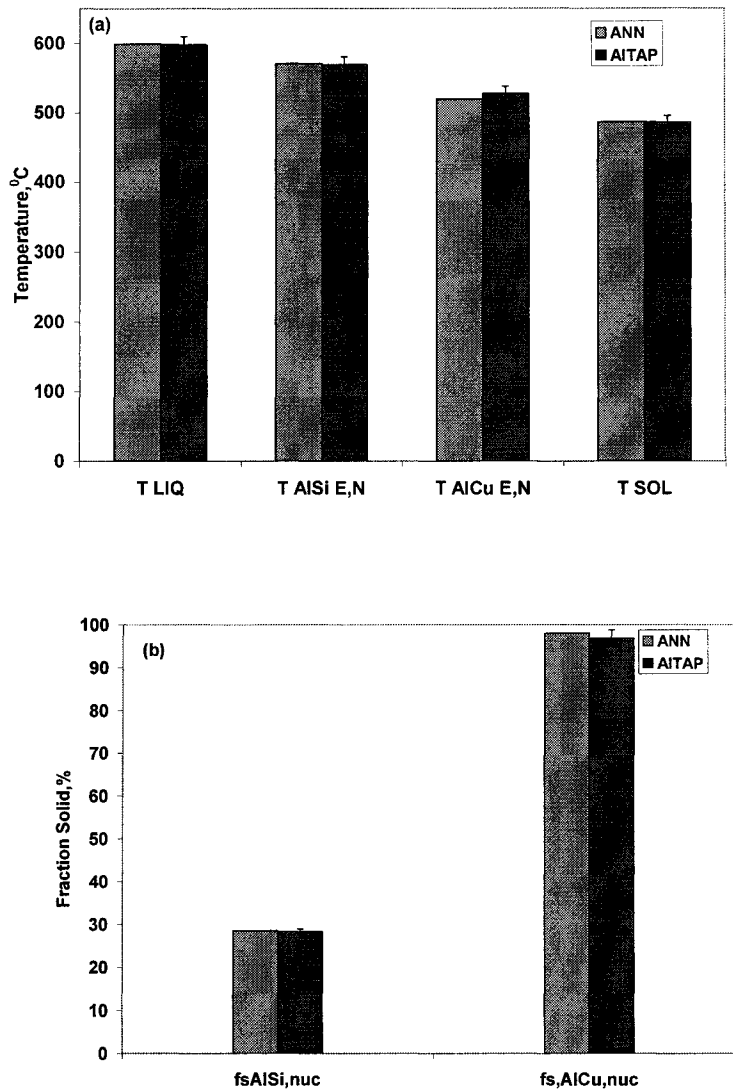


Figure 7.6: Comparison of the AITAP experimental and ANN predicted (a) Temperature and (b) Fraction Solid characteristics of the 9 wt.%Si-1 wt.% Cu alloy.

**Table 7.4. Architecture of the function approximation MLP neural network for modeling the TA parameters of the 3XX Al Alloys.**

Number of hidden layers	Number of neurons in the hidden layer	Number of neurons in the output layer	Transfer function of the hidden layers	Transfer function of the output layer	Training algorithm
1	10	6	tangent sigmoid	linear	Bayesian regularization in combination with Levenberg-Marquardt training

## 7.4 Optimization of the Si and Cu Levels of the 3XX Aluminum Alloys

Si and Cu are the major alloying elements in the W319 alloy, presently used by WAP. Hence, what is meant by optimization is to develop a new alloy by finding the levels of these elements at which the cast component properties are improved while maintaining a price lower than that of the W319 alloy. Ren (2000) used the linear weighted optimization method to find the optimal levels of Si and Cu present in the 3XX Al alloys. This work has reported that 9 wt.% Si- 2 wt.% Cu are the optimum levels for Si and Cu. However, this work did not study Si levels above 9 wt.%. Therefore, this result cannot be concluded as the optimal alloy composition in a general sense. In the present work, Si contents up to 11 wt.% (close to the eutectic composition) and Cu contents up to 4 wt.% were investigated.

The first step of optimization is to develop analytical expressions of the casting characteristics as functions of Si and Cu levels. This can be stated mathematically as:

$$y = f_n(\text{Si}, \text{Cu})$$

where y is the casting characteristic of interest (eg. SDAS, Grain Size, Hardness etc.) and Si and Cu are the silicon and copper contents respectively.

These functional relationships can be formulated from the experimental data by using either multiple regression analysis or response surface analysis using the Minitab™ statistical software. In the following Sections, the analytical expressions for each casting characteristic are presented and the rationale (underlying metallurgical principles) behind the observed trends are discussed. It must also be noted that TA test samples of the 3XX Al alloys were solidified close to equilibrium solidification conditions ( $\sim 0.13$  °C/sec), which represents the most unfavourable condition for achieving casting integrity and mechanical properties. Therefore the relationships discussed below are valid only for 3XX Al alloys at close to equilibrium solidification conditions.

### 7.4.1 Secondary Dendrite Arm Spacing (SDAS) and Grain Size (GS)

The mathematical expressions for the SDAS and GS are given in equations 7.7 and 7.8 respectively.

$$\text{SDAS (microns)} = 120.54 - 4.63\text{Si} - 10.16\text{Cu} + 0.56\text{SiCu} \quad (R^2=0.95) \quad (7.7)$$

$$\text{GS (microns)} = 171.84 + 343.28\text{Si} + 20\text{Cu} \quad (\text{R}^2=0.99) \quad (7.8)$$

where Si and Cu are the silicon and copper contents of the alloy given in wt.%.

The experimental data that is used for the development of the above equations is presented in Table 7.5.

It is evident from the equation 7.7 that the SDAS decreases with the addition of Si and Cu. SDAS is primarily controlled by the solidification rate, but when the solidification rate is constant, as in this case, it is influenced by the chemical composition of the alloy. The distribution coefficient ( $k$ ) of 3XX alloys is less than one, which means that, during the solidification, solutes are getting rejected into the Al melt. As the solute content (Si and Cu) in the 3XX alloy increases, more surface area is needed for the solidifying dendrites to diffuse the solutes through the solid-liquid interface. The dendrite increases its surface area by increasing the number of dendrite arms and as a result the dendrite arm spacing decreases.

SDAS measures the overall fineness of the casting microstructure. As the SDAS decreases, the amount of porosity in the casting also decreases. This is because when the SDAS is smaller, the residual liquid is split into a large number of small interdendritic regions. The surface tension in these regions exceeds the gas pressure of the pores, and hence pore formation is prevented (Campbell, 1991). Smaller SDAS will lead to finer intermetallics, and a better homogenization heat treatment with a shorter Solution Treatment time. Therefore, as the SDAS decreases, the mechanical properties of the castings are improved (Gruzleski, 2000).

Equation 7.8 shows that the Grain Size increases with the addition of Si and Cu to the 3XX alloys. The reader may be surprised by this apparent contradiction, because the Grain Size is expected to decrease as the SDAS decreases (Grains are actually called as a collection of dendrites). This anomaly can be explained by the mechanism of the dendrite growth involved. When the solute concentration in the Al alloy increases, the radius of the solidifying dendrite tips decreases because a sharper tip can reject the solute more effectively. Due to the capillary effect of the dendrite tips with a smaller radius,

**Table 7.5: The Experimental data set used for the development of the equations given in Section 7.4 for optimization of the 3XX Al-Si alloys.**

Si (wt.%)	Cu (wt.%)	DAS ( $\mu\text{m}$ )	GS ( $\mu\text{m}$ )	S-Range ( $^{\circ}\text{C}$ )	Hardness (HB)	LH (kJ/kg)	Cost (\$/MT)
4.85	1.03	89.89	1890.00	147.30	61.00	407.60	287.30
5.01	2.06	84.38	1910.00	144.90	71.20	415.15	309.50
4.89	3.85	67.11	1930.00	135.67	79.25	420.15	335.38
7.13	0.96	79.70	*	127.97	72.80	434.75	341.01
7.05	1.98	74.36	2700.00	129.67	81.20	435.40	356.62
6.75	4.38	61.43	*	122.75	92.75	442.25	391.16
9.16	1.05	75.75	*	112.25	80.75	467.05	357.98
9.02	2.44	68.80	3200.00	109.85	81.50	467.05	380.90
8.95	4.38	59.70	3250.00	103.28	87.40	461.15	412.89
10.84	0.94	67.93	*	98.67	73.60	472.65	345.33
10.67	1.95	57.98	*	99.70	86.60	485.95	364.08
10.55	4.36	51.37	4000.00	85.03	101.60	499.75	405.11

they tend to grow faster and impinge on neighbouring dendrites in a short time (think of how fast water rises in a capillary tube). As a result more dendrites are involved in the formation of a grain, and hence the Grain Size increases (Johnsson, 1995).

Campbell (1991) has suggested that in the case of castings, the most important structural measurement is the SDAS. The classical Hall-Petch equation based on Grain Size is not strictly followed in the case of castings, because there exists no grain boundary between the dendrite arms to stop the movement of a slip plane.

#### 7.4.2 Solidification Range

Solidification Range (SR) is defined as the temperature difference between the liquidus and solidus temperatures of the alloy. If the SR is longer, the extent of mushy zone feeding will be higher and as a result the liquid melt has to traverse through tortuous interdendritic regions. If the feeding in these regions is not sufficient, micro shrinkage will occur in the unfed region (Boudrault et al., 1997). Tagiev et al. (1996) have reported that when the SR is narrower, the casting mechanical properties are higher.

The equation for the solidification range is given as:

$$\text{SR } (^{\circ}\text{C}) = 192.841 - 8.298 \text{ Si} - 3.738 \text{ Cu} \quad (\text{R}^2 = 0.98) \quad (7.9)$$

equation 7.9 shows that the SR decreases with the addition of the solutes. As the solute concentration in the alloy increases, its liquidus temperature decreases, while the solidus temperature remains unchanged with solute addition as it is dependent only on the composition of the low melting point impurity elements (Table 7.3 shows that the solidus temperature is not changed by the addition of Si and Cu). As a result the difference between these two temperatures decreases with the addition of the solutes.

#### 7.4.3. Latent Heat of Solidification

The relationship between latent heat of solidification and the chemistry is given by equation 7.10.

$$\text{Latent Heat (kJ/kg)} = 343.083 + 12.416 \text{ Si} + 3.88 \text{ Cu} \quad (\text{R}^2 = 0.96) \quad (7.10)$$

The latent heat of solidification increases with the increase in Si and Cu contents. As the latent heat increases the fluidity of the alloy also increases, and this will lead to better

feeding characteristics during solidification (Hu and Pan, 1998). Therefore, in the optimization routine, it has been attempted to maximize the latent heat of solidification.

#### 7.4.4 Brinell Hardness

The relation between Si and Cu contents and the Brinell Hardness of the as cast TA test samples is developed from the experimental data and is presented in equation 7.11.

$$\text{HB} = 21.52 + 8.94 \text{ Si} + 8.3 \text{ Cu} - 0.42 \text{ Si}^2 - 0.61 \text{ Cu}^2 + 0.06 \text{ Si Cu} \quad (\text{R}^2 = 0.87) \quad (7.11)$$

As per the Ford Engineering Specification WSE-M2A-151-A2-A4 the Brinell Hardness of the heat treated components should be between 85-115 HB. Therefore, in the optimization routine, the lower bound for hardness was set to be 85 HB.

#### 7.4.5 Price of the Alloy

The prices of the 3XX Al alloys used in this study are appraised by Alcan International (Major, 2004). The expression for the price as a function of the Si and Cu content is given below.

$$\text{Price (\$/MT)} = 21.935 + 69.69 \text{ Si} + 16.33 \text{ Cu} - 3.81 \text{ Si}^2 \quad (\text{R}^2 = 0.99) \quad (7.12)$$

The price of the optimized alloy should be lower than that of the 7 wt.% Si-4 wt.% Cu alloy (\$ 391/MT), as the Si and Cu contents of this alloy are similar to the W319 alloy.

#### 7.4.6 Optimization of the Si and Cu Contents of the 3XX Aluminum Alloys Using the Desirability Function Approach

The optimal levels of Si and Cu was determined using the desirability function method for the simultaneous optimization of several response variables proposed by Derringer and Suich (1980). This method is often used to solve product development problems where a set of independent variables must be fine-tuned to obtain a desirable combination of response variables. In this method, firstly, the functional relationships between the response variables of interest and the independent variables (in this case Si and Cu levels) are developed using the polynomial functions. The lower bound, the upper bound and the target value for the response are input by the user. Then, using the desirability function each response variable is transformed to a desirability value  $d_i$ , where  $0 \leq d_i \leq 1$ . The value of  $d_i$  increases as the “desirability” of the corresponding



response variable increases. When the goal is to minimize the response, any value above the upper bound of the response has zero desirability and any value below the lower bound of the response has a desirability of 1. The reverse is true when the goal is to maximize a response. The desirability function is calculated using the equation 7.13.

$$d_i = f_i(y)^{w_i} \tag{7.13}$$

where  $w_i$  is the weight (0.1 -10) for response for ‘i’ and the function  $f_i(y)$  depends on whether to hit a target value, minimize the response or maximize the response. The weight defines the shape of the desirability function for each response. When the weight is less than 1, lesser emphasis is placed on the target, and a response value far from the target may have a high desirability. When the weight is one, equal emphasis is placed on the target as well the bounds, and when the weight is close to 10 greater emphasis is placed on the target. Any response value closer to the target may have a high desirability.

The values  $f_i(y)$  are calculated as follows (Minitab, 2004):

When the goal is to minimize the response,

$$f_i(y) = \begin{cases} 1; y < T \\ \left(\frac{y - U}{T - U}\right); T < y < U \\ 0; y > U \end{cases} \tag{7.14}$$

When the goal is to maximize the response,

$$f_i(y) = \begin{cases} 0; y < L \\ \left(\frac{y - L}{T - L}\right); L < y < T \\ 1; y > T \end{cases} \tag{7.15}$$

where,  $y$  is the response value,  $U$  and  $L$  are the upper and lower bounds for the response , $i$ , and  $T$  is the target. The individual desirability's of the responses are combined to get the composite desirability ( $D$ ), which is the weighted geometric mean of the individual desirability's for the responses:

$$D = \left(d_1^{I_1} * d_2^{I_2} * \dots * d_n^{I_n}\right)^{1/(I_1+I_2+\dots+I_n)} \tag{7.16}$$

where  $I_i$  is the importance of the response  $i$  (0.1-10). Larger values of  $I$  (close to 10), will correspond to more important responses and smaller values to less important responses. Finally, the optimum solution is obtained by maximizing  $D$ . The response optimizer tool in the Minitab<sup>TM</sup> statistical Software has been used for this optimization. Response optimizer maximizes the desirability function using the reduced gradient algorithm (Luenberger, 1984). The upper and lower bounds, the target values, weight and the importance for each response variable for this problem are given in Table 7.6. These bounds were decided by using the WSE-M2A-151-A1/A3 Ford Engineering Material specifications.

The optimal levels of Si and Cu were found to be 10.65 wt.% and 2.08 wt.% respectively. This composition of Si and Cu lies within the chemical composition specified for the Al 332 alloy according to the American Aluminum Association (AAA) system for the alloy nomenclature (Davis, 1993). The maximum composite desirability is 0.0021. The predicted values of the responses in the as cast conditions and the corresponding desirability values at the optimal levels are given in Table 7.7. The optimal levels of Si and Cu were found to be closer to the eutectic composition. This has vindicated the decision to go beyond 9 wt.% Si which was the maximum level studied by Ren (2000) and Mackay (2003). Fuchs and Wappelhorst (2003) reported that Al-10SiMg alloy was used recently for making cylinder heads for the Audi V6-TDI engine. Lucas et al. (2004) reported that high silicon contents have a refining effect on the  $\beta$ -Al<sub>3</sub>FeSi platelets because the growth times of these phases are reduced by the increase in the level of Si.

The characteristic TA parameters for the optimal alloy were predicted using Artificial Neural Network (ANN) and the data are tabulated in Table 7.8. It can be seen from this Table that liquidus temperature of this new alloy is only 575<sup>0</sup>C while that of the W319 alloy is ~600<sup>0</sup>C. Therefore, the superheat temperature of the new alloy can be set to ~25<sup>0</sup>C lower than that of the presently used W319 alloy. This will result in additional energy and cost savings when implementing this alloy into the regular production at WAP.

**Table 7.6: The upper and lower bounds, target values, weight and importance of the response variables**

Response	Goal	Lower Bound	Target	Upper Bound	Weight	Importance
DAS ( $\mu\text{m}$ )	Minimum	51	51	70	10	10
SR ( $^{\circ}\text{C}$ )	Minimum	85	85	120	1	1
HB	Maximum	85	100	100	1	1
Latent Heat(kJ/kg)	Maximum	450	500	500	1	1
GS (microns)	Minimum	1890	1890	4000	1	1
Price (\$/MT)	Minimum	300	300	370	1	1

**Table 7.7: Predicted values of the responses in the as-cast condition and their desirabilities at the optimal levels of Si (10.65 wt.%) and Cu (2.08 wt.%).**

Response	Predicted Value	Desirability, $d_i$
DAS ( $\mu\text{m}$ )	62.43	0.0001
SR ( $^{\circ}\text{C}$ )	96.62	0.68
HB	85.24	0.02
Latent Heat(kJ/kg)	483.48	0.67
GS (microns)	3871.72	0.06
Price (\$/MT)	366.35	0.04

**Table 7.8: TA parameters of the optimal Al 332 Alloy with 10.65 wt.% Si-2.08 wt.% Cu predicted using Artificial Neural Network (ANN).**

TA Parameter	Predicted Value
$T_{LIQ}$	575.2 <sup>0</sup> C
$T_{E,NUC}^{Al-Si}$	571 <sup>0</sup> C
$fS_{E,NUC}^{Al-Si}$	9.0 %
$T_{E,NUC}^{Al-Cu}$	501.1 <sup>0</sup> C
$fS_{E,NUC}^{Al-Cu}$	97.7 %
$T_{SOL}$	478.1 <sup>0</sup> C

## 8. Conclusions and Recommendations

### 8.1 Introduction

The primary objective of this dissertation was the quality control and improvement of the W319 alloy cast engine blocks produced at the Windsor Aluminum Plant (WAP). Initially, the present Quality Control system at WAP was critically evaluated and the areas for improvement were recognized. Based on the suggestions of this work, some of the recommendations (for example, new control limits for Sn and Pb, and optimum maintenance period for the Cosworth pump) have already been implemented at WAP. The decision from the top management of the NEMAK Canada and Ford Motor Company is awaited to implement the rest of the recommendations. Apart from this, the project has also made significant contributions to academic research as well as to the aluminum casting industry in introducing new quality control tools. The important conclusions and recommendations that are drawn from this project are listed below:

1. The comparison of the thermal characteristics of the ingot, melt and engine block bulkhead samples show that, the liquidus temperature ( $T_{LIQ}$ ) of the block samples are 7 to 8 °C higher than that of the ingot and melt samples. This is due to the macro and micro segregation of the alloying elements like Cu in the block test samples resulting in a slightly different bulkhead chemistry in the engine block bulkhead (Section 6.2).
2. The heating curve analysis using UMSA can be used as a tool for the benchmarking of the ingot suppliers. The start temperature of the alloy melting ( $T_m$ ) can be used as the criterion for grading of the ingots. Higher  $T_m$  value implies that the maximum dissolution of the Cu rich phases can be attained in a shorter time, because a higher TSR temperature can be used in the TSR furnace without the danger of incipient melting (Section 6.2.1). Therefore, thermal characterization of the ingots using UMSA heating curve analysis is recommended as a tool for the certification of the ingots.
3. The Repeatability and Reproducibility (R&R) studies of AITAP and Alu-Delta have shown that the Alu-Delta TA system is not capable of detecting the day to day

variations in the WAP process, whereas ALTAP is able of detecting the small but important day to day variations. Therefore, it is highly recommended that the Alu-Delta TA system be replaced with the ALTAP, along with the Unbiased Melt Sampling Device (UMSD) (Section 6.3.1).

4. The Tukey control chart limits (upper and lower) were established for Thermal Analysis temperature parameters for the on-line process control at WAP using the ALTAP. These control charts will help the process engineers to distinguish between chance causes that are due to the inherent variations in the process and the variations due to assignable causes that show a real shift in the process (Section 6.3.2.2).
5. An Artificial Neural Network (ANN) model was developed for the on-line prediction of the Silicon Modification Level (SiML) of the W319 alloy using Thermal Analysis (TA) parameters. This software can be used as an on-line quality control tool in an Aluminum casting plant, that will act as an advisory system for process engineers to control the morphology of the eutectic silicon particles (Section 6.4).
6. The statistical analysis of the WAP process parameters (eg. chemistry, pump profile etc.) of south and north rollovers revealed that Fe and Mn are the only two elements that have a significant influence on the bulkhead porosity of 3.0L engine blocks. When Fe and Mn levels are closer to their upper specification limits the probability of producing a low shrink porosity casting is significantly higher (0.73). An operating window has been created to control the Fe and Mn levels during regular production at WAP. The operating window for Fe is from 0.36 to 0.39 wt.% and for Mn is from 0.24 to 0.26 wt.%. The size of this operating window is very narrow because it has been set up using the current chemistry data from WAP and therefore further research is recommended for the expansion of the size of this operating window (Section 6.5.1).
7. The UMSA metallurgical simulations of the WAP TSR and Artificial Aging processes and the statistical analysis of the melt chemistry and bulkhead hardness data as well as the Image Analysis of the 3.0 V6 engine blocks have shown that elevated levels of Sn (~400 ppm) and Pb (~300 ppm) significantly reduce the Brinell Hardness (HB) of the engine block bulkhead(s). Since Cu phases dissolve well during solution treatment (in the presence of elevated levels of Sn), Sn may be suppressing the

formation of the Cu strengthening precipitates during Artificial Aging (Section 6.5.2.4). In addition to this, high levels of Sn and Pb were found to lower the start temperature of the W319 alloy melting. This temperature is the maximum safe TSR furnace temperature without the occurrence of incipient melting. Therefore, it has been recommended to WAP management to revise the existing control limits for Sn and Pb to be 0.005 wt.% and 0.025 wt.%, respectively, and this has been implemented (Section 6.5.2.4). For these new control limits, the present TSR and Artificial Aging parameters remain unchanged.

8. The Reliability studies of the electromagnetic pump have shown that, as a result of the new Preventive Maintenance Policy adopted by WAP in 2002, the distribution of the pump life changes from exponential to extreme value distribution. The Mean Time Between Failures (MTBF) increased from 19,505 cycles to 43,904 cycles (225%). The present Preventive Maintenance Policy of 45,000 cycles exceeds the MTBF (43,904 cycles). Based on the recommendations of this work WAP has changed the pump maintenance period from 45,000 cycles to 43,000 cycles (Section 6.6.1.2).
9. The Novel Solution Treatment During Solidification (NSTS) process will eliminate the detrimental incipient melting problem of the W319 alloy that is very common with the conventional solution treatment process. NSTS is also able to homogenize (lower standard deviation in matrix microhardness across the casting) the matrix in a much shorter time (66 minutes) resulting in large cost and energy savings. The mechanical properties of the NSTS treated samples are similar to that of the conventionally heat treated 3.0 L V6 engine block mechanical properties.

This work has further demonstrated the capabilities of the Artificial Neural Network-Simulated Annealing optimization tool as discussed elsewhere in the literature. The software developed in this dissertation is a general purpose tool that can optimize the parameters of any process (Section 6.7).

The NSTS process can be incorporated into the TSR routine at WAP by slight modification of the existing equipment. The sand mold after casting should be transferred to the TSR furnace as quickly as possible. The casting may be cooled down below the solidus temperature, but can be reheated to the required solution temperature. Alternatively, the TSR furnace can be designed to have multi zones. The

first zone is for the rapid sand removal from the casting. This zone should have a higher temperature as long as the sand continues to shield the castings from exposure to temperatures above 540<sup>0</sup>C to avoid the Si eutectic melting. The second zone will bring the casting to the solution treatment temperature. The quenching and Artificial Aging can be further designed based on the resulting casting structure.

10. The previous IRC work has shown that the Si<sub>EQ</sub> methodology can be used to predict the characteristic reaction temperatures and the latent heat of solidification of 3XX aluminum alloys. This work has introduced a novel method to calculate the Growth Restriction Factor (GRF) of the 3XX aluminum alloys using the Si<sub>EQ</sub> methodology. The GRF was found to have a linear relationship with the Grain Size (GS) for 3XX Al alloys having Si contents from 5-11 wt.% (Section 7.2).
11. A novel method has been proposed to calculate the latent heat of solidification of the multicomponent hypoeutectic 3XX Al alloys using cooling curve Thermal Analysis (TA). The fraction solid at the Al-Si eutectic nucleation point ( $f_s^{Al-Si}_{E,NUC}$ ) was found to have a negative linear correlation with the latent heat of solidification. Therefore, TA can be used as an inexpensive and simple way to calculate the latent heat of solidification of 3XX Al Alloys as compared to Differential Scanning Calorimetry (DSC) (Section 7.3).
12. Artificial Neural Networks (ANN) were found to predict the thermal characteristics (Temperatures and fraction solid) of the 3XX Al Alloys accurately (Section 7.3.1). Therefore, a trained neural network can be used as an on-line Quality Control Tool at ingot and casting plants, and can be used to design new alloys and processes and for the computer modeling of the solidification processes.
13. A new alloy (Al 332) (Si=10.5 wt.% and Cu=2.0 wt.%) has been developed by optimizing the Si and Cu levels of the 3XX Al Alloys that will improve the cast component characteristics and will lower the alloy price (Section 7.3). It has been recommended that this alloy should replace the presently used W319 alloy at WAP. The predicted structural and thermal characteristics of this alloy were found to satisfy the WSE-M2A-151-A2/A4 Engineering Specification requirements (Section 7.4).



## 8.2 Scope for Future Work

This dissertation has opened avenues for further academic and industrial research in the metallurgy of Aluminum-Silicon castings. This work has shown that neural networks in combination with Thermal Analysis can be used to predict the Silicon Modification Level of the W319 Alloy. Based on the encouraging results in this work, future step will be to extend the predictive abilities of the ANN to more metallurgical parameters such as Dendrite Arm Spacing, Grain Size, Area Percent of Cu Rich Phases, and Area Percent Porosity of the cast components.

An operating window for Fe and Mn (Conclusions 6) has been created as a guideline for the regular production at WAP so as to minimize shrink porosity levels in the engine bulk bulkhead. However, Taylor (1999b) reports that the “critical Fe content” for an Al alloy that has a Si level similar to that of W319 is 0.5 wt.%, where porosity is at a minimum. Therefore, there is a good chance that the size of this operating window can be increased (by increasing the levels of Fe and Mn), and can be maintained at no additional cost. In order to do this, the effect of Fe levels above 0.4 wt.% on shrink porosity formation should be studied and the “critical Fe content” for the W319 alloy should be established by conducting further research in this area.

The optimal alloy (Al 332) proposed in Conclusions 13, needs to be studied through actual plant trials and verification of cast component characteristics. The cast component characteristics of the engine blocks manufactured with the new alloy need to be compared with the W319 alloy engine blocks before implementing the alloy into the regular production of the engine blocks at WAP. Moreover, since the Si level of the new alloy is higher (10.5 wt.%), most likely a higher level of Fe up to 0.7 wt.% could be used in this alloy. This will further reduce the price of the alloy. Therefore, further studies are suggested to optimize the Fe and Mn levels of the newly proposed alloy.

Even though the processes and raw materials are quite different, the PWQC approach presented in this dissertation for the WAP could be applied to the Quality Control and Improvement of other casting facilities as well. The analysis of the present QC system will help to identify the areas where critical control and further improvement are necessary. The statistical analysis of the process data will enable the process engineers

to identify the important process parameters, and hence to introduce additional quality control tools (eg. control charts, revision of the present specification limits, Preventive Maintenance of critical machinery, optimization of the process parameters etc.) to closely monitor these parameters. This will minimize the process variability and will ensure consistent product quality. Introducing a new alloy or a new process may result in a quantum leap in the product quality. However, this would require a large initial capital investment. Therefore, engineering economic analysis should be performed between the existing process and the new process before making a decision to introduce a new process.

# **Appendix 1: Calibration of the Thermal Analysis Platform**

## **1.0 Introduction**

In order to achieve the highest degree of accuracy and precision in the temperature measurements, the AITAP and UMSA TA platforms were calibrated before the Thermal Analysis experiments. This was achieved by calibrating the TA platform against a National Institute Standards and Technology (NIST) traceable Resistance Temperature Detector (RTD) Probe. The procedure for the calibration of AITAP is explained in detail in the following sections. The calibration procedure for the UMSA is exactly the same as AITAP except that the TA platform that measured the temperature was UMSA instead of AITAP (See Figure 3). Both AITAP and UMSA used thermocouple for measuring the temperature. Therefore, a brief introduction to thermocouples is presented below.

## **1.1 Introduction to Thermocouples**

A thermocouple is a sensor for measuring temperature. The working principle of a thermocouple is the Seebeck effect. The Seebeck effect states that when two dissimilar metal wires are connected with each other in a loop to form two junctions that are maintained at two different temperatures a voltage potential or electro-motive force (emf) will be generated and the current will flow through the loop circuit. The current will be proportional to the difference in temperature between the junctions and the metals used. Thermocouples are available in different combinations of metals. The four most common types of thermocouples are J, K, T, and E. Each type has a different temperature range of operation, although the maximum temperature varies with the diameter of the wire used in the thermocouple (Northern Illinois University, 2001). The most commonly used thermocouple types and their temperature ranges are given in the Table 1.

The thermocouple that was used by the NSERC/Ford-NEMAK/University of Windsor Industrial Chair (IRC) in Light Metals Casting Technology for Thermal Analysis (TA) was Type K.

**Table 1: Thermocouple Types and Temperature Ranges (Omega Engineering Inc., 2000)**

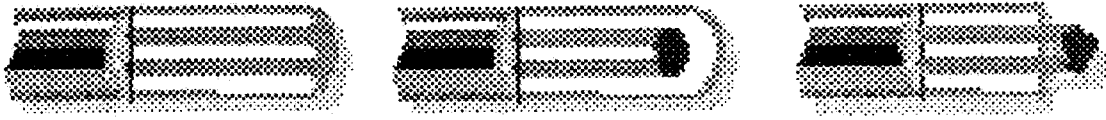
<b>Thermocouple Type</b>	<b>Thermocouple Alloy</b>	<b>Maximum Working Temperature (°C)</b>	<b>Comments</b>
J	Iron - Constantan	870 °C	Suitable for reducing atmospheres
K	Chromel - Alumel	1260 °C	Recommended for use in clean oxidizing atmospheres.
T	Copper - Constantan	400 °C	Recommended for mildly oxidizing and reducing atmospheres. Suitable for applications where moisture is present.
E	Chromel - Constantan	870 °C	This thermocouple has the highest emf output of any standard metallic thermocouple.

The solidification range of the Al 319 alloy is from 610 °C to 495 °C and the solidification range of the Al 356 alloy is from 610 °C to 540 °C. The Type K thermocouple is made of chromel alloy and alumel alloy. The nominal composition of chromel alloy is Ni-10 Cr and that of alumel alloy is Ni-3Mn-2Al-1Si (Kinzie, 1973). Alumel alloy is the negative leg and chromel alloy is the positive leg of the Type K thermocouple.

Sheathed thermocouple probes are available with one of the three junction types: grounded, ungrounded, or exposed. At the tip of the grounded junction probe, thermocouple wires are physically attached to the inside of the probe wall. This results in good heat transfer from the outside, through the probe wall to the thermocouple junction. In an ungrounded probe the thermocouple junction is detached from the probe wall. The response time is slowed down from the grounded style but this offers electrical isolation. In the exposed junction style, the thermocouple protrudes out of the tip of the sheath and is exposed to the surrounding environment. This type offers the best response time but is limited in use to non-corrosive and non-pressurized applications (Omega Engineering Inc., 2001). Figure 1 illustrates the three junction types discussed above.

## **1.2 Calibration of the RTD Probe**

The goal of the calibration is to quantitatively relate measurements made using one measurement platform (AITAP) to that of another (Resistance Temperature Detector (RTD)) (NIST, 2001). The RTD probe used by the IRC was calibrated in an International Standards Organization (ISO) certified laboratory located in Windsor (ISO-10012). The certificate of calibration is shown in Figure 2. This means that the IRC's RTD probe is traceable to NIST (National Institute of Standards and Technology) standards. During the calibration, the temperature measured by the thermocouple is related to the true temperature using a regression equation. The true temperature is calculated from the calibration data of the RTD probe as seen in the attached certificate (See Figure 2). A calibration curve is also constructed by plotting the true temperature versus the thermocouple temperature. This procedure is explained in detail in subsequent pages.



# Grounded Ungrounded Exposed

Figure 1: Different types of thermocouple junctions (Omega Engineering Inc., 2001).

**ISOLAB Inc.**  
**Calibration Services**  
 7475 Tranby Ave. Windsor, Ont N8S 2B7

**Appendix 1**

---

**Certificate of Calibration**

02/11/2000	Certificate Number: 350001	Page
<b>Gage ID:</b> 0035-T2113-5206 <b>Gage S/N:</b> T 2113-5206 <b>Description:</b> Omega Digital RTD Thermometer <b>Unit of Meas:</b> Multiple <b>Cal. Date:</b> 02/10/2000 <b>Next Due:</b> 02/10/2001 <b>Pass:</b> Yes		<b>Location:</b> Ford IRC, Essex Hall 209 <b>Cal. Freq.:</b> 12 MONTHS <b>Customer Information:</b> University of Windsor IRC, Essex Hall 209 2807 Union St. Windsor, ON N8S 3P4

**Certification Statement:** It is hereby certified that the above described instrument conforms to the original manufacturer's specifications and has been calibrated using standards whose accuracies are traceable to the National Institute of Standards and Technology (NIST) and/or the National Research Council (NRC) or have been derived from accepted values of natural physical constants or have been derived by the ratio type of self calibration techniques. Our calibration system satisfies ISO-9000. ISOLAB is assessed to ISO-10012.

**Procedure Name:**

<b>Findings:</b> Manufacturer's specification for Unit/Probe System combination is 0.1 up to 200 C and 0.2 at 400 C Probe ID#507911338 reads 0.2 C/100.75 ohms in ice bath.	<b>Environmental Conditions</b> Temp.: 21 C Humidity: 39 %
---	--

↓

Standard ID	Minimum Uncertainty	Nominal Units	Maximum Toler	Before After	Accuracy	Fail Before Fail After	Limit
Point 1 (225.69 ohms)	349.800	350.000	350.200	349.907	-0.093	No	No
AD15 - Crompton Decade Box - Due Dec '00		deg C	V	349.907	-0.093	No	No
Point 2 (247.08 ohms)	399.800	400.000	400.200	399.905	-0.095	No	No
AD15 - Crompton Decade Box - Due Dec '00		deg C	V	399.905	-0.095	No	No
Point 3 (254.14 ohms)	449.800	450.000	450.200	449.899	-0.107	No	No
AD15 - Crompton Decade Box - Due Dec '00		deg C	V	449.899	-0.107	No	No
Point 4 (280.93 ohms)	499.800	500.000	500.200	499.870	-0.130	No	No
AD15 - Crompton Decade Box - Due Dec '00		deg C	V	499.870	-0.130	No	No
Point 5 (297.43 ohms)	549.800	550.000	550.200	549.892	-0.108	No	No
AD15 - Crompton Decade Box - Due Dec '00		deg C	V	549.892	-0.108	No	No
Point 6 (313.85 ohms)	599.800	600.000	600.200	599.909	-0.091	No	No
AD15 - Crompton Decade Box - Due Dec '00		deg C	V	599.909	-0.091	No	No
Point 7 (329.57 ohms)	649.800	650.000	650.200	649.980	-0.020	No	No
AD15 - Crompton Decade Box - Due Dec '00		deg C	V	649.980	-0.020	No	No

Calibrated by: [Signature] Date: Feb 10/00  
 Approved by: [Signature] Date: Feb 11, 2000

Figure 2: Calibration Certificate for the RTD Probe.

## **2. Experimental Procedure**

Figure 3 and Figure 4 show the experimental set up for calibration. The experimental set up consists of a Desk Top computer loaded with the Aluminum Thermal Analysis Platform (AITAP) software. AITAP has been developed using the National Instruments Labview™ graphical programming language. The computer is connected to the National Instruments SCXI Data Acquisition System that collects thermocouple(s) temperature data for a given time frame. AITAP plots the time-temperature curve and saves it as a Microsoft Excel™ Comma Separated Values (.csv) file. The technical specifications of the thermocouples that were calibrated are given in Table 2. In the remainder of the text, the three kinds of thermocouples were identified as 0.062”, 0.040”, and Low Mass respectively. Six thermocouples were inserted into the brass cylindrical block of a Carbolite® (Model EURO THERM 902P) furnace. The RTD probe was also inserted into the block from the opposite side as shown in Figure 3. The model of the RTD probe was OMEGA DP95. It can measure temperatures from  $-199^{\circ}\text{C}$  to  $800^{\circ}\text{C}$ . The furnace can be heated up to maximum of  $1200^{\circ}\text{C}$ . The heating process in the furnace can be programmed. The graph in Figure 5 explains the heating program used for the calibration.

First, the furnace was heated to  $200^{\circ}\text{C}$  for 30 minutes (ramping). Then the furnace stayed at this temperature for 30 minutes (dwelling). The furnace temperature stabilized around the set point after 15 minutes of dwelling. At this point AITAP was started and the temperature data was recorded for 15 minutes. The RTD temperature was also recorded manually, at intervals of 30 seconds for the same period. Then the program rises the temperature to the next set temperature ( $275^{\circ}\text{C}$ ). The temperatures were recorded when the RTD temperature stabilized around  $275^{\circ}\text{C}$ . The same procedure was repeated and the temperatures were recorded for other set points (i.e.  $350^{\circ}\text{C}$ ,  $425^{\circ}\text{C}$ ,  $500^{\circ}\text{C}$ ,  $575^{\circ}\text{C}$ ,  $650^{\circ}\text{C}$ , and  $725^{\circ}\text{C}$ ). This covers the temperature range of interest for the IRC.

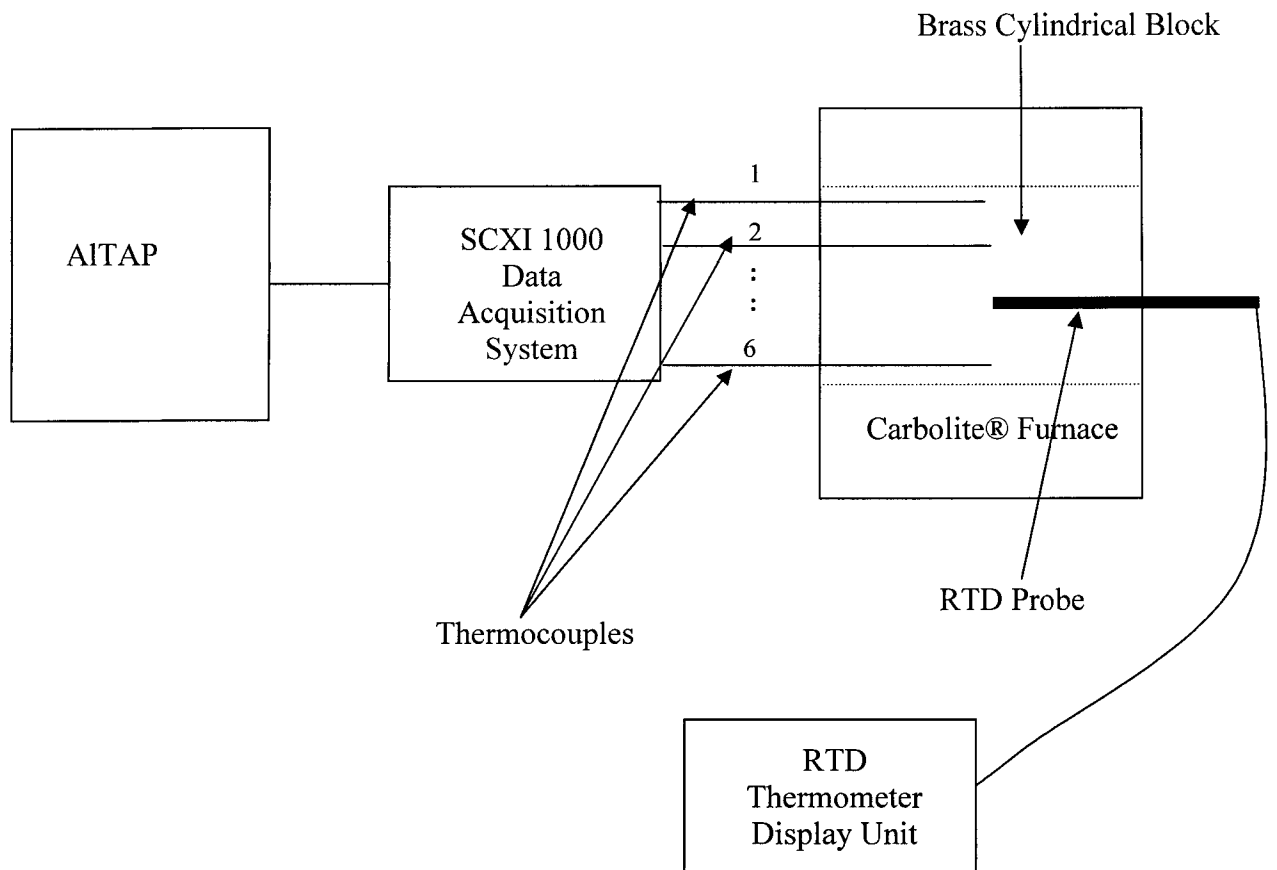


Figure 3: Schematic Diagram of the Experimental Setup for the Calibration of the AITAP.

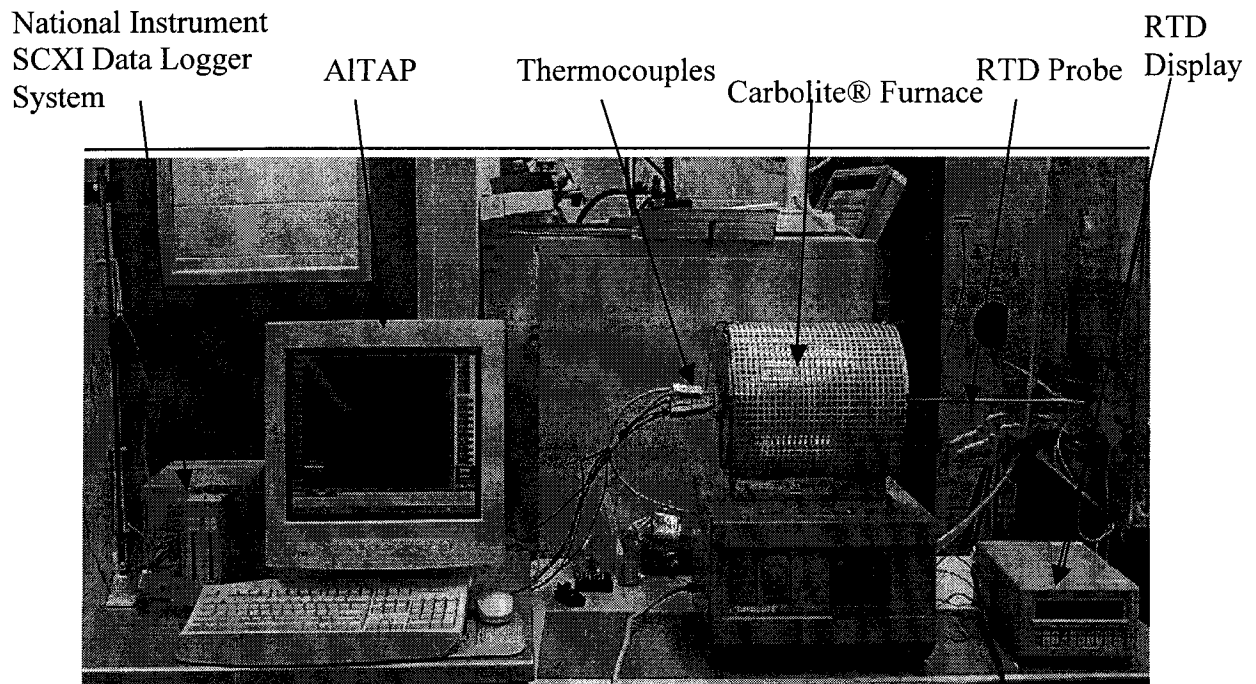


Figure 4: Photograph of the experimental set up for the calibration of AITAP.



**Table 2: Technical details of the calibrated Thermocouples: Type K, Length = 6”(152.4 mm).**

Number of Thermocouples calibrated	Thermocouple Outer Diameter in/mm	Sheathing Material	Thermocouple Wire Diameter in/mm	Junction Type	Manufacturer
2	0.062”/ 1.57	304 SS	0.010”/ 0.25	ungrounded	Omega
2	0.040”/ 1.02	304 SS	0.006”/ 0.15	ungrounded	Omega
2	0.045”/ 1.14 (Low Thermal Mass)	No sheath (base ceramic)	0.0055”/ 0.14	exposed	IRC

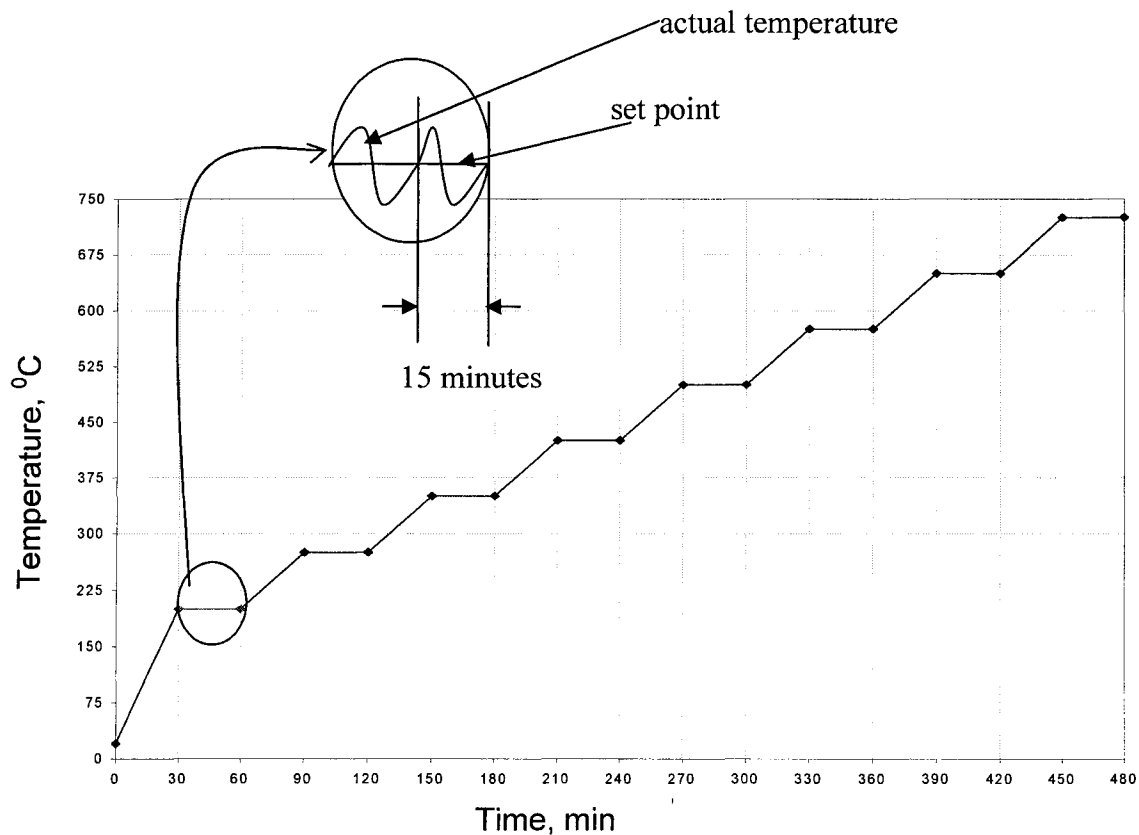


Figure 5: Heating program for calibration of ALTAP. The zoomed section in the inset shows the actual temperature variation around the set point. The 15 minute temperature recording period is also shown.

### 3. Results and Discussion

A calibration curve was plotted (Figure 6) for the RTD probe using the Isolab Inc. calibration data. A linear regression equation was established between the True Temperature ( $T_{TRUE}$ ) and the temperature measured by the RTD ( $T_{RTD}$ ). The equation and the coefficient of determination ( $R^2$  value) of the equation are given below:

$$T_{TRUE} = 0.99983 * T_{RTD} + 0.17272 \dots\dots\dots (1)$$

$$R^2 = 0.99999992$$

The temperatures of the RTD probe recorded during the experiment at each set point were converted to the True Temperature using the equation 1 in the following generalized form:

$$(T_{TRUE})_{i,j} = 0.99983 * (T_{RTD})_{i,j} + 0.17272 \dots\dots\dots (2)$$

$i = 1, 2, \dots, 31; j = 1, 2, \dots, 8.$

$j$  represents the 8 chosen set points: 200 °C, 275 °C, ....., and 725 °C.

$(T_{TRUE})_{i,j}$  = The True Temperature at the  $i^{th}$  point of time for the  $j^{th}$  set point.

$(T_{RTD})_{i,j}$  = The RTD Temperature at the  $i^{th}$  point of time for the  $j^{th}$  set point.

During the calibration process the temperature of the thermocouple that was measured by the ALTAP was related to the True Temperature. The mean of the 31 temperature readings recorded over the 15 minutes was calculated at each set point for the True Temperature ( $\bar{T}_{TRUE}$ ) and for the Thermocouple Temperature ( $\bar{T}_{TC\alpha}$ ) using the following equations:

$$(\bar{T}_{TRUE})_j = \sum_{i=1}^{31} \frac{(T_{TRUE})_{ij}}{31}; j=1, 2, \dots, 8 \dots\dots\dots (3)$$

$$(\bar{T}_{TC\alpha})_j = \sum_{i=1}^{31} \frac{(T_{TC\alpha})_{ij}}{31}; j=1, 2, \dots, 8 \dots\dots\dots (4)$$

$(\bar{T}_{TRUE})_j$  = The mean True Temperature at the  $j^{th}$  set point.

$(\bar{T}_{TC\alpha})_j$  = The mean Thermocouple Temperature at the  $j^{th}$  set point.

$(T_{TC\alpha})_{ij}$  = The Thermocouple Temperature at the  $i^{th}$  point of time for the  $j^{th}$  set point.

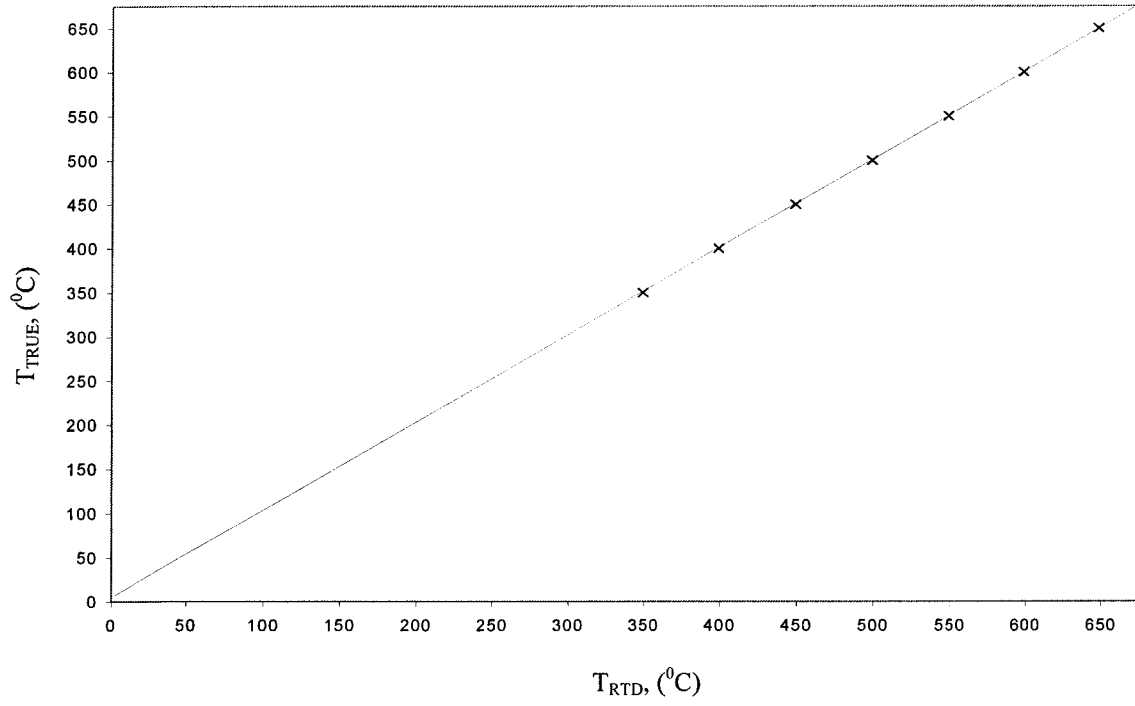


Figure 6: The Calibration Curve for the RTD probe.

Using this data the calibration curves were plotted and are shown in Figure 7, Figure 8, and Figure 9. The linear and quadratic regression equations relating  $(T_{TRUE})$  and the Thermocouple Temperature before calibration  $(T_{TC\alpha})$  are also given (equations 5-10). The corresponding coefficient of determination ( $R^2$  values) values are also presented.

### 3.1 Analysis of the Measurement Error

The absolute mean percentage error of the thermocouples was calculated at each set point using the equation 11 (Nicholas and White, 1994):

$$(\%ME_{\alpha})_j = \left[ \frac{(\bar{T}_{TRUE})_j - (\bar{T}_{TC\alpha})_j}{(\bar{T}_{TRUE})_j} \right] * 100; j = 1, 2, \dots, 8. \quad (11)$$

where,

$(\%ME_{\alpha})_j$  = Absolute mean percentage error in the measurement at the  $j^{\text{th}}$  set point

$(\bar{T}_{TRUE})_j$  = Mean True Temperature at the  $j^{\text{th}}$  set point.

$(\bar{T}_{TC\alpha})_j$  = Mean Thermocouple Temperature at the  $j^{\text{th}}$  set point.

$$(\bar{T}_{TRUE})_j = \sum_{i=1}^{31} \frac{(T_{TRUE})_{ij}}{31}; j=1, 2, \dots, 8. \quad (12).$$

$$(\bar{T}_{TC\alpha})_j = \sum_{i=1}^{31} \frac{(T_{TC\alpha})_{ij}}{31}; j=1, 2, \dots, 8. \quad (13).$$

$j$  represents the 8 chosen set points

$(T_{TRUE})_{ij}$  = True temperature at the  $i^{\text{th}}$  point of time for the  $j^{\text{th}}$  set point.

$(T_{TC\alpha})_{ij}$  = Thermocouple temperature at the  $i^{\text{th}}$  point of time for the  $j^{\text{th}}$  set point

The absolute mean percentage errors  $(\%ME_{\alpha})_j$  were plotted against the set point for the three kinds of thermocouples that were calibrated. The graphs are shown in Figure 10, Figure 11, and Figure 12. The measurement error at the  $i^{\text{th}}$  point of time for the  $j^{\text{th}}$  set point is given by (Nicholas and White, 1994):

$$(E_{\alpha})_{ij} = (T_{TRUE})_{ij} - (T_{TC\alpha})_{ij}; i=1, 2, 3, \dots, 31; j=1, 2, \dots, 8. \quad (14).$$

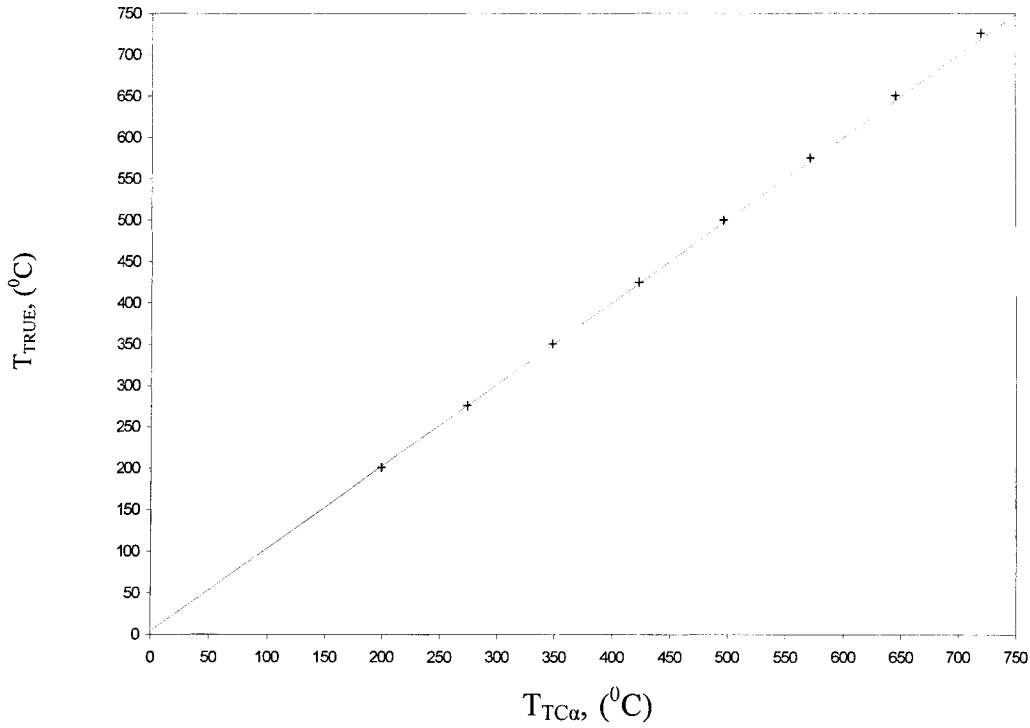


Figure 7: Calibration Curve for the 0.062” Thermocouple.

$$T_{\text{TRUE}} = 1.00951 * T_{\text{TC}\alpha} - 1.67295 \quad (5)$$

$$R^2 = 0.99999742.$$

$$T_{\text{TRUE}} = 0.0000064 * T_{\text{TC}\alpha}^2 + 1.00368 * T_{\text{TC}\alpha} - 0.51524 \quad (6)$$

$$R^2 = 0.99999830.$$

It can be seen from the above equations that the  $R^2$ -values of the linear and quadratic equations differ only in the sixth decimal place. This shows that the linear regression is sufficient for calibration and therefore, the algorithm used by ALTAP for calibration is the linear regression.

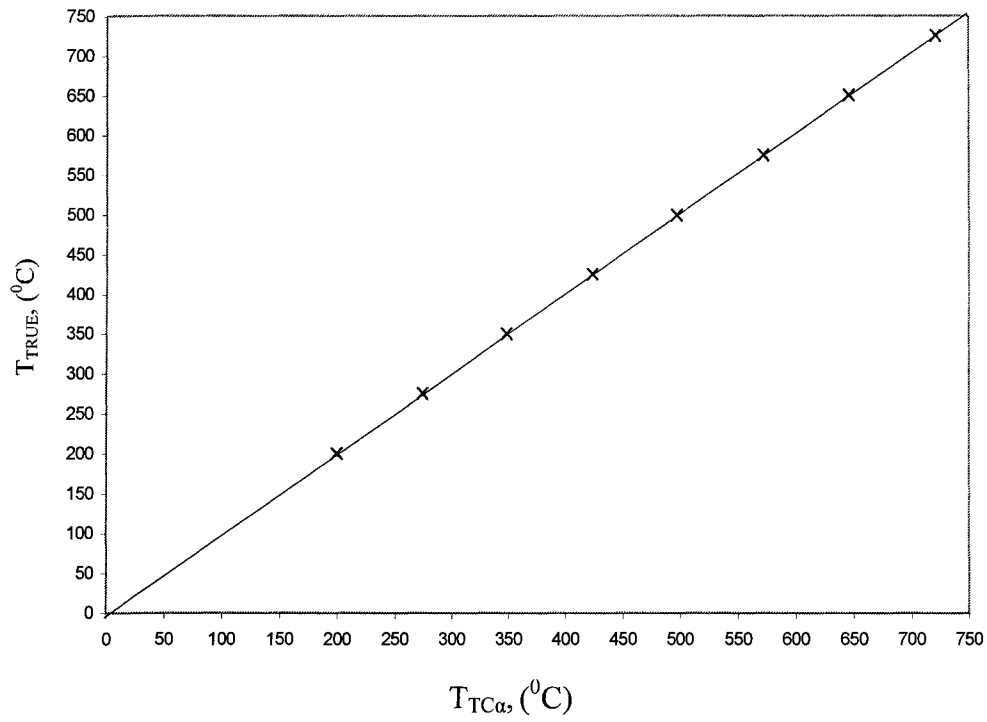


Figure 8: Calibration Curve for the 0.040'' Thermocouple.

$$T_{\text{TRUE}} = 1.00799 * T_{\text{TC}\alpha} - 1.42982 \quad (7)$$

$$R^2 = 0.99999939$$

$$T_{\text{TRUE}} = 0.0000017 * T_{\text{TC}\alpha}^2 + 1.00639 * T_{\text{TC}\alpha} - 1.11126 \quad (8)$$

$$R^2 = 0.99999945$$

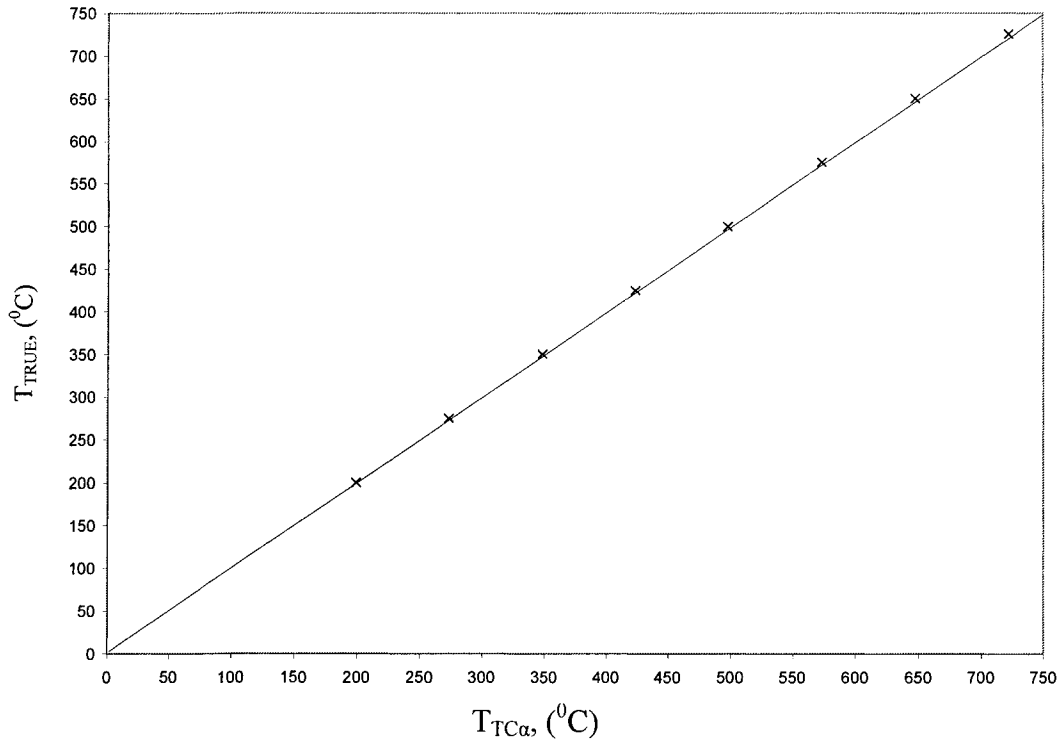


Figure 9: Calibration Curve for the Low Thermal Mass Thermocouple.

$$T_{TRUE} = 1.00333 * T_{TC\alpha} + 0.70325 \quad (9).$$

$$R^2 = 0.99999580$$

$$T_{TRUE} = 0.00000085 * T_{TC\alpha}^2 + 1.00254 * T_{TC\alpha} + 0.85832 \quad (10).$$

$$R^2 = 0.99999582$$

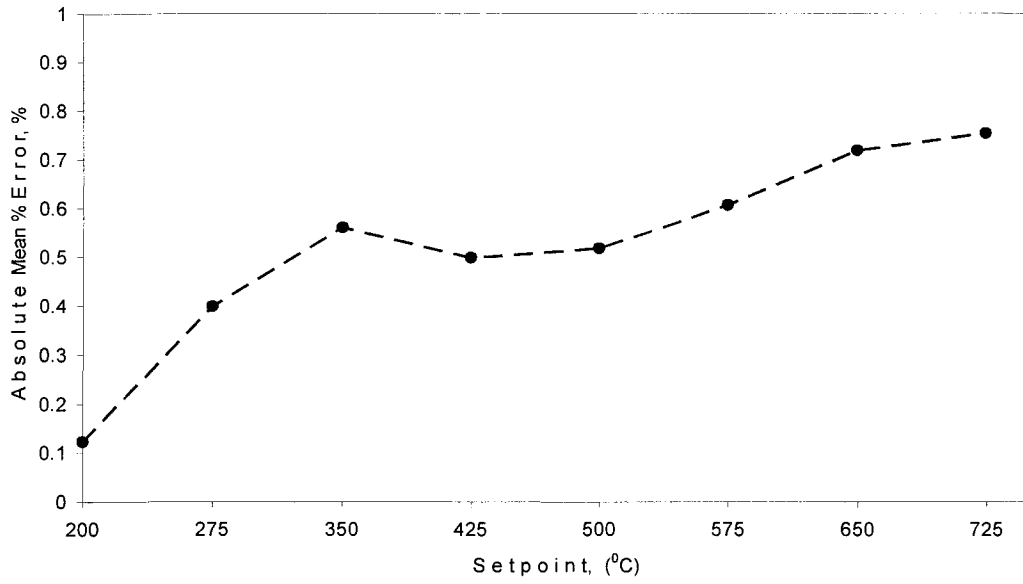


Figure 10: Absolute Mean Percentage Error of the 0.062” thermocouple (%ME<sub>a</sub>).

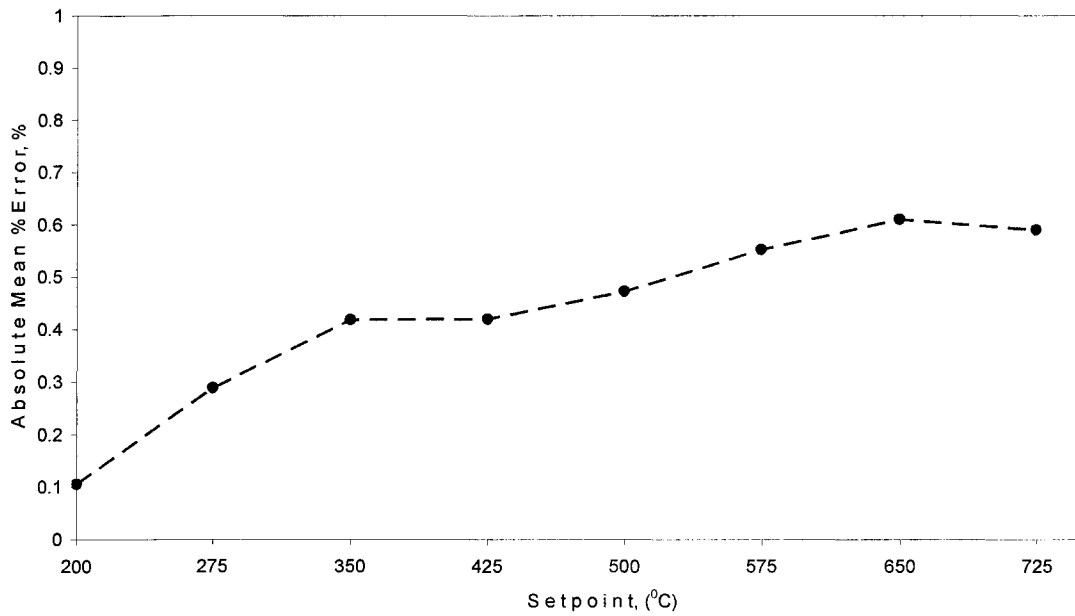


Figure 11: Absolute Mean Percentage Error of the 0.040” thermocouple (%ME<sub>a</sub>).



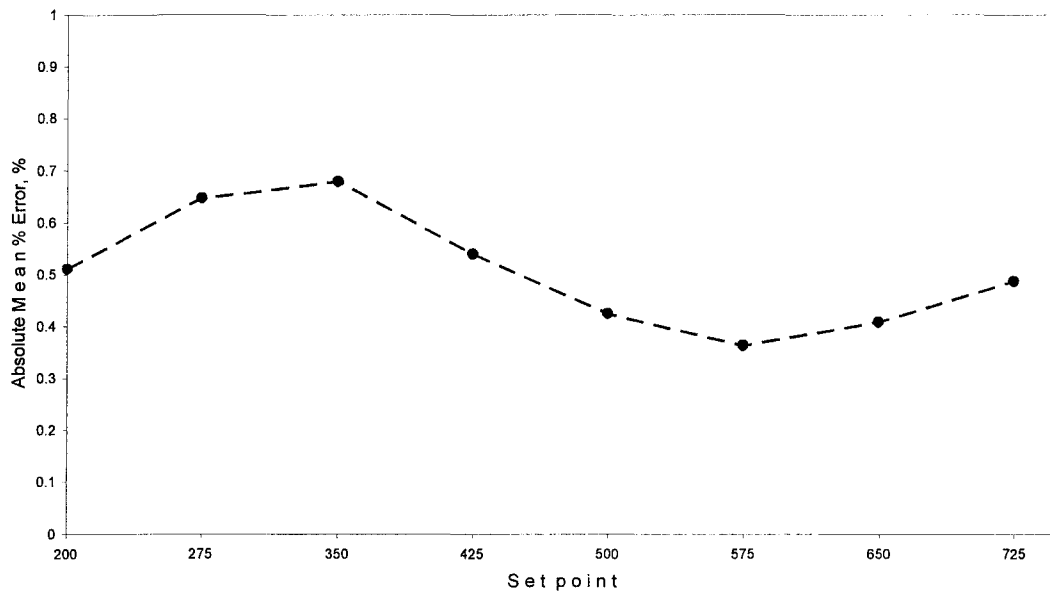


Figure 12: Absolute Mean Percentage Error of the Low Thermal Mass Thermocouple (%ME<sub>α</sub>).

The distribution of this error was tested at the set points using a probability plot and was found to have a normal distribution. For example, the probability plots of the 3 kinds of thermocouples at the set point 575 °C are shown in Figure 13. Since all the data points were plotted between the 95% confidence intervals, the assumption of normal distribution is reasonable (Minitab, 2000). The statistical software Minitab™ was used for this analysis. Since the population is normally distributed with an unknown mean and unknown variance, a random sample of the distribution would follow a student t-distribution (Montgomery, 1999). Using the t-statistic the 95% confidence intervals of the thermocouple temperature were computed for three selected set points: 500 °C, 575 °C, and 650 °C. The results are given in the following Tables 3, 4, and 5.

### 3.2 Calibration of the AITAP

A calibration file, which contained the mean True Temperature  $(\bar{T}_{TRUE})_j$  values and the mean thermocouple temperature values  $(\bar{T}_{TC\alpha})_j$  at each set point, was created for each kind of thermocouple. A sample calibration file is shown in Figure 14. The extension of this file is “.cal”. By entering the respective calibration file name in the AITAP software, the calibration and was executed during the real time temperature measurements. See Figure 15. The regression equation was applied to correct the measured temperature before writing the data to a file.

### 4. Conclusions

- The TA platforms were calibrated by using a calibrated RTD probe.
- The algorithm used by AITAP and UMSA for calibration was linear regression. The calibration curves showed that a linear fit was sufficient because the R<sup>2</sup>- value of the linear equation differed from that of the quadratic equation only in the sixth decimal place. The software of the TA platform corrected its measured temperature to the true temperature by applying the linear regression equation before writing the temperature data to the ‘.csv’ file.
- The distribution of the measurement error was normal and the confidence intervals of the error could be established using the student t-statistic.

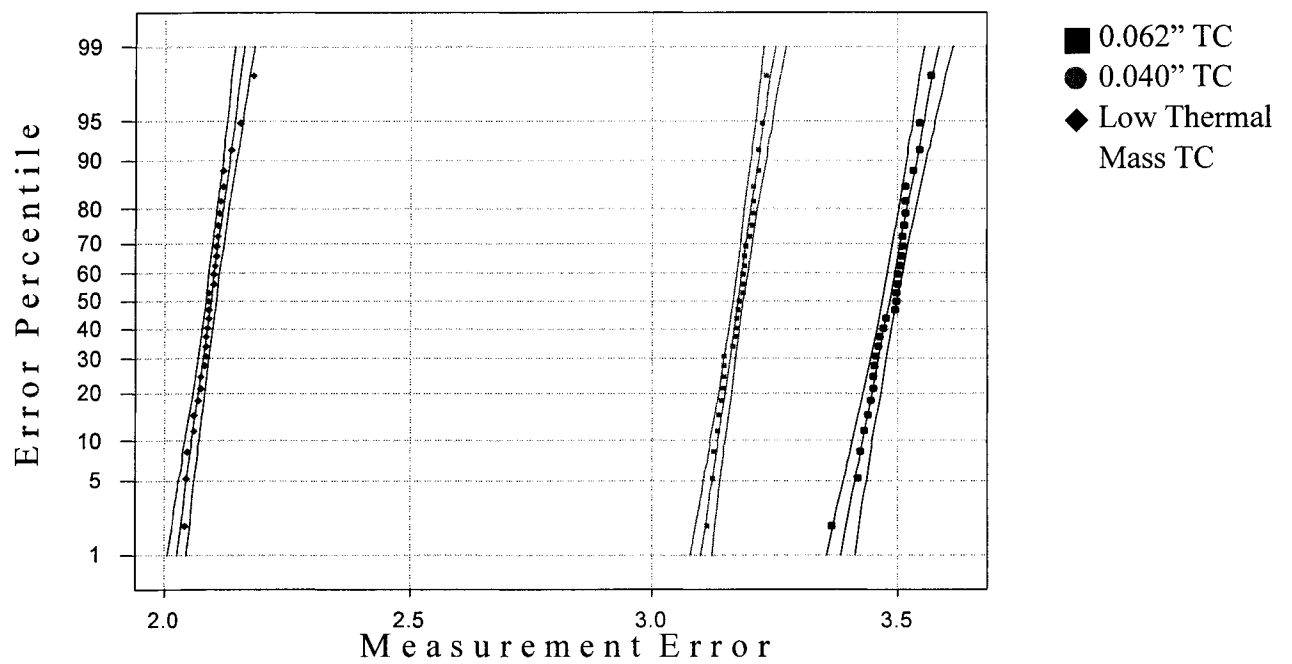


Figure13: Normal Probability plots of the measurement errors for the thermocouples at the set point 575 °C

**Table 3: 95% Confidence Intervals (CI) for the 0.062” thermocouple**

Set point °C	$(\bar{T}_{TC\alpha})_j$ °C	Lower CI °C	Upper CI °C
425 °C	422.863	422.846	422.880
500 °C	496.684	496.697	496.671
575 °C	571.463	571.448	571.479
650 °C	645.462	645.449	645.476

**Table 4: 95% Confidence Intervals (CI) for the 0.040” thermocouple**

Set point °C	$(\bar{T}_{TC\alpha})_j$ °C	Lower CI °C	Upper CI °C
425 °C	423.199	423.188	423.209
500 °C	496.932	496.922	496.943
575 °C	571.771	571.76	571.78
650 °C	646.166	646.155	646.178

**Table 5: 95% Confidence Intervals (CI) for the Low Mass thermocouple**

Set point °C	$(\bar{T}_{TC\alpha})_j$ °C	Lower CI °C	Upper CI °C
425 °C	422.687	422.674	422.699
500 °C	497.147	497.138	497.157
575 °C	572.856	572.845	572.867
650 °C	647.478	647.463	647.493

TRUE-TEMP.	"0.040"" TC"
199.6679032	199.5974155
274.7051935	274.0409703
350.3000000	348.4535032
424.8773871	423.1985819
499.1753548	496.9318752
574.8686129	571.7714458
650.0660645	646.1664110
725.3042581	721.0787606

Figure 14: Calibration file for the 0.40” Thermocouple.

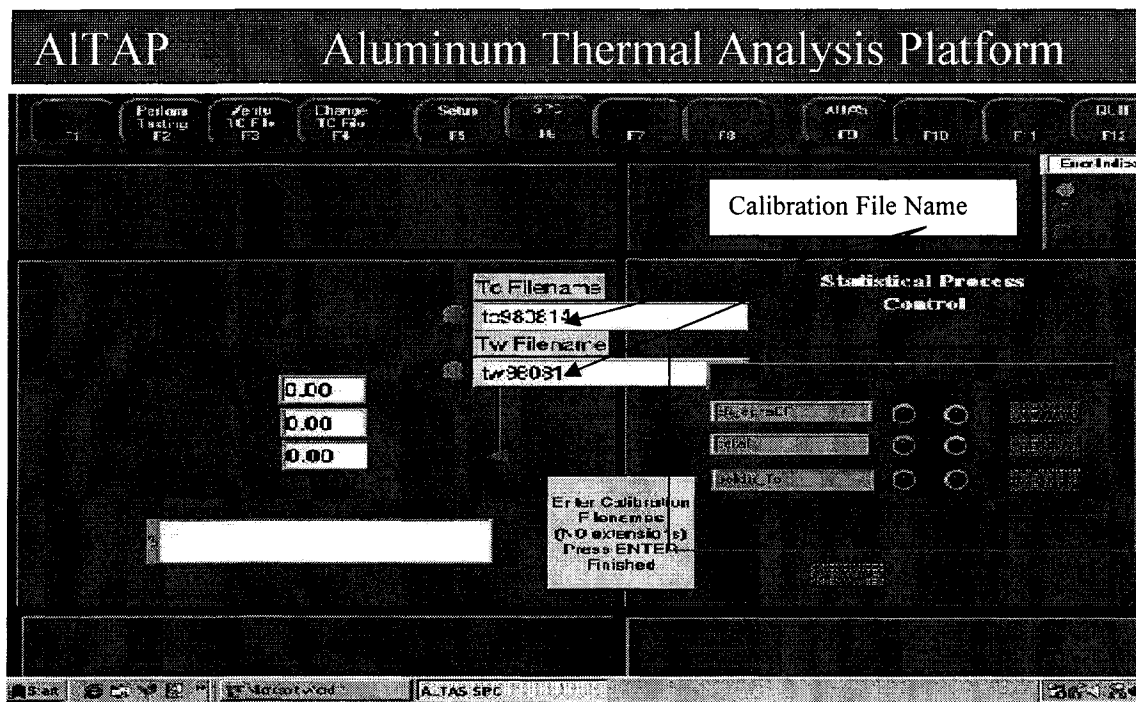


Figure 15: Inputting the Calibration file name into AITAP.

## **Appendix 2:**

### **Determination of Characteristic Thermal Analysis Parameters**

#### **2.0 Introduction**

This Appendix describes the algorithms for the detection of the characteristic TA parameters discussed in this dissertation. Although, the algorithms are explained here using the W319 alloy, it is also applicable to any Al-Si alloy. It is not easy to detect exactly the characteristic reaction temperatures directly from the cooling curve. When the First Derivative ( $dT/dt$ ) versus time ( $t$ ) is plotted, one can easily detect the TA parameters corresponding to a characteristic reaction from the sharp and sudden shifts observed in the cooling rate. Cooling rate is a synonym for the First Derivative, which is actually the rate of change of temperature in unit time. The Computer Aided Cooling Curve Analysis (CACCA) using Newtonian assumptions was used for calculation of the First Derivative, Base Line and the Fraction Solid (Kierkus and Sokolowski, 1999). Before beginning the calculations, advanced noise filtering and smoothing techniques were used to eliminate the inherent noise from the temperature data and to get a smooth signal. Figure 1 shows the cooling curve, fraction solid curve and the First Derivative curve for the W319 Al alloy used at the Windsor Aluminum Plant (WAP). The algorithms for the detection of the characteristic reaction temperatures and fraction solids are explained in the following sections:

#### **2.1 Liquidus Temperature ( $T_{LIQ}$ )**

This is the temperature at which  $\alpha$ -Al dendrites begin to solidify from the liquid. This point indicates the beginning of mass feeding.  $T_{LIQ}$  is detected using the first derivative curve. In Figure 1, the intersection point of the tangents 1 and 2 to the first derivative curve correspond to the Liquidus Temperature.

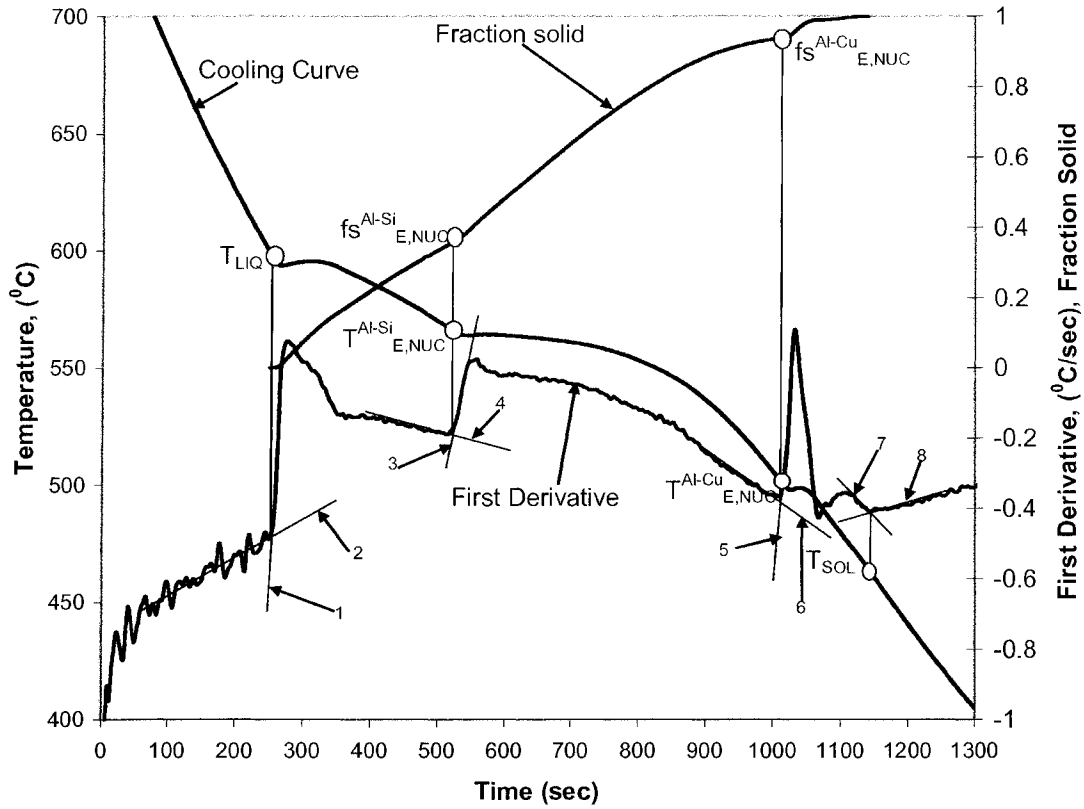


Figure 1: Cooling (Blue), First Derivative (Pink) and fraction solid (Red) curves of the W319 alloy

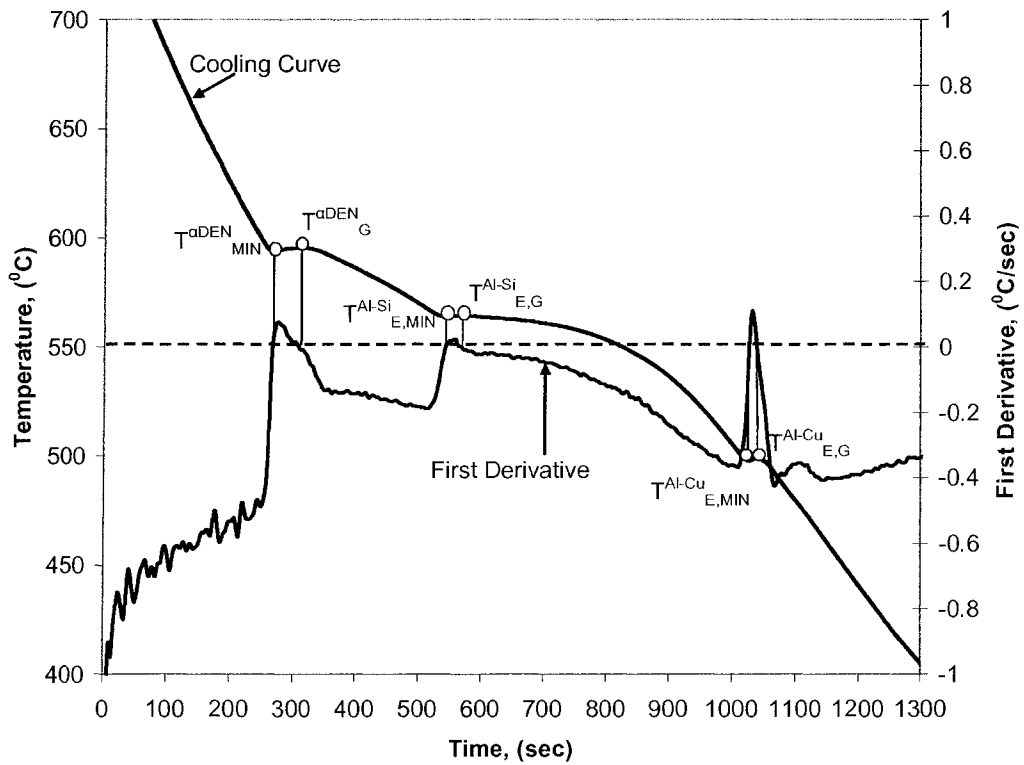


Figure 2: Determination of the minimum and growth characteristic reaction temperatures

## **2.2 $\alpha$ -Al Dendrite Undercooling Temperature ( $T^{\alpha\text{DEN}}_{\text{MIN}}$ )**

At this point the latent heat released by the growing dendrites balances the heat extracted from the sample. After this point the temperature of the melt rises to the steady state growth temperature. This point is detected as seen in Figure 2. This is the point where the value of the First derivative becomes zero for the first time.

## **2.3 $\alpha$ -Al Dendrite Recalescence Temperature ( $T^{\alpha\text{DEN}}_{\text{G}}$ )**

This is the point of maximum steady state growth of the  $\alpha$ -Al dendrites. After this point the heat loss of the sample starts again. This point corresponds to the point where the First derivative becomes zero again for the second time (Refer to Figure 2).

## **2.4 Dendrite Coherency Point Temperature (DCP) ( $T^{\alpha\text{DEN}}_{\text{COH}}$ )**

At this point the dendrite tips of neighbouring grains come in contact with each other becoming fixed at their locations and forming a skeleton throughout the sample. This point marks the transition from mass feeding to interdendritic feeding. DCP is detected using the algorithm proposed by Djurdjevic et al (2001c). In Figure 3, the point at which the First Derivative is at its maximum corresponds to the DCP. The projection of this point on the temperature axis gives the DCP temperature.

## **2.5 Dendrite Coherency Point Fraction Solid (DCP) ( $fs^{\alpha\text{DEN}}_{\text{COH}}$ )**

In Figure 3, the projection of the maximum value of the first derivative on the fraction solid curve provides the value of the DCP fraction solid.

## **2.6 Aluminum Silicon Eutectic Nucleation Temperature ( $T^{\text{Al-Si}}_{\text{E,NUC}}$ )**

When the Si composition in the remaining liquid reaches the eutectic composition, Al-Si eutectic starts to form. This point is given by the intersection of tangents 3 and 4 to the first derivative curve as seen in Figure 1.



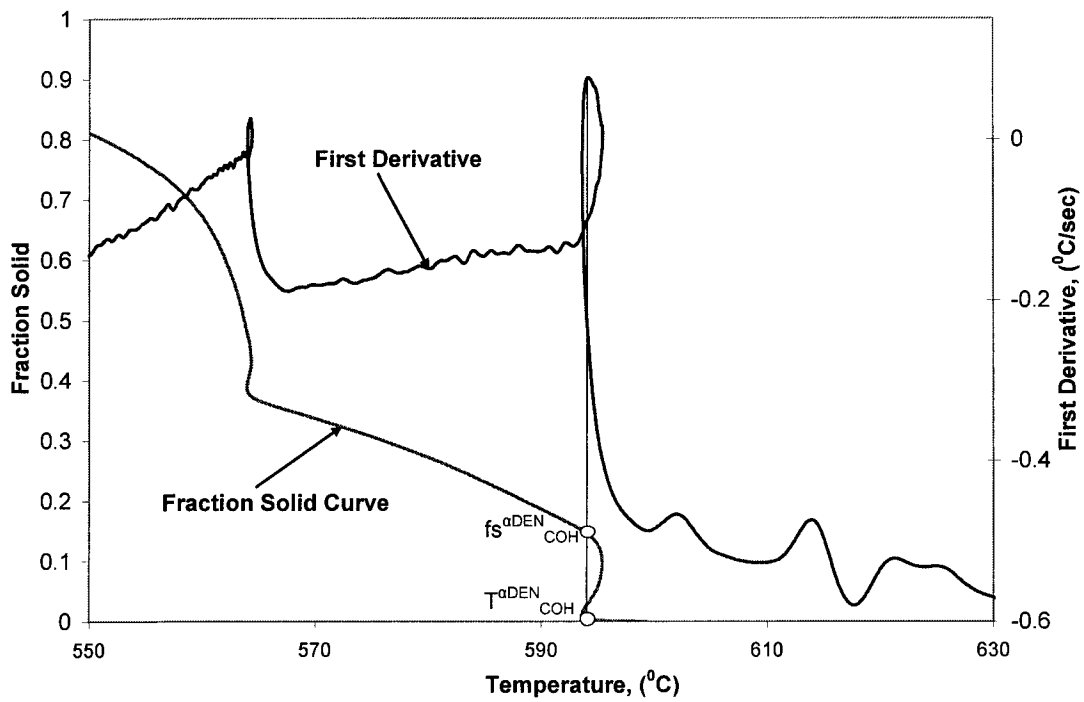


Figure 3 : Determination of the Dendrite Coherency Point (DCP) Temperature and Fraction Solid.

### **2.7 Aluminum Silicon Eutectic Nucleation Fraction Solid ( $f_s^{\text{Al-Si}}_{\text{E,NUC}}$ )**

In Figure 1, the projection of the point of intersection of tangents 3 and 4 on the fraction solid curve gives the value of the fraction solid at the nucleation of the Aluminum Silicon Eutectic.

### **2.8 Aluminum Silicon Eutectic Minimum Temperature ( $T^{\text{Al-Si}}_{\text{E,MIN}}$ )**

At this point the heat generated due to the eutectic growth becomes equal to heat loss from the test sample. In Figure 2, the point at which the value of the first derivative becomes zero for the third time corresponds to the Silicon Eutectic Minimum Temperature.

### **2.9 Aluminum Silicon Eutectic Growth Temperature ( $T^{\text{Al-Si}}_{\text{E,G}}$ )**

This point is characterized by considerable eutectic growth. This parameter is used to gauge the morphology of the Al-Si structure. From Figure 2, the point at which the value of the first derivative becomes zero for the fourth time immediately after the Al-Si eutectic minimum reaction corresponds to the Aluminum Silicon Eutectic Growth reaction temperature.

### **2.10 Aluminum Copper Eutectic Nucleation Temperature ( $T^{\text{Al-Cu}}_{\text{E,N}}$ )**

This point indicates the start of the formation of the Al-Cu eutectic as the remaining liquid becomes enriched with Cu and Si. The temperature and duration of this phenomenon can be used to establish adequate solution treatment parameters. The algorithm for the detection of this point is similar to that of algorithms for the detection of the nucleation temperatures already discussed. This is the point of intersection of tangents 5 and 6 to the first derivative curve as seen in Figure 1.

### **2.11 Aluminum Copper Eutectic Nucleation Fraction Solid ( $f_s^{\text{Al-Cu}}_{\text{E,N}}$ )**

In Figure 1, the projection of the point of intersection of tangents 5 and 6 on the fraction solid curve gives the value of the fraction solid at the nucleation of the Aluminum Copper Eutectic.

### **2.12 Aluminum Copper Eutectic Minimum Temperature ( $T_{E,MIN}^{Al-Cu}$ )**

This is the temperature at which the latent heat release due to the formation of the Al-Cu eutectic equals that of the heat loss from the sample. In Figure 2, the point at which the value of the first derivative becomes zero for the fifth time corresponds to the Copper Eutectic Minimum Temperature.

### **2.13 Aluminum Copper Eutectic Growth Temperature ( $T_{E,G}^{Al-Cu}$ )**

This is the maximum temperature corresponding to the steady state growth of the Copper rich eutectic phase. At this temperature the sample experiences a temperature rise because the latent heat release due to eutectic formation surmounts the heat extraction from the sample. In Figure 2, the point at which the value of the first derivative becomes zero for the sixth time immediately after the Al-Cu eutectic minimum reaction corresponds to the Aluminum Copper Eutectic Growth reaction temperature.

### **2.14 Solidus Temperature ( $T_{SOL}$ )**

This temperature indicates the completion of the solidification process. This point is detected using the First Derivative curve in as seen Figure 1. This point corresponds to the point of intersection of tangents 7 and 8 drawn on the first derivative curve. The value of the fraction solid at this point is one.

## References

- Alu-Select, "Tempers Overview", [on line Nov. 4, 2004],  
<http://aluminium.matter.org.uk/aluselect/tempers.htm>
- Apelian, D., Dorfmueller, A., Hitchcock, T., "The Cost-value Relationship of Metal Casting Technology", *Modern Casting*, V.86, No.11, pp.39-43, (November, 1996).
- Ashby, M. F., "Multi-Objective Optimization in Material Design and Selection", *Acta Materialia*, V.48, pp. 359-369, (2000).
- Ashland Inc., "The Ashland Process", Technical Bulletin No. 1798-1, Ashland Chemical Company, Ohio, (1994).
- ASM International, *ASM Handbook, Heat Treating*, The Materials Information Society, V.4, Ohio, pp. 863,(1992).
- Bäckerud, L, Chai, G., Tamminen, J., "Solidification Characteristics of Aluminum Alloys", *AFS/SKANALUMINIUM*, Illinois, (1990).
- Bäckerud, L., "How Does a Good Grain Refiner Work?", *Light Metals Age*, V.43, pp.6-12, (Oct.1983).
- Barlow, J. O. and Stefanescu, D. M., "Computer-Aided Cooling Curve Analysis Revisited," *AFS Transactions*, V.105, pp. 349-354, (1997).
- Beale, M. H., Demuth, H. B., Hagan, M. T., *Neural Network Design*, University of Colorado Bookstore, Boulder, Colorado, (2002).
- Beale, M., Demuth, H., *Neural Network Toolbox, User's Guide Version 4*, The Math Works Inc., Natick, Massachusetts, (2001).
- Bhadeshia, H. K .D. H., "Neural Networks in Materials Science", *ISIJ International*, V. 39, No.10, pp. 966-979, (1999).
- Boudreault, G., Samuel, A. M., Samuel, F. H., Doty, H. W., "Porosity Formation in 319 Aluminum Alloy Sand Castings in Relation to Product Quality for Automotive Applications", *Light Metals*, 36<sup>th</sup> Annual Conference of Metallurgists, Sudbury, Ontario, pp. 369-384, (1997).
- Brahma, D. E. O., Deb, K, Jha, S., Sudhakar, V., Sridhar, N. V., "Optimal Operating Conditions for the Primary End of an Integrated Steel Plant: Genetic Adaptive Search and Classical Techniques", *ISIJ International*, V. 38, No. 1, pp. 98-105, (1998).

- Burford, J., Personal Communication, [Nov.4, 2004].
- Byczynski, G. E., Djurdjevic, M. B., Francis, R., Kierkus, W. T., Lashkari, R. S., Sokolowski, J. H., "Modelling of the Latent Heat of Solidification of the Multi-Component Al-Si Alloys Using Thermal Analysis", Proceedings of the 15<sup>th</sup> International Conference of the Foundry Industry, Monterrey, Mexico, (2003).
- Byczynski, G. E., "The Strength and Fatigue Performance of 319 Aluminum Alloy Castings", Ph.D Thesis, University of Birmingham, (2002).
- Calcaterra, S., Campana, G., Tomesani, L., "Prediction of Mechanical Properties in Spheroidal Cast Iron by Neural Networks", Journal of Materials Processing Technology, V. 104, pp. 74-80, (2000).
- Campbell, J., "Castings", Butterworth – Heinemann Ltd., Oxford, UK, (1991).
- Campbell, J., "The Origin of Porosity in Castings", Proceedings of the 4<sup>th</sup> Asian Foundry Congress", Queensland, Australia, pp. 33-50, (1996).
- Chagoya, G. P., "Development of a Knowledge Based System for the Control of 319-Al Melt Quality and Prediction of Casting Characteristics", MASc. Thesis, University of Windsor, Windsor, (2001).
- Chakraborti, N., Mukherjee, A., "Optimization of Continuous Casting Mould Parameters Using Genetic Algorithms and Other Allied Techniques", Iron and Steel Making, V. 27, No. 3, pp. 243- 247, (2000).
- Chaudhury, S., Shankar, S., Apelian., D., Wert, J. V., "Short Cycle Heat Treating with Fluidized Beds: Microstructure Evolution", Proceedings of the AFS International Conference on Structural Aluminum Castings", Florida, pp.305-320, (2003).
- Chen, C., Wang, Z.P., Xu, J.L., "Neural Network Model in Predicting Mechanical Properties of Ductile Iron", AFS Transactions, V.110, pp. 1-7, (2002).
- Chen, X "The Effect of Novel Solution Treatment During the Solidification Process on the Structure and Mechanical Properties of the W319 Alloy", MASc. Thesis, University of Windsor, (2003).
- Chen, X., Kasprzak, M., Kasprzak, W., Sokolowski, J.H., "A Novel Solution Treatment with the Solidification Process as a Novel Economical Heat Treatment for Aluminum Based Castings", Proceedings of the 15<sup>th</sup> International Conference of the Foundry Industry, Monterrey, Mexico, (2003).
- Cloás, A.I.G, Valtierra, S., Cano, S., Mojica, J.F., "Aging in Heat Treatable Cast Aluminum Alloy", Proceedings of the 1<sup>st</sup> International Automotive Heat Treating Conference, Puerto Vallarta, Mexico, pp. 372-384, (1998).

- CMI Novacast Inc., "Electromagnetic Pump Operating Principle", [on line Nov.10, 2004]  
<http://www.cminovacast.com/CMItechpaper1.html#fig3back>
- Compos-Velho, H. F., Issamoto, Luz, J. I., Mikki, F. T., Oliviera, P. P. B., "A Neural Network Approach in a Backward Heat Conduction Problem", Proceedings of the IV Brazilian Conference on Neural Networks, pp. 019-024, (1999).
- Cosworth Technology, "Cosworth Process: Zircon Sand", [on line Nov. 6, 2004a]  
[http://www.cosworth-technology.co.uk/400\\_castings/430\\_zircon.htm](http://www.cosworth-technology.co.uk/400_castings/430_zircon.htm)
- Cosworth Technology, "Cosworth Process: Methodology", [on line Sept. 28, 2004b]  
[http://www.cosworth-technology.co.uk/400\\_castings/440\\_methodology.htm](http://www.cosworth-technology.co.uk/400_castings/440_methodology.htm).
- Crepeau, P.N., "Effect of Fe in Al-Si Casting Alloys: A Critical Review", AFS Transactions, V.103, pp.361-366, (1995).
- Dasgupta, R., Brown, C.C, Marek, S., "The Effect of Increased Magnesium Content on the Mechanical Properties of Sand Cast 319 Aluminum Alloys", AFS Transactions , V.97, pp.245-254, (1989).
- Dash, M., Makhlof, M., "Effect of Key Alloying Elements on the Feeding Characteristics of Aluminum-Silicon Alloys", Journal of Light Metals, V.1, pp. 251-265, (2001).
- Davis, J. R, " ASM Specialty Handbook: Aluminum and Aluminum Alloys", ASM International, Ohio, (1993).
- Denton, J. R, Spittle, J. A., "Solidification and Susceptibility of Hydrogen Absorption of Al-Si Alloys Containing Strontium", Materials Science and Technology, V.1, pp. (305-311), (1985).
- Derringer, G., Suich, R., "Simultaneous Optimization of Several Response Variables", Journal of Quality Technology, V. 12, No. 4, pp. 214-219, (1980).
- Devore, J. L., "Probability and Statistics for Engineering and the Sciences", 5th Ed., pp. 339, Duxbury Publishing Co., Pacific Grove, California, (1999).
- Dinnis, C. M., Taylor, J. A., Dahle, A. K., "Porosity Formation and Eutectic Growth in Al-Si-Cu-Mg Alloys Containing Iron and Manganese", Proceedings of the 9<sup>th</sup> International Conference on Aluminum Alloys", Brisbane, Australia, pp. 1016-1021, (2004).
- Dieter, G.E., "Mechanical Metallurgy", McGraw-Hill, New York, (1976).
- Djurdjevic, M. B., Kierkus, W.T., Personal Communication, Unpublished Data, (2000).

- Djurdjevic, M. B., Kasprzak, W., Kierkus, C. A., Kierkus, W. T., Sokolowski, J. H., "Quantification of Cu Enriched Phases in Synthetic 3XX Aluminum Alloys Using the Thermal Analysis Technique" AFS Transactions, V.109, pp. 1-13,(2001a).
- Djurdjevic, M. B., Jiang, H., Sokolowski, J. H., "On-line prediction of aluminum-silicon eutectic modification level using thermal analysis", Materials Characterization, V.46, pp. 31-38, (2001b).
- Djurdjevic, M. B., Kierkus, W. T., Sokolowski J. H., Evans, W., "Detection of the Dendrite Coherency Point of Al-3XX Series of Alloys using a Single Sensor Thermal Analysis Technique", Light Metals Symposium, Toronto, pp. 443-450, (2001c).
- Djurdjevic, M. B., Sokolowski, J. H., Hasenbusch, R., "Assessment of the Hydrogen Level in 319 Aluminum Alloy Melts using the Thermal Analysis Technique", Light Metals, Seattle, pp. 889-896, (2002a).
- Djurdjevic, M.B., Kierkus, W.T., Sokolowski, J.H., "Analysis of the Solidification Path of the 3XX Family of Aluminum Alloys", Technical Report submitted to the NEMAK Canada Corporation, Windsor, (October 2002b).
- Djurdjevic, M.B., Mitrasinovic, A., Sokolowski, J.H., "Development of the Silicon Equivalent Algorithm and Its Application for the Calculation of the Characteristic Temperatures of Solidification of Multicomponent 3XX Series of Al Alloys", Proceedings of the 15<sup>th</sup> International Conference and exposition of the Foundry Industry", Monterrey, Mexico, (2003a).
- Djurdjevic, M. B, Chen, X., Sokolowski, J. H., "Latent Heat Released During Solidification of 3XX Series of Aluminum Alloys", AFS Transactions, V.111, (2003b).
- Djurdjevic, M. B, Francis, R., Lashkari, R. S., Ngom, A., Sokolowski, J. H., "Applications of Artificial Neural Networks in the Prediction of Aluminum Silicon Modification Level of W319 Aluminum Alloys", AFS Transactions, V.111, (2003c).
- Djurdjevic, M. B., Francis, R., Sokolowski, J. H., Djuric, B., "Effect of Chemistry and Cooling Rate on the SDAS of the Hypoeutectic 3XX Aluminum Alloys", Proceedings of the 2<sup>nd</sup> International Symposium Light Metal and Composite Materials" Belgrade, pp.29-30, (2004a).
- Djurjevic, M.B., Francis, R., Sokolowski, J.H., Emadi, D., Sahoo, M., "Comparison of Different Analytical Methods for the Calculation of the Latent Heat of Solidification of 3XX Aluminum Alloys", Materials Science and Engineering A386, pp.277-283, (2004b).

- Easton, M. A., StJohn, D. H., "A Model of Grain Refinement Incorporating Alloy Constitution and Potency of Heterogeneous Nucleant Particles", *Acta Materialia*, V.49, pp.1867-1878, (2001).
- Emadi, D., Gruzleski, J.E., Toguri, J.M., "The Effect of Na and Sr Modification on Surface Tension and Volumetric Shrinkage of A356 Alloy and Their Influence on Porosity Formation", *Metallurgical Transactions B*, 24B, pp. 1055-1063, (1993).
- Foresee, F. D., Hagan, M. T., "Gauss-Newton Approximation to Bayesian Learning", *International Conference on Neural Networks*, V. 3, pp. 1930-1935, (1997).
- Foti, R., "Three Suppliers Share the Latest in Coldbox Binder Systems", *Modern Casting*, pp. 45-49, (June 1999).
- Francis, R., Kierkus, W. T., Sokolowski, J. H., "Calibration of the Thermocouples Used for the Thermal Analysis", *IRC, Report*, Windsor, (Nov. 2001).
- Fras, E., Kapturkiewicz, W., Burbilko, A., Lopez, H. F., "A New Concept in Thermal Analysis of Castings", *AFS Transactions*, V.101, pp. 505-511, (1993).
- Fuchs, H., Wappelhorst, M., "Light Metal Materials for Engine Blocks and Cylinder Heads Subject to Heavy Stress Loads", *MTZ Worldwide*, V.64, pp.49-53, (2003).
- Gallois, B., Sigworth, G.K., "An Analysis of Eutectic Modification", *Proceedings of the Conference on Thermal Analysis of Molten Aluminum*, Illinois, pp.101-119, (1984).
- Geng, P., Tseng, M., Qian, C., "ANN Optimization Method for High Strength High Fracture Toughness Steels.", *Journal of Materials Science and Technology*, V.14, pp.185-187, (1998).
- George Mason University, "Process Improvement: Advice", [online Nov. 23, 2004a], [http://gunston.doit.gmu.edu/healthscience/708/which\\_8.htm](http://gunston.doit.gmu.edu/healthscience/708/which_8.htm)
- George Mason University, "Process Improvement: Tukey Charts", [online Nov. 23, 2004b], <http://gunston.doit.gmu.edu/healthscience/708/frTukey.asp#Assignment>
- Gouwens, P. R., and Gouwens, L. A., "Controlled Pouring of Aluminum Castings", [online Sept. 28, 2004], <http://www.cminovacast.com/CMIttechpaper4.html#top>.
- Gruzleski, J.E., "Microstructure Development During Metal Casting", *AFS Inc.*, Illinois, (2000).
- Gruzleski, J. E., Closset, B. M., "The Treatment of Liquid Aluminum Silicon Alloys", *AFS Inc.*, Illinois, (1990).



- Gustafsson, G. Thorvaldsson, T. Dunlop, G.L., "The Influence of Fe and Cr on the Microstructure of Cast Al-Si-Mg Alloys", *Met. Trans.*, V. 17A, pp. 45-52, (1986).
- Heine, H. J., "Using Master Alloys for Aluminum Grain Refinement and Modification", *Foundry M & T*, pp. 31-40, (May 1985).
- Heusler, L., Schneider, W., "Influence of Alloying Elements on the Thermal Analysis Results of Al-Si Cast Alloys", *Journal of Light Metals*, V.2, pp.17-26, (2002).
- Hu, J. F., Pan, E. N., "Determination of Latent Heat and Changes in Solid Fraction during Solidification of Al-Si Alloys by the CA-CCA Method", *International Journal of Cast Metals Research*, V.10, pp. 307-319, (1998).
- IRC Brochure, "A Novel Industry Wide Thermal Quality Control Platform (NTQCP) for Materials, Processes and Cast Components", Windsor, (2004a).
- IRC Brochure, "Aluminum Thermal Analysis Platforms for Integrated Characterization of Master Alloys, Ingots, Melts, Cast Components and their Processes", Windsor, (2004b).
- Jiang, H., Kierkus, W. T., Sokolowski, J. H., "Determining Dendrite Coherency Point Characteristic of Al Alloys Using the Single Thermocouple Technique", *AFS Transactions*, V.68, pp.169-172, (1999).
- Johnsson, M., "Grain Refinement of Aluminum Studied by use of a Thermal Analytical Technique", *Thermochimica Acta*, V. 256, pp.107-121, (1995).
- Jolly, M., Cox, M., Harding, R., Griffiths, B., Campbell, J., "Quiescent Filling Applied to Investment Castings", *Modern Casting*, pp 36-39, (Dec. 2002).
- Juan, H., Yu, S.F., Lee, B.Y., "The Optimal Cutting Parameter Selection of Production Cost in HSM for SKD61 Tool Steels", *International Journal of Machine Tools and Manufacture*, V. 43, pp. 679-686, (2003).
- Kanicki, D.P., "Changing casting demands shape Ford's New Foundry", *Modern Casting*, 24-27, (Sept. 1994).
- Kasprzak, M., Kasprzak, W., Kierkus, W. T., Sokolowski, J. H., "Method and Apparatus for Universal Metallurgical Simulation and Analysis", Patent, PCT/CA02/01903, Canada, (2002).
- Kasprzak, W., Kierkus C. A., Kierkus W. T, Sokolowski J. H., Kasprzak M., Evans, W. J., "The Structure and Matrix Microhardness of the 319 Aluminum Alloy After Isothermal Holding During the Solidification Process", *AFS Transactions*, V.109, pp. 1-13, (2001).

- Keist, J., Bergman, C., "Short Cycle Heat Treating with Fluidized Beds: Optimizing Mechanical Properties", Proceedings of the AFS International Conference on Structural Aluminum Castings", Florida, pp.297-304, (2003).
- Kierkus, W. T., Djurdjevic, M. B., Sokolowski, J. H., "A Comparative Study of Cooling Curve Parameters for Different Thermal Mass Crucibles and Thermocouple Assemblies", IRC Confidential Report, Windsor, (June, 2002).
- Kierkus, W. T., Sokolowski, J. H., "Recent Advances in Cooling Curve Analysis: A New Method for determining the 'Base Line' Equation", AFS Transactions, V.107, pp.161-167, (1999).
- Kinzie P.A., "Thermocouple Temperature Measurement", John Wiley & Sons Inc. New York, (1973).
- Kirgin, K.H., "Shipments to Rebound 3% in '02: Begin Healthy Expansion", Modern Casting, pp.24-28, (January, 2002).
- Kirkpatrick,S., Gellatt, C. D., Vechhi, M. P., "Optimization by Simulated Annealing", Science, V. 220 (4958), pp.671-680, (1983).
- Kozhanov, V. A., Alekseichuk, I. S., Bychkov, Yu. B., "Selective Effect of Mn on the Form of Iron Bearing Phases in Silumins", Tsventye Metally., V.26, pp.91-92, (1985).
- Kusiak, J., Kuziak, R., "Modelling of the Microstructure and Mechanical Properties of Steel Using the Artificial Neural Network", Journal of Materials Processing Technology, V.127, pp.115-121, (2002).
- Lasa, L., Rodriguez-Ibabe,J. M., "Characterization of the Dissolution of the Al<sub>2</sub>Cu Phase in Two Al-Si-Cu-Mg Casting Alloys Using Calorimetry", Materials Characterization, V.48, pp. 371-378, (2002).
- Lehr, M. A., Rumelhart, D. E., Widrow, B., " The Basic Ideas in Neural Networks", Communications of the ACM, , V. 37, No. 3, pp. 87-92, (March 1994).
- Li, D., Liu, Y., Meng, F., Zhang, Y., "Study on Thermal Analysis Models Used in Grey Cast Iron Quality Prediction", International Journal of Cast Metals Research, V.11, pp. 391 –394, (1999).
- Liu, L., Samuel, A. M., Samuel, F. H., Doty, H. W., Valtierra, S., "Influence of Oxides on Porosity formation in Sr treated Al-Si Casting Alloys", Journal of Materials Science, V. 38, pp.1255-1267, (2003).

- Louvo, A., "The Development of Melt Quality Control Systems Based on Derivative Thermal Analysis and the Microcomputer", Proceedings of the Conference on Thermal Analysis of Molten Aluminum", Illinois, pp.143-153, (1984).
- Lu, S., Hellawell, A., "Modification and Refinement of Cast Al-Si alloys", Light Metals, pp. 989-993, (1995).
- Lucas, A., Cáceres, C.H., Taylor, J.A., "Effect of the Si Content on the Size of the  $\beta$ -Al<sub>3</sub>FeSi Intermetallics in Al-Si-Cu-Mg Casting Alloys", Proceedings of the 9<sup>th</sup> International Conference on Aluminum Alloys, Brisbane, Australia, pp. 1216-1221, (2004).
- Luenberger, D. G., "Linear and Nonlinear Programming", Second Edition, Addison-Wesley Publishing, Massachusetts, (1984).
- Lumely, R. N., Polmear, I. J., Morton, A. J., "The Utilization of Secondary Aging to Improve the Mechanical Properties of Aluminum Alloys", Proceedings of the 1<sup>st</sup> International Light Metals Technology Conference, Brisbane, Australia, pp.377-382, (2003).
- Mackay, R.I., "Development of a New-Durable Al-Si Alloy for the Next Generation of the Engine Block Casting" Doctoral Dissertation, University of Windsor, (2003).
- MacKenzie, S.D., "Quenching and the Control of Residual Stresses and Distortion in Aluminum", Proceedings of the AFS International Conference on Structural Aluminum Castings", Florida, pp.287-296, (2003).
- Major, F., Apelian, D., "A Microstructural Atlas of Common Commercial Al-Si-X Structural Castings" Proceedings of the AFS International Conference on Structural Aluminum Castings", Florida, pp. 267-285, (2003).
- Major, F., Personal Communication, (March, 2004).
- Major, J. F., McLeod, A., Rutter, J. W., "Designed Experimentation: Microstructural Optimization of Al AA512 for the PM Process and Its Possible Use as a Structural Die Casting", AFS Transactions, V.108, pp. 287-296, (2000).
- Makhlouf, M., and Guthy, H.V., "The Aluminum-Silicon Eutectic Reaction: Mechanisms and Crystallography", Journal of Light Metals, V.1, 199-218, (2001).
- Makhlouf, M. M., Apelian, D., Chaudhury, S.K., Bergman, C., "Heat Treatment of Aluminum Cast Components in Fluidized Beds", Proceedings of the 1<sup>st</sup> International Light Metals Technology Conference, Brisbane, Australia, pp.371-376, (2003).

- Malinov, S., McKeown, J. J., Sha, W., “Modelling the Correlation between Processing Parameters and Properties in Titanium Alloys using Artificial Neural Network”, *Computational Materials Science*, V. 21, pp. 375-394, (2001).
- Malinov, S., Sha, W., “Application of Artificial Neural Networks for Modelling Correlations in Titanium Alloys”, *Materials Science and Engineering A365*, pp.202-211, (2004).
- McDonald, S. D., Nogita, K., Dahle, A. K., Taylor, J. A., St.John, D. H., “Eutectic Solidification and Porosity Formation in Al-Si Alloys: Role of Strontium”, *AFS Transactions*, Vol. 108 pp. 463-470, (2000).
- Metropolis, N., Rosenbluth, A., Teller, A., Teller, E., “Equation of State Calculations by Fast Computing Machines”, *Journal of Chemical Physics*, 21, pp.1087-1092, (1953).
- Meyer, P., Plumail, F., “Development of a new casting process for aluminum cylinder blocks at MONTUPET: the Sand Hybrid Low Pressure Process” Technical Report, Montupet S.A., (May 2002).
- Minitab Inc., “Calculating the variance components (VarComp column) in a Gage R&R Study (Nested) by hand”, [online], Sept.19, 2004a.  
<http://www.minitab.com/support/docs/varcomp.pdf>
- Minitab Inc., “Users Guide 2: Data Analysis and Quality Tools”, Pennsylvania, (2000).
- Minitab Inc., “How MINITAB calculates the desirability values when using the Response Optimizer?”, [Online] October, 19, 2004b.  
<http://www.minitab.com/support/docs/DesirabilityCalculations.pdf>
- Mitra, A. “Fundamentals of Quality Control and Improvement”, Macmillan Publishing Company, New York, (1993).
- Mitrasinovic, A., “Development of Thermal Analysis and Analytical Techniques for the Assessment of Porosity and Metallurgical Characteristics in 3XX Aluminum Alloys”, MASC Thesis, University of Windsor, (2004).
- Mohanty P. S., Gruzleski, J. E., “Mechanisms of Grain Refinement in Aluminum”, *Acta Metallurgica et Materilia* 43(5), pp. 2001-2012, (1995).
- Montgomery D. C, Runger G. C, “ Applied Statistics and Probability for Engineers”, John Wiley & Sons Inc., New York, (1999).
- Montgomery, D. C., “Design Analysis of Experiments”, John Wiley & Sons, Inc., New York, (2001).

- Morice, J., "History of Thermal Analysis and its Applications", Proceedings of the Conference on Thermal Analysis of Molten Aluminum", Illinois, pp.37-75, (1984).
- Moustafa, M.A., Samuel, F.H., Doty, H.W., Valtierra, S., "Effect of Mg and Cu Additions on the Microstructural Characteristics and Tensile Properties of Sr-modified Al-Si Eutectic Alloys", Int. J. Cast Metals Res., V.14, 235-253, (2002).
- Murali, S., Raman, K.S., Murthy, K.S.S., "Effect of Magnesium, Iron, and Solidification Rates on the Fracture Toughness of Al-7Si-0.3Mg Casting Alloy", Materials Science and Engineering, A151, pp.1-10, (1992).
- Narayanan A., L., Samuel, F. H., Gruzleski, J. E., "Crystallization Behavior of Iron-Containing Intermetallic Compounds in 319 Aluminum Alloy", Met. and Mat. Trans, V. 25A, pp. 1761-1773, (1994).
- Narayanan, A. L., "Crystallization and Dissolution Studies of Iron Intermetallics in Al-Si Alloys", Ph.D. Thesis, McGill University, Montreal, (1994).
- Narayanan, A. L., Samuel, F.H., "Dissolution of Iron Intermetallics in the Al-Si Alloy through Non-Equilibrium Heat Treatment", Metallurgical and Materials Transactions A, V. 26(8), pp. 2164-2170, (1995).
- National Institute of Standards and Technology (NIST), "Calibration", [online] Sep 20, 2001, <http://www.itl.nist.gov/div898/handbook/pmd/section1/pmd132.htm>
- Nicholas J. V., White D. R., "Traceable Temperatures: An Introduction to Temperature Measurement and Calibration", John Wiley & Sons Inc., New York, (1994).
- Nogita, K., Dahle, A.K., "Eutectic Solidification in hypoeutectic Al-Si alloys: Electron Backscatter Diffraction Analysis", Materials Characterization, 46, pp.305-310, (2001).
- Nogita, K., McDonald, S. D, Dahle, A. K, "Modification of Al-Si Alloys", Proceedings of the 9<sup>th</sup> International Conference on Aluminum Alloys, Brisbane, Australia, pp. 945-950, (2004).
- Northern Illinois University – Department of Mechanical Engineering, "Thermocouple Calibration ", [online] Sep. 18, 2001, [http://www.kostic.niu.edu/tc\\_cal.html](http://www.kostic.niu.edu/tc_cal.html)
- Novacast, "ATAS<sup>®</sup> - Product Overview", [online] Sept. 12, (2004).  
<http://www.novacast.se/atasover.htm>
- Old Dominion University – Department of Electrical and Computer Engineering, "A Comparison of Three Neural Network Architectures for Automatic Speech

- Recognition ”, [online] Sep. 16, 2002.,  
<http://web.odu.edu/engr/speechlab/paper2.pdf>.
- Omega Engineering, Inc., “Introduction to Thermocouples”, [online] Sep 18, 2001,  
<http://www.omega.com/techref/themointro.html>
- Omega Engineering, Inc., “The Temperature Handbook™, 21<sup>st</sup> Century™ Edition ”, pp Z-39, (2000).
- Park, J., Kim, K. J., Kang, D. Y, Lee, Y., Kim, Y. H., “An Experimental Study on the Optimization of the Powder Forging Parameters for an Aluminum Alloy Piston”, *Journal of Materials Processing Technology*, V.113, 486-492, (2001).
- Perzyk, M., Kochanski, A. W., “Prediction of Ductile Iron Quality by Artificial Neural Networks”, *Journal of Materials Processing Technology*, V.109, pp.305-307,(2001).
- Pharm, D. T., Karaboga, D., “Intelligent Optimization Techniques”, Springer Verlag Ltd., London, (2000).
- Pospichal, J., Svozil, D., Vladimir, K., “Introduction to Multi-layer-feed-forward Networks”, *Chemometrics and Intelligent Laboratory Systems*, V. 39, pp. 43-62, (1997).
- Ren, Q., “Optimization of 3XX Aluminum alloy Microstructures and Mechanical Properties for New Generation Ford Motor Company Engine Blocks”, Masters Thesis, University of Windsor, Windsor, (2000).
- Ross.P. J., "Taguchi Techniques for Quality Engineering: Loss Functions, Orthogonal Experiments, Parameter and Tolerance Design", McGraw-Hill, New York, (1988).
- Sablonnière,H., de la, Samuel, F. H., “Solution Heat Treatment of 319 Aluminum Alloy containing ~0.5wt.%Mg Part 1-Solidification and Tensile Properties”, *International Journal of Cast Metals Research.*, V. 9, pp. 195-211, (1996a).
- Sablonnière,H., de la, Samuel, F. H., “Solution Heat Treatment of 319 Aluminum Alloy containing ~0.5wt.%Mg Part 2-Microstructure and Fractography”, *International Journal of Cast Metals Research.*, V.9, pp. 213-225, (1996b).
- Sadagopan, D., Pitchumani, R., “Application of Genetic Algorithms to Optimal Tailoring of Composite Materials”, 58, pp. 571-589, (1998).
- Saga, M., Kikuchi, M., “Effect of Sn Addition on the two-Step Aging Behavior in Al-Mg-Si Alloys for Automotive Applications”, *Proceedings of the 9<sup>th</sup> International Conference on Aluminum Alloys*”, Brisbane, Australia, pp.520-526, (2004).

- Samuel, A. M., Samuel, F. H., Villeneuve, C., Doty, H. W., Valtierra, S., "Effect of Trace Elements on  $\beta$ -Al<sub>5</sub>FeSi Characteristics, Porosity, and Tensile Properties of Al-Si-Cu (319) Cast Alloys", *International Journal of Cast Metals Research*, V.14, pp. 97-120, (2001).
- Schleg, F.P., "Technology of Metal Casting", AFS Inc., Illinois, USA, pp.215, (2003).
- Schmidt, D.C., "Eliminating modeling 'Trial and Error' with Casting Process Optimization", *Modern Casting*, , pp. 37-39, (August 2001).
- Sigworth, G.K., Guzowski, M.M., "Grain Refining of Hypoeutectic Al-Si Alloys", *AFS Trans.*, V.93, p.907-912. , (1985).
- Sigworth, G. K., Shivkumar, S., Apelian, D., "The Influence of Molten Metal Processing on Mechanical Properties of Cast Al-Si-Mg Alloys", *AFS Transactions*, V.97, , pp.811-824, (1989).
- Sigworth, G. K., Wang, C., Huang, H., Berry, J. T., "Porosity Formation in Modified and Unmodified Al-Si Castings", *AFS Transactions*, V.102, pp. 245-261, (1994).
- Sillèn, R. V., "Artificial Intelligence", *Cast Metal Times*, pp.15-17, (March, 2002).
- Sillèn, R. V., "Optimizing Iron Quality through Artificial Intelligence", *Modern Casting*, pp. 43-46, (November, 1996).
- Sokolowski, J. H., Djurdjevic, M. B., Kierkus, C. A., Northwood, D. O., "Improvement of 319 Aluminum Alloy Casting Durability by High Temperature Solution Treatment", *Journal of Materials Processing Technology*, V.109, pp.174-180, (2001).
- Sokolowski, J.H., Kierkus, C.A., Brosnan, B., Evans, W.J., "What Causes Electromagnetic Pump Clogging," *Modern Casting*, V. 93, n. 1, pp. 39-42, (January, 2003).
- Sokolowski, J. H., Kierkus, C. A., Brosnan, B., Evans, W. J., "Formation of Insoluble Ti (Al, Si)<sub>3</sub> Crystals in 356 Alloy Castings and Their Sedimentation in Foundry Equipment: Causes, Effects and Solutions", *AFS Transactions*, V.21, pp. 491-495, (2000).
- Sokolowski, J. H., Sun, X. C., Byczynski, G., Northwood, D. O., Penrod, D. E., Thomas, R., Esseltine, A., "The Removal of Copper-phase segregation and Subsequent Improvement in Mechanical Properties of Cast 319 Aluminum Alloys by a Two-Stage Solution Heat Treatment", *Journal of Materials Processing Technology*, V. 53, pp. 385-392, (1995).

- Song, R.G., Zhang, Q.Z., "Heat Treatment Technique Optimization for 7175 Aluminum Alloy by an Artificial Neural Network and Genetic Algorithm", *Journal of Materials Processing Technology*, V. 117, pp. 84-88, (2001a).
- Song, R. G., Zhang, Q. Z., Tseng, M. K, Zhang, B.J., "The Application of Artificial Neural Networks to the Investigation of Aging Dynamics in 7175 Aluminum Alloys", *Materials Science and Engineering: C3*, pp. 39-41, (1995).
- Song, R. G., Zhang, Q. Z., "Heat Treatment Optimization for 7175 Aluminum Alloy by Genetic Algorithm", *Materials Science and Engineering C*, 17, pp. 113-137, (2001b).
- Spada, A.T., "Castech: Mexico's New Aluminum Casting Heavyweight", *Modern Casting*, pp. 26-29, (July, 2000).
- Syrcos, G. P., "Die Casting Process Optimization Using Taguchi Methods", *Journal of Materials Processing Technology*, V. 135, pp.68-74, (2003).
- Tagiev, E., Holčec, S., Belov, N., "Optimization of the High Strength Casting Aluminum Alloys", *Materials Science Forum*, Vols. 217-222, pp. 289-292, (1996).
- Tarn, Y.S., Ma, S.C., Chung, L.K., "Determination of Optimal Cutting Parameters in Wire Electrical Discharge Machining", *International Journal of Machine Tools Manufacturing*, V.35, No.12, pp. 1693-1701, (1995).
- Taylor J. A., "Metal Related Castability Effects in Al Foundry Alloys", *Cast Metals* V.8, No.4, pp.225-252, (1995).
- Taylor J. A., Schaffer G. B., StJohn, D. H., "The Role of Iron in the Formation of Porosity in Al-Si-Cu-Based Casting Alloys: Part III. A Microstructural Model", *Metallurgical and Materials Transactions A*, V. 30, No. 6, pp. 1657-1662, (June 1999a).
- Taylor J.A.; Schaffer G.B.; StJohn D.H., "The Role of Iron in the Formation of Porosity in Al-Si-Cu-Based Casting Alloys: Part II. A Phase-Diagram Approach", *Metallurgical and Materials Transactions A*, V. 30, No. 6, pp. 1651-1656, (June 1999b).
- Tuttle, B. L., "Principles of Thermal Analysis for Molten Metal Process Control", *Proceedings of the Conference on Thermal Analysis of Molten Aluminum*, Illinois, pp.1-36, (1984).
- Valtierra, S.G, Mojica, B., Francisco, J., Oscar, G.O., "Method and Apparatus for Simplified Production of Heat Treatable Aluminum Alloy Castings", *US Patent #5,922,147*, (1999).



- Viswanathan, S., Sikka, V.K., Brody, H.D., "Using Solidification Parameters to Predict Porosity Distribution in Alloy Castings", *Journal of Materials Science*, pp.37-40, (September 1992).
- Waldner, P., Königsberger, E., Gamsjäger, H., "Computer-assisted Optimization of Cobalt Base Alloy Compositions", *Journal of Alloys and Compounds*, V.220, pp. 148-151, (1995).
- Wang, G., Bian, X., Wang, W., Zhang, J., "Influence of Cu and Minor Elements on Solution Treatment of Al-Si-Cu-Mg Cast Alloys", *Materials Letters*, V.57, pp.4083-4087, (2003a).
- Wang, Q., Li, Y. X., Li, X. C., "Grain Refinement of Al-7Si Alloys and Efficiency Assessment by Recognition of Cooling Curves", *Metallurgical and Materials Transactions A*, V.34A, pp. 1175-1182, (2003b).
- Wheeler, D.J., Lyday, R.W., "Evaluating the Measurement Process", 2<sup>nd</sup> Edition, SPC Press, Tennessee, (1989).
- Yarlagadda, K.D.V.P., Chiang, E.C.W., "A Neural Network System for the Prediction of Process Parameters in Pressure Die Casting", *Journal of Materials Processing Technology*, V.89-90, pp. 583-590, (1999).
- Zalensas, D. L., "Aluminum Casting Technology" 2<sup>nd</sup> Edition, AFS Inc., Illinois, (1993).
- Zhu, A.W., Gable, B.M., Shiflet, G.J., Starke Jr., E.A., "The Intelligent Design of Age Hardenable Wrought Aluminum Alloys", *Advanced Engineering Materials*, V.4, No. 11, pp. 839-846, (2002).

## VITA AUCTORIS

NAME: Robin Francis  
PLACE OF BIRTH: Kerala, India  
YEAR OF BIRTH: 1973  
EDUCATION: Mahatma Gandhi University, Kerala, India.  
1990-1993 BSc. (Chemistry).  
Anna University, Chennai, India.  
1993-1996 BTech. (Rubber Technology)  
Indian Institute of Technology (IIT), Kharagpur, India.  
1997-1999 MTech. (Reliability and Quality Engineering)  
University of Windsor, Windsor, Ontario, Canada  
2000- 2005 Ph.D. (Manufacturing Systems Engineering)

### LIST OF PUBLICATIONS:

- Djordjevic, M. B., **Francis, R.**, Sokolowski, J. H., Emadi, D., Sahoo, M., “Comparison of different analytical methods for the calculation of latent heat of solidification of 3XX aluminum alloys”, *Materials Science and Engineering A*, 386, pp. 277-283, (2004).
- Djordjevic, M. B., **Francis, R.**, Sokolowski, J. H., Djuric, B., “Effect of Chemistry and Cooling Rate on the SDAS of the Hypoeutectic 3XX Aluminum Alloys”, 2<sup>nd</sup> International Symposium on Light Metals and Composite Materials, Belgrade, pp. 29-30, (May 2004).
- Byczynski, G., Djurdjevic, M. B., **Francis, R.**, Kierkus, W. T., Lashkari, R. S., Sokolowski, J. H., “Modeling of the Latent Heat of Solidification of the Multi-component Al-Si Alloys Using Thermal Analysis”, *Proceedings of the 15<sup>th</sup> International Conference and Exposition of the Foundry Industry*, Monterrey, Mexico, (October, 2003).
- Djordjevic, M. B., **Francis, R.**, Lashkari, R. S., Ngom, A., Sokolowski, J. H., “Application of Artificial Neural Networks in the Prediction of the Aluminum Silicon Modification Level of W319 Aluminum Alloys”, *AFS Transactions*, (03-095), Vol. 111, (2003).